Final Report

DEVELOPMENT OF A NOVEL APPROACH FOR FATIGUE LIFE PREDICTION OF STRUCTURAL MATERIALS

(N00014-05-1-0777)

Yanyao Jiang
Department of Mechanical Engineering (312)
University of Nevada, Reno
Reno, NV 89557
Phone: 775-784-4510, Fax: 775-784-1701, E-mail: yjiang@unr.edu

20090220317

Submitted to

Dr. **Asuri K. Vasudevan**

Scientific Officer
Office of Naval Research, Code-332
875 North Randolph Street, Suite 1425, Room- 629
Arlington, VA 22203

December 2008

DTIC® DEFENSE TECHNICAL INFORMATION CENTER

Information for the Defense Community

Month Day Year

DTIC® has determined on 02 23 2009 *that this Technical Document has the Distribution Statement checked below. The current distribution for this document can be found in the DTIC® Technical Report Database.*

☒ **DISTRIBUTION STATEMENT A.** Approved for public release; distribution is unlimited.

☐ **© COPYRIGHTED.** U.S. Government or Federal Rights License. All other rights and uses except those permitted by copyright law are reserved by the copyright owner.

☐ **DISTRIBUTION STATEMENT B.** Distribution authorized to U.S. Government agencies only. Other requests for this document shall be referred to controlling office.

☐ **DISTRIBUTION STATEMENT C.** Distribution authorized to U.S. Government Agencies and their contractors. Other requests for this document shall be referred to controlling office.

☐ **DISTRIBUTION STATEMENT D.** Distribution authorized to the Department of Defense and U.S. DoD contractors only. Other requests shall be referred to controlling office.

☐ **DISTRIBUTION STATEMENT E.** Distribution authorized to DoD Components only. Other requests shall be referred to controlling office.

☐ **DISTRIBUTION STATEMENT F.** Further dissemination only as directed by controlling office or higher DoD authority.

Distribution Statement F is also used when a document does not contain a distribution statement and no distribution statement can be determined.

☐ **DISTRIBUTION STATEMENT X.** Distribution authorized to U.S. Government Agencies and private individuals or enterprises eligible to obtain export-controlled technical data in accordance with DoDD 5230.25.

REPORT DOCUMENTATION PAGE

Form Approved
OMB No. 0704-0188

The public reporting burden for this collection of information is estimated to average 1 hour per response, including the time for reviewing instructions, searching existing data sources, gathering and maintaining the data needed, and completing and reviewing the collection of information. Send comments regarding this burden estimate or any other aspect of this collection of information, including suggestions for reducing the burden, to Department of Defense, Washington Headquarters Services, Directorate for Information Operations and Reports (0704-0188), 1215 Jefferson Davis Highway, Suite 1204, Arlington, VA 22202-4302. Respondents should be aware that notwithstanding any other provision of law, no person shall be subject to any penalty for failing to comply with a collection of information if it does not display a currently valid OMB control number.

PLEASE DO NOT RETURN YOUR FORM TO THE ABOVE ADDRESS.

1. REPORT DATE *(DD-MM-YYYY)*
12-29-2008

2. REPORT TYPE
Final Report

3. DATES COVERED *(From - To)*
April 2005-December 2008

4. TITLE AND SUBTITLE
DEVELOPMENT OF A NOVEL APPROACH FOR FATIGUE LIFE PREDICTION OF STRUCTURAL MATERIALS

5a. CONTRACT NUMBER
N00014-05-1-0777

5b. GRANT NUMBER

5c. PROGRAM ELEMENT NUMBER

6. AUTHOR(S)
Yanyao Jiang

5d. PROJECT NUMBER

5e. TASK NUMBER

5f. WORK UNIT NUMBER

7. PERFORMING ORGANIZATION NAME(S) AND ADDRESS(ES)
Department of Mechanical Engineering (312)
University of Nevada, Reno
Reno, NV 89557

8. PERFORMING ORGANIZATION REPORT NUMBER

9. SPONSORING/MONITORING AGENCY NAME(S) AND ADDRESS(ES)
Asuri K. Vasudevan, Scientific Officer
Office of Naval Research, Code-332
875 North Randolph Street, Suite 1425, Room- 629
Arlington, VA 22203

10. SPONSOR/MONITOR'S ACRONYM(S)

11. SPONSOR/MONITOR'S REPORT NUMBER(S)

12. DISTRIBUTION/AVAILABILITY STATEMENT

13. SUPPLEMENTARY NOTES

14. ABSTRACT

Experiments were conducted to study the fatigue initiation and crack growth of four structural materials: aluminum 7075T651 alloy, stainless steel AL6-XN, stainless steel 304L, and Aerospace Steel 4340. It was confirmed that fatigue can occur under compression-compression loading for the aluminum alloy. Results from multiaxial fatigue experiments revealed that the fatigue cracking behavior was material and loading amplitude dependent. Under cyclic pure shear loading, the S-N curves of aluminum alloy and the stainless steel AL6-XN displayed a distinct kink that was related to a change in the cracking behavior. The R-ratio affected the crack growth of all the four materials under investigation. For the7075T651 and AL6-XN, a single overload resulted in an immediate reduction in the crack growth rate in the subsequent loading. For the AISI 304L alloy and 4340 steel, a short-lived increase in crack growth was observed right after the application of an overload. A new approach was found to be promising for the prediction of the crack growth from a notch, the R-ratio effect, and the effect of the overload.

15. SUBJECT TERMS
Fatigue, cyclic plasticity, crack growth, R-ratio effect, overload effect, aluminum alloy, AL6-XN, 4340 steel

16. SECURITY CLASSIFICATION OF:			17. LIMITATION OF ABSTRACT	18. NUMBER OF PAGES	19a. NAME OF RESPONSIBLE PERSON
a. REPORT	b. ABSTRACT	c. THIS PAGE			Yanyao Jiang
					19b. TELEPHONE NUMBER *(Include area code)*
U	U	U	UU	142	775-784-4510

Standard Form 298 (Rev. 8/98)
Prescribed by ANSI Std. Z39.18

Development of A Novel Approach for Fatigue Life Prediction of Structural Materials

SUMMARY

The objectives of the research are to (i) bridge the two stages of fatigue process by developing an innovative and robust approach for the fatigue damage assessment of structural materials, (ii) develop numerical models for accurate and reliable elastic-plastic stress analysis, (iii) demonstrate the viability, suitability, and superiority of the approach with benchmark experiments and, (iv) develop an accurate internal stress analysis model that can be incorporated into the *two-parameter* (ΔK-K_{max}) methodology to consider the short crack and overload/underload effects.

Extensive experiments were conducted to study the fatigue initiation and crack growth of four structural materials: aluminum 7075T651 alloy, stainless steel AL6-XN, stainless steel 304L, and Aerospace Steel 4340. Fatigue and cyclic plasticity experiments were conducted to explore the fundamental deformation and fatigue properties of the structural materials. By using the aluminum alloy, it was experimentally confirmed that fatigue can occur under compression-compression loading. Results from multiaxial fatigue experiments revealed that the fatigue cracking behavior was material dependent and loading amplitude dependent. Under cyclic pure shear loading, the *S-N* curves of aluminum alloy 7075T651 and stainless steel AL6-XN displayed a distinct kink that was related to a change in the cracking behavior. Several multiaxial fatigue criteria were evaluated by using the experimental crack initiation results.

The comprehensive crack growth experiments on the structural materials provided a solid base to understand the influences of different factors. The *R*-ratio affected the crack growth of all the four materials under investigation. For the aluminum alloy and AL6-XN stainless steel, a single overload resulted in an immediate reduction in the crack growth rate in the subsequent loading. For the AISI 304L alloy and 4340 aerospace steel, a short-lived increase in crack growth was observed right after the application of an overload. Such an increase in crack growth rate is especially pronounced in 4340 material. The crack growth rate decreased and reached a minimum rate before it gradually approached to the stable crack growth observed under constant amplitude loading. The crack growth behavior under high-low sequence loading displayed a similar phenomenon to that was observed for the overload. The *two-parameter* (ΔK-K_{max}) model was found to be able to model the *R*-ratio effect well for all the four materials under investigation. By considering the plastic zones created by the applied load, the driving force concept combining ΔK and K_{max} can be used to model the overload effect and the high-low loading sequence effect. The new approach based upon cyclic plasticity and crack initiation of the material was found to be promising for the prediction of the crack growth from a notch, the *R*-ratio effect, and the effect of the overload.

TABLE OF CONTENTS

LIST OF TABLES

LIST OF FIGURES

I. EXPERIMENTS

1 70705-T651 ALUMINUM ALLOY

Aluminum alloys are widely used in the aircraft industry due to the high strength-to-density ratio. Extensive studies have been conducted to understand the fatigue behavior of aluminum alloys over the years. Most experimental studies on aluminum alloys were concentrated on uniaxial tension-compression loading with the mean stress effects [1-4]. Stress-life and strain-life methods are often used based on the stabilized stress-strain hysteresis loops. It is often found that in the lower plastic strain region, the Coffin-Manson relationship does not obey the single slope behavior for the aluminum alloys. Endo and Morrow [1] observed that the usual linear log-log relationships between the fatigue life and the elastic and plastic strains did not provide an adequate correlation of the experimental results for 2024-T4 and 7075-T6 aluminum alloys. Sanders et al. [5] showed that the plots of the plastic strain amplitude versus the fatigue life for the aluminum alloys reflected the linearity of the Coffin-Manson relationship down to a critical level of plastic strain. The deviation of the fatigue results of the aluminum alloys from the single slope behavior of a Coffin-Manson plot was related to the relative inability of the microstructure to develop homogenous slip during low plastic strain cycling. Fatemi et al. [6] applied a bi-linear relationship to the stress amplitude versus fatigue life curve of 14 aluminum alloys, including 7075 aluminum alloy. It was shown that the bi-linear S-N model provided a better representation of the data than the commonly used single slope linear approach.

On the microstructural level, it was observed that cracked constituent particles represented the majority of the observed fatigue crack nucleation sites in several aircraft aluminum alloys [7]. These constituent particles, which are inherent in the material, are formed during the cooling process when some of the alloying elements solidify more rapidly than the aluminum. The distribution of these particle sizes was treated as the initial crack sizes in predicting fatigue life [7]. A microstructure based multiscale fatigue model was developed to estimate the fatigue behavior of 7075 aluminum alloy with the consideration of damage incubation, microstructurally small crack growth, and long crack growth [8].

Despite comprehensive work, many questions remain to be answered. Limited efforts have been made on the multiaxial fatigue study of the aluminum alloys. Particularly, the cracking behavior of the aluminum alloys under different stress states has not been well investigated. In the current study, extensive fatigue experiments were conducted on 7075-T651 aluminum alloy under uniaxial, torsion, and axial-torsion loading. Different mean stresses were applied in the experiments to study the mean stress effect on fatigue behavior. Cracking behavior under different stress states was studied. Fatigue under compression-compression loading was experimentally investigated. The Smith-Watson-Topper (SWT) fatigue criterion and a modified SWT parameter were evaluated based on the experimental results.

In addition, series of crack propagation experiments were conducted on notched standard and non-standard compact tension (CT) specimens. The experiments were designed to examine the effect of *R*-ratio, overloading, underloading and high-low sequential loading under Mode I loading. The cracking behavior of the material under a combined loading of Mode I and Mode II was also studied. Notch effects on the fatigue behavior of the material are examined. Finally, an experimental investigation of crack propagation in mixed Mode I and Mode III conditions under combined axial-torsion loading was performed.

1.1 *MATERIAL*

The as-received materials were in cold-rolled state with three different geometries: plate with a thickness of 5 mm and cylindrical bars with diameters of 38 mm and 25.4 mm, respectively. The materials were acquired commercially in different stocks. An inspection of the microstructure was conducted to identify whether or not the materials were practically identical. Figure 1 shows the optical microstructures of the three batches of the materials used in the current investigation. Each stereography was synthesized from three microstructures taken on the sections perpendicular to the rolling (*x*) direction, the normal (*y*) direction, and the transversal (*z*) direction. The etchant used in microscopic examination was Keller's reagent (2ml HF (48%), 3ml HCl, 5ml HNO_3, 190 ml H_2O). Dark particle-like precipitates in the microstructures are $Cr_2Mg_3Al_{18}$ and $(Fe,Mn)Al_6$.

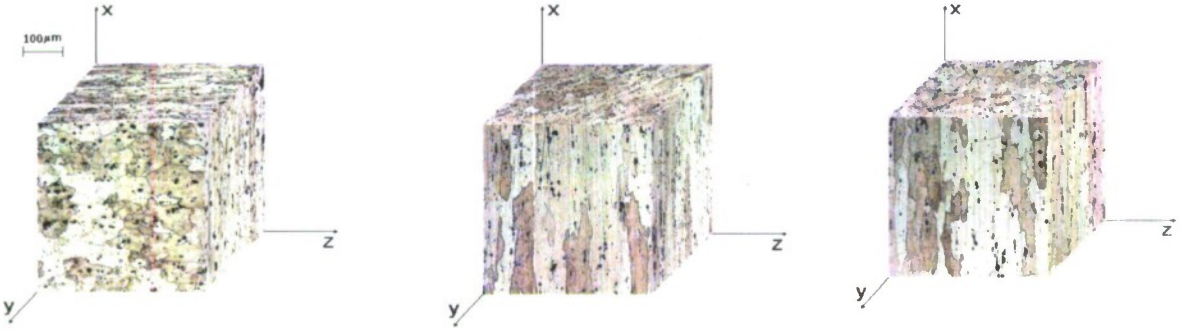

(a) Plate (b) 38 mm diameter bar (c) 25.4 mm diameter bar

Fig.1 Stereographic microstructure of the 70705-T651 ALUMINUM ALLOY

For the plate specimen, equiaxial grains were observed on the rolling plane (section perpendicular to the normal direction). The grain size varies from 10 microns to 100 microns. The average grain size is approximately 50 microns. On the sections perpendicular to the rolling direction and the transverse direction, fibrous grains were observed. The average thickness of grains is approximately 7 microns. It is a typical microstructure after cold rolling (disk-like grains). The two types of bars with different diameters have practically identical microstructures. On the section perpendicular to the axis, the grain size ranges from 10 microns to 40 microns. On the section parallel to the axis, fibrous grains are observed. The average length of grains along axial direction is about 70 microns. It is a typical microstructure after cold-drawn or cold extrusion (fibrous grains).

Regular monotonic experiments were conducted to determine the static material properties of the material and the results are summarized in Table 1. The true fracture stress and the true fracture strain of the material were obtained by conducting a monotonic torsion experiment using the solid shaft specimen. Figure 2 shows the shear stress-shear strain curve obtained from a round solid specimen subjected to monotonic torsion. The surface strain was measured by using an extensometer and the surface stress was determined following the Nadai's formula [9]. The torsion of a solid shaft can provide an experimental means to determine the true fracture stress and true fracture strain.

Table 1 Static material properties of 7075-T651

Elasticity Modulus, E	71.7GPa
Shear Modulus, G	27.5GPa
Poisson's Ratio, μ	0.306
Yield Stress, $\sigma_{0.2}$	501 MPa
Ultimate Strength, S_u	561 MPa
Elongation, e_f	9.7%
Reduction in Area, RA	29.1 %
True Shear Fracture Stress, τ_f	379 MPa
True Shear Fracture Strain, γ_f	0.42

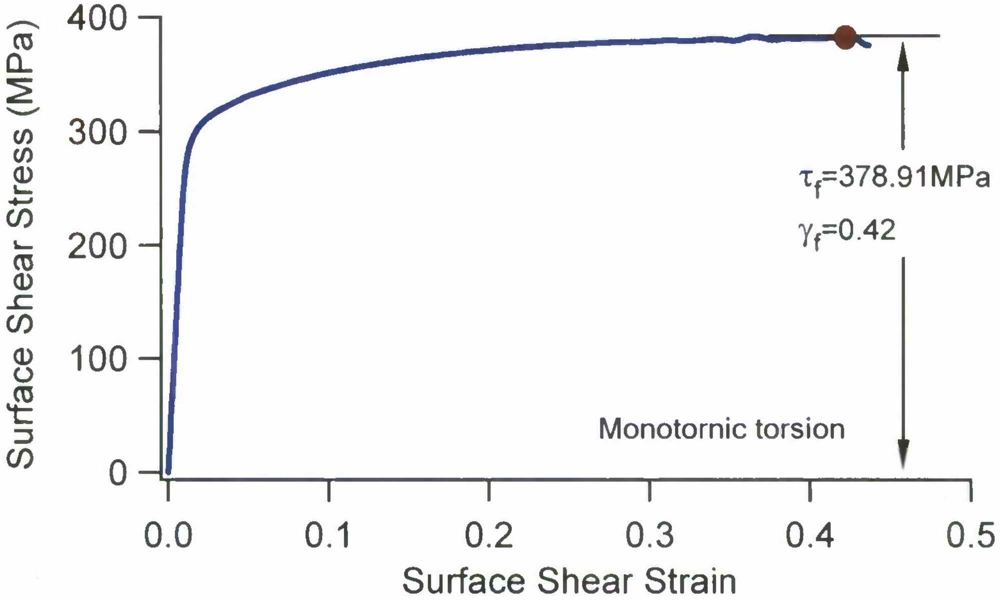

Fig.2 Shear stress-shear strain curve obtained from monotonic torsion of solid shaft specimen

1.2 *CRACK INITIATION EXPERIMENTS UNDER CONSTANT AMPLITUDE LOADING*

1.2.1 Specimens and testing equipment

Four types of smooth specimens, as shown in Fig.3, were used for fatigue and deformation experiments. They were uniaxial dog-bone shaped plate specimens (Fig.3(a)), uniaxial solid cylindrical specimens (Fig.3(b)), solid cylindrical specimen for torsion (Fig.3(c)), and tubular specimens for axial-torsion loading (Fig.3(d)). The dog-bone plate specimens were machined from a large plate. Both the uniaxial cylindrical solid specimen and the specimens for torsion were fabricated from a cylindrical bar with a diameter of 25.4 mm. A solid bar with a diameter of 38mm was used to fabricate the tubular specimens.

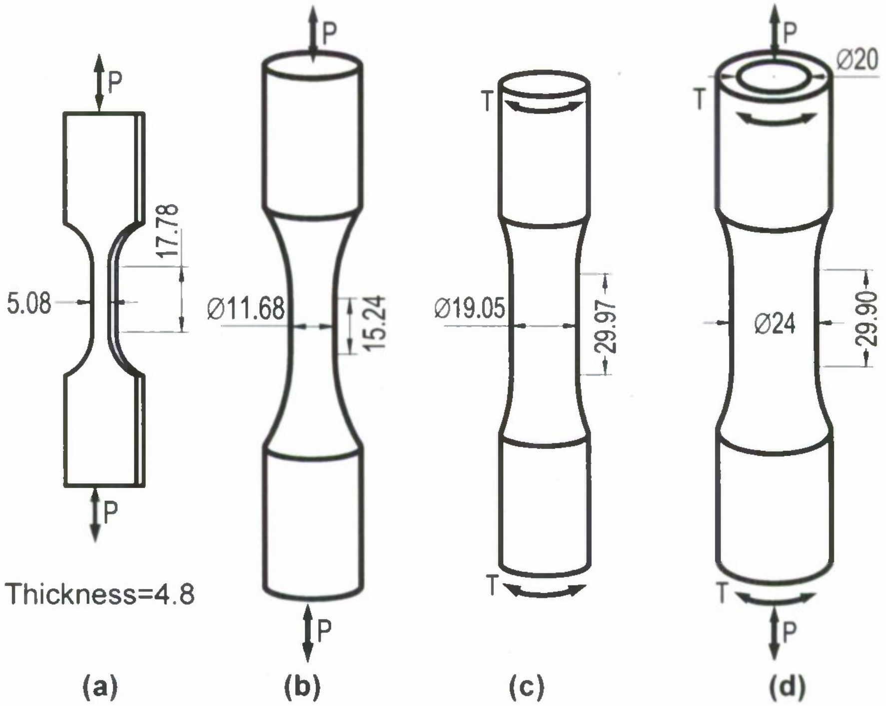

Fig.3 Specimens and loading conditions (all dimensions in mm)

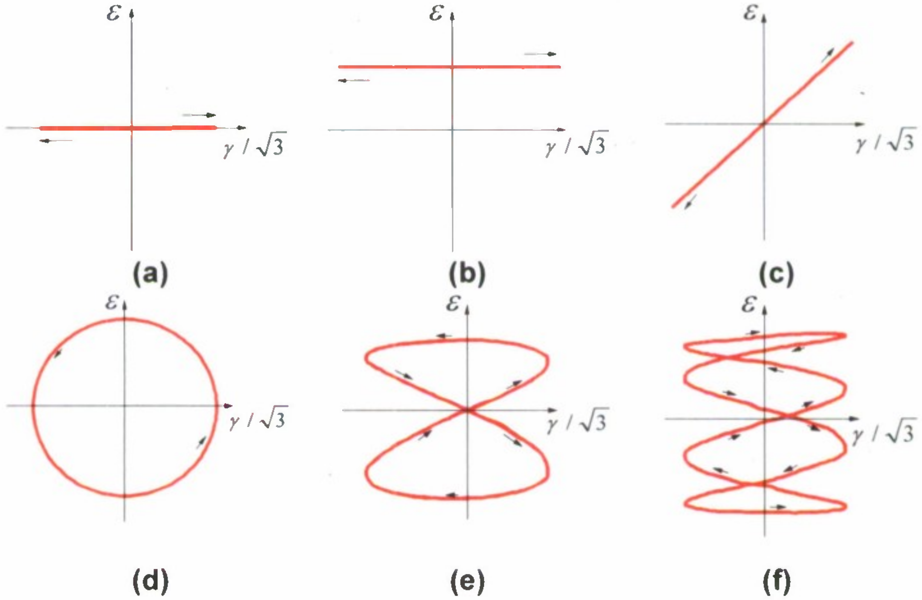

Fig.4 Loading paths for axial-torsion loading using tubular specimens

The loading conditions for four types of specimens are illustrated in Fig.3. For the tubular specimens, Fig.4 shows the six loading paths used in the axial-torsion experiments. Figure 4(a) is pure shear loading, and Fig.4(b) is the loading case with fully reversed shear and a static axial stress. Figure 4(c) is the proportional loading path. Figure 4(d) is a circular shaped axial-torsion nonproportional loading path. Loading paths shown in Fig.4(e) and Fig.4(f) are nonproportional loading paths with the ratios of the torsion loading frequency over the axial loading frequency being two and four, respectively.

An Instron Servohydraulic tension-torsion load frame was used for the fatigue experiments using the solid cylindrical specimens and the tubular specimens shown in Fig.3. The testing system, which has a capacity of ±2800 N·m in torque and ±222 kN in axial load, is equipped with the Instron 8800 electronic control, computer control, and data acquisition. A 12.7mm gage length uniaxial extensometer was used for the measurement of the strain in the gage section of the uniaxial specimen. The extensometer has a range of ±5% strain. For the tubular specimens and the specimens for torsion, a modified MTS extensometer was attached to the gage section of the specimen to measure the axial, shear, and diametral strains. The extensometer had a range of ± 5% in the axial strain, a range of ± 3 degrees in the torsion deformation, and 0.25 mm in the diametral direction. An Instron 8870 load frame with 8800 electronics and computer control was used for some of the uniaxial fatigue experiments using the plate specimens. The load cell of the testing machine has a capability of ±25kN axial load. All the experiments were conducted in ambient air.

1.2.2 Results of experiments

The detailed experimental fatigue results were summarized in Tables 2~5 and shown Figs. 5~9.

Table 2 Results from plate and dog-bone cylindrical uniaxial specimens

a) Dog-bone cylindrical uniaxial specimens under fully reversed strain-controlled loading

Spec #	$\frac{\Delta\varepsilon}{2}$ %	$\frac{\Delta\sigma}{2}$ MPa	σ_m MPa	N_f cycles	Spec #.	$\frac{\Delta\varepsilon}{2}$ %	$\frac{\Delta\sigma}{2}$ MPa	σ_m MPa	N_f cycles
TorS43	3.09	630.8	-0.2	25	TorS37	0.51	361.6	-3.6	9,112
TorS45_2	2.55	614.0	-2.3	58	TorS32	0.42	299.6	1.5	27,011
TorS41	2.02	592.9	-3.3	73	TorS33	0.34	240.0	1.1	99,287
TorS44	1.53	567.5	-5.2	125	TorS38	0.28	200.2	0.6	919,687
TorS39_2	1.23	555.2	-7.8	194	TorS34_1	0.21	150.0	0.4	1,063,477
TorS40	1.02	533.8	-7.2	390	TorS45_1	0.30	214.9	1.0	1,090,639
TorS34_2	0.81	512.2	-7.3	794	TorS39_1	0.29	210.1	1.4	1,108,763
TorS36	0.72	485.5	8.9	917					
TorS35	0.56	400.1	2.8	3,073					
TorS42	0.49	349.7	2.1	7,144					

$\Delta\varepsilon/2$ = axial strain amplitude, $\Delta\sigma/2$ = axial stress amplitude, σ_m =mean stress, N_f = fatigue life

Note: TorSxx_1 (xx is the specimen number) was tested without failure and TorSxx_2 was the same specimen tested after the first step. The second step usually had a much higher load amplitude than that of the first step.

b) 0° plate specimen

Spec No.	$\frac{\Delta\varepsilon}{2}$ %	$\frac{\Delta\sigma}{2}$ MPa	σ_m MPa	N_f cycles	Spec No.	$\frac{\Delta\varepsilon}{2}$ %	$\frac{\Delta\sigma}{2}$ MPa	σ_m MPa	N_f cycles
0-56	4.00	627.5	3.5	5	0-17	0.29	210.2	15.5	109,557
0-55	3.92	625.2	5.7	7	0-12	0.27	191.4	0.7	116,333
0-53	2.92	600.1	-1.3	14	0-41	0.22	157.0	0.7	182,900
0-52	2.43	584.5	-2.9	15	0-28	0.24	167.4	0.6	624,994
0-51	2.44	583.8	-1.8	34	0-29	0.21	154.1	-0.1	1,079,668
0-34	1.53	537.9	-4.3	45	0-25	0.40	268.1	268.2	5,275
0-39	1.23	528.4	-8.7	112	0-19	0.41	284.7	221.3	6,144
0-32	1.02	511.5	-9.3	200	0-23	0.40	280.1	159.9	12,288
0-57	0.91	509.5	-13.2	415	0-22	0.32	220.1	220.0	17,885
0-33	0.82	493.2	-7.4	512	0-21	0.29	200.5	200.5	34,956
0-10	0.71	489.3	0.2	945	0-24	0.25	177.6	177.7	54,680
0-18	0.65	488.4	-39.0	713	0-20	0.21	146.6	146.6	209,237
0-03	0.60	434.5	-36.0	3,357	0-27	0.19	133.0	133.1	1,075,867
0-16	0.61	435.7	73.0	2,055	0-26	0.17	118.7	118.7	1,283,726
0-36	0.64	455.5	-5.8	2,635	0-67	0.19	143.9	240.4	79,324
0-05	0.46	333.2	-22.2	9,010	0-69	0.67	455.5	54.2	871
0-01	0.51	368.8	-54.4	11,504	0-68	0.58	404.0	103.8	1,045
0-15	0.41	301.8	39.1	22,121	0-70	0.50	353.7	152.5	2,862
0-38	0.42	299.3	1.3	27,788	0-71	0.29	203.2	303.5	7,315
0-04	0.42	299.3	-34.4	40,930	0-73	0.22	153.0	354.8	14,782
0-31	0.37	262.4	1.2	47,740	0-72	0.17	121.7	384.6	24,979
0-06	0.36	258.1	1.2	55,470	0-54	0.16	108.4	497.5	11,639
0-07	0.31	222.1	1.0	51,717	0-59	0.11	75.7	432.1	245,801
0-35	0.31	222.0	1.1	58,666	0-55	0.10	70.7	435.8	1,608,028

$\Delta\varepsilon/2$ =axial strain amplitude, $\Delta\sigma/2$ = axial stress amplitude, σ_m =mean stress, N_f = fatigue life

c) 90° plate specimen

Spec No.	$\frac{\Delta\varepsilon}{2}$ %	$\frac{\Delta\sigma}{2}$ MPa	σ_m MPa	N_f cycles	Spec No.	$\frac{\Delta\varepsilon}{2}$ %	$\frac{\Delta\sigma}{2}$ MPa	σ_m MPa	N_f cycles
90-69	3.51	633.7	-5.3	4	90-31	0.23	161.9	0.5	1,450,963
90-41	0.97	515.9	-15.2	175	90-30	0.22	155.3	0.4	1,117,723
90-37	1.07	522.1	-14.3	232	90-24	0.40	268.1	268.0	4,012
90-39	0.72	478.8	-14.6	759	90-19	0.42	293.1	92.4	20,691
90-09	0.77	497.2	-21.7	788	90-21	0.32	222.2	221.9	20,306
90-13	0.70	486.0	-7.4	884	90-22	0.29	200.5	200.4	25,645
90-17	0.73	492.7	11.5	1,212	90-23	0.25	175.9	175.9	45,294
90-40	0.62	439.9	3.2	1,265	90-25	0.25	175.7	175.8	45,967
90-06	0.62	444.0	-9.9	1,880	90-26	0.19	133.0	133.0	196,177
90-15	0.67	473.7	-17.6	2,268	90-28	0.18	127.2	127.3	210,014
90-18	0.47	395.9	-44.7	2,299	90-20	0.21	147.7	147.6	227,619
90-02	0.53	378.3	-31.3	4,429	90-34	0.18	122.8	122.8	716,425
90-42	0.52	370.2	2.7	9,035	90-29	0.18	124.8	124.8	932,194
90-07	0.42	300.1	-19.6	18,120	90-27	0.17	120.1	120.1	1,271,590
90-14	0.48	349.3	-16.9	21,053	90-35	0.17	121.2	121.3	1,415,524
90-08	0.36	259.9	1.3	40,443	90-58	1.12	557.7	69.0	17
90-03	0.35	250.0	1.2	42,650	90-59	0.96	549.2	95.5	22
90-10	0.32	222.6	1.0	104,240	90-60	0.72	507.3	129.4	405
90-16	0.32	228.3	-12.5	164,041	90-61	0.46	323.5	282.9	1,674
90-12	0.28	190.6	0.7	131,072	90-62	0.31	218.1	390.0	3,649
90-38	0.22	161.6	0.1	394,116	90-53	0.15	101.8	405.8	28,813
90-32	0.24	173.7	0.4	625,893	90-52	0.12	82.0	425.5	141,596
90-66	0.21	144.8	-0.8	865,205	90-55	0.13	91.9	413.7	233,252
90-33	0.23	168.4	0.6	1,091,584					

$\Delta\varepsilon/2$ =axial strain amplitude, $\Delta\sigma/2$ =axial stress amplitude, σ_m =mean stress, N_f = fatigue life

Table 3 Uniaxial loading with compressive mean stress

a) One step loading

Spec #	$\frac{\Delta\varepsilon}{2}$ %	$\frac{\Delta\sigma}{2}$ MPa	σ_m MPa	N_f cycles	Spec #	$\frac{\Delta\varepsilon}{2}$ %	$\frac{\Delta\sigma}{2}$ MPa	σ_m MPa	N_f cycles
0-74	0.55	397.0	-96.9	6,513	0-66	0.35	313.1	-278.8	464,808
0-76	0.48	347.4	-147.0	18,217	90-51	0.27	198.7	-99.9	368,183
0-75	0.41	297.1	-197.0	115,601	90-56	0.40	295.5	-246.4	405,747
0-58	0.40	310.2	-262.6	212,001	90-63	0.38	316.3	-285.6	429,914
0-77	0.34	249.2	-148.2	222,563	90-64	0.40	315.0	-292.1	565,104
0-60	0.38	278.6	-215.0	226,682	90-57	0.37	273.3	-223.5	603,299
0-61	0.32	237.5	-161.6	288,283	90-65	0.38	315.3	-297.6	696,820
0-64	0.31	228.3	-169.1	291,220	90-72	0.39	300.9	-302.1	750,172
0-65	0.41	305.0	-268.1	383,667	90-68	0.39	307.0	-298.2	1,098,940
0-63	0.37	274.0	-221.5	406,747					

$\Delta\varepsilon/2$ =axial strain amplitude, $\Delta\sigma/2$ =axial stress amplitude, σ_m =mean stress, N_f =fatigue life

b) Plate and cylindrical specimens under compression-compression, two step loading

Spec No.	Step	$\frac{\Delta\varepsilon}{2}$ %	$\frac{\Delta\sigma}{2}$ MPa	σ_m MPa	N cycles
90-67	I	0.41	305.3	-291.1	498,374
	II		100.0	100.0	62
90-71	I	0.42	301.4	-292.6	472,623
	II		100.0	100.0	52
90-73	I	0.38	300.8	-310.3	802,796
	II		100.0	100.0	419
90-74	I	0.38	292.2	-311.8	880,885
	II		100.0	100.0	1,926
90-75	I	0.44	289.3	-300.3	397,716
	II		100.0	100.0	15,473
90-77	I	0.40	298.3	-299.2	375,132
	II		100.0	100.0	3,198
90-78	I	0.36	274.4	-322.1	982,635
	II		100.0	100.0	19,335
TorS21	I	0.41	308.1	-318.4	1,000,000
	II		100.0	100.0	29,831
TorS22	I	0.42	307.4	-317.2	2,000,000
	II		100.0	100.0	23,867
TorS23	I	0.39	285.8	-290.4	1,371,663
	II		100.0	100.0	15,353
TorS24	I	0.39	288.9	-283.5	2,781,162
	II		100.0	100.0	49,221

$\Delta\varepsilon/2$ =axial strain amplitude, $\Delta\sigma/2$ =axial stress amplitude, σ_m =mean stress, N_f =fatigue life.

Table 4 Pure torsion and cyclic torsion with static axial load for tubular specimens

Load path	Spec #	σ_m MPa	$\frac{\Delta\gamma}{2}$ %	$\frac{\Delta\tau}{2}$ MPa	N_f cycles	Observed Cracking Direction θ^o
(a)	Tu31_2	0	1.97	335.2	152	90
	Tu18	0	1.73	340.0	209	90
	Tu17	0	1.21	315.7	670	5
	Tu42_2	0	1.07	286.6	1807	90
	Tu35	0	0.93	251.0	3,537	90
	Tu16	0	0.93	254.2	4,291	90
	Tu36	0	0.75	203.3	18,842	90
	Tu30	0	0.80	219.0	20,271	90
	Tu15	0	0.69	190.3	178,065	0
	Tu27	0	0.60	167.8	308,144	-45
	Tu24	0	0.69	192.0	328,816	0
	Tu10	0	0.50	136.5	403,731	0
	Tu34	0	0.55	146.9	428,510	-43
	Tu28	0	0.40	110.8	805,783	46
	Tu37	0	0.46	124.5	913,545	-48
	Tu31_1	0	0.45	125.8	>1,005,181	-
	Tu39	0	0.36	101.0	3,867,638	45
(b)	Tu22	200.0	0.69	188.5	12,739	0
	Tu23	-200.0	0.69	192.0	52,986	90
	Tu25	293.1	0.69	189.8	4,394	0
	Tu26	-293.1	0.69	196.7	84,946	90
	Tu40	289.8	0.50	134.2	30,192	0
	Tu41	288.7	0.50	135.4	25,167	0
	Tu42_1	-296.4	0.51	138.8	>2,609,732	-
	Tu44_1	-389.1	0.50	135.6	>2,216,739	-
	Tu44_2	391.6	0.50	131.6	14,489	0

σ_m =static axial stress, $\Delta\gamma/2$ =shear strain amplitude, $\Delta\tau/2$ = shear stress amplitude, N_f =fatigue life.

Note: Tu31_1 was tested without failure and the specimen was tested at a much higher amplitude in a second step Tu31_2.

Table 5 Fatigue experiments conducted using tubular specimens

Load path	Spec #	$\frac{\Delta\varepsilon}{2}$ %	$\frac{\Delta\gamma}{2}$ %	$\frac{\Delta\sigma}{2}$ MPa	$\frac{\Delta\tau}{2}$ MPa	N_f cycles	Observed Cracking Direction θ^o
(c)	Tu06_2	0.64	1.1	370.0	222.9	147	60
	Tu04	0.50	0.86	351.3	222.0	1,967	20
	Tu19	0.22	0.78	165.6	216.2	9,174	90
	Tu20	0.17	0.6	127.2	170.5	59,194	-5
	Tu33	0.23	0.4	166.1	110.4	136,646	90
	Tu05	0.28	0.49	201.3	130.0	45,500	-49
	Tu32	0.21	0.37	153.5	100.3	662,627	-50
	Tu06_1	0.19	0.29	137.4	79.7	>1,018,000	-
	Tu29_1	0.18	0.36	132.4	96.8	>1,031,190	-
(d)	Tu29_2	0.85	1.45	543.7	329.4	146	5
	Tu02_2	0.75	1.30	497.7	319.1	424	-5
	Tu01	0.51	0.87	377.6	241.8	2,487	-5
	Tu21	0.38	0.66	280.4	181.8	10,191	0
	Tu11	0.28	0.49	200.9	131.6	29,439	-30
	Tu03	0.27	0.41	200.6	115.8	41,747	0
	Tu02_1	0.19	0.27	143.1	76.4	>632,258	-
(e)	Tu09	0.49	0.86	352.0	232.0	755	15
	Tu07	0.28	0.49	205.8	137.5	35,804	20
	Tu08	0.20	0.32	147.5	86.9	225,000	-21
(f)	Tu13	0.36	0.63	258.2	175.6	1,145	-30
	Tu14	0.40	0.70	295.0	197.2	2,301	-19
	Tu12	0.28	0.49	203.8	136.3	12,708	-20

$\Delta\varepsilon/2$ =axial strain amplitude, $\Delta\gamma/2$ =shear strain amplitude, $\Delta\sigma/2$ =axial stress amplitude, $\Delta\tau/2$ =shear stress amplitude, N_f =fatigue life.

Note: Tuxx_1(xx is the specimen number) was tested without failure and Tuxx_2 was the same specimen continuously tested at a much higher loading amplitude.

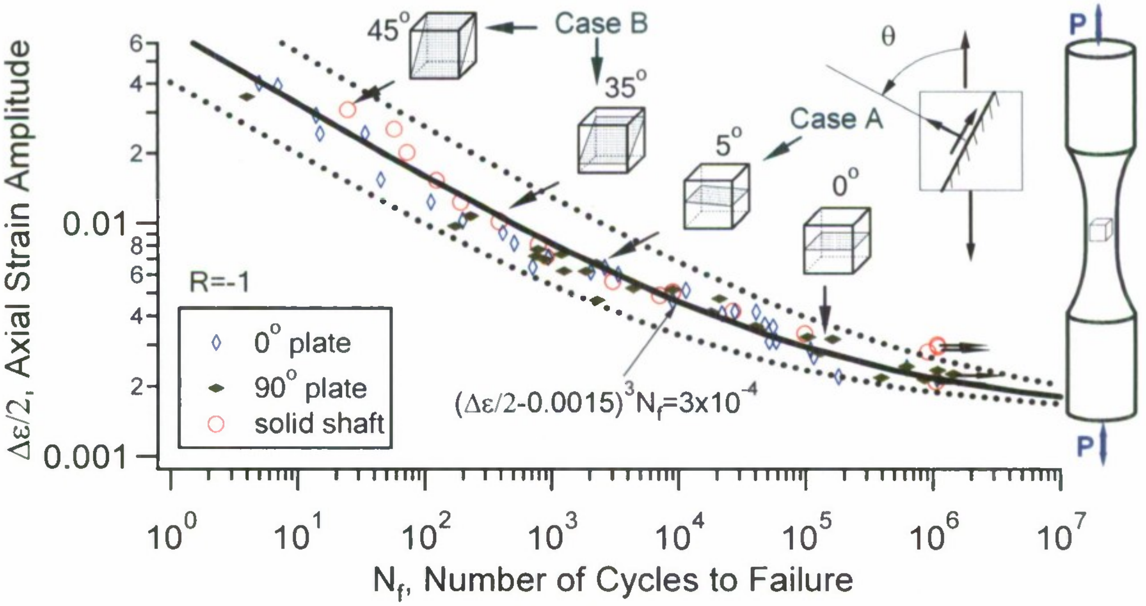

Fig.5 Strain-life and cracking behavior under fully reversed uniaxial loading

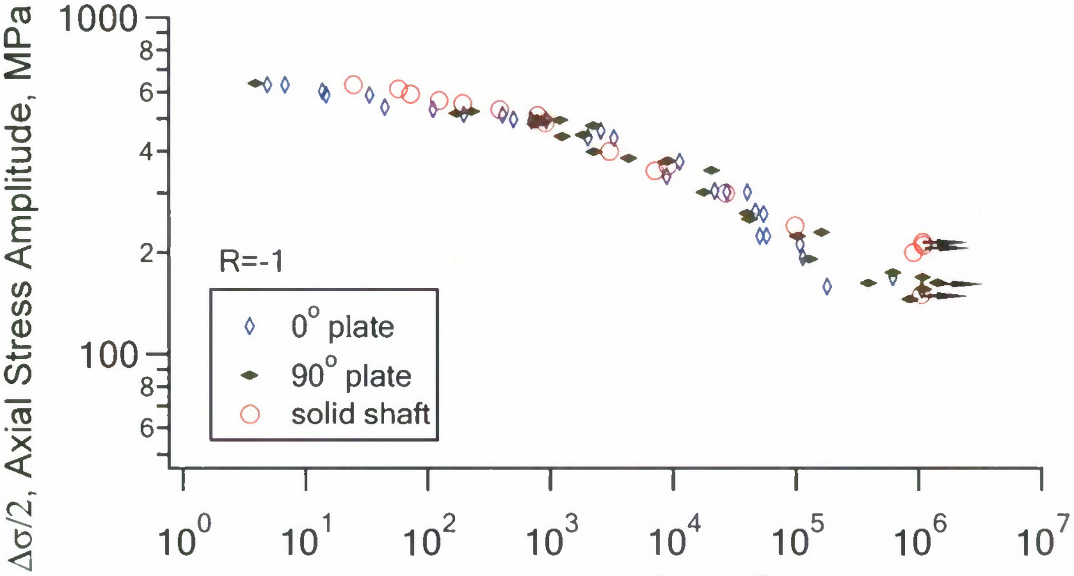

Fig.6 Stress-life under fully reversed uniaxial loading

Figure 5 and Fig.6 show the basic fatigue data and fatigue cracking behavior obtained from the fully reversed uniaxial loading. A data point followed by a horizontal arrow denotes a run-out fatigue experiment. It is evident that the plate specimens with two different orientations and the solid dog-bone cylindrical specimens yielded very similar fatigue results. The detailed stress amplitude, strain amplitude, and fatigue life for each fully reversed uniaxial experiment are listed in Table 2.

The following three-parameter equation is used to describe the strain-life curve for the fully reversed unixial fatigue by best fitting the experimentally obtained data,

$$\left(\frac{\Delta\varepsilon}{2}-\varepsilon_0\right)^{\xi} N_f = C \tag{1}$$

where $\Delta\varepsilon/2$ is the strain amplitude and N_f is the number of cycles to failure. The remaining three symbols, ε_0, ξ and C, are constants obtained by best fitting the experimental data. For 7075-T651, ε_0=0.0015, ξ=3, and C=0.0003. The dotted lines in Fig.5 are the factor-of-five boundaries from that described by Eq.(1). These two lines also show the approximate scatter of the experimental fatigue life data of the material under investigation.

A careful examination of the cracking behavior of the fully reversed uniaxial loading specimens reveals that when the fatigue lives are longer than 2,000 cycles, the cracking planes are consistently perpendicular to the loading axis. When the fatigue lives are lower than 100 cycles, the normal of the cracking planes approaches ±45° from the loading axis. When the fatigue lives are in between 100 and 2,000 cycles, the normal of the cracking plane from the loading axis varies from zero to ±45°. A shear crack can grow in one of two ways [10], illustrated by Case A and Case B in Fig.5. Case A crack is due to the in-plane shear stress. Case B cracks are the result of out-of-plane shear. Case A and Case B cracking were observed when the fatigue lives are less than 2,000 cycles. Over the range of the fatigue lives investigated, a smooth transition of the cracking behavior and a statistically smooth strain-life curve were observed from the specimens under fully reversed uniaxial loading.

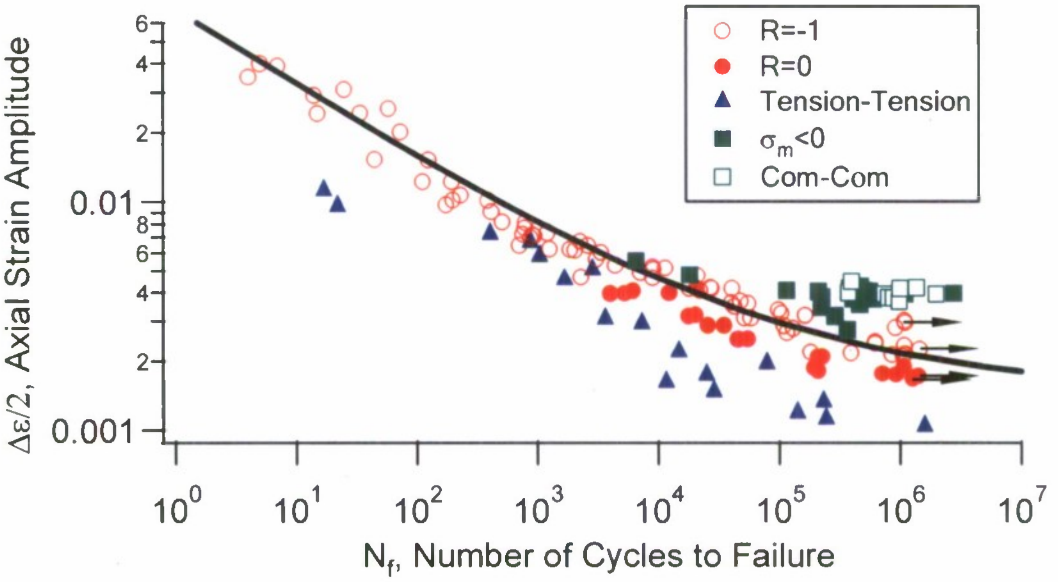

Fig.7 Strain-life of all the uniaxial fatigue experiments

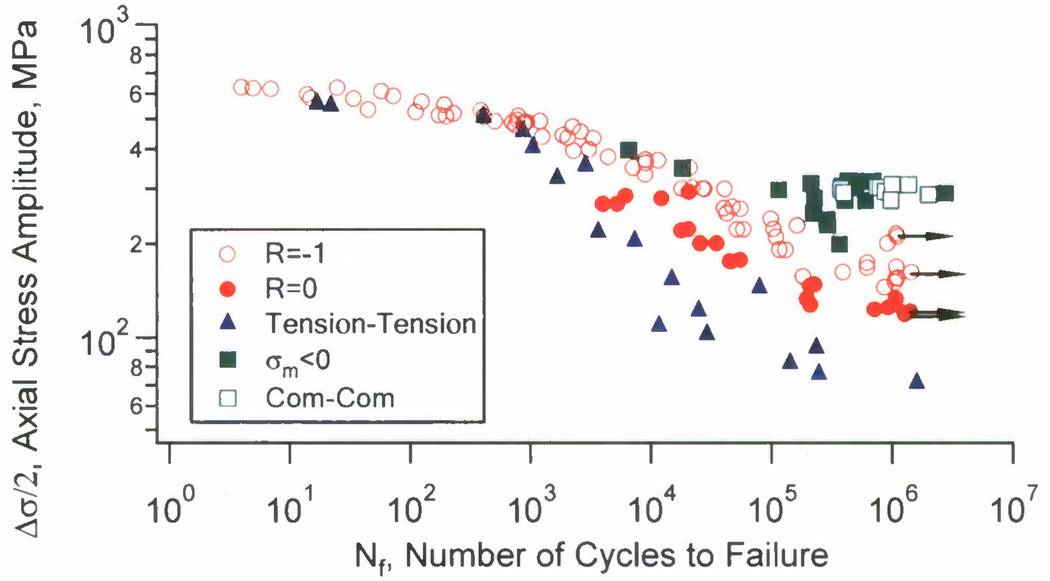

Fig.8 Stress-life of all the uniaxial fatigue experiments

Uniaxial fatigue experiments were conducted with R -ratios ranging from $-\infty$ to 0.5, where R is the ratio of the minimum stress over the maximum stress in a loading cycle. The fatigue results are shown in Figs. 7 and 8, where Fig.7 is the strain-life curve and Fig.8 is the stress-life plot. The solid line in Fig.7 is the strain-life curve described by Eq.(1) by best fitting the fully reversed uniaxial fatigue data. The detailed fatigue results under uniaxial loading are listed in Table 2 and Table 3. Figures 7 and 8 clearly show that the mean stress has a significant influence on fatigue life.

A number of uniaxial specimens were tested under the compression-compression condition with a zero or negative maximum stress in a loading cycle. In order to assess fatigue damage under compression-compression loading, a specimen was subjected to a designated compression-compression loading for up to 10^6 loading cycles. This was followed by a stress-controlled loading with $R = 0$ and a stress amplitude of 100 MPa. According to the results shown in Fig.8, a stress amplitude of 100 MPa with $R = 0$ would result in a fatigue life longer than 10^7 loading cycles. Since fatigue cracks were often initiated on the material plane with its normal along the loading axis (the crack plane was perpendicular to the loading direction), failure of the specimen was difficult to identify under compression-compression loading. The two-step loading can help identify whether or not the compression-compression generated fatigue damage. If the number of loading cycles in the second loading step is significantly long, this may indicate that the fatigue damage created under the first step compression-compression may not have contributed to the fatigue damage. If the specimen fails in the second loading step within a number of loading cycles that is much less than 10^7, the first loading step must have generated significant fatigue damage.

All the 11 uniaxial specimens tested under the compression-compression loading conditions failed in the second step loading with a stress amplitude of 100 MPa and $R = 0$ within very limited number loading cycles (Table 3(b)). The results suggest that fatigue damage was developed under compression-compression loading. In fact, the results show that fatigue damage has reached a failing point already before the application of the second loading step.

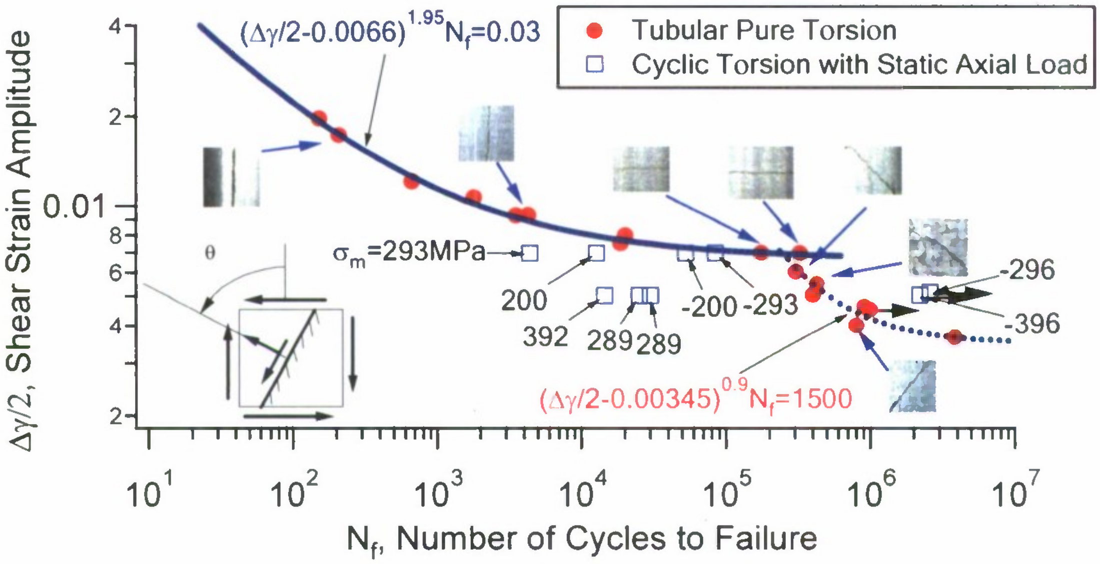

Fig.9 Shear strain amplitude versus fatigue life for pure torsion and torsion with a static axial stress

Figure 9 shows the fatigue results obtained from the pure shear experiments and the fatigue experiments conducted with cyclic shear combined with a static axial stress (loading path (b) in Fig.4). Typical cracking behavior is also shown in Fig.9. Detailed results are listed in Table 4.

Although not conclusive due to the limited number of specimens tested, the results show that a compressive static axial load in fully reversed torsion does not practically influence the fatigue life. A positive static axial static stress significantly reduced the fatigue life. A crack along the axial direction (the normal of the plane is perpendicular to the axial direction) was observed for the specimen tested under fully reversed shear with a compressive static axial stress. The cracking plane is perpendicular to the axial direction when the static axial stress is positive. The observations are consistent with that made by Socie and co-workers [11] for Inconel 718 under a similar loading condition.

A kink around a fatigue life of 3×10^5 cycles was noticed in the shear strain-life curve from pure torsion (Fig.9). Unlike the strain-life for the uniaxial loading (Fig.5) which can be properly described by using the three-parameter equation Eq.(1), the shear strain-life curve can be better described by two curves of the three-parameter equation mathematically identical to Eq.(1) as shown in Fig.9. A further observation of the tested pure shear specimens revealed that the kink in the strain-life curve was associated with the cracking behavior. When the fatigue lives were less than 3×10^5 cycles, the cracking planes were either perpendicular or parallel to the specimen axis. In other words, cracks were found on the maximum shear planes. When the fatigue lives were higher than 3×10^5 cycles, cracks were consistently found to form on the maximum tensile planes (±45° from the specimen axis).

Changes of cracking behavior with the loading magnitude or fatigue life were observed on AISI 304 stainless steel [10], Inconel 718 [11], 1045 steel [12], and an aluminum alloy [13]. However, no kink in the strain-life curves was found to associate with the cracking behavior transition in these materials. Different slopes or discontinuous stress-life curves were often reported from the uniaxial tension-compression experiments for ultra high fatigue lives [14,15]. It is a common observation that kink in the stress-life curve is associated with the crack initiation sites in the specimen. When the fatigue lives are lower, fatigue cracks are initiated on the specimen surface. Crack initiation is often found to occur on subsurface from sites of interior defects.

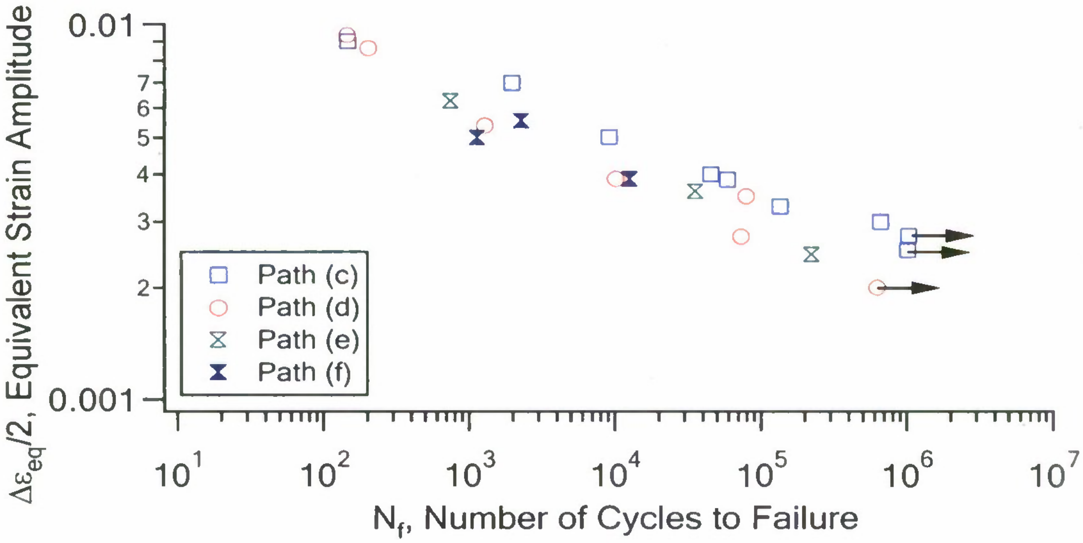

Fig.10 Fatigue under combined axial-torsion loading

Figure 10 summarizes the results obtained from testing the tubular specimens under combined axial-torsion loading. Detailed experimental results are listed in Table 5. An equivalent strain amplitude is used in Fig.10 to represent the loading magnitude under cyclic loading. The equivalent strain amplitude is defined as follows,

$$\left(\frac{\Delta\varepsilon}{2}\right)_{eq} = \sqrt{\left(\frac{\Delta\varepsilon}{2}\right)^2 + \frac{1}{3}\left(\frac{\Delta\gamma}{2}\right)^2} \qquad (2)$$

where $(\Delta\varepsilon\ /2)_{eq}$ is the equivalent strain amplitude, $\Delta\varepsilon/2$ is the axial strain amplitude, and $\Delta\gamma/2$ is the shear stress amplitude. The fatigue experimental results obtained from testing the tubular specimens will be used to evaluate the fatigue models. It should be noted that the only p urpose to use of the equivalent strain is to present the results with a simple and single plot.

The experiments conducted in the current investigation confirm that significant fatigue damage can be produced under compression-compression loading for the 7075-T651 aluminum alloy. Usually, a material is dominated by one type of cracking behavior. In contrast, 7075-T651 aluminum alloy displays shear cracking, mixed cracking, and tensile cracking dependent on the loading magnitude. Earlier investigations indicate that many materials are dominated by mixed cracking behavior [53, 59], and few, such as stainless steels, exhibit primarily tensile cracking behavior. Very few materials display predominant shear cracking behavior. One characteristic of the fatigue behavior of 7075-T651 is the distinct kink observed in the shear strain versus fatigue life curve (Fig.9) that is accompanied by the change of cracking behavior. To the best of the author's knowledge, such a torsion fatigue behavior has never been documented for an aluminum alloy when the fatigue life is less than 10^7 cycles. A kink was observed in the strain-life curve of an induction hardened steel where the gradient material properties resulted in subsurface cracking [85].

1.3 *CRACK GROWTH EXPERIMENTS*

1.3.1 Description

Both standard and non-standard compact specimens of 7075-T651 aluminum alloy were used in the fatigue crack growth fatigue experiments. The dimensions of the standard specimen are shown in Fig.11(a). Notches with four different sizes were machined using either the EDM (Electro-discharging machining) or a diamond saw. Notch 1 was a sharp slot with a length of 1.0 mm cut by a diamond saw and a width of 0.325 mm. Notch 2 contained a hole with a radius of 1.27 mm. The holes in Notch 3 and Notch 4 had a radius of 3.5 mm and 6.35mm, respectively. The dimensions of the non-standard compact specimens are shown in Fig.11(b). These specimens were designed to study the fatigue crack growth behavior with changing loading direction. The specimens were first subjected to Mode I loading. After the crack reached a certain length, the external loading direction was changed 30° from the original loading direction. The results of Mode I loading experiments are reported together with those obtained from the standard compact specimens. Four-hole specimens shown in Fig.11(c) were used in mixed mode (Mode I and Mode III) crack growth experiments under combined axial-torsion loading conditions.

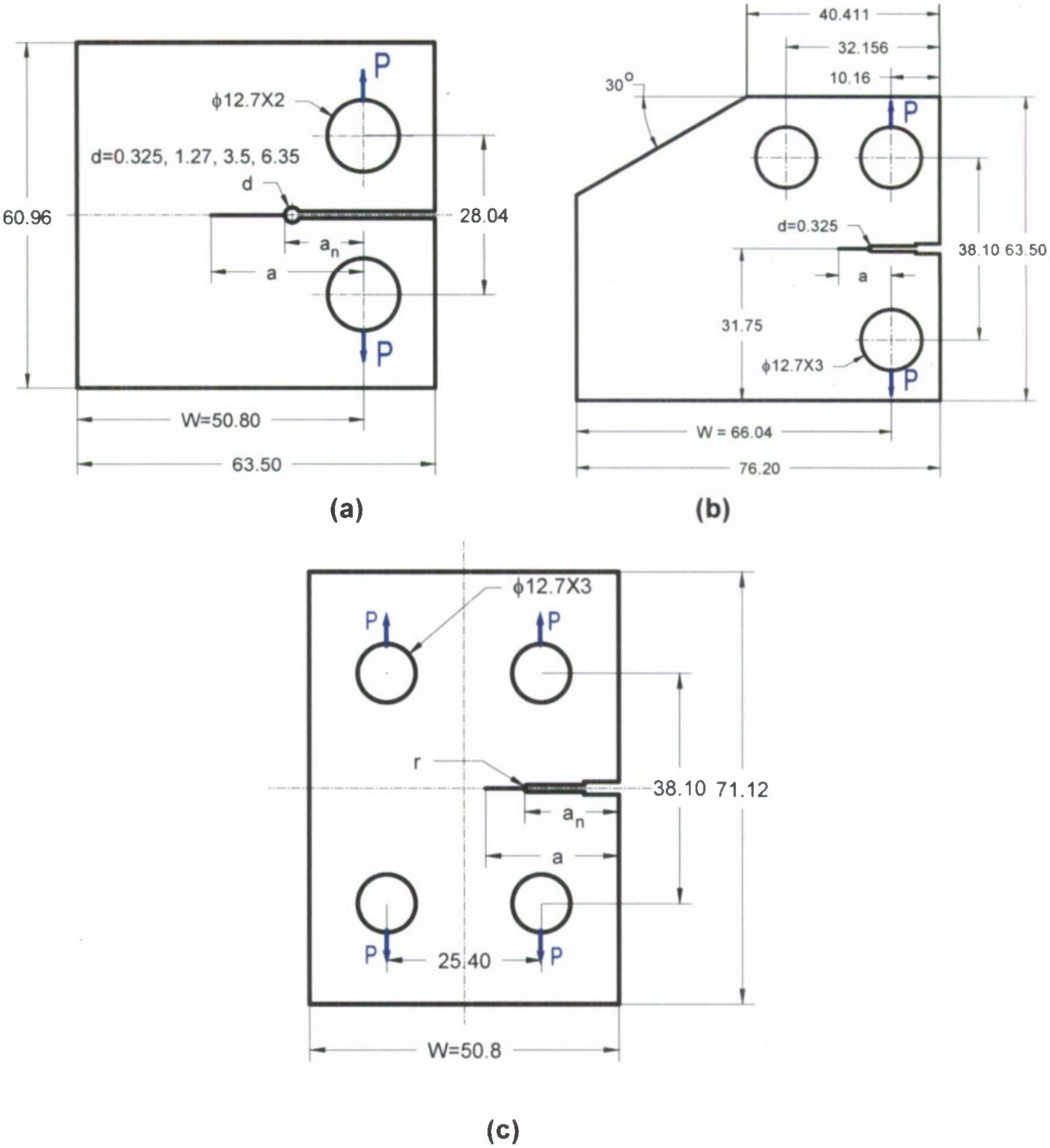

(a) (b)

(c)

Fig.11 Notched specimens used for crack growth experiments (all dimensions in mm, thickness=4.85mm)

Both EDM and diamond saw cut result in minimal residual stress near the notch due to the very slow material removal rate by the two methods. After the notches were machined, one side of the specimens was finely polished to facilitate crack growth measurement using an optical reading micrometer. The experiments were carried out using an Instron 8872 load frame with a 25 kN load capacity and 8800 electronics with computer control and data acquisition. Depending on the load magnitude, the loading frequencies ranged from 1 to 10 Hz. The crack length was measured using an optical reading microscope with a magnification of 40.

The compact specimens were cut from cold rolled 7075-T651 plates. Experiments were conducted with the cracks orientated to the rolling direction (0 degree) and the direction perpendicular to the rolling direction (90 degree). The experimental loading conditions are summarized in Tables 6 and 7. The first part of the specimen designation (the first column in the tables) specifies the crack orientation of the testing specimen with respect to the rolling direction of the cold-rolled aluminum plate.

17 specimens were tested under the constant amplitude loading condition with five different R-ratios (0.1, 0.5, 0.75, -1, and -2) (Table 6). Three specimens, 0_C11, 0_C10 and 0_C27, listed in Table 6 were non-standard compact specimen (Fig.11(b)). All the rest of the experiments reported in the current study employed the standard compact specimen (Fig.11(a)). Most of the experiments were tested from crack initiation till a significant long crack length. "Number of cycles when a=0.5mm" in Table 6 reflects the crack "initiation" life of the specimen corresponding to a fatigue crack size of 0.5 mm measured from the root of the notch. The fatigue life, N_f, is the number of the loading cycles from the start of the experiment till the termination of the experiment when the crack size was a_f. It should be noted that a_f was not the crack size before the final fracture of the specimen.

Table 6 Experimental conditions for fatigue crack growth under constant amplitude loading

Spec#	R-ratio	$\Delta P/2$ (kN)	f (Hz)	Notch diameter (mm)	Notch depth /precrack a_n (mm)	Number of cycles when a=0.5 mm (cycle)	N_f (cycle)	a_f (mm)
0_C01	0.1	2.700	1~10	1.59	3.54	15,910	24,787	18.73
90_C01	0.1	1.350	1~10	0.20	4.78	24,270	109,000	30.34
0_C02	0.1	1.125	1~10	0.20	4.46	21,140	177,830	29.89
0_C03	0.1	0.720	1~10	*	7.26	205,300	498,900	34.55
0_C12	0.1	1.350	1~10	0.20	6.75	21,200	84,303	18.16
90_C02	0.5	0.575	1~10	*	5.11	143,800	881,650	43.11
0_C04	0.5	0.575	1~10	*	6.00	57,780	480,240	30.39
90_C19	0.5	0.750	1~10	**	7.04	34,790	175,520	27.39
0_C05	0.75	0.575	1~10	*	6.18	35,480	240,800	23.98
0_C07	0.75	0.575	1~10	*	5.33	48,830	298,583	25.14
90_C18	0.75	0.625	1~10	0.28	4.83	99,470	360,958	22.36
0_C06	-1	1.600	1~10	0.20	5.38	113,400	519,548	33.44
0_C20	-1	3.500	1	7.11	6.48	1,372	18,968	16.62
90_C13	-2	2.400	1~10	3.48	7.42	73,220	439,100	33.89
0_C10	0.1	1.350	1~10	0.33	0.142	29390	123,188	10.86
0_C11	0.1	1.350	1~10	0.33	0.327	16560	141,841	19.953
0_C27	0.1	1.125	1~10	0.33	0.457	31700	230,358	14.753

R-ratio = minimum load over the maximum load in a loading cycle $\Delta P/2$ = loading amplitude

a_n = distance between the notch root and the line of action of the externally applied load

f = loading frequency N_f = total cycles a_f =final crack length

*Pre-cracked with cyclic load of R =0.1, $\Delta P/2$ =1.35kN.

**Pre-cracked with cyclic load of R =0.5, $\Delta P/2$ =1.25kN

0_C11, 0_C10 and 0_C27 are the non-standard specimens shown in Fig.1(b)

Three specimens were subjected to a single overload during the constant-amplitude loading crack growth experiments and two specimens were tested with a single underload (Table 7). One specimen was subjected to high-low sequence loading. An illustration of the single overload, underload, and high-low sequence loading is shown in Fig.12.

Table 7 Constant amplitude loading with a single overload or underload

Spec#	R-ratio	$\Delta P/2$	f	Notch diameter	Notch depth a_n	P_{OL}	N_{OL}	a_{OL}	N_f	a_f
		(kN)	(Hz)	(mm)	(mm)	(kN)	(cycle)	(mm)	(cycle)	(mm)
90_C03	0.1	1.35	1~10	0.20	4.23	6.0	86,542	8.45	135,296	32.34
90_C16	0.1	1.35	1~10	0.33	6.74	6.0	51,400	15.33	87,828	26.02
90_C14	-1	2.00	1~10	1.27	6.64	6.0	140,336	16.75	478,927	32.66
90_C15	0.1	1.50	1~10	3.48	6.91	-6.0	108,668	12.14	125,015	24.46
90_C22	0.1	1.125	1~10	1.27	0.35	-10.0	168801	12.74	198,109	21.82

P_{OL} = magnitude of the overload/underload a_{OL} = crack length at overloading/underloading

N_{OL} = number of cycles of the constant amplitude loading before overloading/underloading

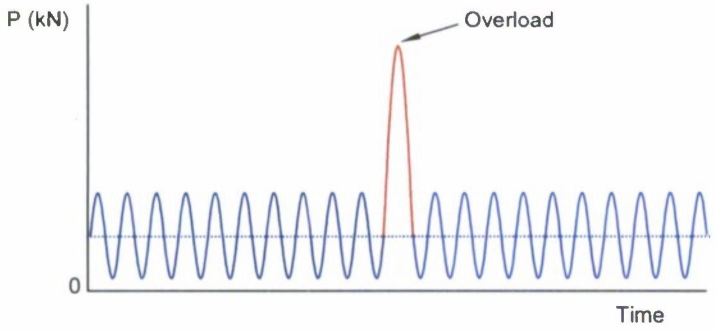

(a)

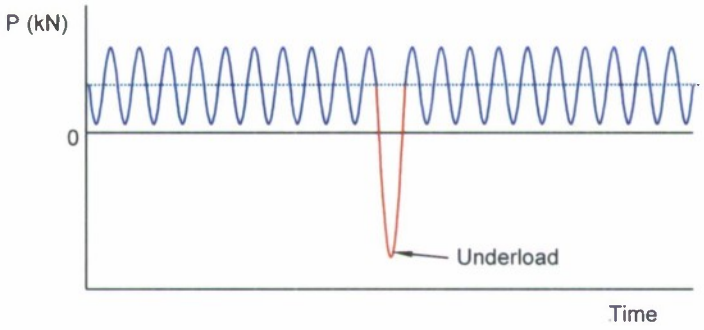

(b)

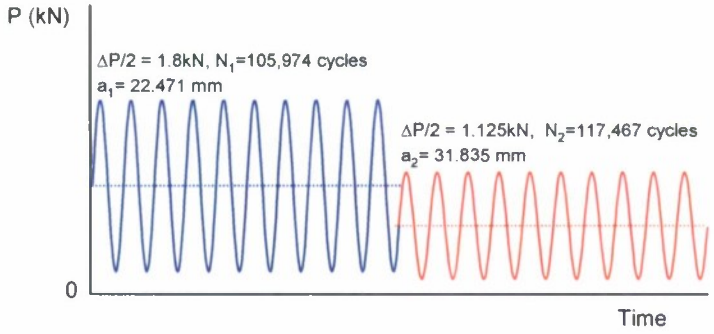

(c)

Fig.12 Illustration of loading histories: (a) overloading; (b) underloading; (c) high-low sequence loading

Among the three specimens for overloading experiments, two specimens were tested with a stress ratio of R=0.1 and load amplitude of $\Delta P/2$=1.35 kN. With a load magnitude of 6.0kN, the overload ratio (overload over the maximum load in the constant amplitude loading) was 2.0. The overload was applied when the crack length was 8.45 mm and 14.96 mm, respectively, on these two specimens. A third specimen was subjected to a constant amplitude loading with R= -1 and $\Delta P/2$=2 kN. The overload ratio was 3 and the overload was applied when the crack length was 16.537 mm. After the application of an overload, the specimen underwent constant amplitude loading identical to that before the overload.

Two specimens were tested with a single underload during the crack propagation experiments with the underloads being -6 kN and -10 kN, respectively (Table 7). The underloads were applied when the crack lengths were 12.14mm and 12.74 mm, respectively for the two specimens.

One experiment was conducted under high-low sequence loading (Fig.12(c)). The specimen had a notch of 6.35 in diameter. The notch depth was 8.813 mm. Both loading steps had a R-ratio of 0.1. The stress amplitude in the first step loading was 1.8 kN. After the crack length reaches 22.47 mm, the loading amplitude was switched to 1.125 kN (Fig.12(c)).

Generally, a compact specimen is not recommended for tension-compression loading (R<0). In the current investigation, the two loading holes in the compact specimen were machined to have a tight tolerance so that the gap between the pin in the loading fixture and the hole in the specimen was minimal. For the range of the testing frequencies used in the experiments, the maximum and minimum loads dictate the fatigue behavior. The experiments indicated that the maximum and minimum loads can be controlled accurately with the compact specimen for the R<0 loading cases.

A parabolic curve was adopted to best fit a set of five successive data points in the experimentally obtained relationship between the crack length and the number of loading cycles. The crack growth rate at the middle point (the third point) was determined from the derivative of the parabola.

The stress intensity factor for the compact specimen was calculated using the following formula:

$$K = \frac{P(2+\alpha)}{B\sqrt{W}(1-\alpha)^{3/2}}(0.866+4.64\alpha-13.32\alpha^2+14.72\alpha^3-5.6\alpha^4) \tag{3}$$

where,

$$\alpha = \frac{a}{W} \tag{4}$$

The symbol B in Eq.(3) denotes the thickness of the compact specimen and W is the distance between the applied force P and the left edge of the specimen (refer to Fig.11). The symbol a in Eq.(4) is the crack length measured from the line of the application of the external load, P. According to the ASTM standard E647 [16], the equation is valid when $\alpha > 0.2$. The finite element (FE) method was used to determine the stress intensity factor when $\alpha < 0.2$. The results of the finite element calculation were compared with those obtained from using Eq. (3) in Fig.13.

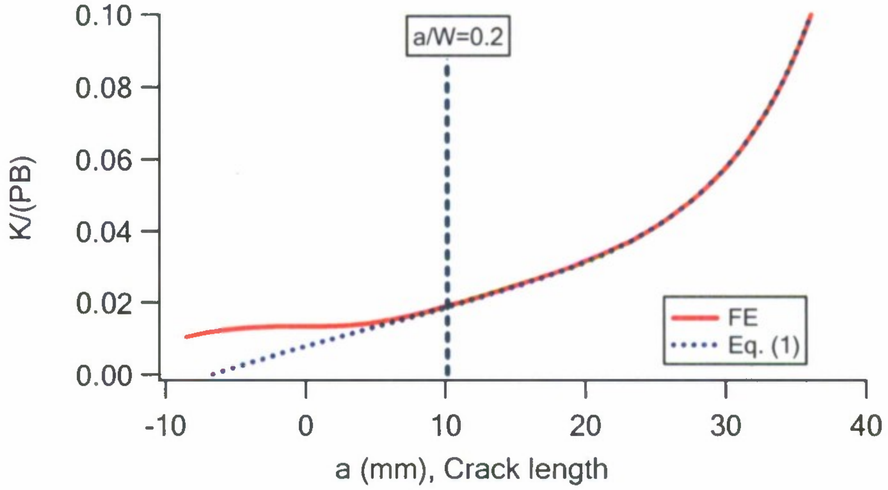

Fig.13 Stress intensity factor obtained from using Eq.(3) and that from the FE method for the standard compact specimen

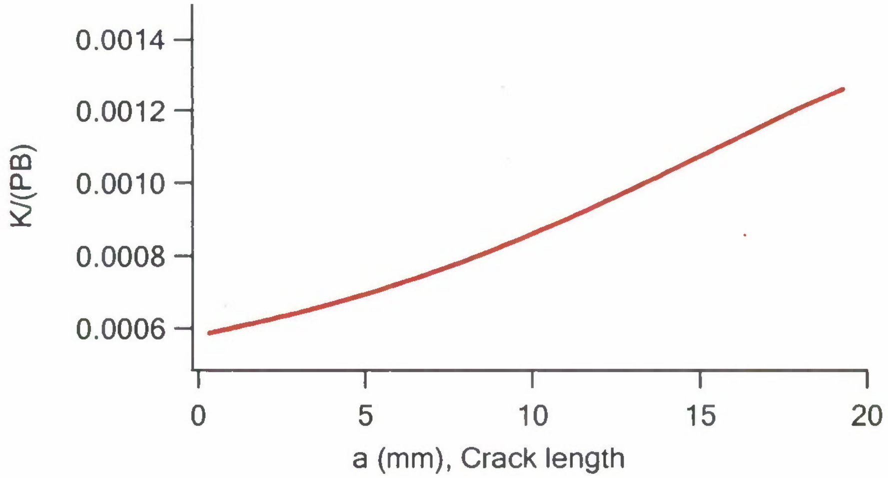

Fig.14 Stress intensity factor for the non-standard compact specimen obtained from the FE method

For the nonstandard compact specimen (Fig.11(b)), the FE method was used to determine the stress intensity factor. For the given geometry and dimensions shown in Fig.11(b), the relationship between the normalized stress intensity factor and the crack length is shown in Fig.14.

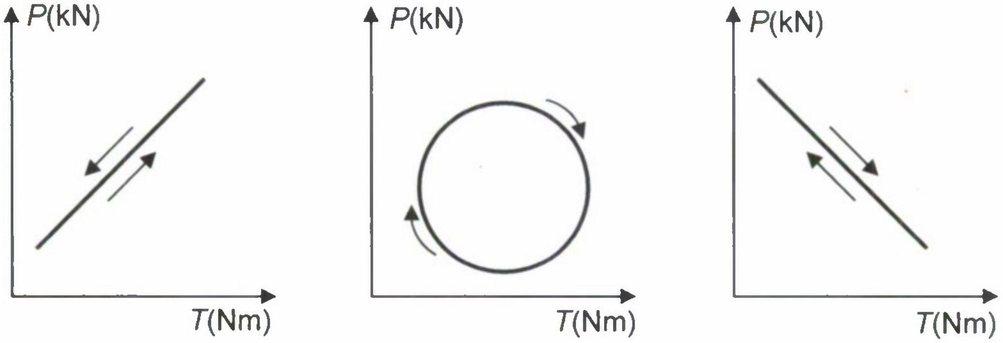

(a) (b) (c)

Fig.15 Loading paths used in mixed mode crack growth experiments

Table 8 Mixed Mode I-Mode III Crack Growth Experiments

Spec#	R -ratio for tension	$\Delta P/2$ (kN)	R -ratio for torsion	$\Delta T/2$ (Nm)	f (Hz)	Notch radius r (mm)	Thickness t (mm)	Notch depth a_n (mm)	Loading Path (Fig.15)
BC05	0.1	5.4	0	15	2	0.626	4.85	8.027	a
BC06	0.1	5.4	0	15	2	0.626	4.85	8.677	b
BC07	0.1	5.4	0	15	5	0.626	4.84	7.704	c
BC08	0.1	5.4	0	15	2	0.626	4.87	8.210	a
BC10	0.1	6.75	0	18.75	2.5	0.626	4.83	8.569	b
BC11	0.1	6.75	0	18.75	2.5	0.626	4.88	8.062	a
BC12	0.1	6.75	0	18.75	2.5	0.626	4.87	8.192	c

Six specimens were tested in the crack propagation experiments under axial-torsion loading conditions. The configuration of the specimen is shown in Fig.11(c). The specimens were clamped into the specimen holder with four bolts and placed into biaxial Instron servo hydraulic machine for fatigue testing. Three loading paths shown in Fig.15 were applied in order to investigate the influence of loading conditions on the crack growth rate.

1.3.2 Crack growth rate under constant amplitude loading

Figure 16 summarizes the experimental crack growth results under constant amplitude loading in the traditional form of crack growth rate versus the stress intensity factor range. For a given R -ratio, the fatigue rate curves with different loading amplitudes were practically coincident. Since specimens with two different orientations with respect to the rolling direction were used, the results also suggest that the cold rolling process of the material does not practically influence the fatigue crack growth results. Results shown in Fig.5 and Fig.6 revealed that the plate specimens with two different orientations yielded very similar deformation and fatigue crack initiation results.

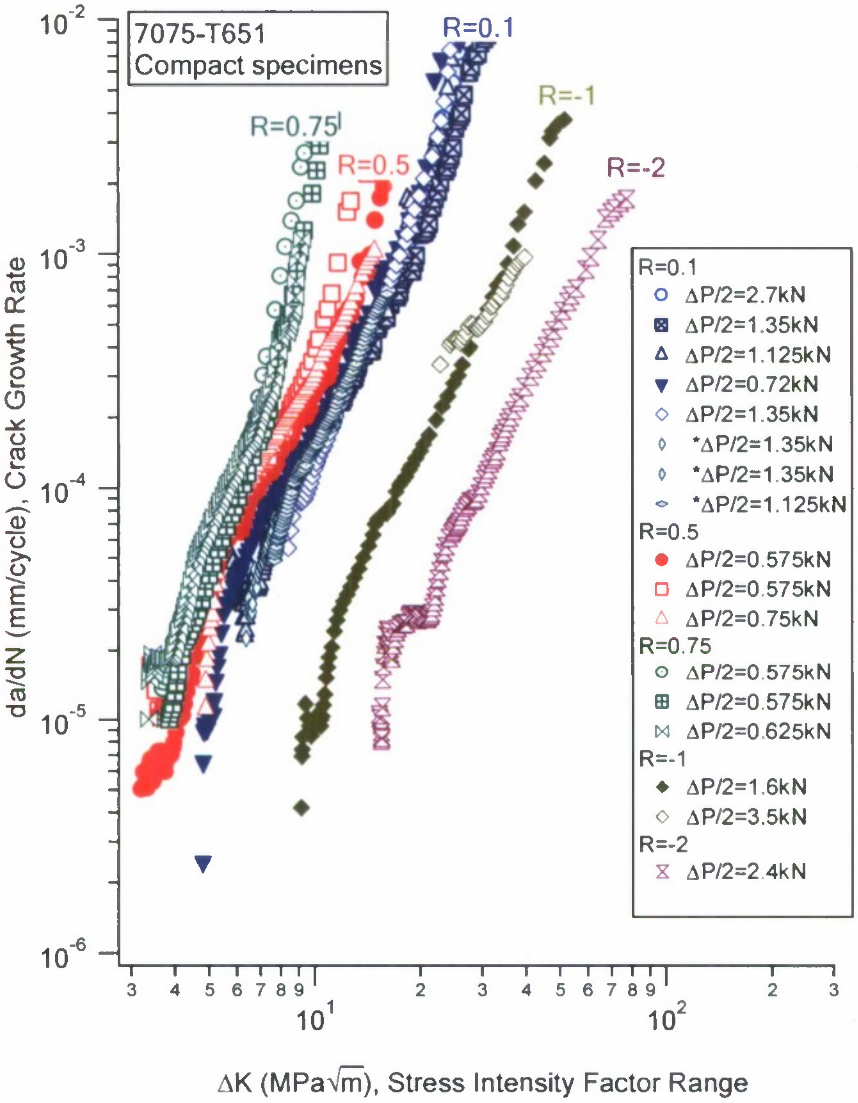

Fig.16 Crack propagation under constant amplitude loading with the effect of the R -ratio (7075-T651 aluminum alloy)

The material displays a significant R -ratio effect. With identical stress intensity factor range, a higher R -ratio results in a higher crack growth rate. Although the threshold was not experimentally measured, the tendency indicates that the threshold value of the stress intensity factor range increases as the R -ratio decreases. It should be noted that among the 14 standard specimens tested under constant amplitude loading, six specimens started with a pre-crack and the rest eight specimens started with the notches formed either by EDM or diamond saw cut (refer to Table 6). The early crack growth also reflects the notch effect. The experimental results of the three non-standard specimens are shown together in Fig.16. At the same R -ratio, the crack growth curves of the non-standard specimens (marked with "*" in the legend of Fig.16) are almost coincident with those of the standard specimens. It is obvious that the specimen geometry has no significant influence on the crack growth curve as long as the stress intensity factor range and the R-ratio are kept identical. This confirms that the nonstandard specimens can be used reliably for some special purpose, such as the investigation of the effect of changing the loading direction on the crack propagation behavior.

An observation of the crack profiles on both the front and back surfaces of a specimen indicates that the crack profile on the front surface was almost identical to that on the back surface. The crack plane is approximately flat and perpendicular to the external loading direction.

1.3.3 Single overload experiments

Three specimens were tested with a single overload and the experimental results are shown in Fig.17. After overloading, the growth rate decreased drastically to a minimum value. The crack growth rate recovered rapidly and then gradually approached the stable growth of the constant amplitude loading. This tendency of the crack growth rate after overloading was consistent with that observed by von Euw et al. [17]. When the R-ratio kept the same, the size of the transient zone was larger when the overloading occurred at a longer crack length. It is apparent that the transient zone size is determined by the plastic zone caused by the overloading. The influence of the overload diminished after the crack propagated out of the influencing zone created by overloading. To reduce the redundancy, the model predictions which will be discussed in a later section are presented together in Fig.17.

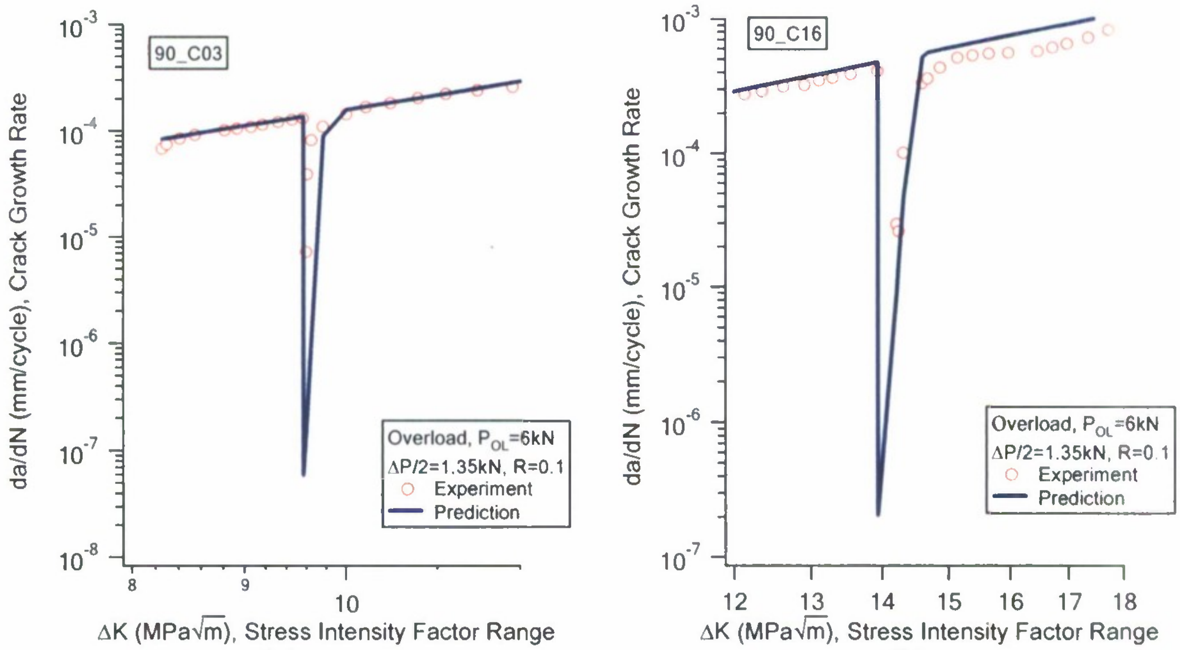

(a)　　(b)

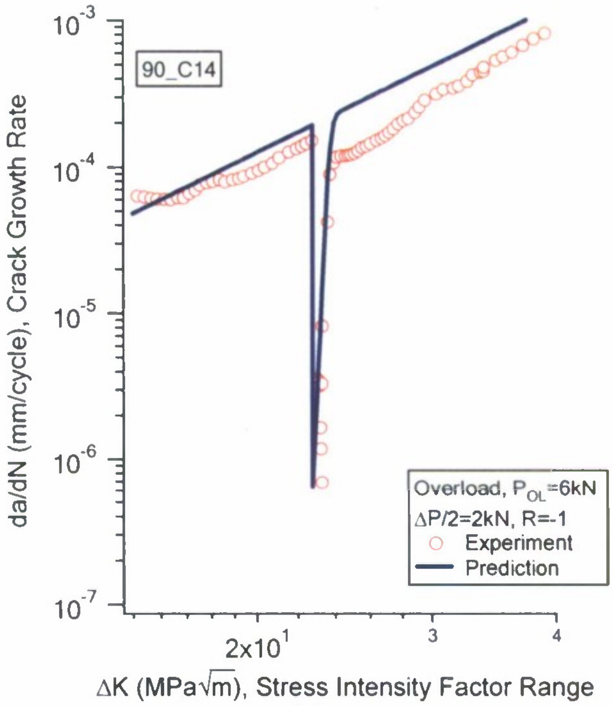

(c)

Fig.17 Overload effect on crack growth (7075-T651 aluminum alloy)

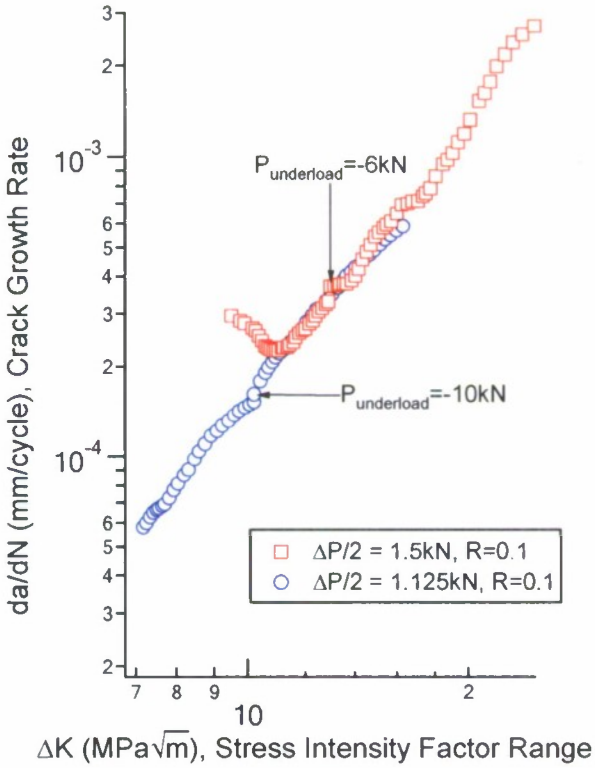

Fig.18 Underload effect on crack growth (7075-T651 aluminum alloy)

Figure 18 shows the experimentally obtained fatigue crack growth rates for two specimens subjected to underload (compressive overload) in constant amplitude loading. The effect of the underload on the specimen subjected to a lower constant amplitude ($\Delta P/2$ =1.125 kN, $P_{underload}$ =-10 kN) was not apparent. For the specimen subjected to a higher constant amplitude ($\Delta P/2$ =1.5 kN, $P_{underload}$ =-6 kN), the underload resulted in a identifiable but insignificant acceleration in crack growth rate. Right after underloading, the fatigue crack growth rate increased immediately to a higher value. The subsequent crack growth rate was approximately constant before the crack propagated through the influencing zone created by the underload. The growth rate resumed the normal level expected for the constant amplitude loading after the crack penetrated the influencing zone. Comparing with the overloading effect, the underloading effect was short-lived and insignificant.

1.3.4 High-Low loading sequence experiments

Figure 19 shows the experimental crack growth results from the two-step high-low sequence experiments. The first loading step had a loading amplitude of 1.8 kN and the second step had a loading amplitude of 1.125 kN. The load ratio in both steps was 0.1. After switching the load amplitude from a high value to a low value, the stress intensity factor was reduced greatly. In order to represent the experimental result clearly, the crack length instead of the stress intensity factor range was adopted for the horizontal axis in Fig.19. The crack growth behavior in the second loading step resembles that observed from the overloading effect. Upon the reduction in loading amplitude after the completion of the first step, the crack growth rate decreased drastically until a minimum value was reached. Thereafter, the crack growth rate increased rapidly as the crack length extended. The increase in the crack growth rate with the crack extension slowed down as the crack approached the boundary of the plastic zone of approximately 1.00 mm created by the previous loading step. Stable crack growth was resumed thereafter.

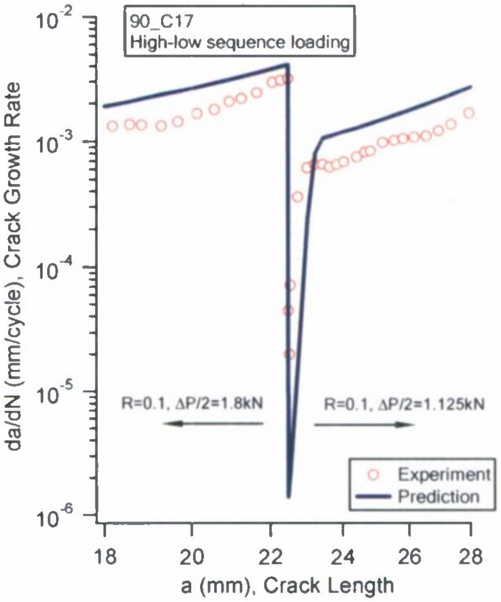

Fig.19 Crack propagation under two-step high-low sequence loading (7075-T651 aluminum alloy)

1.3.5 Crack propagation under combined axial-torsion loading

The experimental results of crack propagation under combined axial-torsion loading are summarized in Fig.20 and are represented in crack length-crack growth rate coordinates. The combination of tension-compression loading with out of plane torsion simulates the crack propagation in mixed Mode I and Mode III. Three loading paths were applied to the specimens (Fig.15). One loading condition represents the proportional loading (Fig.15(a)) and the other two loading scenarios represent the non-proportional. In all of the experiments, the *R*-ratio in tension-compression was kept equal to 0.1, while the R-ratio in torsion was equal to zero. The loading amplitudes are identical in the three loading paths.

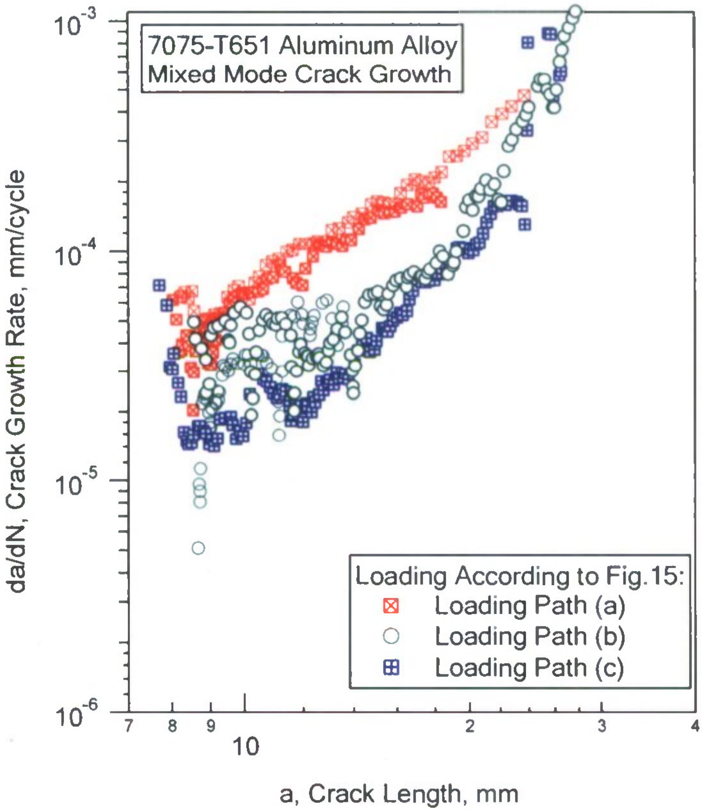

Fig.20 Crack propagation under combined axial-torsion loading

Based on the results represented in Fig.20, it can be concluded that the proportional loading produces the highest crack growth rates in 7075-T651 alloy. The nonproportional loading paths (Fig.15(b)(c)) generated similar crack growth results. The crack growth curve corresponding to the 90-degree out-of-phase axial-torsion loading path(Fig.15(b)) lies slightly above that of the loading path of Fig.15(c).

In order to determine the details of cracking profile under mixed mode loading conditions, Specimen BC05 was sectioned into several thin slices parallel to the specimen surface, which were examined using a microscope. By combining the microphotographs of the crack, it was possible to reconstruct the overall picture of cracking profile. The plane of the crack within the thickness of the specimen under combined axial-torsion loading appears to be inclined at a certain angle with respect to the plane normal to the specimen surface, which is shown in Fig.21.

The angle of inclination was measured to be 32^0. The details of the proportional combine axial-torsion experiment performed on the specimen BC05 can be found in Table 8.

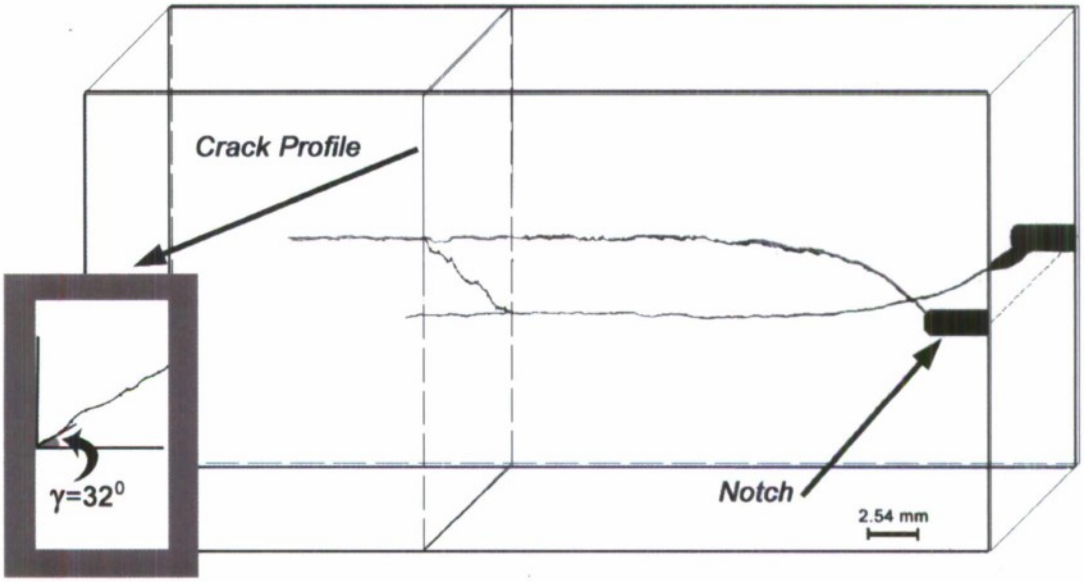

Fig.21 Crack profile under proportional axial-torsion fatigue loading

2 AISI 304L AUSTENITIC STAINLESS STEEL

The AISI 304L stainless steel belongs to a class of 300-type austenitic stainless steels and has been widely used in engineering applications requiring a resistance to the corrosive environment. The material has been employed in applications ranging from pharmaceutical equipment to piping in the nuclear reactors.

Significant research has been conducted on the fatigue behavior of the 304L steel since the introduction of the alloy into the industrial practice. Atanasiu [18] presented the results of crack growth experiments performed using CT specimens for three different *R*-ratios. The influence of the *R*-ratio on crack growth and threshold was observed. At the same time, as an effort to improve the fatigue properties of the steel, an extensive experimental study on the fatigue crack growth was performed to investigate the influence of the internal hydrogen on crack propagation [19]. It was shown that the introduction of the hydrogen into the metastable austenitic steel decreased the rate of crack propagation. An effect of the application of a single tensile overload on crack growth rate in 316L steel was investigated by Wheatley et al [20]. A short period of crack growth rate acceleration after the application of the overload was observed. The crack growth acceleration right after overloading was associated with cracking from voids within the plastic zone created by overloading.

The austenitic matrix in the 300-series stainless steels is unstable and it transforms to martensite under plastic deformation [21]. The martensitic transformation is temperature dependant [21]. Investigations were carried out targeting the phase transformations during fatigue of 304L and the influence on the fatigue crack propagation [22-26]. It was found [22] that by decreasing the mechanical stability of austenite (either by changing the composition or by lowering the temperature to martensite start temperature on cooling), the fatigue crack growth rate can be decreased when the *R*-ratios were low. Krupp et al [26] experimentally investigated the influence of the carbon content on the martensitic transformation. The hardening part of the cyclic transient curves obtained from testing un-notched smooth specimens was attributed to the phase transformation and the magnitude of such hardening was found to be a function of the carbon content in the stainless steel. Experimental investigations on fatigue cracking from the δ-ferrite/γ interface in the 304L steel [27, 28] revealed the dependence of the cracking mechanism on the directionality of the δ-ferrite fibers.

Without venturing into microscopic details and phase transformations, the current study emphasizes comprehensive fatigue experiments performed on AISI 304L stainless steel. The experiments include the crack initiation tests using smooth specimens as well as fatigue crack growth experiments with notch CT specimens. The main goal was to study the cyclic plasticity behavior, trends of the strain-life curves, influence of the mean stress over the wide range of the *R*-ratios, and loading histories on fatigue crack growth at the macroscopic level.

2.1 *MATERIAL*

AISI 304L stainless steel belongs to the class of austenitic stainless steels of 300 series. It can be distinguished from AISI 304 steel by lower content of carbon (letter L in the material designation) and higher content of chromium. The chemical composition of 304L steel is shown in Table 9 [21].

Table 9 Chemical composition of 304L stainless steel (%)

C	Mn	Si	Cr	Ni	P	S
0.03	2.0	1.00	18.0-20.0	8.0-12.0	0.045	0.03

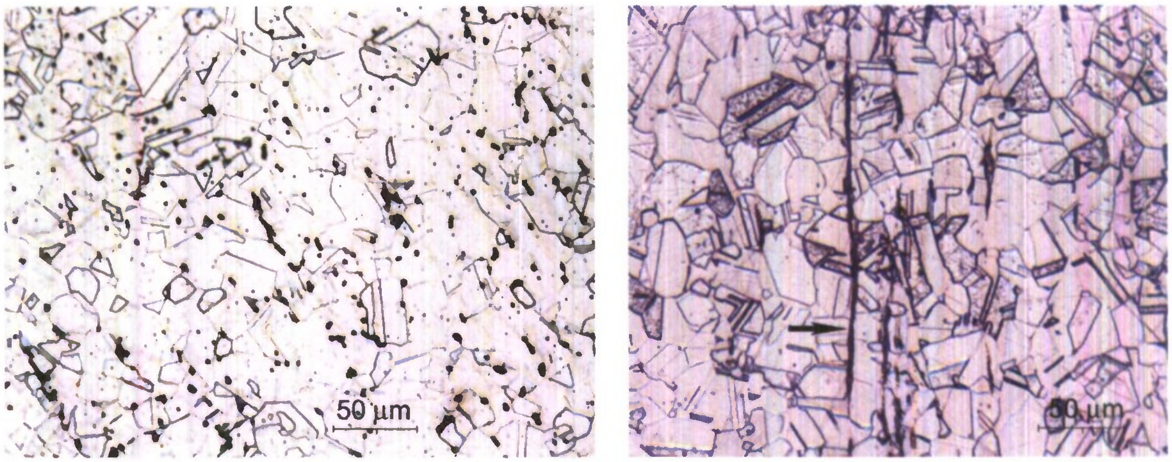

(a) (b)

Fig.22 Microstructure of AISI 304L stainless steel. a) perpendicular to the rolling direction; b) along the rolling direction. Magnification X800

The specimens for the fatigue experiments were machined from the supplied cold rolled bar. The microstructure of "as received" 304L steel is shown in Fig.22. The presence of the δ-ferrite stringers can be observed from the photographs in Fig.22 (indicated by the arrow in Fig. 22(b)). These stringers run along the rolling direction of the bar.

2.2 *CRACK INITIATION TESTS UNDER CONSTANT AMPLITUDE LOADING*

Twenty two specimens were tested in fully reversed strain-controlled fatigue experiments. The types of specimens used are dog-bone shaped specimens for axial tension compression tests and tubular specimens for pure torsion and axial-torsion non-proportional tests. The standard specimen design described previously for 7075-T651 aluminum alloy (Fig.3) was used in the present experiments. Three types of tests were performed: axial tension-compression, pure torsion and non-proportional 90^0 out-of-phase axial-torsion (Fig.4). The details of the tests are arranged in Table 10.

Table 10 Strain controlled fully reversed fatigue tests. Material 304L

Testing Type	Spec#	f, Hz	$\Delta\varepsilon/2$, %	$\Delta\sigma/2$, MPa	$\Delta\gamma/2$, %	$\Delta\tau/2$, MPa	N_f ,cycles
Tension-Compression	SS304-04	0.12	1.50	866.7	-	-	328
	SS304-09	0.15	1.00	635.0	-	-	680
	SS304-06	0.50	0.60	498.4	-	-	3,540
	SS304-01	0.80	0.40	424.7	-	-	20,450
	SS304-10	2.00	0.32	376.1	-	-	44,600
	SS304-02	2.50	0.30	382.3	-	-	98,501
	SS304-03	2.00	0.28	388.0	-	-	308,500
	SS304-07	5.00	0.26	360.9	-	-	184,000
	SS304-04*	8.00	0.25	374.3	-	-	1,050,500
Pure Torsion. Tubular Specimens	SS304-T12	0.12	-	-	2.41	410.7	800
	SS304-T09	0.20	-	-	1.73	279.3	2,380
	SS304-T08	0.40	-	-	1.04	242.8	10,880
	SS304-T13	0.60	-	-	0.87	250.3	30,400
	SS304-T04	0.80	-	-	0.69	220.2	90,321
	SS304-T07	1.50	-	-	0.55	188.2	293,501
	SS304-T10	1.50	-	-	0.43	208.2	1,659,410
Non-Proportional 90^0 out-of-phase	SS304-T16	0.10	0.40	500.5	0.69	309.7	1,250
	SS304-T02	0.12	0.35	517.1	0.61	319.8	1,646
	SS304-T15	0.20	0.30	419.9	0.52	258.1	4,400
	SS304-T17	0.25	0.28	410.6	0.48	249.3	11,000
	SS304-T11	0.25	0.25	377.4	0.43	232.2	12,800
	SS304-T05	0.50	0.20	302.8	0.35	186.7	21,535
	SS304-T14	1.00	0.18	264.0	0.31	162.0	59,465
	SS304-T02*	1.50	0.17	277.4	0.29	171.8	1,000,000
	SS304-T12*	2.00	0.15	246.5	0.26	152.4	655,000

**The specimen did not fail*

f – frequency of applied loading;
$\Delta\varepsilon/2$ – amplitude of applied axial strain;
$\Delta\gamma/2$ – amplitude of applied shear strain;
$\Delta\sigma/2$ – axial stress amplitude;
$\Delta\tau/2$ – shear stress amplitude;
N_f – number of cycles to failure.

2.2.1 Cyclic plasticity behavior

Figure 23 represents the cyclic hardening curves based on the data collected during the experiments. Due to the specifics of the testing equipment, in some cases the pre-set value of the strain amplitude is not reached immediately at the beginning of the test. Therefore, the stabilization period, during which the strain control reaches its designed value, has been removed from the graphs in Fig.23. It can be seen from the Fig.23 (a,b) that when tested in tension-compression and pure torsion, the material exhibits a period of cyclic softening followed by cyclic hardening until the failure of the specimen. The amount of cyclic hardening clearly depends on the level of applied strain amplitude. This cyclic hardening is a result of plasticity induced transformation from austenite to martensite in meta-stable austenitic steel such as 304L [26]. The plots in Fig.23 are arranged in terms of equivalent stress and strain which facilitates the comparison between curves corresponding to different types of loading. By comparing the cyclic hardening curves for tension-compression and pure torsion it can also be noted that the stress levels in case of tension compression are much higher than the stresses under pure torsion loading with the corresponding equivalent strain amplitudes. In addition, the cyclic hardening prior to failure is more pronounced in pure torsion cases when the specimens tested under low equivalent strain amplitudes are compared.

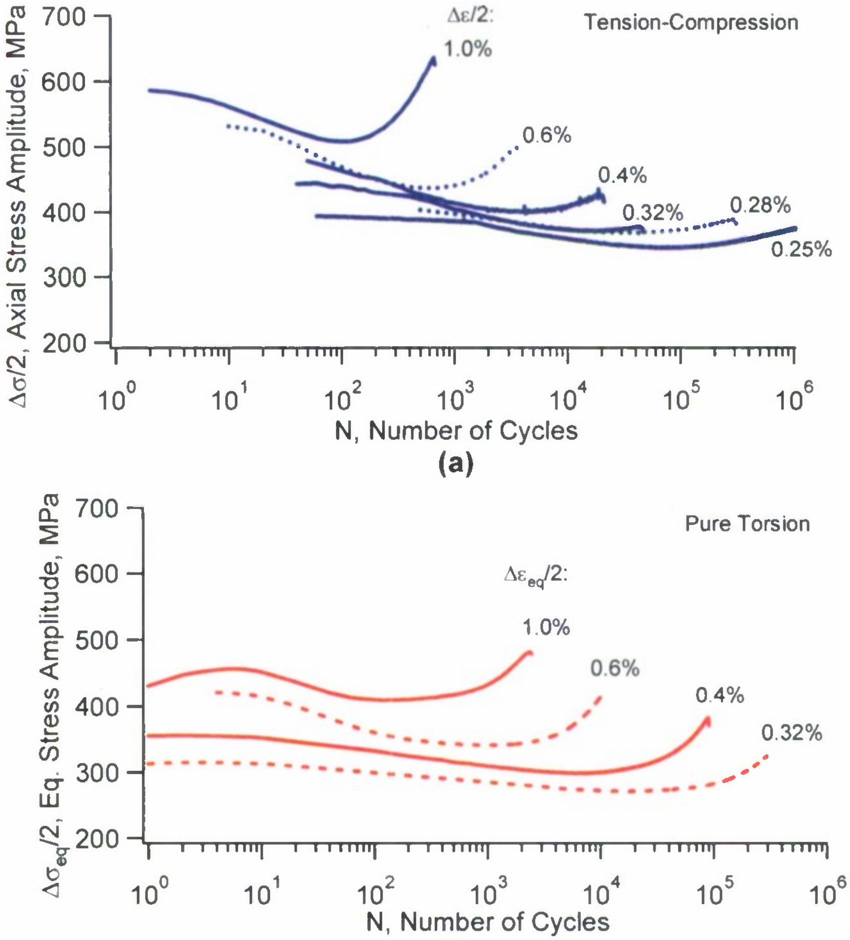

(a)

(b)

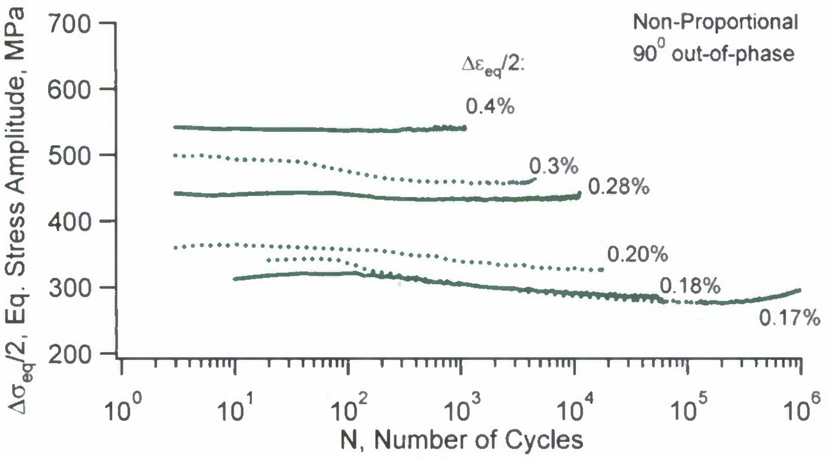

(c)

Fig.23 Cyclic hardening behavior (AISI 304L): (a) tension-compression; (b) pure torsion; (c) 90^0 out-of-phase non-proportional loading

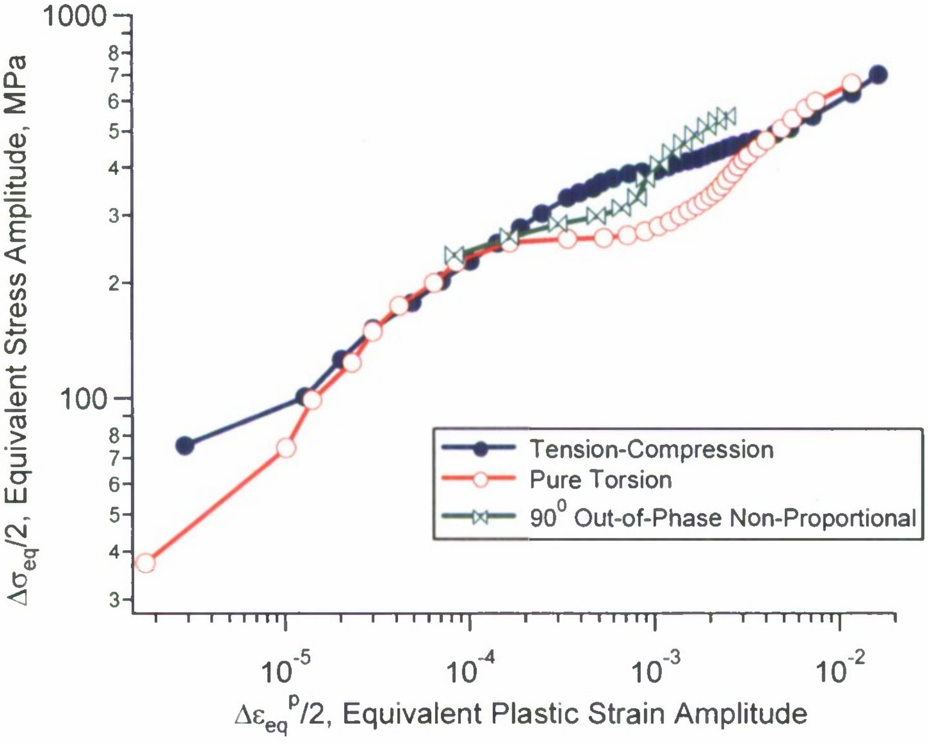

Fig.24 Cyclic stress-strain curves (AISI 304L)

In order to obtain a cyclic stress-strain curve (CSSC), three specimens were tested in incremental step conditions under three different loading paths. The resulting curves are shown in Fig.24. As can be seen from Fig.24 the material displays rather peculiar behavior. At the region of low plastic strain amplitudes, all three curves come together, however at the onset of the quasi-plateau regime the curves corresponding to different loading conditions behave differently. The quasi-plateau of CSSC corresponding to tension-compression lies higher than one corresponding to pure torsion and the quasi plateau of non-proportional curve lies between them. At the end of quasi plateau regime, the curve corresponding to 90^0 out-of-phase axial-torsion loading comes higher than the curve corresponding to uniaxial tension-compression loading. Therefore, the material displays non-proportional hardening only at high levels of applied strain.

2.2.2 Strain-life curve and cracking observations

The results of the fatigue experiments are combined and displayed as the strain-life curves (also known as Coffin-Manson curves) as shown in Fig.25. The vertical axis in Fig.25 represents amplitude of applied equivalent strain and the horizontal axis represents the fatigue life of the specimen. An arrow next to the data point means that the specimen did not fail at the end of experiment. Since the results are represented using equivalent strain a comparison between the fatigue curves corresponding to different loading can be made. It can be seen that the fatigue life of specimens tested in pure torsion is higher than the life of tension-compression specimens. At the same time, the shortest fatigue life is observed for the specimens tested in 90^0 out-of-phase loading condition. The strain-life curves run approximately parallel to each other and tend to merge together in the high cycle fatigue region.

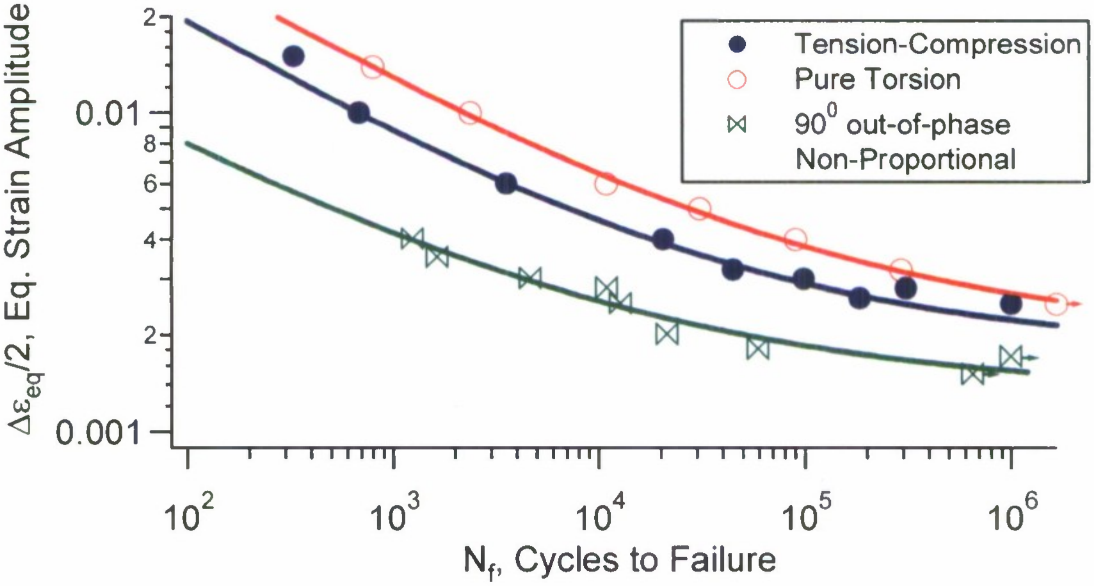

Fig.25 Strain-life curves corresponding to three types of loading (AISI 304L)

It was observed that the cracking behavior of specimens tested in pure torsion depends on the level of the applied strain amplitude. The cracks of the six specimens tested in pure torsion were photographed and the angles of crack orientation were measured. The details are shown in Fig.26. The crack orientation can be defined by the angle formed by the normal to the cracking plane and the vertical axis of the specimen. From the photographs of the fatal cracks shown in Fig.26 it can be seen that the cracks developed in the tests under high strain amplitude $(\Delta\gamma/2 > 1.0\%)$ tend to orient at either 0^0 or 90^0 with respect to the vertical axis of the specimen (planes of maximum shear). At the same time that cracks in the specimens tested under low amplitudes of applied strain are oriented at the angles close to 45^0 (along the planes of maximum tensile stress).

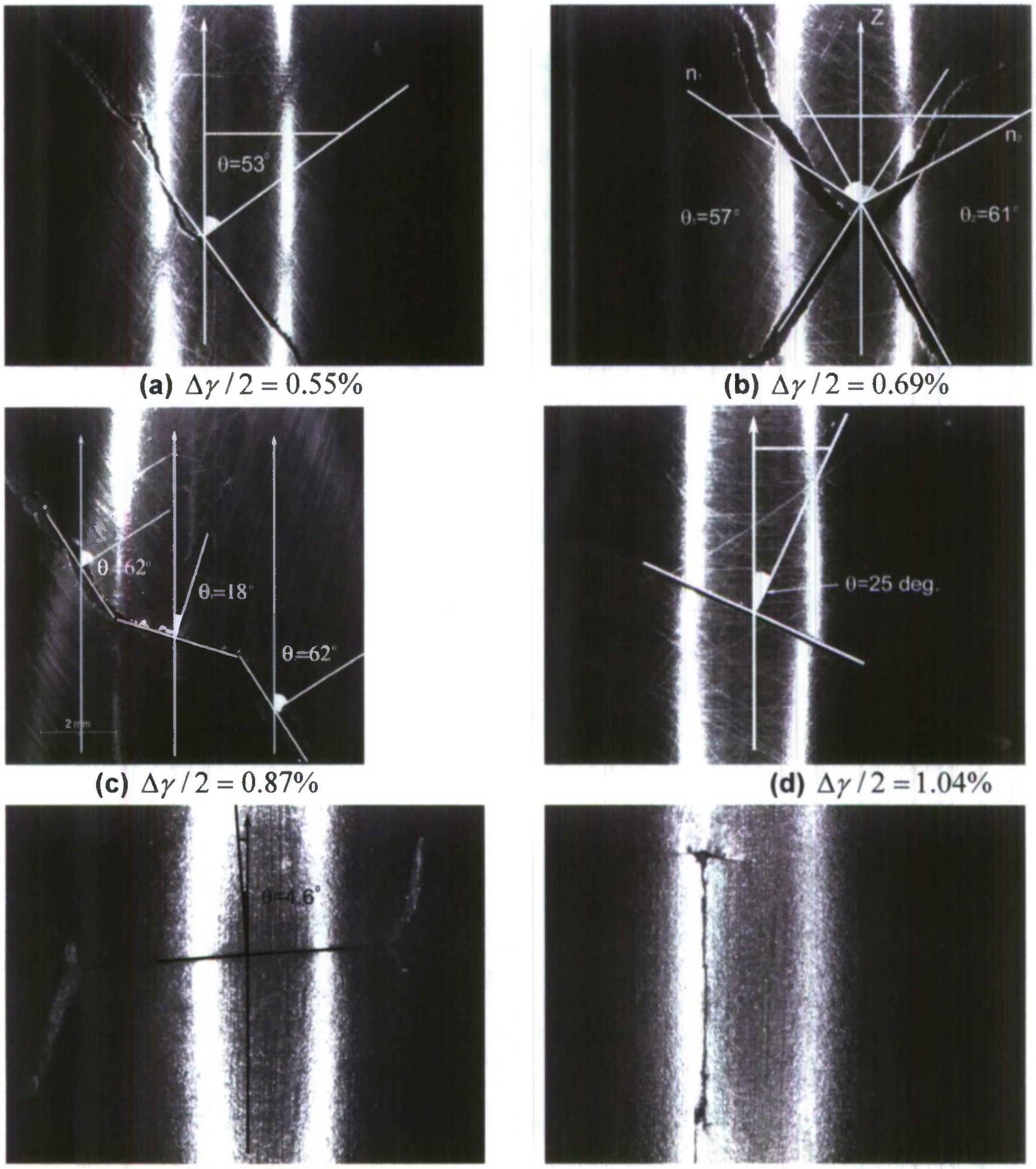

(a) $\Delta\gamma/2 = 0.55\%$ **(b)** $\Delta\gamma/2 = 0.69\%$

(c) $\Delta\gamma/2 = 0.87\%$ **(d)** $\Delta\gamma/2 = 1.04\%$

(e) $\Delta\gamma/2 = 1.73\%$ **(f)** $\Delta\gamma/2 = 2.41\%$

Fig.26 Dependence of fatigue cracking orientation on loading amplitude in pure torsion

2.3 *CRACK GROWTH EXPERIMENTS*

Fatigue crack growth experiments for 304L stainless steel were performed on round compact tension (CT) specimens with a single notch under sinusoidal load-controlled loading in laboratory environment at room temperature. All the specimens have a thickness of 3.8mm. The

U-shape notches were made using the Electric Discharge Machine (EDM) in order to avoid residual stresses resulting from a traditional saw cutting. The design of the specimens is shown in Fig. 26.

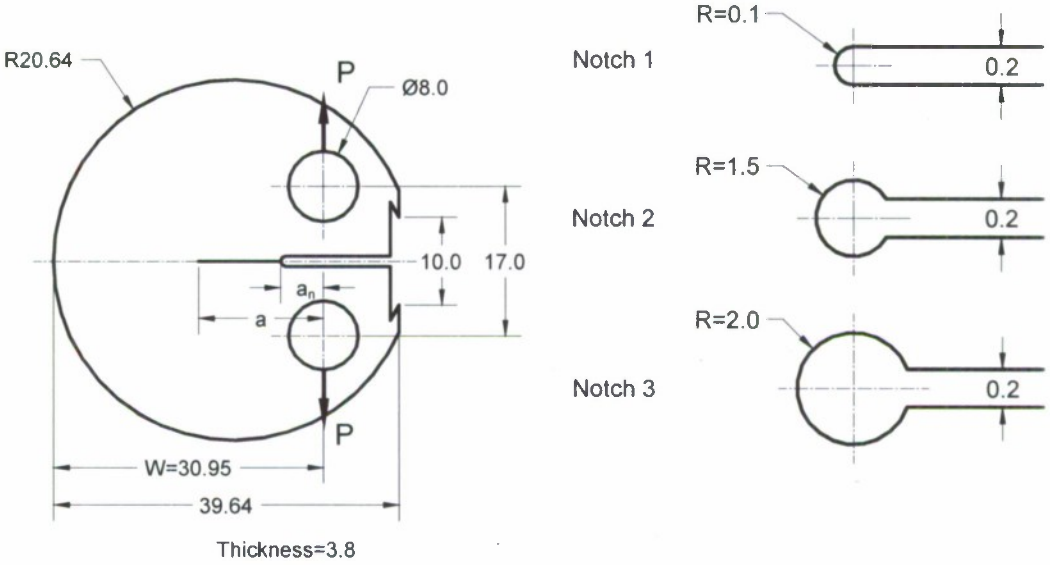

Fig.27 Design of the compact tension specimen for AISI 304L stainless steel

Crack extension from notch root was measured using an optical reading microscope with a magnification of 40. To facilitate convenient crack extension measurement, one side of each specimen was polished enough finely before installation on the test machine. The loading conditions include constant amplitude loading with different *R*-ratios, constant amplitude loading with a single tensile overload or compression underload applied at certain crack length, as well as two-step sequence loading.

A traditional way of representing the crack growth results by using the stress intensity factor range (ΔK) was employed in the present investigation. It should be mentioned that the formula traditionally used for stress intensity factor [16] is not applicable for small cracks ($\alpha < 0.2$, where $\alpha = a/W$ and a is the crack length, W is the width of the specimen).

$$\begin{cases} \Delta K = \Delta P \cdot C \cdot F(\alpha), \\ C = \dfrac{1}{\sqrt{W} \cdot t}, \quad \alpha = \dfrac{a}{W}, \\ F(\alpha) = \dfrac{(2+\alpha)(0.76 + 4.8\alpha - 11.58\alpha^2 + 11.43\alpha^3 - 4.08\alpha^4)}{(1-\alpha)^{3/2}} \end{cases} \tag{5}$$

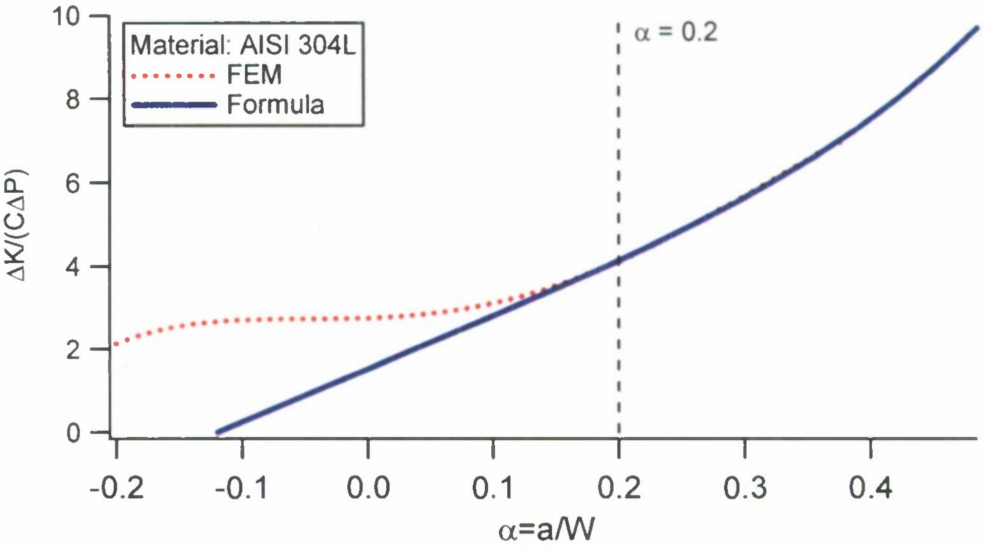

Fig.28 Stress intensity factor obtained by using Eq.(5) and FE method

The finite element method (FEM) was employed in order to obtain the values of stress intensity factor at small crack length. In Fig. 28, the results of FE method are represented in dimensionless form and are compared to the function $F(\alpha)$ from Eq.(5). The polynomial fit of 6th power was used to fit the dimensionless function obtained with FEM as a function of $\alpha = a/W$ and this function can be used to obtain stress intensity factors for all specimens used in the experiments on AISI 304L material. All results of the crack propagation experiments in the present report are represented using stress intensity factor range obtained by FEM simulations.

2.3.1 Constant amplitude experiments

The details of the experiments conducted under constant-amplitude loading with the R-ratios ranging from -1 to 0.85 are listed in Table 11. It should be noted that the crack length is measured from the line of action of the applied load (Fig.27). A negative value of the crack length is possible and it signifies that the crack tip is on the right side of the line of the action of the applied load.

Figure 29 shows the results of the crack growth experiments performed under the constant amplitude loading conditions with six different R-ratios ranging from -1 to 0.85 (see Table 11). The figure also includes the result of the pre-cracking step ($R = 0$, $\Delta P/2 = 2.5kN$) for specimen C16 which was subsequently conducted with $R = 0.85$. The early stage crack growth is influenced by the notch geometry as well as the amplitude of the applied load. With an identical R-ratio of 0.1, the curves show different early crack growth behavior with different loading amplitudes. The $da/dN - \Delta K$ curve for a higher loading amplitude ($\Delta P/2 = 2.475kN$) reaches a stable growth regime almost immediately after initiation. At the same time, the $da/dN - \Delta K$ curve obtained from the test with a lower applied load ($\Delta P/2 = 2.2kN$) demonstrates a short crack-like phenomenon at the onset of cracking. Such a phenomenon is especially pronounced in the case of $R = -1$ experiment. As the crack length exceeds the size of the notch influencing zone, the crack growth rate becomes stable and can be approximately represented by a constant slope in the log-log $da/dN - \Delta K$ representation.

Table 11 Constant amplitude loading: AISI 304L

Spec #	R-ratio	$\Delta P/2$ (kN)	f (Hz)	Notch radius (mm)	Notch depth /precrack a_n (mm)	$N_{0.5}$ (cycle)	N_f (cycle)	a_f (mm)
C01	0.1	2.475	2~20	0.188	-1.340	28,568	259,320	12.899
C06	0.1	1.800	2~20	0.105	-1.095	90,574	1,076,324	16.027
C20	0.2	2.000	1~10	2.016	7.382	61,193	84,093	13.062
C02	0.5	1.750	1~20	0.130	-1.311	54,631	323,461	14.131
C17	0.5	1.800	2~15	0.072	-1.516	42,422	261,265	10.329
C03	0.75	1.000	5~20	0.152	-1.216	499,915	1,483,387	10.394
C18	0.75	0.950	10~20	0.090	-1.526	371,680	1,406,365	10.572
C16	0.85	0.540	10~20	*	3.338	255,793	1,707,078	11.843
C14	-1	5.000	0.5~4	**	5.635	2,089	15,059	12.895
C24	-1	3.200	2~3	0.992	2.361	15,772	215,494	14.173

R-ratio = the ratio of the minimum load over the maximum load in a loading cycle

$\Delta P/2$ = external loading amplitude f = loading frequency

a_n =notch depth or pre-crack length measured from the line of action of the applied load

$N_{0.5}$ =number of loading cycles when the crack length from the notch root is 0.5 mm

N_f =number of loading cycles when the test was terminated

a_f =crack length measured from the line of the applied load at the termination of the test

* pre-cracked with cyclic load of R =0.1, $\Delta P/2$ =2.5kN

** pre-cracked with cyclic load of R =-1, $\Delta P/2$ =3.0kN

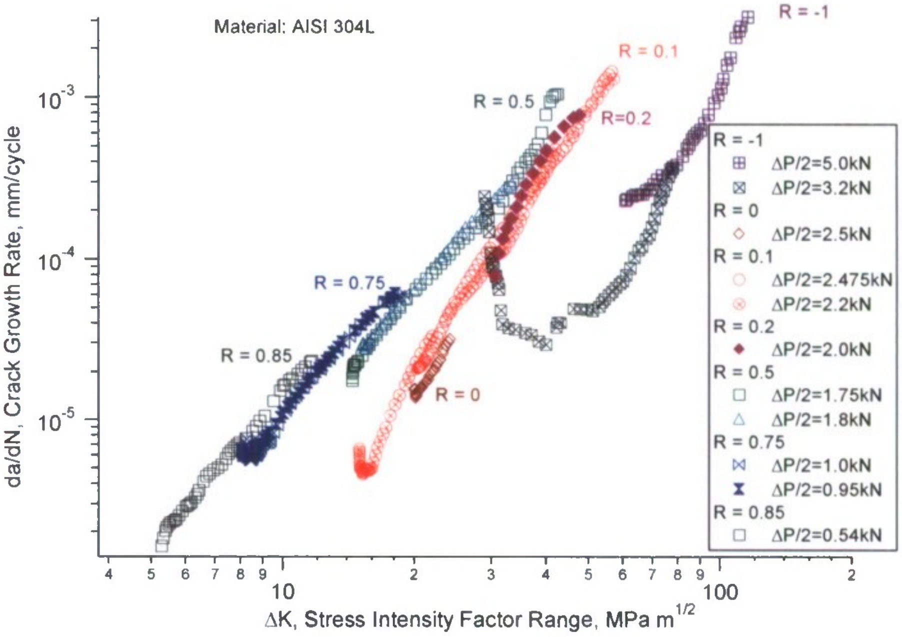

Fig.29 Crack propagation under constant amplitude loading with the effect of the R-ratio (AISI 304L)

The experimental results shown in Fig. 29 reveal the *R*-ratio effect, typical for stainless steels, with the data curves corresponding to different *R*-ratios being approximately parallel to each other. It should be mentioned that the pre-cracking was used for the specimen tested under *R*=-1 condition and the part corresponding to the stable crack growth is represented in Fig.29.

2.3.2 Single overload experiments

Seven CT specimens were tested under constant amplitude loading with a single overload or underload. The details of the overload experiments are represented in Table 12.

Table 12 Crack growth experiments with single overload/underload

Spec#	R-ratio	$\Delta P/2$	f	Notch radius	Notch depth a_n	P_{OL}	N_{OL}	a_{OL}	N_f	a_f
		(kN)	(Hz)	(mm)	(mm)	(kN)	(cycle)	(mm)	(cycle)	(mm)
C04	0.1	2.250	2~20	0.129	-1.2165	7.0	338,195	5.3365	401,721	11.5825
C05	0.1	2.250	3~20	0.112	-1.1255	8.0	269,423	5.4585	368,191	11.2585
C09	0.1	1.800	1~20	0.1095	-1.0685	7.0	947,353	8.2975	1,106,536	14.4345
C11	0.1	1.800	1~20	0.125	-1.153	8.0	752,718	5.377	1,344,659	13.501
C13	0.1	2.250	2~15	0.120	-1.133	-9.0	387,427	5.014	425,582	12.099
C22	0.1	2.700	0.5~10	1.659	4.2535	-9.0	102,865	7.6245	108,586	11.5135
C23	0.1	1.800	3~20	0.1145	-1.4835	-9.0	684,340	6.3735	731,360	11.4995

P_{OL} = magnitude of overload or underload

N_{OL} = number of cycles of constant amplitude loading before overloading or underloading

a_{OL} = crack length measured from the line of action of the applied load at overloading or underloading

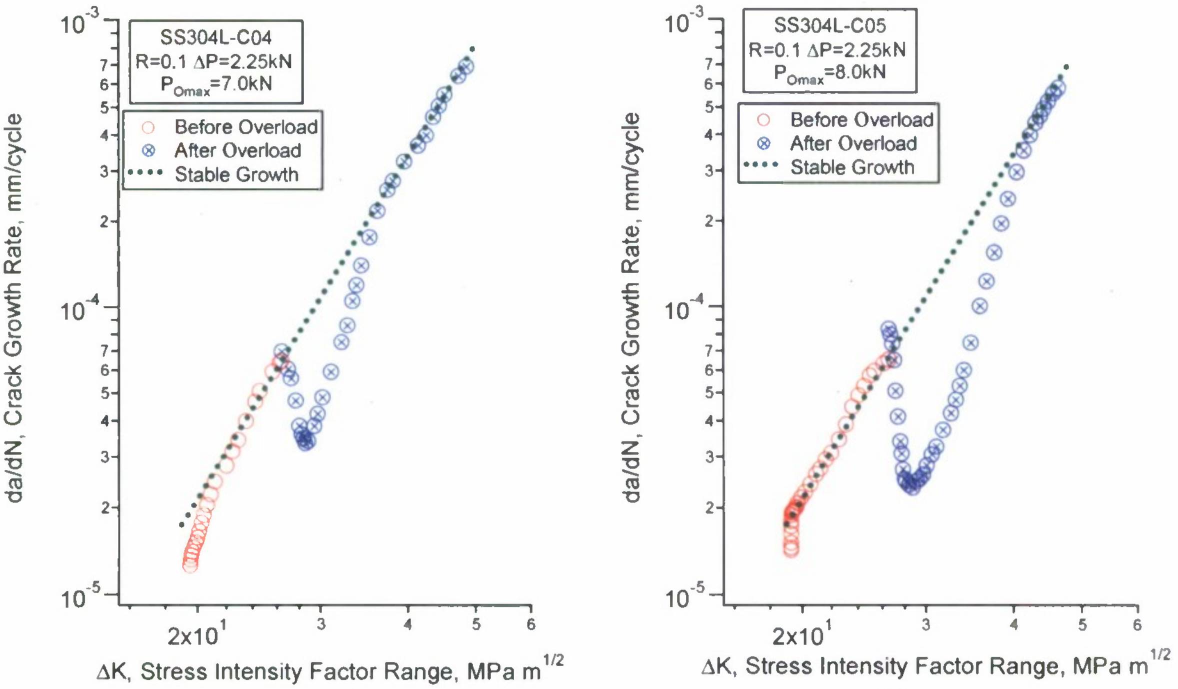

(a) (b)

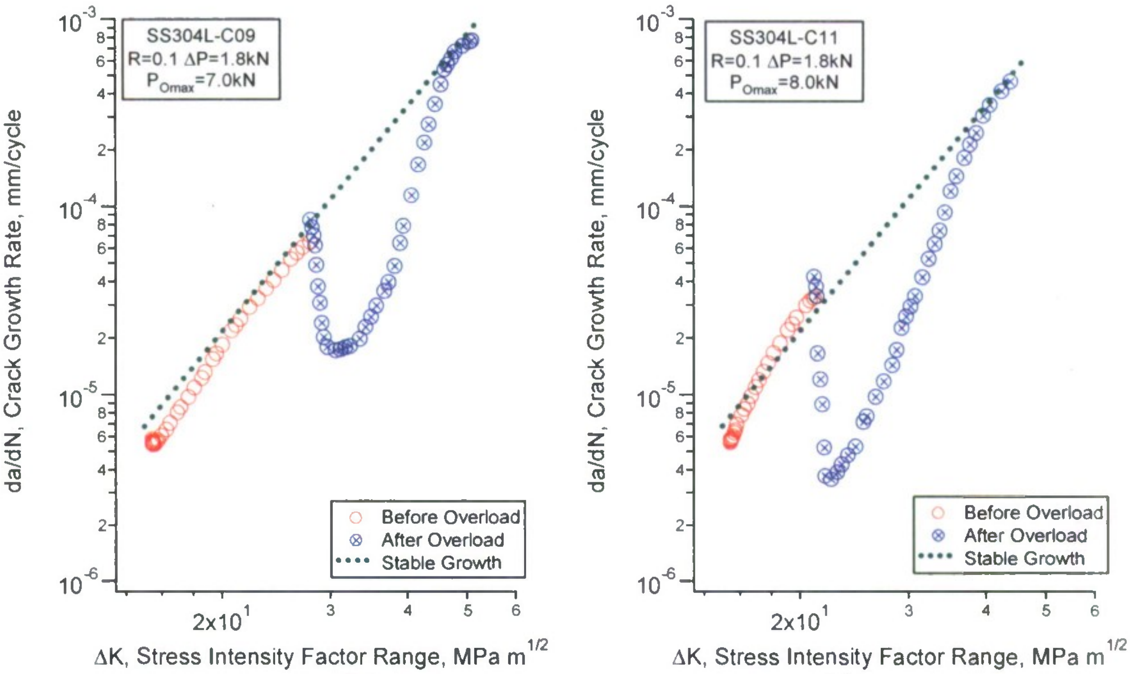

(c) (d)

Fig.30 Overload effect on crack growth (AISI 304L)

The results of overload experiments are shown in Fig. 30. The thick dotted line in each plot represents the stable crack growth rate in order to facilitate the observation of overload effect. From Fig.30 it can be seen that application of a tensile overload causes significant crack growth retardation. The level of such retardation clearly depends on the magnitude of overload as well as on amplitude of applied load. It should be noticed, that the short period of acceleration of crack growth can be observed immediately after application of overload. Then the crack growth slows down reaching a minimum point. With further application of loading cycles the crack growth rate reaches a stable growth curve. Such behavior has been observed previously from the experiments on 316L stainless steel [20] and the crack acceleration upon application of overload was attributed to the cracking from voids within the overload plastic zone.

Three specimens were subjected to single-cycle underloading (compressive overload) in the otherwise constant-amplitude loading histories. Figure 31 demonstrates the results of the experiments. The markers represent the experimentally obtained data points and the thick dotted lines represent the stable crack growth line obtained from the Paris law for R=0.1 loading shown in Fig.29. In all of the three experiments, the magnitude of the applied underload was kept the same and was 9 kN. The plots within the Fig. 31 are arranged in the order of increasing amplitude of constant loading applied in the corresponding experiments. It can be seen from Fig. 31 that unlike the effect produced by overload, underloading results in an acceleration in crack growth of the subsequent loading cycles right after the application of the overload. Such an acceleration is not as prominent as the crack growth retardation after overloading. However, the underload effect is not insignificant and it cannot be neglected. It should be noticed from Fig. 31 that the magnitude of crack growth rate acceleration depends on the amplitude of the applied load during the constant amplitude loading part of the experiment. In general, with the same magnitude of underload, the specimen tested under the lower constant load amplitude produces a greater acceleration in crack growth right after the application of the underload.

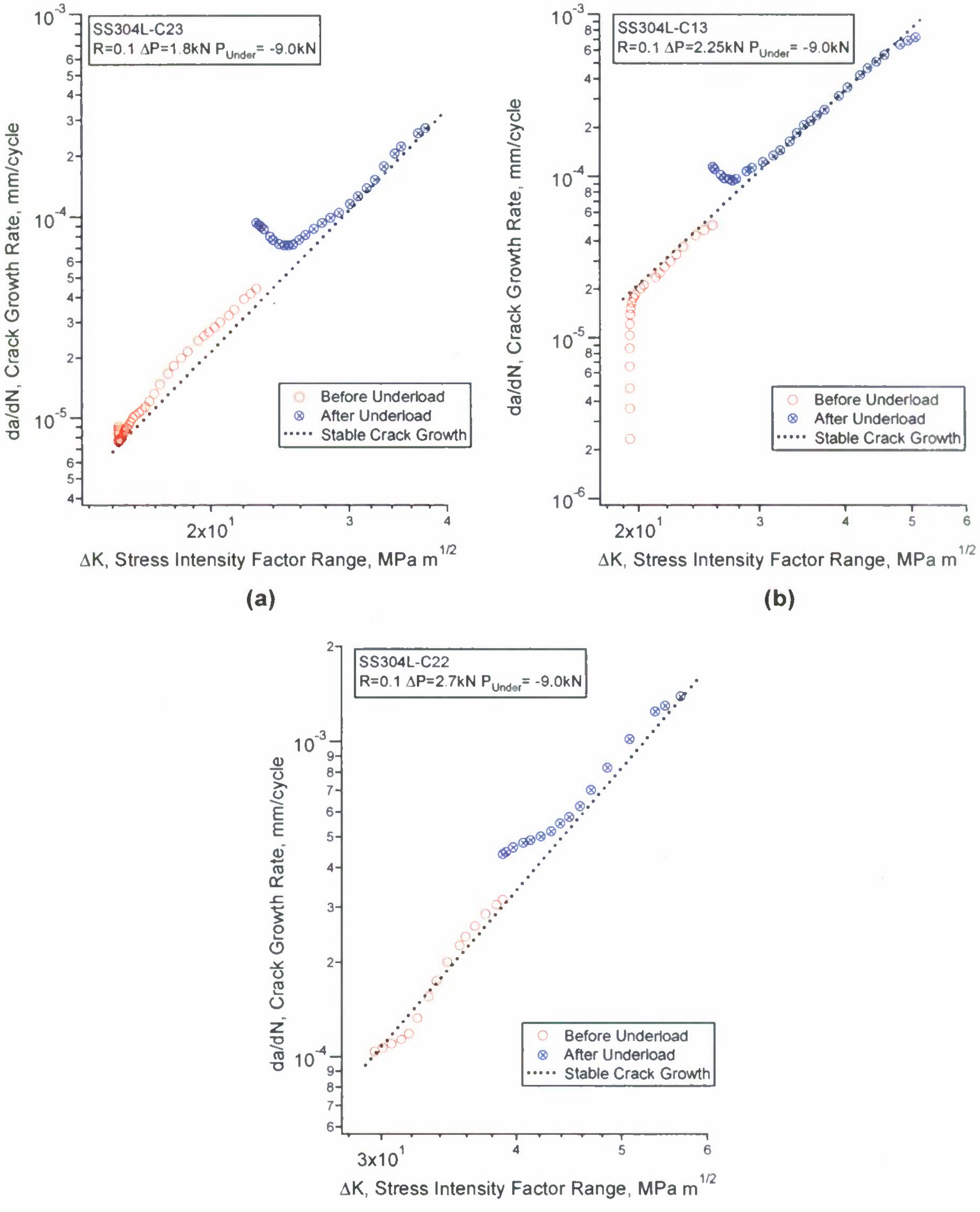

(a) **(b)**

(c)

Fig.31 Underload effect on crack growth (AISI 304L)

2.3.3 High-Low sequence loading

Three experiments were conducted to study the influence of the high-low sequence loading on crack growth. The details of the testing conditions are listed Table 13. It should be stressed that in all of the three experiments, the values of the load amplitude at the higher load steps were kept identical and the loading amplitudes in the second (lower) loading were the same. Referring to Fig. 32 for the detailed loading conditions, the maximum load was the same for the two loading steps in one specimen (Fig. 32(a)). In the second specimen, the minimum load was identical in the two loading steps (Fig. 32(b)). The third specimen experienced two-step loading with identical *R*-ratio in the two loading steps. The results of the experiments are shown in Fig. 33. Due to the fact that the amplitude of the loading is not the same in the two steps of the high-low experiment, the stress intensity factor range is not continuous throughout the experiment.

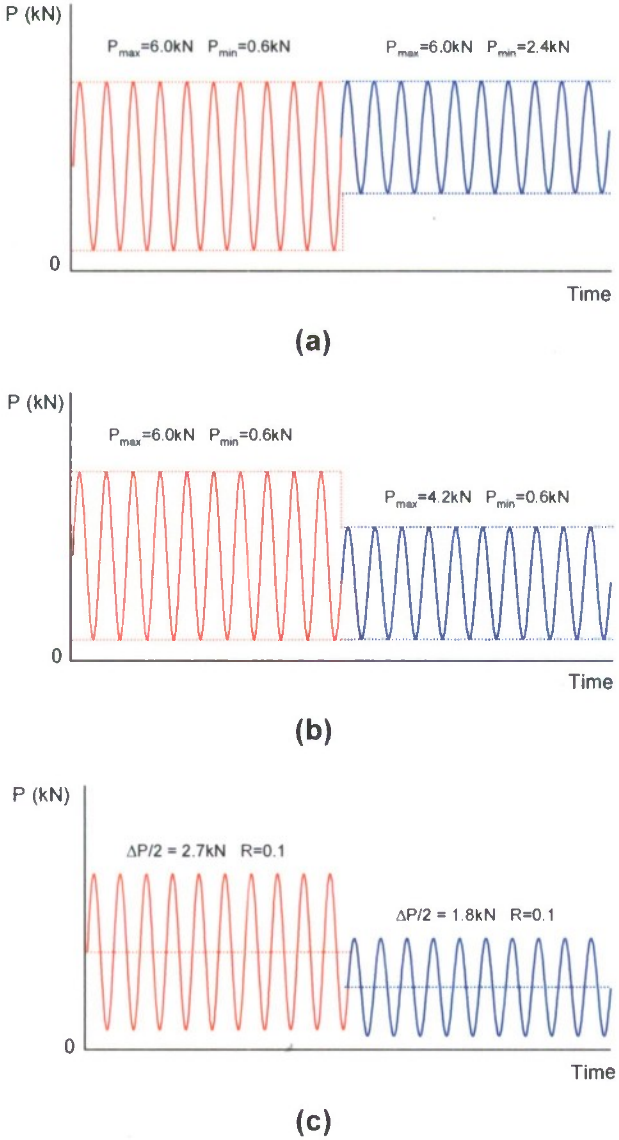

Fig.32 Schematic of High-Low experiments

Table 13 High-low sequence loading

Spec#	R_1 – ratio	R_2 – ratio	$\Delta P_1/2$ (kN)	$\Delta P_2/2$ (kN)	f (Hz)	Notch radius (mm)	Notch depth a_n (mm)	N_H (cycle)	a_H (mm)	N_f (cycle)	a_f (mm)
C07	0.1	0.4	2.700	1.800	2~20	0.102	-1.169	152,618	5.020	208,000	12.203
C08	0.1	0.143	2.700	1.800	1~15	0.104	-1.162	143,956	4.428	385,888	11.847
C19	0.1	0.1	2.700	1.800	1~10	0.099	-1.600	111,351	4.593	418,477	12.549

R_1 = R-ratio in higher amplitude loading

R_2 = R-ratio in lower amplitude loading

$\Delta P_1/2$ =loading amplitude in higher amplitude loading

$\Delta P_2/2$ = loading amplitude in lower amplitude loading

N_H = number of cycles at the termination of the higher loading

a_H =crack length measured from the line of action of the applied load at the termination of the higher loading

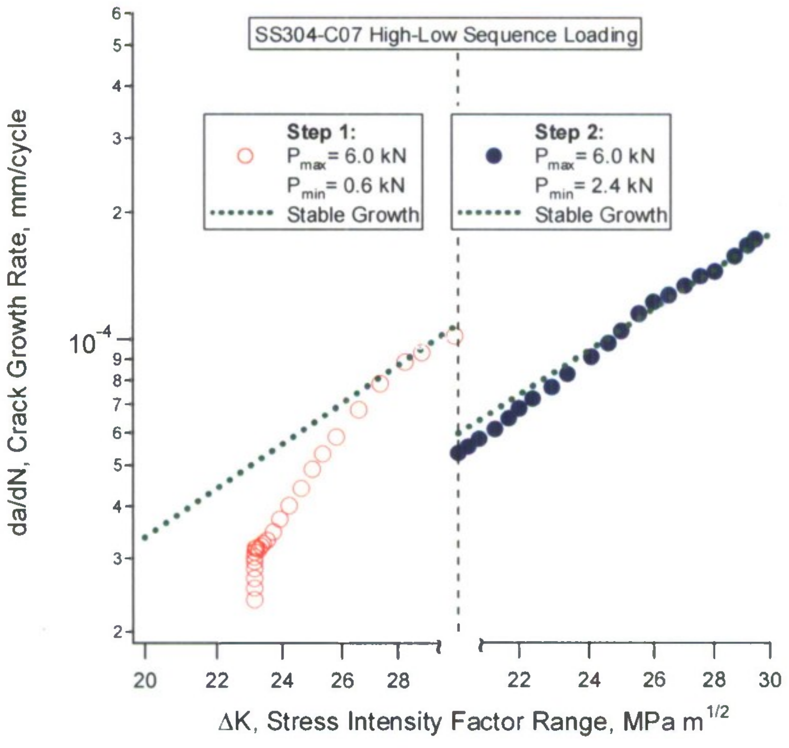

(a)

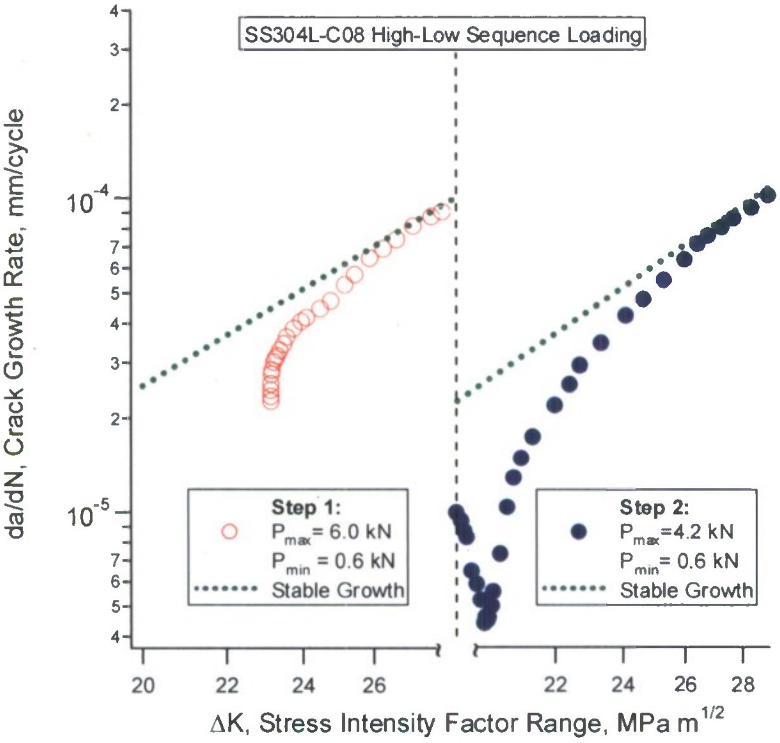

(b)

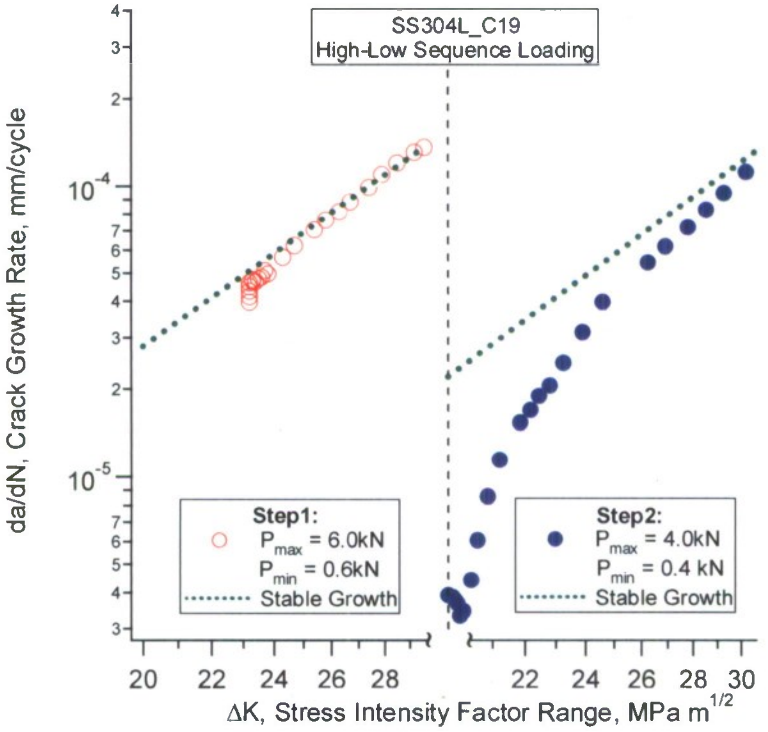

(c)

Fig.33 High-Low sequence loading. (a) same maximum load; (b) same minimum load; (c) same *R*-ratio

The horizontal axis in the plots in Fig. 33 represents the stress intensity factor range and is broken into two parts corresponding to the high amplitude and low amplitude parts of the test. The values of ΔK are not continuous at the transition from one loading step to another. In each of the plots the dotted line corresponds to the stable crack growth under constant amplitude loading. The results shown in Fig. 33 reveal that the influence of the high-low sequence loading depends on the details in the lower amplitude loading step. When the maximum load was kept the same in the two loading steps, the higher loading step had practically no influence on the crack growth of the second loading step with a lower load amplitude (Fig. 33(a)). However, significant crack growth retardation was observed on the other two specimens, resembling the overload effect shown in Fig. 30.

3 AL6-XN SUPERAUSTENITIC STAINLESS STEEL

Stainless steels of austenitic type are known for their desirable ductility and high corrosion resistance. Among a variety of stainless steels, the AL6-XN alloy is distinguished by its extreme stability of austenite which does not transform to martensite over a wide range of temperature and plastic deformation. While AL6-XN possesses an excellent formability typical for traditional metastable austenitic steels, there is no plasticity-induced martensitic transformation under cold working. Therefore, the alloy is commonly referred to as a super-austenitic stainless steel. AL6-XN is a relatively new material, developed by Allegheny Ludlum Corporation, and was originally designed for seawater applications – offshore platforms. The material exhibits a much greater resistance to chloride pitting, crevice corrosion, and stress-corrosion cracking than the 300-series stainless steels [29].

The AL6-XN alloy has been used in a variety of applications ranging from chemical processing tanks to nuclear plant service water piping that require resistance to corrosive environments. The high levels of chromium, nickel, molybdenum, and nitrogen provide an excellent resistance to chloride corrosion and stress corrosion cracking. Despite the wide engineering application, the AL6-XN alloy has not been extensively studied for the mechanical properties. Since the original development of AL6-XN steel was targeted towards the off-shore platform applications, the corrosion resistance to the salt water environments [30-32] was a concern. Other work on the properties of the stainless steel has been done primarily in the microstructural features [29, 33] and [34] and crack propagation in the welds [35, 36]. Modeling of the plastic behavior was conducted based in particular on crystal plasticity theories [37-39].

New and advanced technique for three-dimensional analysis of the microstructure was developed and applied to the AL6-XN steel by Lewis and co-workers [33]. The technique is a combination of a serial sectioning and electron backscatter diffraction (EBSD) which allows for a reconstruction of individual grains with boundary conditions in three dimensions. The data obtained by the microstructure analysis can be used for crystal plasticity modeling. Valuable observations were made by Stauffer et al [34] who explored the connection between the microstructural bands of AL6-XN with the failure mechanism under static loading. For the tensile specimens oriented in such a way that the microstructural chemical (or composition) bands were parallel to the loading axis, the fracture crack was observed to penetrate along the microstructural band. As a result, the specimen showed splitting along the tensile axis. Such an observation reveals a degree of anisotropy of the material which is worthwhile to investigate further through an observation of the fatigue crack growth mechanism under cyclic loading.

A plasticity theory developed by Voyiadjis and Abed [39] was applied to AL6-XN and the predicted results were compared with the experimental data obtained by Nemat-Nasser et al [29] for the monotonic compression experiments over a wide range of strain rates and temperatures. The plasticity model is based on the dislocation interaction mechanisms. The model considers the strain rate and temperature influences on the plastic deformation of the material and takes into account the thermal activation analysis and the decomposition of the flow stress into the thermal and athermal parts.

The investigation on the fatigue behavior of AL6-XN alloy has been limited to welds. Full scale welded I-beams were studied for the fatigue behavior of several weld details (longitudinal fillet, simulated bulkhead and groove welds) [36]. Constant amplitude experiments were conducted. The influence of the grain size of the welded material on the fatigue crack propagation in the gas metal arc welds of 316L and AL6-XN steels were investigated [35]. It was concluded that the large grain size of welded material improved the fatigue resistance.

The current study focuses on an experimental investigation of the cyclic plasticity and fatigue of the AL6-XN stainless steel. Experiments were conducted with solid specimens subjected to uniaxial loading and tubular specimens under pure torsion and combined axial-torsion loading. The experiments were performed under the strain-controlled condition with strain amplitudes ranging from 0.17% to 1.4%. The stress-strain response was collected during the fatigue experiments which will allow for an understanding of the cyclic plasticity behavior of the material. An observation on the cracking mechanisms was performed. In addition, three critical plane multiaxial fatigue criteria were evaluated based on the experimental results. The capability of the fatigue criteria in predicting the fatigue lives and the cracking directions was assessed.

The current work was aimed at a detailed experimental study on the crack growth behavior of the AL6-XN material. The experiments were conducted using a number of round compact tension (CT) specimens under different loading conditions. The primary goal was to investigate the crack growth behavior with the influences of the R-ratios (ratio of the minimum load to the maximum load in cycle), the underload and overload, and the application of high-low loading sequence on the crack growth. The results of the crack growth experiments conducted on the AL6-XN stainless steel were used to evaluate the applicability of the two-parameter model for constant amplitude crack growth experiments and the Wheeler model for variable amplitude loading. A modification to the Wheeler model was introduced in order to better predict the crack growth behavior under variable amplitude loading.

3.1 *MATERIAL*

The chemical composition of AL6-XN stainless steel is shown in Table 14 [33]. The microstructure of AL6-XN is shown in Fig.34.

Table 14 Chemical composition of AL6-XN stainless steel (%)

C	Cr	Ni	Si	Mn	Mo	N	Cu
0.016	20.34	23.93	0.29	0.40	6.25	0.226	0.25

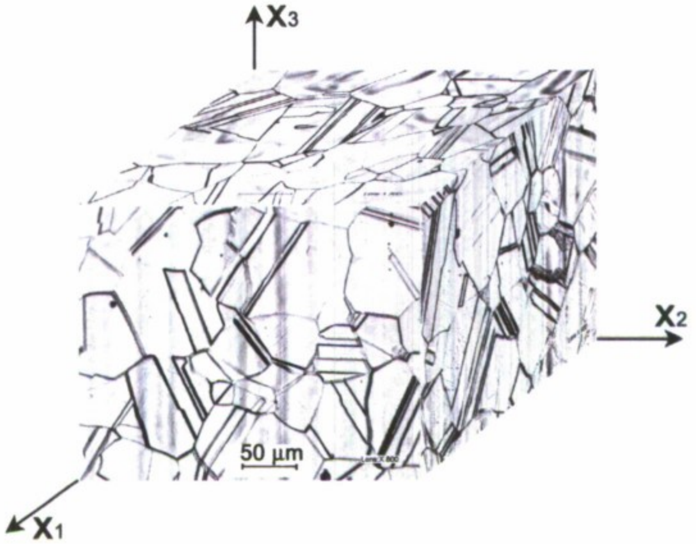

Fig.34 Microstructure of AL6-XN stainless steel – three-dimensional view. Magnification: X800. Etching: V2A, room temperature

The microstructure is observed to be a stable austenite with a substantial amount of twinning. Dark bands that run in the vertical direction can be noticed. They are the compositional bands and are the regions of Cr and Mo enrichment [33]. During dendritic solidification, the microstructural banding occurs, resulting in pools of alloying elements. Under subsequent rolling, those regions become elongated forming the microstructural bands. The properties of compositional microstructural bands were studied in detail by Stauffer et al [34]. It was determined, that the bands have elevated levels of Chromium and Molybdenum and decreased levels of Iron and Nickel. In addition, the microstructural bands have higher hardness that the matrix. The presence of such bands may introduce a certain degree of anisotropy to the macroscopic mechanical properties of AL6-XN material.

Table 15 Mechanical properties of AL6-XN steel

Elasticity Modulus, E	195GPa
Shear Modulus, G	76 GPa
Poisson's Ratio, μ	0.3
Yield Stress, σ_y	380 MPa
True Fracture Stress, σ_f	1133.2 MPa
Endurance Limit, σ_0	300 MPa

The static and cyclic material properties are listed in Table 15. The endurance limit was determined as the stress corresponding to the strain endurance limit from the fatigue strain-life curve as described in Section 3.2.3. The true fracture stress was obtained from the monotonic torsion test. The shear stress-shear strain curve is shown in Fig. 35. The true fracture stress was found to be $\tau_f = 654.25MPa$. This gives an equivalent true fracture stress in tension to be $\sigma_f = 1133.2MPa$.

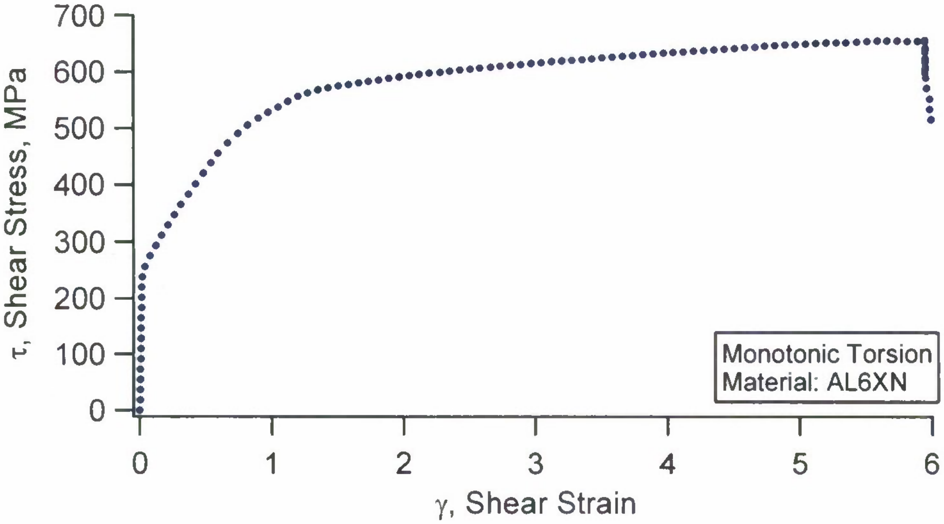

Fig.35 Shear stress-shear strain curve (AL6-XN)

3.2 *CRACK INITIATION EXPERIMENTS*

3.2.1 Experiment

Three types of specimens were used in the experiments. They were: dog-bone shaped specimens for tension-compression tests, solid shaft for pure torsion tests and tubular specimens used in pure torsion and non-proportional loading experiments. The length of the gage section was designed in order to accommodate the axial or biaxial extensometer. The geometry of the specimens is shown in Fig.36. It should be noted that the design of the tubular specimens used for fatigue tests on AL6-XN alloy differs from that used for tests on AISI 304L and 7075-T651 alloys described previously in the report.

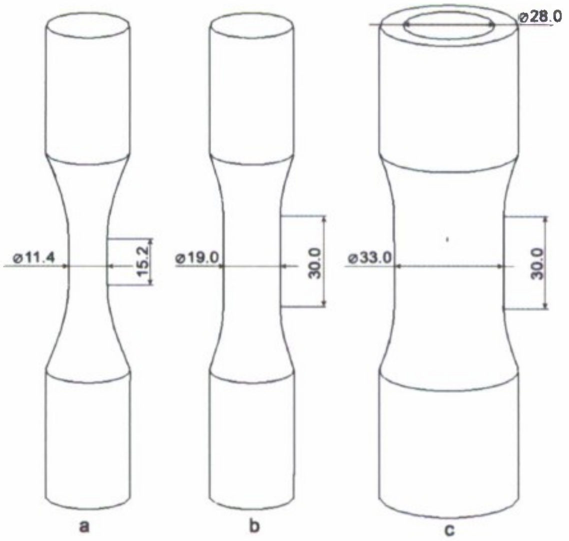

Fig.36 Geometry of the specimens used in fatigue experiments on AL6-XN alloy (all dimensions are in mm). a) tension-compression specimen; b) solid shaft specimen; c) tubular specimen

Strain-controlled constant amplitude tension-compression, pure torsion, and non-proportional 90^0 out-of-phase tests were performed in order to generate Coffin-Manson curve, investigate cyclic plasticity properties and observe cracking behavior of AL6-XN stainless steel. All tests were performed in fully reversed loading, i.e. the mean strains were zero. The details of the tests are represented in Table 16.

Table 16 Strain-controlled fully reversed fatigue tests (AL6-XN)

Testing Type	Spec#	f, Hz	$\Delta\varepsilon/2$, %	$\Delta\sigma/2$, MPa	$\Delta\gamma/2$, %	$\Delta\tau/2$, MPa	N_f, cycles
Tension-Compression	XN07	0.20	1.00	429.5	-	-	3,121
	XN10	0.40	0.60	347.0	-	-	11,287
	XN14	0.50	0.40	325.6	-	-	29,146
	XN08	1.25	0.30	307.4	-	-	64,019
	XN11	2.00	0.24	308.4	-	-	126,000
	XN13	2.50	0.20	305.5	-	-	445,991
	XN12	5.00	0.18	306.9	-	-	1,250,000
Pure Torsion. Solid Shaft Specimens	XN21	0.10	-	-	2.43	366.9	2,480
	XN06	0.25	-	-	1.73	266.7	9,000
	XN03	0.50	-	-	1.04	207.1	32,000
	XN23	0.50	-	-	1.04	207.1	60,000
	XN20	0.50	-	-	1.00	205.2	50,000
	XN22	0.60	-	-	0.95	202.5	74,000
	XN01	1.00	-	-	0.69	192.3	179,501
	XN04	2.00	-	-	0.52	188.6	430,000
Pure Torsion. Tubular Specimens	AL6-XN-T08	0.2	-	-	1.30	230.6	11,600
	AL6-XN-T01	0.2	-	-	1.20	209.1	14,520
	AL6-XN-T09	0.3	-	-	1.04	208.4	17,400
	AL6-XN-T03	0.5	-	-	0.86	199.1	97,702
	AL6-XN-T05	0.7	-	-	0.66	192.6	192,130
	AL6-XN-T02	0.8	-	-	0.52	190.6	450,821
	AL6-XN-T04	2.0	-	-	0.43	185.3	745,000
Non-Proportional 90^0 out-of-phase	AL6-XN-T12	0.1	0.50	643.0	0.86	398.4	1,440
	AL6-XN-T15	0.2	0.40	508.3	0.69	321.1	3,480
	AL6-XN-T13	0.4	0.32	418.4	0.55	262.8	8,220
	AL6-XN-T11	0.5	0.26	359.4	0.45	226.3	21,300
	AL6-XN-T14	1.0	0.20	310.8	0.35	198.9	47,500
	AL6-XN-T06	2.0	0.17	288.9	0.29	181.1	346,931

f – frequency of applied loading; $\Delta\varepsilon/2$ – amplitude of applied axial strain;
$\Delta\gamma/2$ – amplitude of applied shear strain; $\Delta\sigma/2$ – axial stress amplitude;
$\Delta\tau/2$ – shear stress amplitude; N_f – number of cycles to failure.

3.2.2 Cyclic plasticity behavior

The cyclic hardening curves for the constant amplitude strain controlled tests are shown in Fig.37. From the Fig.37(a)(b) it can be seen that when tested under pure torsion and axial tension-compression conditions the material exhibits gradual softening until failure of the specimen. The rate of the cyclic softening clearly depends on the magnitude of the applied strain. With the low strain amplitudes, the softening rate diminishes and the stress amplitude becomes stable. Under high strain amplitudes the stress amplitude decreases continuously until failure.

Such softening behavior distinguishes AL6-XN from 300 series of stainless steel. In case of metastable steels (for instance 304 or 316) the softening is followed by cyclic hardening which is attributed to the formation of martensite from austenite by plastic deformation [33]. Since austenite is highly stable in AL6-XN steel due to the high content of Nickel and Nitrogen, no such plasticity induced martensitic transformation occurs and the material softens under cyclic loading. In addition, it should be noted that the levels of stresses are generally higher for the torsion specimens than those for the specimens tested under tension-compression.

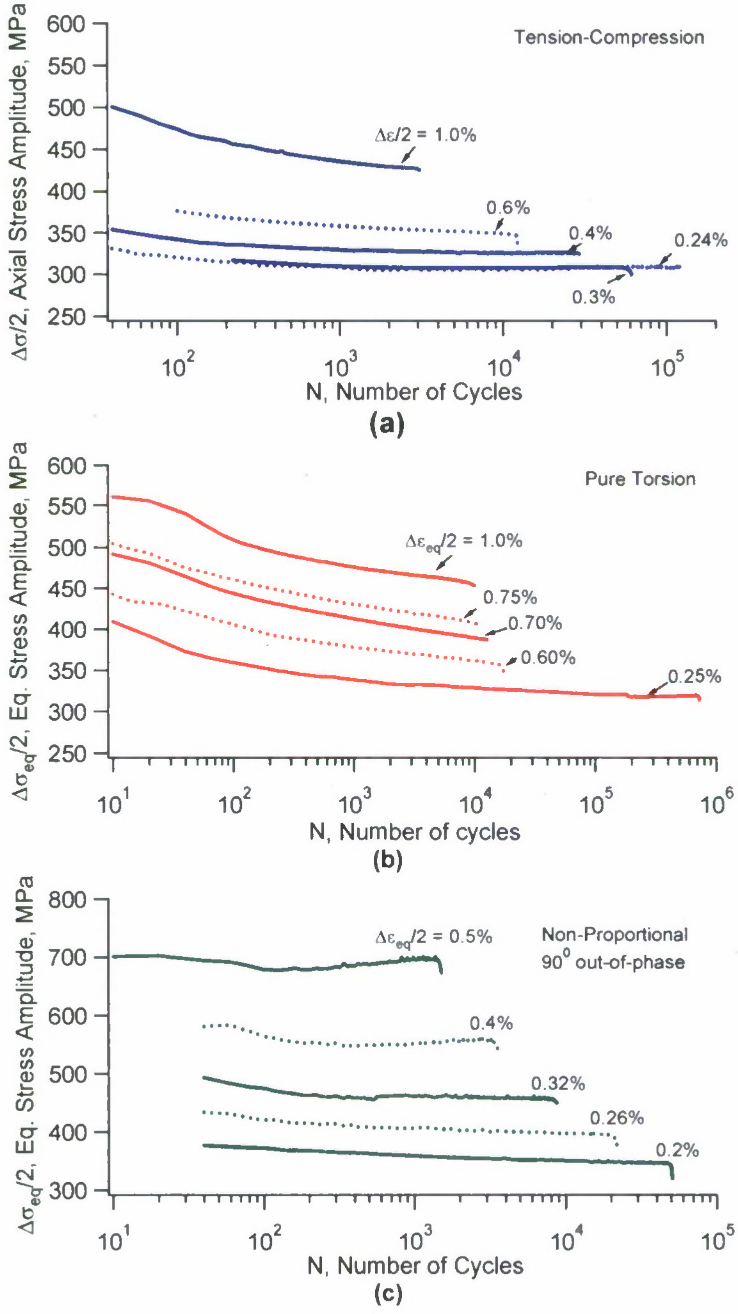

Fig.37 Cyclic hardening behavior of AL-6XN steel. a) tension-compression; b) pure torsion; c) non-proportional 90^0 out-of-phase

Because the AL6-XN alloy exhibits cyclic softening, there is no stabilization of the stress-strain response. Therefore, it is difficult to define stabilized stress amplitude in an unambiguous way. In fact, under high strain amplitude, the stress response of the material never becomes stable. As a rule, the value of the stress amplitude in Table 16 was recorded at 80% of fatigue life of the specimen. This rule was impelled by the fact that the stress amplitudes corresponding to 80% of fatigue life, when placed on the cyclic stress-strain curve, follow the cyclic stress-strain curve produced by the incremental step experiments.

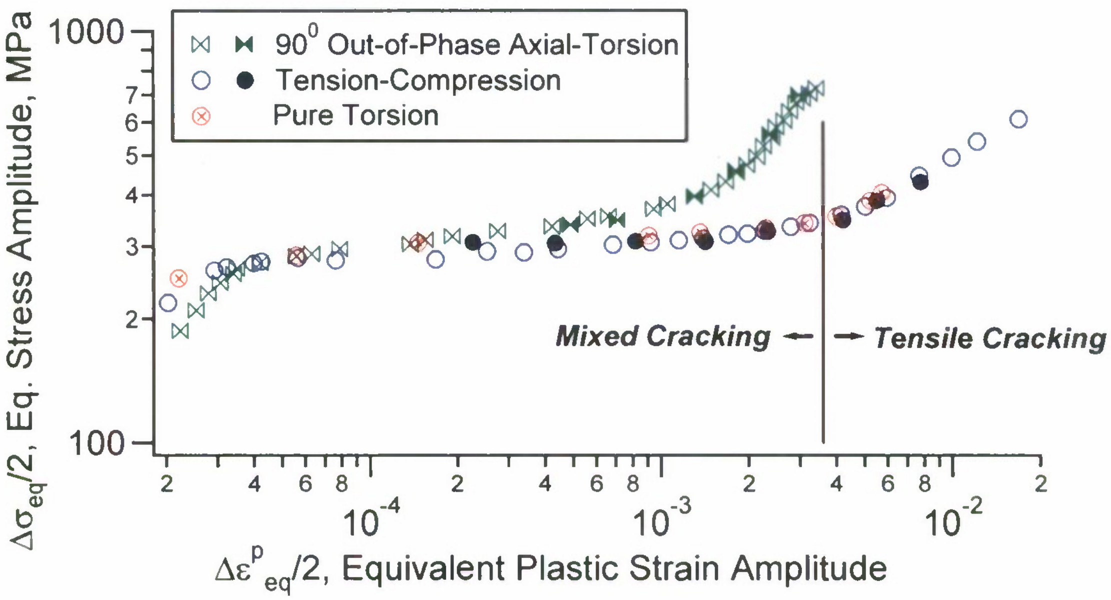

Fig.38 Cyclic Stress-Strain Curves of AL6-XN stainless steel

Two specimens were tested with incremental step loading in order to generate cyclic stress-strain curves (CSSCs) for this material. These incremental step tests were performed under uniaxial tension-compression and non-proportional 90^0 out-of-phase loading conditions. Figure 38 shows the results of incremental step tests together with the results based on stress-strain response from individual specimens tested in fatigue experiments (filled markers). For the purpose of brevity, the change in cracking behavior that will be discussed in a later section is also shown in Fig.38. A quasi-plateau can be observed in the cyclic stress-strain curve obtained from the tension-compression experiments shown in Fig.38 starting at the level of an equivalent stress magnitude approximately equal to 260MPa. This stress corresponds to the endurance limit, as observed from the *S-N* curve in tension-compression. When the equivalent plastic strain magnitude is higher than 2×10^{-4}, the cyclic stress-strain curve for non-proportional axial-torsion loading lies above the corresponding curve in tension-compression which indicates the presence of non-proportional hardening. Non-proportional hardening, the additional hardening due to the non-proportional loading, becomes more significant as the plastic strain magnitude increases.

Figure 39 shows the selected hysteresis loops taken at 80% of fatigue life and represented in strain range – stress range coordinates. The loops were taken from the axial tension-compression experiments. By arranging the plots in range coordinates with the lower tips of the loops positioned at the origin an illustration of non-Masing behavior for the AL6-XN alloy can be provided. If material displays Masing behavior, the upper branches of the loops fall on one curve. It can be seen from Fig.39 that material under consideration shows non-Masing behavior.

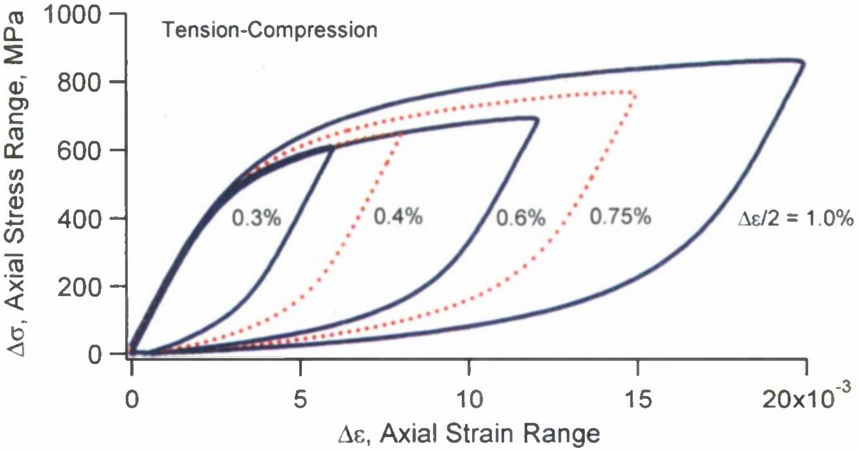

Fig.39 Selected stress-strain hysteresis loops taken at 80% of fatigue life

3.2.3 Strain-life curve

The fatigue results of the tests described in Table 16 are shown in Fig.40 and are represented in strain-life form (Coffin-Manson curves) with the vertical axis representing the equivalent strain amplitude and horizontal axis representing the number of cycles until the failure of the specimen.

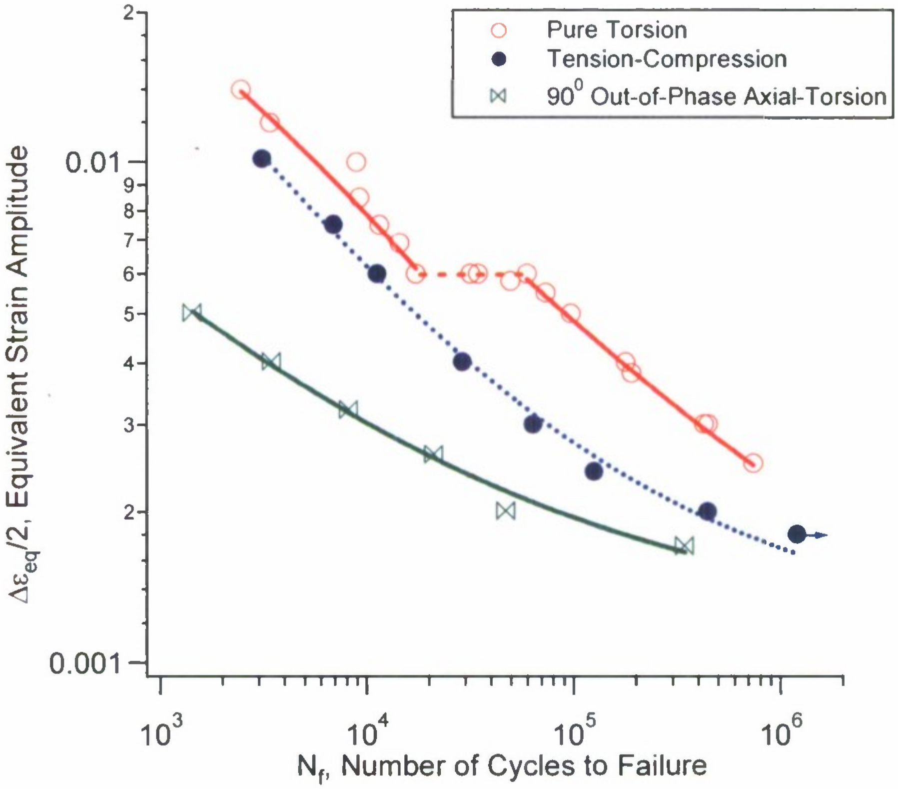

Fig.40 Strain-life curves: AL6-XN alloy

With the same equivalent strain amplitude, results shown in Fig.40 indicate that the fatigue lives for torsion are higher than the fatigue lives under tension-compression. The fatigue lives of the specimens subjected to 90^0 out-of-phase axial-torsion loading are the shortest among the three loading paths for the same equivalent strain amplitudes. The difference is more significant for larger strain amplitudes. The three fatigue curves come closer in the high cycle fatigue regime. The strain-life curves under tension-compression and 90^0 out-of-phase axial-torsion loading appear smooth as can be expected for most engineering materials. However, the strain-life curve under pure torsion displays a noticeable phenomenon. In the region associated with higher strain amplitudes (from 0.6% to 1.4%) the fatigue life curve for pure torsion comes close to the curve for tension-compression. The second region (0.25% to 0.6% of equivalent strain amplitude) is characterized by longer fatigue lives. Between those regions, the transition part can be seen, in which the fatigue life varies greatly even with the same applied strain amplitude.

The endurance limit for the AL6-XN steel is found from the tension-compression fatigue data. The corresponding Coffin-Manson curve is fitted using Eq. (1) as shown in Fig.41. The endurance limit from the fit is $\varepsilon_0 = 0.00132$. The stress amplitude, corresponding to this strain amplitude can be found from the cyclic stress-strain curve for this material, which is obtained as a result of incremental step test.

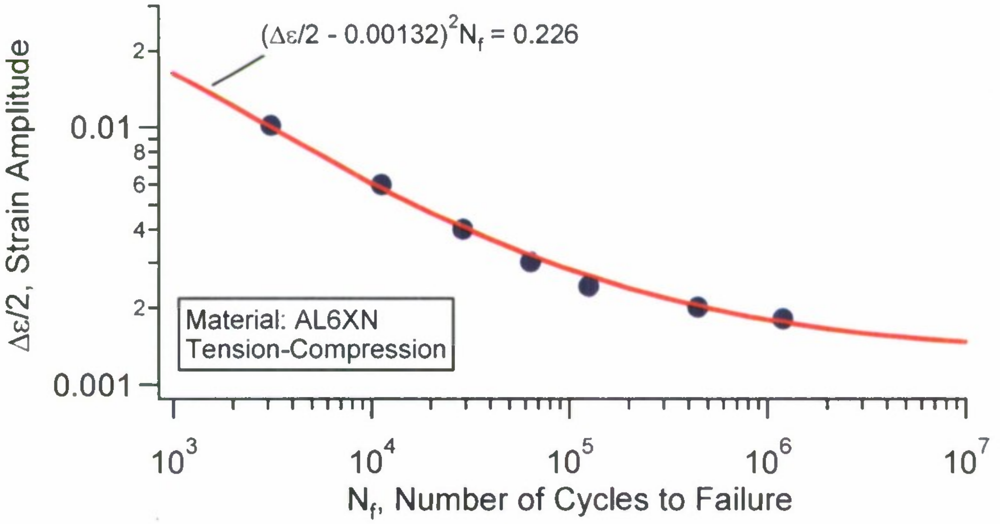

Fig.41 Tension-compression strain-life curve for AL6-XN

3.2.4 Cracking observations

Each region of the strain-life curve in pure torsion described in section 3.2.3 is associated with specific orientation of the fatigue cracks. The orientation of the crack is defined by the angle formed by the normal to the cracking plane and the vertical axis of the specimen, as shown in the insert in Fig.42. The schematics of the cracking behavior in pure torsion is shown in Fig. 42 and in order to facilitate discussion, the shear strain amplitude is plotted against the fatigue life. The observed cracking behavior in pure torsion is shown next to the corresponding data points in Fig.42 together with the three selective photographs of the cracks corresponding to the different regions in the strain-life curve.

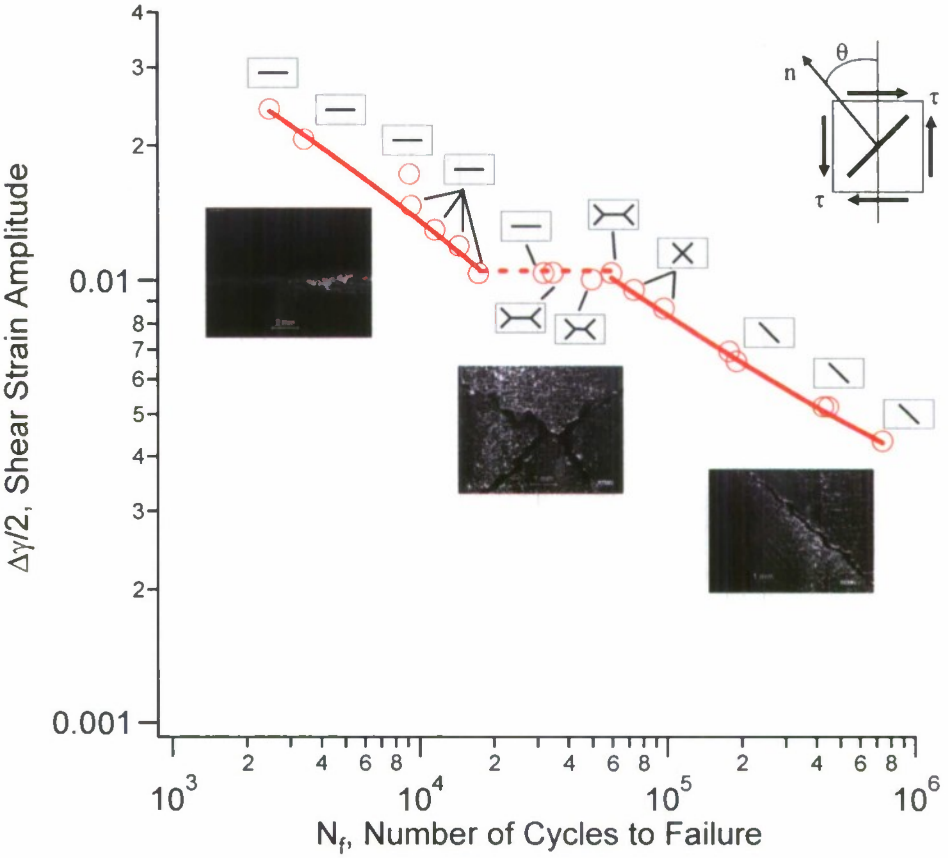

Fig.42 Orientation of fatigue cracks

From Fig.42, it can be seen, that at lower strain amplitudes the specimen fails with single crack oriented at 45^0 with respect to the axis of the specimen. With increasing applied strain, the single 45^0 crack transforms into "X-shaped" crack. The horizontal central portion of the X-shaped crack then becomes more pronounced until the 45^0 branches disappear and the crack becomes truly horizontal. It can be seen that the small change in shear strain amplitude from 0.85% to 1.04% results in a dramatic change in the cracking behavior of this material under pure torsion. The typical cracks associated with different regions of the strain-life curve are shown in the photographs below (Fig.43).

The point of change in cracking behavior can also be identified on a cyclic stress-strain curve as shown in Fig.38. It can be established, based on the experiments, that when the equivalent plastic strain amplitude is less than 3.7×10^{-3} or the equivalent stress amplitude is less than 360 MPa, the material displays tensile cracking. Above these values, the material under investigation exhibits mixed cracking. The transition between the two cracking modes occurs approximately at the end of the quasi-plateau regime on the CSSC. This demarcation line will be used to determine a material constant in a multiaxial fatigue criterion that will be discussed in later section.

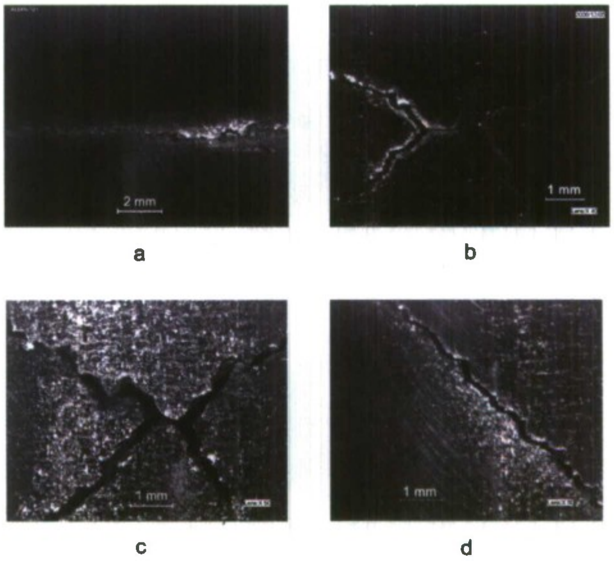

a b c d

Fig.43 Cracking orientation under different equivalent strain amplitudes. (a) $\Delta\varepsilon/2 = 0.6\%$; (b) $\Delta\varepsilon/2 = 0.58\%$; (c) $\Delta\varepsilon/2 = 0.50\%$, (d) $\Delta\varepsilon/2 = 0.30\%$

In the case of tension-compression loading the cracks are oriented at 0^0 with respect to the loading axis. One specimen was chosen to investigate the mechanism of crack propagation. The portion of the specimen containing the crack was sectioned, polished and etched in order to reveal the grain structure and to study the details of crack propagating through the thickness of the specimen. The details of the cracking are shown in the Fig.44. The figure depicts the cross-section of the tension-compression specimen (tested under $\Delta\varepsilon/2 = 0.2\%$ strain amplitude) containing the crack. The total length of the crack was measured to be 1.4 mm. The crack starts at the surface of the specimen and propagates through the grains – i.e. the crack growth is intragranular.

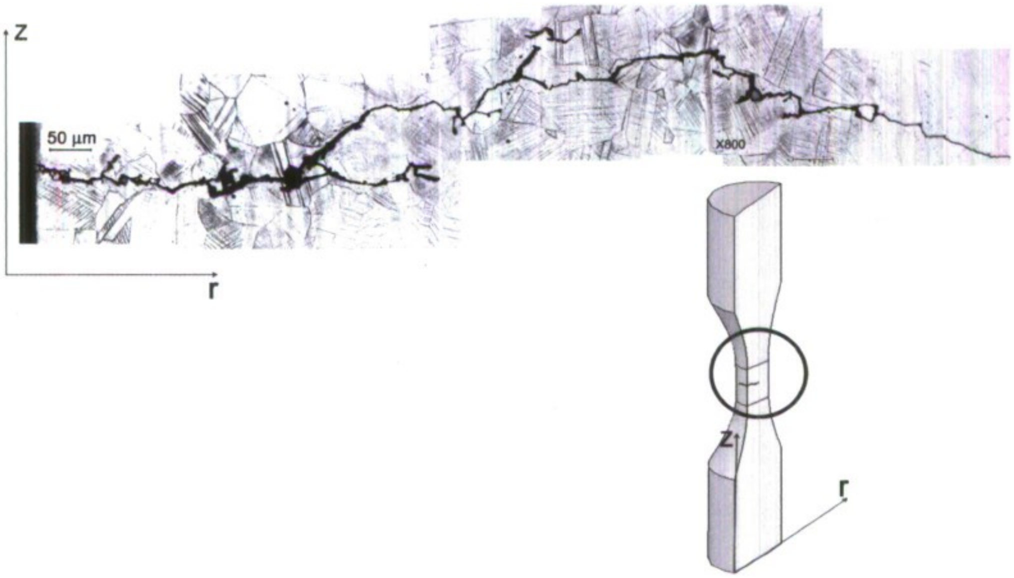

Fig.44 Crack propagation through the thickness of the specimen

3.3 *CRACK GROWTH EXPERIMENTS*

An experimental investigation of fatigue crack growth in AL6-XN stainless steel was conducted using standard compact tension (CT) specimens. The series of experiments were designed and performed in order to investigate in details the major features of crack growth behavior: effect of R-ratio (the ratio of the minimum load to the maximum applied load in a cycle) together with the influence of the size of the notch root, effect of tensile and compressive overloads and behavior under two step high – low amplitude loading conditions.

Round compact tension specimens were machined from as-received AL6-XN round bar with a diameter of 44.44 mm in the transversal direction. The design of the specimens is shown in Fig.45. The thickness of the specimens was 3.8 mm. The notches were cut using the EDM (electro-discharge machine) process in order to eliminate cold work associated with traditional saw cutting. One side of the specimens was polished in order to facilitate the observation of crack growth. No heat treatment was done to the specimens prior to testing. The crack growth experiments were conducted using an Instron 8870 material testing machine with a 25 kN capacity load cell. The testing facility was equipped with computer control. All the experiments were performed in ambient air. Crack propagation was observed and measured by means of an optical microscope with a magnification of X40. Four types of experiments were performed: constant amplitude loading, single overload, single underload and high-low sequence loading. The results of the crack growth tests are represented in a standard way as a crack growth rate (da/dN) versus the stress intensity factor range (ΔK) for a given loading condition. The values of ΔK were obtained through a finite element analysis as described previously in the report.

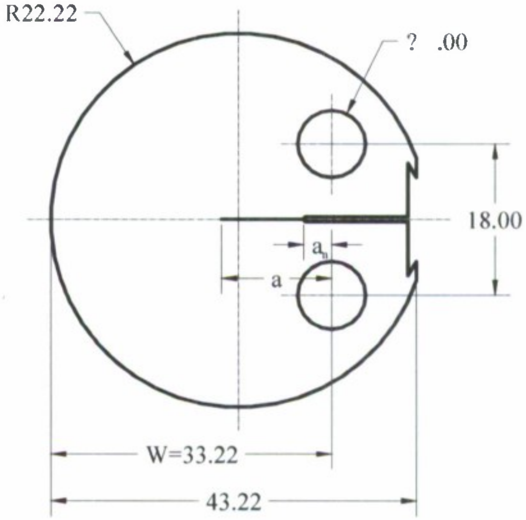

Fig.45 Compact tension specimen for the AL6-XN alloy

3.3.1 Constant amplitude experiments

The details of the experiments conducted under constant-amplitude loading with the R-ratios ranging from -1 to 0.85 are listed in Table 17. In order to facilitate the crack growth experiment with $R = 0.85$, pre-cracking was used for Specimen C28 and the crack length (as measured from the line of the load application) at the end of pre-cracking step is reported as the notch depth in

Table 17. The final crack length for this specimen is reported as that measured from the crack length at the end of pre-cracking. The pre-cracking for Specimen C28 was performed under the loading conditions: $R = 0;\ \Delta P/2 = 2.5kN$.

Table 17 Constant amplitude loading for the AL6-XN alloy

Spec#	R-ratio	$\Delta P/2$ (kN)	f (Hz)	Notch diameter (mm)	Notch depth /precrack a_n (mm)	Number of cycles when a=0.5 mm (cycle)	N_f (cycle)	a_f (mm)
C01	0.1	2.475	1~15	0.423	0.844	66,475	394,630	16.691
C02	0.1	2.250	1~10	0.402	0.304	90,118	563,892	19.703
C04	0.1	2.025	1~15	0.410	0.211	274,762	1,299,728	18.665
C20	0.1	2.250	2~10	1.124	0.579	175,425	709,582	10.003
C08	0.5	1.750	2~10	0.280	0.079	113,093	612,670	16.242
C19	0.5	1.500	1~10	0.237	0.026	180,503	996,150	14.018
C10	0.75	1.000	2~20	0.274	0.154	808,973	2,784,847	15.324
C21	0.75	1.125	5~15	0.215	0.071	338,089	1,399,690	9.306
C23	-1	4.000	0.5~3	0.235	0.033	2,479	269,391	16.746
C28	0.85	0.680	10~20	0.115	5.244	135,880	1,211,963	7.643

R-ratio = minimum load over the maximum load in a loading cycle

$\Delta P/2$ = loading amplitude f = loading frequency

a_n = distance between the notch root and the line of action of the externally applied load

N_f = total cycles a_f =final crack length

Generally, a compact specimen is not recommended for tension-compression loading (R <0). In the current investigation, the two loading holes in the compact specimen were machined to have a tight tolerance so that the gap between the pin in the loading fixture and the hole in the specimen was minimal. For the range of the testing frequencies used in the experiments, the maximum and minimum loads dictate the fatigue behavior. The experiments indicated that the maximum and minimum loads can be controlled accurately with the compact specimen for the R <0 loading cases.

The crack growth rate was calculated from the experimentally obtained measurements of a crack length as a function of number of loading cycles. The growth rate is then is derived using a parabolic curve fitting based on seven data points and taking the derivative in the middle point. Figure 46 shows the results of the crack growth under constant amplitude loading with different *R*-ratios and loading amplitudes. The vertical axis represents the crack growth rate and the horizontal axis represents the stress intensity factor range. No pre-cracking was used and each experiment started with constant loading amplitude and proceeded until the crack length reached a certain value (as illustrated in Table 17). It can be seen that the material displays significant *R*-ratio effect with the data curves corresponding to different *R*-ratios being approximately parallel to each other. In addition it can be observed that the short crack regime for the specimen tested with $R = -1$ extends for considerably large range of crack length.

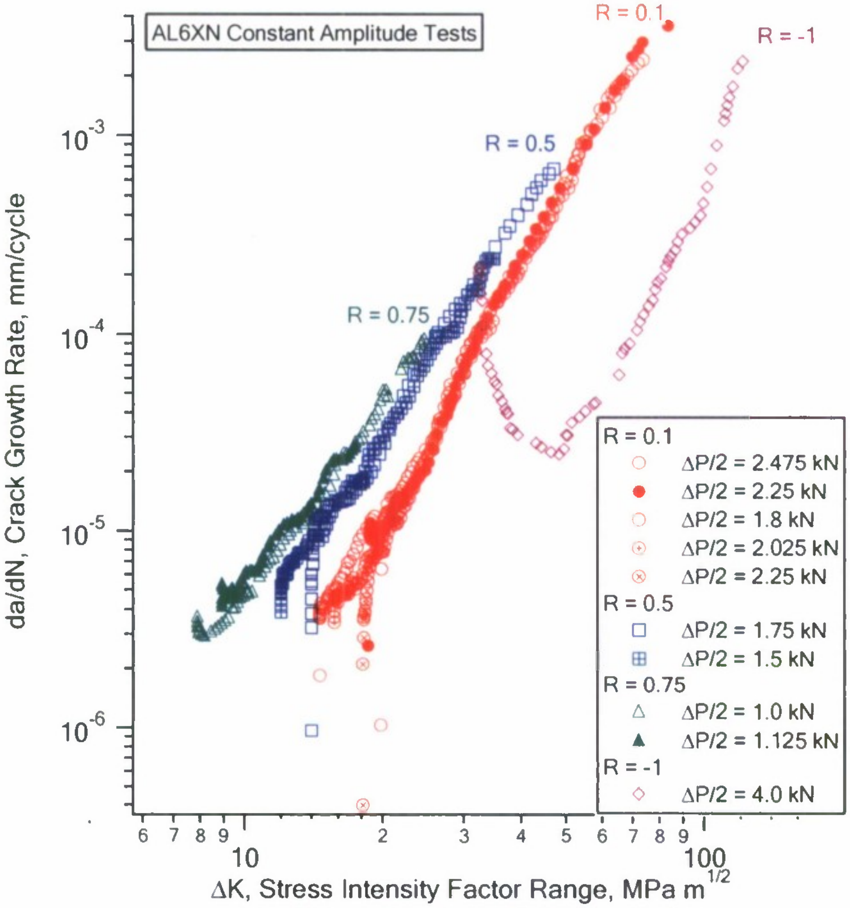

Fig.46 Crack growth results under constant amplitude loading

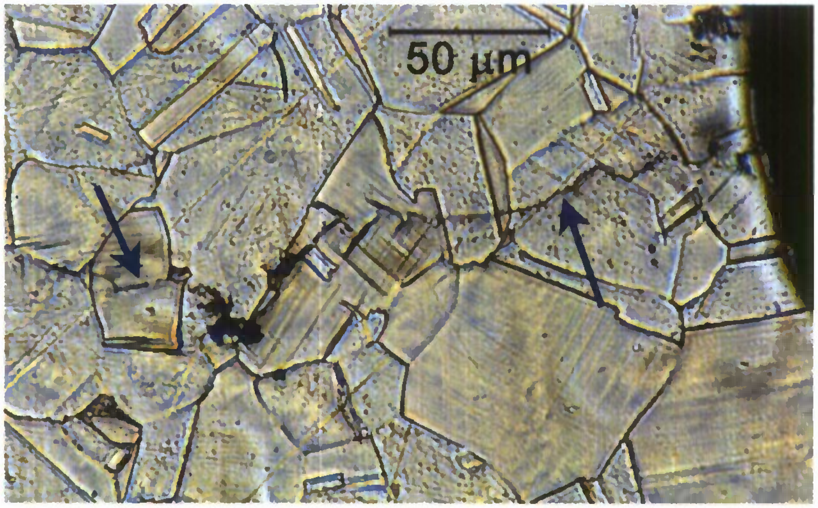

Fig.47 Microstructural observation of fatigue crack growth in AL6-XN steel

In order to investigate the microstructural mechanism of crack propagation, the area close to the notch root of one of the specimens was etched and the specimen was tested under conditions R = 0.1, $\Delta P/2$ = 1.8 kN. The crack starting from the notch was then observed under a microscope. Figure 47 shows photograph of the fatigue crack propagating through the austenite matrix. The crack path is indicated by the arrows in the figure.

As a result of excessive plastic deformation, a considerable amount of developed persistent slip bands (PSB) can be observed on the photograph in Fig. 47. The photograph reveals that the crack develops through the grains, i.e. the crack propagation mechanism is intragranular. High resistance to the intergranular cracking can be expected in this material, taking into account absence of carbide formation at the grain boundaries in AL6-XN steel.

3.3.2 Single overload experiments

Five specimens were tested under constant amplitude load with single overload (high magnitude tensile load applied over one cycle) and underload (compressive load applied over one cycle). The detailed loading conditions of these experiments are summarized in Table 18.

Table 18 Constant amplitude loading with a single overload (underload)

Spec#	R-ratio	$\Delta P/2$ (kN)	f (Hz)	Notch diameter (mm)	Notch depth a_n (mm)	P_{OL} (kN)	N_{OL} (cycle)	a_{OL} (mm)	N_f (cycle)	a_f (mm)
C14	0.1	2.25	1~15	0.257	-0.056	8.0	560,479	7.54	746,196	16.501
C17	0.1	1.80	1~15	0.254	-0.069	8.0	1,394,380	10.185	1,727,727	16.690
C24	0.1	2.25	1~15	0.232	-0.310	8.0	543,255	6.868	723,829	15.692
C18	0.1	2.25	1~15	0.205	0.086	-9.0	765,414	7.37	803,731	13.926
C25	0.1	1.80	3~15	0.220	-0.181	-9.5	1,575,890	10.106	1,608,048	14.294

P_{OL} = magnitude of the overload or underload N_{OL} = number of cycles before overload

a_{OL} = crack length at overload, as measured from the notch root

The results of overload tests are represented in Fig.48. The dashed line in each plot shows the stable crack growth under a constant amplitude loading and is described by the Paris law. It can be seen, that application of overload after the period of constant amplitude loading greatly influences subsequent crack growth behavior. Significant retardation of the crack growth after overload can be observed. The magnitude of such retardation is approximately the same in all three cases depicted in Fig.48. As the crack extends beyond the plastic zone introduced by overload, the crack growth rate gradually reaches the stable regime.

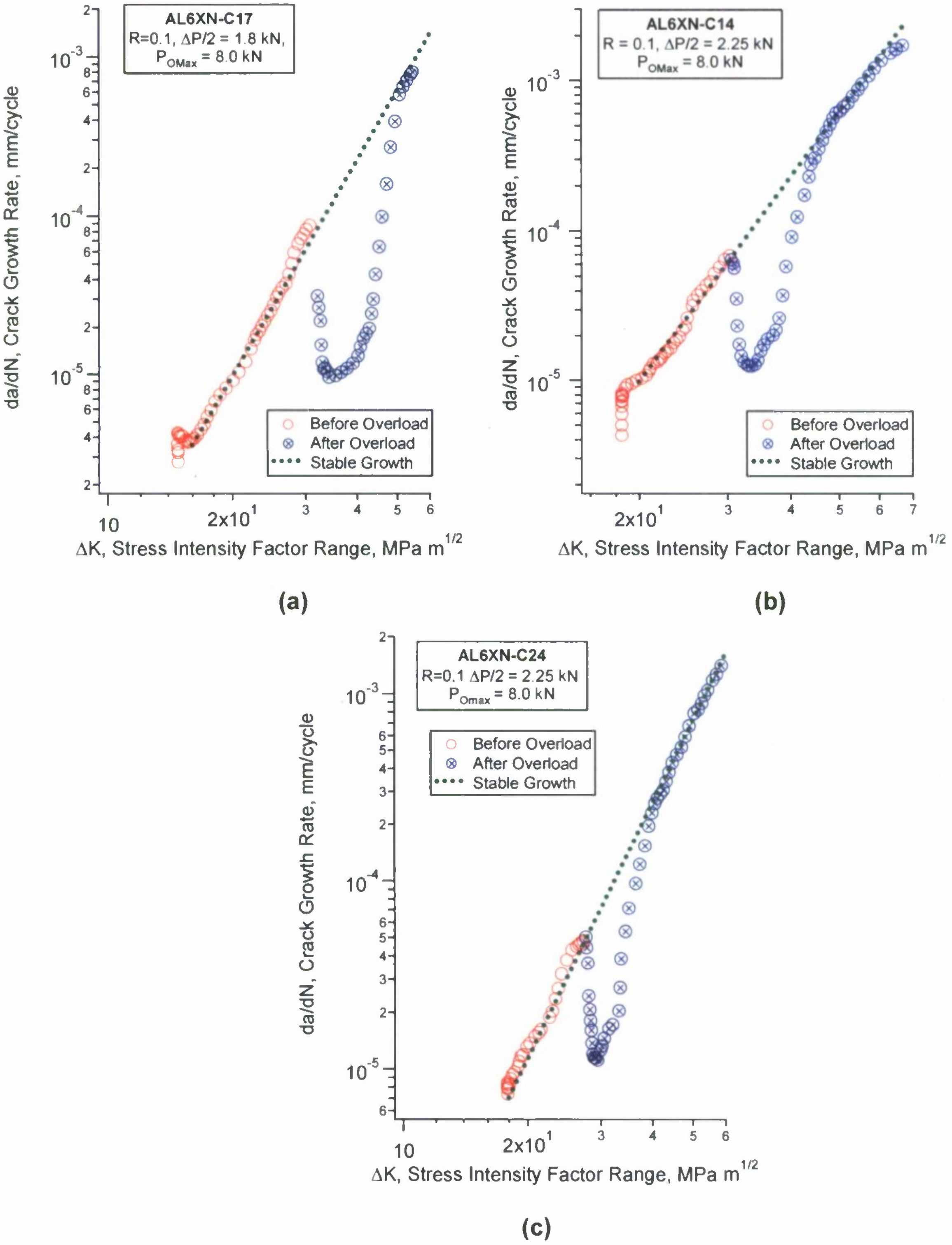

(a)

(b)

(c)

Fig.48 Effect of single overload on crack growth

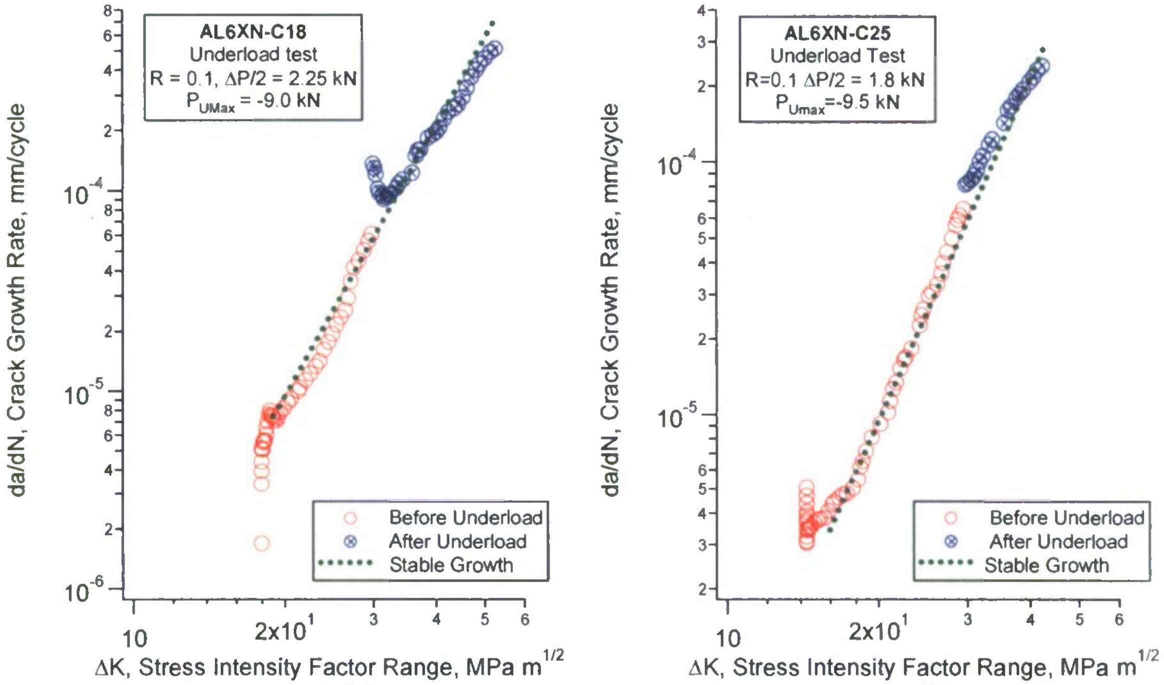

(a) (b)

Fig.49 Effect of compressive overload on crack growth

Figure 49 shows the results of tests performed with single underload (compressive overload). No retardation of the crack growth can be seen in this case and, in fact, the crack growth accelerated immediately after application of the compressive load. This acceleration is pronounced in the case of higher loading amplitude (Fig.49(a)) and is vanishingly small in the case of lower loading amplitude (Fig.49(b)). The effect of underload has a very short life and the crack growth returns to the stable regime rather quickly. Thus, it is possible to make a conclusion, that application of compressive overload does not influence significantly the crack growth.

3.3.3 High-Low loading sequence

Details of the high-low sequence loading experiments are represented in Table 19.

Table 19 High-low loading sequence

Spec#	R_1- ratio	R_2- ratio	$\Delta P_1/2$ (kN)	$\Delta P_2/2$ (kN)	f (Hz)	Notch diameter (mm)	Notch depth a_n (mm)	N_H (cycle)	a_H (mm)	N_f (cycle)	a_f (mm)
C15	0.1	0.4	2.70	1.80	2~10	0.218	-0.067	298,270	5.884	387,756	13.941
C16	0.1	0.143	2.70	1.80	1~15	0.176	-0.006	261,142	5.388	538,831	12.787
C26	0.1	0.1	2.70	1.80	1~15	0.225	-0.034	199,607	4.982	743,163	14,953

$R_1 =$ R-ratio of the first step $R_2 =$ R-ratio of the lower loading amplitude step

$\Delta P_1/2 =$ higher loading amplitude $\Delta P_2/2 =$ lower loading amplitude

N_H = number of cycles in the higher amplitude step

a_H = crack length at the termination of the high amplitude test, as measured from the notch root

Figure 50 shows a schematic illustration of the loading condition for the two-step high-low loading sequence experiment. The experiments were designed in the way, similar to that described above for AISI 304L steel. One of the tests was conducted with the maximum load being the same in both high and low steps (Fig.50(a)) and the second test was done with the same minimum load in both steps (Fig.50(b)). Finally, the third specimen was tested under condition that the *R*-ratio was kept constant throughout the experiment (Fig.50(c)). The results are shown in Fig. 51.

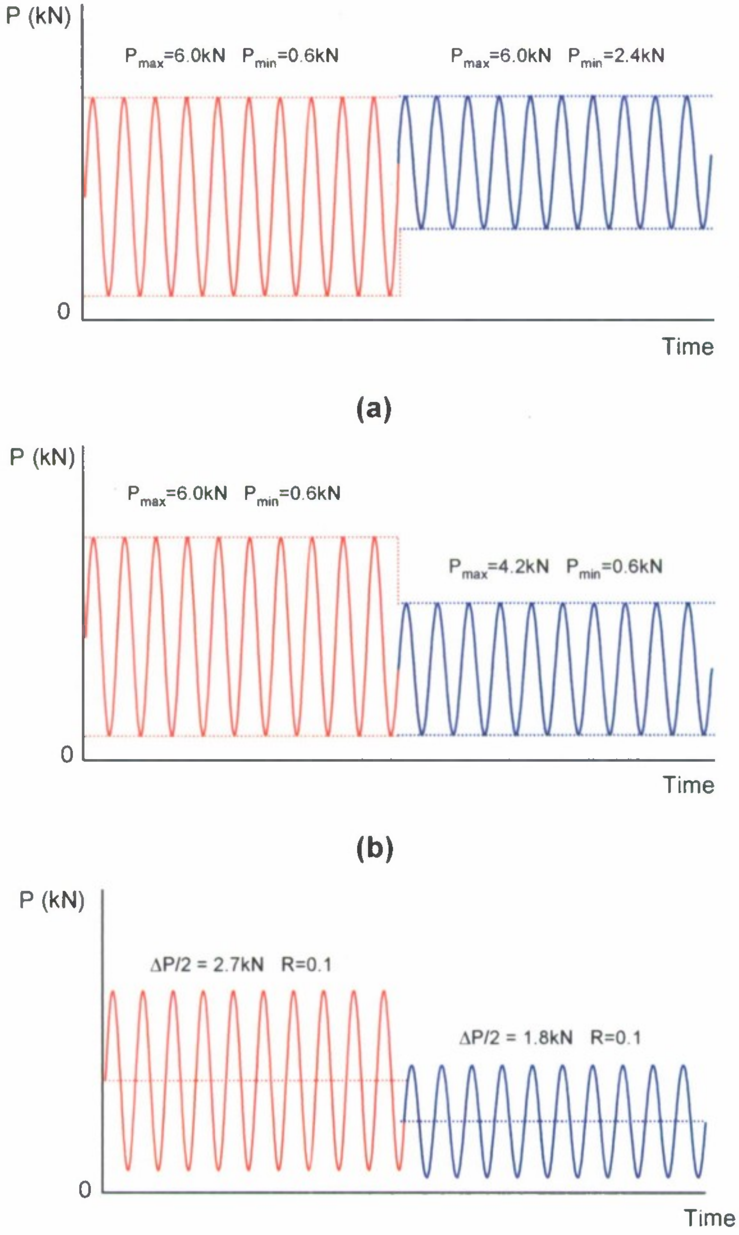

(a)

(b)

(c)

Fig.50 Schematic illustration of high-low experiments

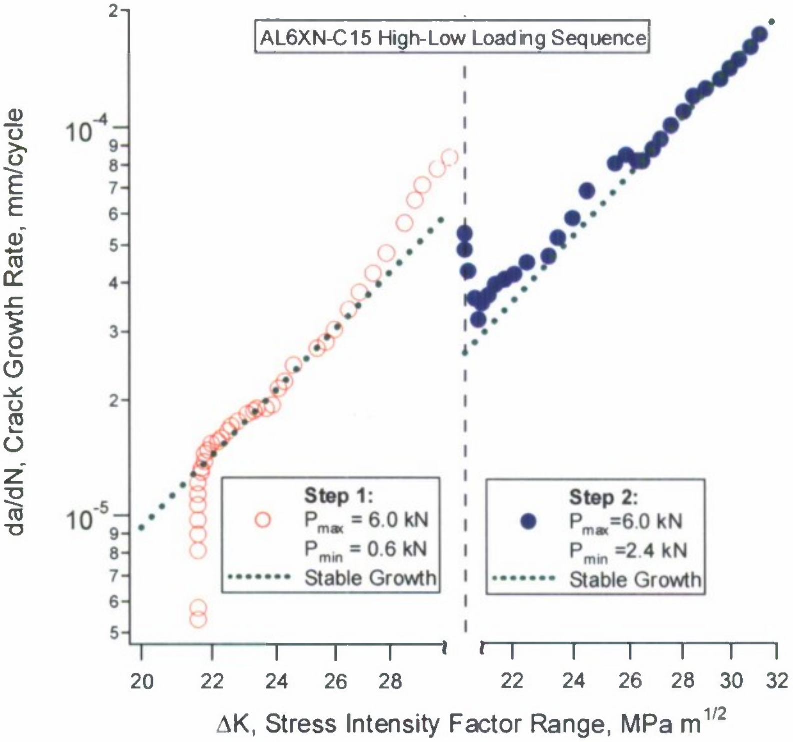
AL6XN-C15 High-Low Loading Sequence
da/dN, Crack Growth Rate, mm/cycle
2
10^{-4}
9
8
7
6
5
4
3
2
10^{-5}
9
8
7
6
5
Step 1:
P_{max} = 6.0 kN
P_{min} = 0.6 kN
Stable Growth
Step 2:
P_{max}=6.0 kN
P_{min} =2.4 kN
Stable Growth
20
22
24
26
28
22
24
26
28
30
32
ΔK, Stress Intensity Factor Range, MPa $m^{1/2}$

(a)

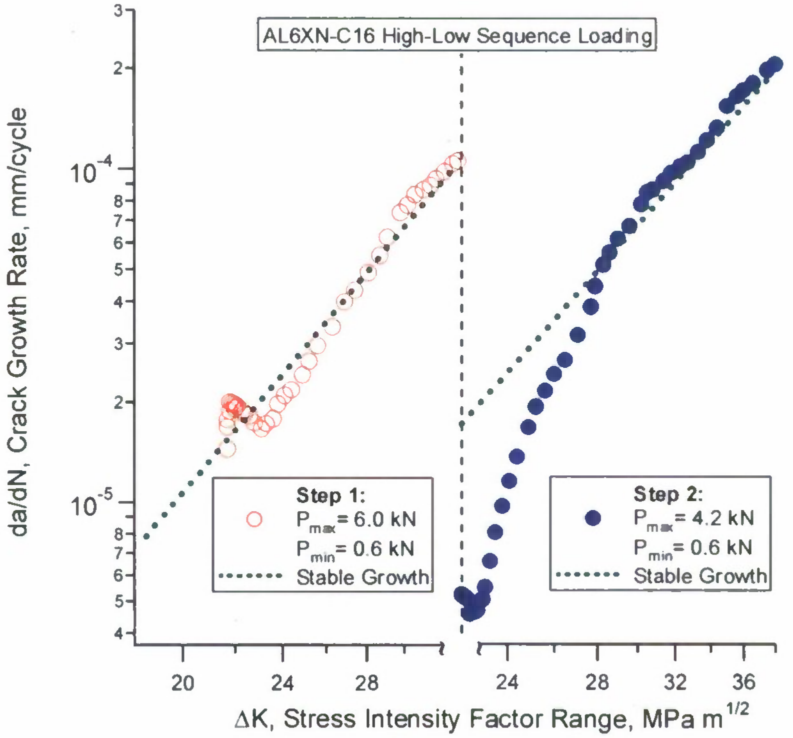
AL6XN-C16 High-Low Sequence Loading
da/dN, Crack Growth Rate, mm/cycle
3
2
10^{-4}
8
7
6
5
4
3
2
10^{-5}
8
7
6
5
4
Step 1:
P_{max}= 6.0 kN
P_{min}= 0.6 kN
Stable Growth
Step 2:
P_{max}= 4.2 kN
P_{min}= 0.6 kN
Stable Growth
20
24
28
24
28
32
36
ΔK, Stress Intensity Factor Range, MPa $m^{1/2}$

(b)

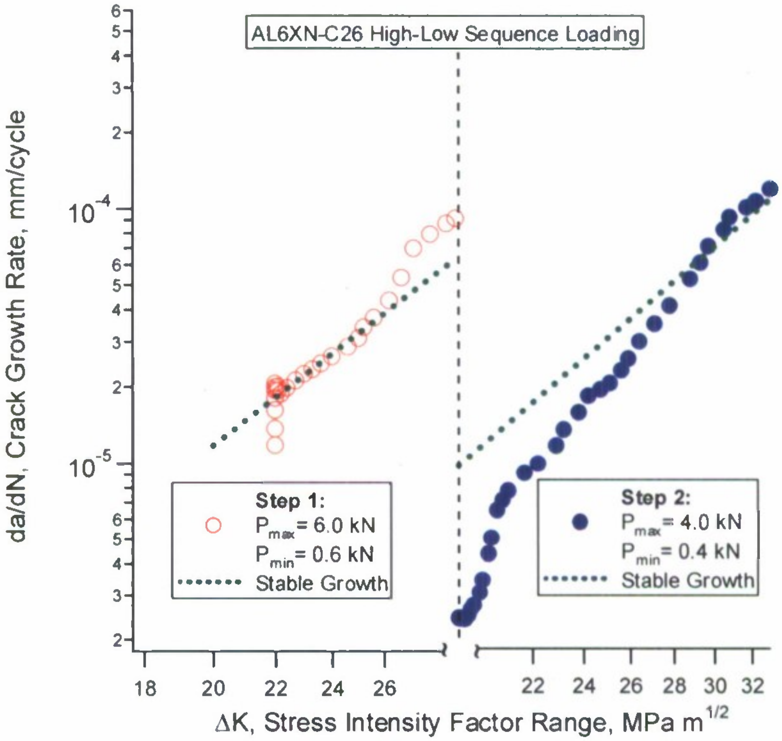

(c)

Fig.51 High-Low loading sequence experiments

The horizontal axis in the plots in Fig. 51 represents the stress intensity factor range and is broken into two parts corresponding to the high amplitude and low amplitude parts of the test. The values of ΔK are not continuous at the transition from one loading step to another. In each of the plots the dotted line corresponds to the stable crack growth under constant amplitude loading. It can be seen that the transition to the low amplitude test (Fig.51(a)) when the maximum amplitude is constant in both steps has no effect on crack growth rate. At the same time a crack growth retardation in the low amplitude step can be observed when the specimen is tested with either same minimum load (Fig.51(b)) or the same *R*-ratio (Fig.51(c)). In the latter cases the effect of application of high-low loading sequence can be compared to the effect produced by single overload tests.

4. AISI 4340VM AEROSPACE STEEL

4340 alloy steel is a ferritic alloy and has been widely used in aeronautic applications, landing gears, reductors, etc. It comes in two varieties – as air melted and as vacuum arc melted (VM). The process of vacuum melting produces a material with lower percent of inclusions and gas phases, which in general would increase fatigue resistance of the alloy.

The Aerospace high strength steel 4340 is not new to the industry and the mechanical and fatigue properties of this alloy have been studied over the years [40-43]. Much of the effort was targeted towards investigation of fatigue behavior in different environments (environmentally influenced fatigue) [44-46]. Extensive study of fatigue crack growth in 4340 steel was done by

Liaw et al. [40]. The crack growth behavior was studied under different *R*-ratios in different gaseous environments. It was shown, that the effect of *R*-ratio is more pronounced in laboratory air environment than in dry hydrogen and dry helium environments. In addition, an interesting phenomenon was observed that the crack growth rate behavior, namely the effect of R-ratio, is very similar in wet hydrogen and in dry environments.

It is known that the heat treatment can change the fatigue properties of the material. The effect of type and fraction of secondary phase on the fatigue crack growth behavior of 4340 steel was experimentally studied by Hwang et al. [47]. The second phase in the alloy produced by different types of heat treatment can be bainite or tempered martensite. It was shown, that due to the ductility of martensitic second phase, the specimens treated by interrupt quenching, which produces tempered martensite, displayed higher resistance to the fatigue crack growth.

The fatigue crack growth response of 4340 steel under variable amplitude has also been studied [48-50]. Investigation of fatigue crack growth behavior in 4340 alloy subjected to Mode I and Mode II overloads was done by Nayed-Hashemi [50]. It was shown that while Mode I overload retards the crack propagation, the overloading in Mode II produces an opposite effect promoting the crack growth acceleration after overloading.

Due to the high cost of production by vacuum arc melting, air-melted variety of 4340 steel is used in most of application and the research of mechanical properties has been done on conventionally air-melted material. While the static material properties do not change significantly depending on the production method, the fatigue properties under cyclic loading for vacuum-melted 4340 steel can be different than those of conventionally produced material.

The current section of the report describes the results of experimental work done on fatigue behavior of 4340 VM aerospace steel. Fatigue crack initiation experiments were conducted on smooth dog-bone shaped specimens. The primary goal was investigation of transient behavior under cyclic loading, behavior of *S-N* curve, and orientation of fatal cracks. Crack growth experiments were done using round compact tension specimens and the goal of experimental work was to investigate R-ratio effect on crack growth under constant amplitude loading as well as effects of overloads and sequence loading.

4.1 CRACK INITIATION EXPERIMENTS

The smooth specimens for crack initiation experiments were machined from as-received commercially available 4340 VM Aerospace steel supplied as a round bar with diameter of 25.4 mm. The chemical composition of 4340 steel is shown in Table 20. The fatigue crack initiation experiments included tests under fully reversed strain-controlled tension-compression and fully reversed torsion. Two types of specimens were utilized in the experiments: uniaxial dog-bone shaped cylindrical specimens and solid shaft specimens for pure torsion. The dimensions of the specimens are shown in Fig. 52.

Table 20 Chemical composition of 4340 Aerospace steel, wt%

C	Cr	Mn	Mo	Ni
0.37	0.70	0.70	0.20	1.83

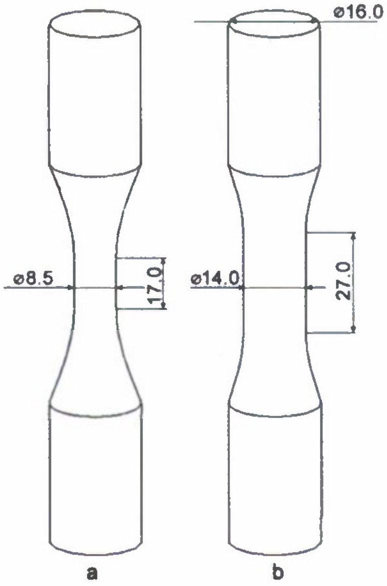

Fig.52 Specimens used in crack initiation experiments on 4340 VM steel

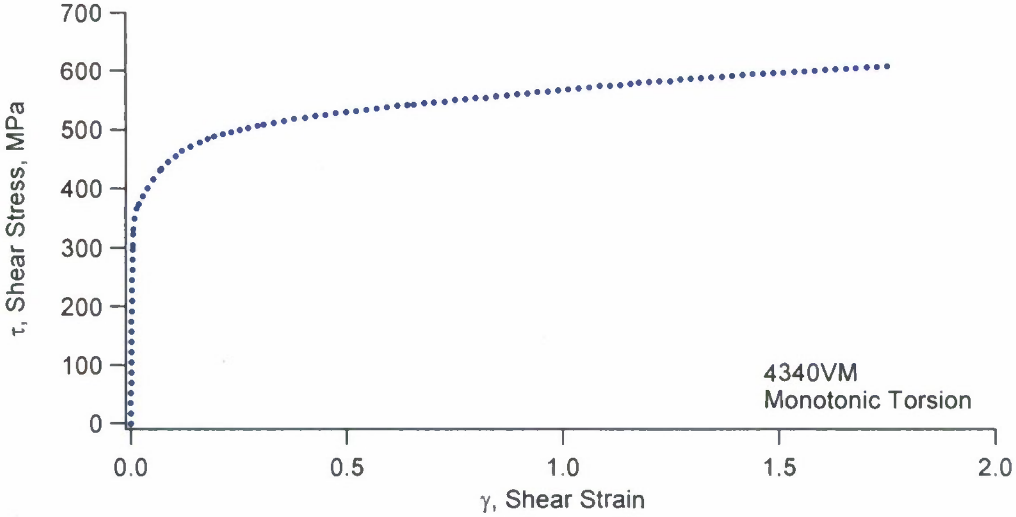

Fig.53 Monotonic torsion curve obtained by testing 4340 VM Aerospace steel

Table 21 Material properties of 4340 VM

Elasticity Modulus, E	212 GPa
Shear Modulus, G	68.24 GPa
Poisson's Ratio, μ	0.3
Yield Stress, σ_y	470 MPa
True Fracture Stress, σ_f	1050 MPa
Endurance Limit, σ_0	383 MPa

An Instron biaxial tension-torsion hydraulic testing machine was used for the experiments. The axial load cell has a capacity of 222 kN and the torque cell has a capacity of 2825 N-m. All experiments were conducted with computer control and data acquisition software.

In order to determine the static material properties, one of the specimens was subjected to pure monotonic torsion loading. The resulting shear stress-shear strain curve is shown in Fig. 53. The surface strain was measured by using an extensometer and the surface stress was determined following the Nadai's formula [9]. The static material properties of 4340VM steel together with the endurance limit are arranged in Table 21.

For the uniaxial tension-compression experiments, an extensometer with a gage length of 12.7 mm and a range of 5.0% was used to measure the axial strain. For the torsion and axial-torsion experiments, an extensometer capable of measuring axial, shear, and diametral strains was used. The extensometer has a range of 5% in the axial strain measurement and 3% in the shear strain. All of the experiments were conducted in ambient air. The details of the fatigue experiments are summarized in Table 22.

Table 22 Strain-controlled fatigue experiments for 4340VM aerospace steel

Type of Test	Specimen #	*f*, *Hz*	$\Delta\varepsilon/2$	$\Delta\gamma/2$	N_f, Cycles
Uniaxial Tension-Compression	VM-05	0.10	0.0100	...	500
	VM-03	0.25	0.0070	...	780
	VM-01	0.50	0.0050	...	4,700
	VM-06	1.00	0.0040	...	8,100
	VM-02	1.00	0.0030	...	36,710
	VM-04	2.50	0.0025	...	105,100
	VM-09	4.00	0.0022	...	304,500
	VM-07	4.00	0.0020	...	>1,210,500
Solid Shaft Pure Torsion	VM-23	0.10	...	0.0242	820
	VM-14	0.10	...	0.0173	1,700
	VM-20	0.10	...	0.0147	2,880
	VM-17	0.20	...	0.0121	3,100
	VM-19	0.25	...	0.0104	7,400
	VM-15	0.25	...	0.0087	13,400
	VM-18	0.50	...	0.0069	30,100
	VM-21	1.00	...	0.0057	80,500
	VM-13	0.50	...	0.0052	81,300
	VM-16	2.00	...	0.0043	244,000
	VM-22	2.00	...	0.0034	752,000

f – frequency of applied loading; $\Delta\varepsilon/2$ – amplitude of applied axial strain;
$\Delta\gamma/2$ – amplitude of applied shear strain; N_f – number of cycles to failure.

One of the tension-compression specimens was tested under incremental step loading to generate the cyclic stress-strain curve (CSSC). The results, combined with the stress-strain output values collected during the fatigue tests on individual specimens, are shown in Fig. 54. A typical quasi-plateau can be observed with the stress amplitude level at about 400 MPa.

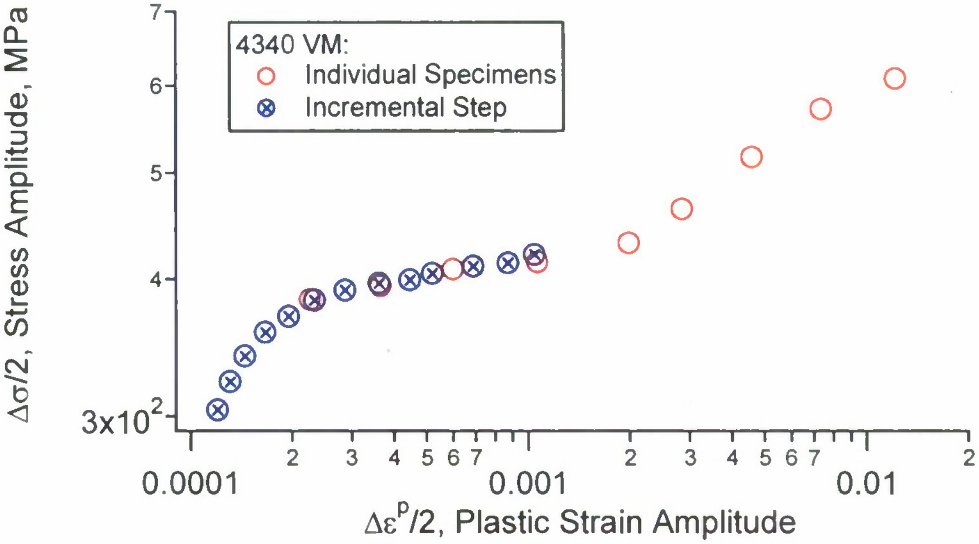

Fig.54 CSSC of 4340VM aerospace steel

Figure 55 represents the cyclic hardening curves based on the data collected during the experiments. Due to the specifics of the testing equipment, in some cases the pre-set value of the strain amplitude is not reached immediately at the beginning of the test. Therefore, the stabilization period, during which the strain control reaches its designed value, has been removed from the graphs in Fig.55. It can be seen in Fig.55 that material demonstrates cyclic softening as the number of loading cycles increases. The amount of softening depends on the level of the applied strain amplitude and is more pronounced under higher values of strain.

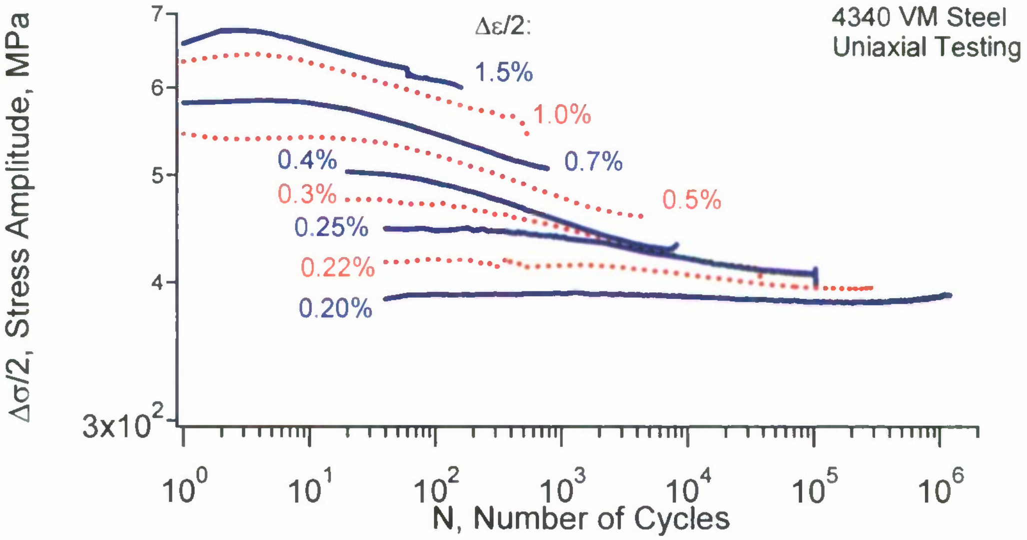

Fig.55 Cyclic behavior of 4340 VM aerospace steel

The non-Masing behavior (the strain range effect) is demonstrated in Fig.56 which shows the hysteresis loops obtained at the half-life of the specimens and plotted in stress-strain range coordinates. If the material displays Masing behavior, all the upper braches of the hysteresis loops shown in Fig.56 should coincide. It is evident from Fig. 56 that 4340 VM steel displays non-Masing behavior or strain range effect particularly when the loading amplitude is large.

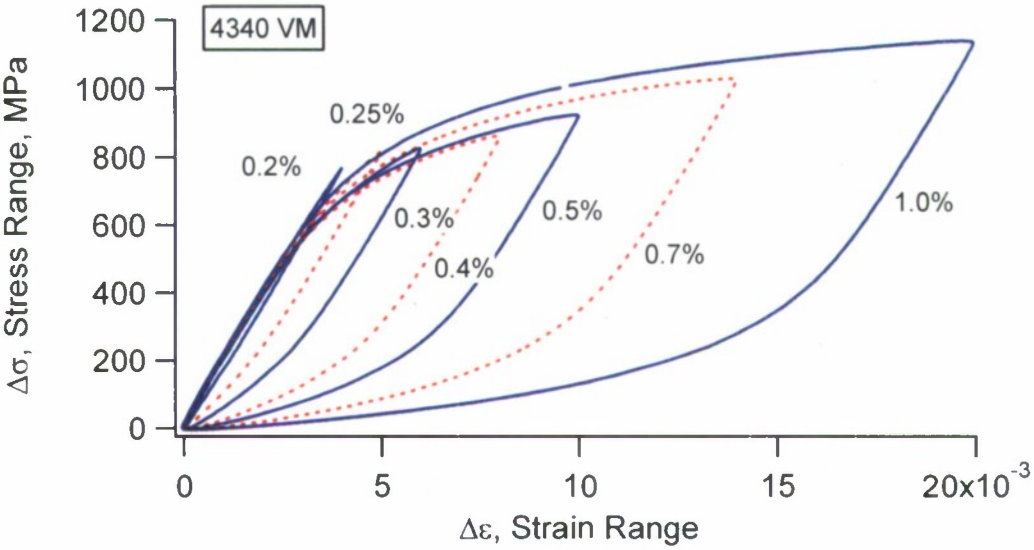

Fig.56 Non-Masing behavior of 4340 VM steel

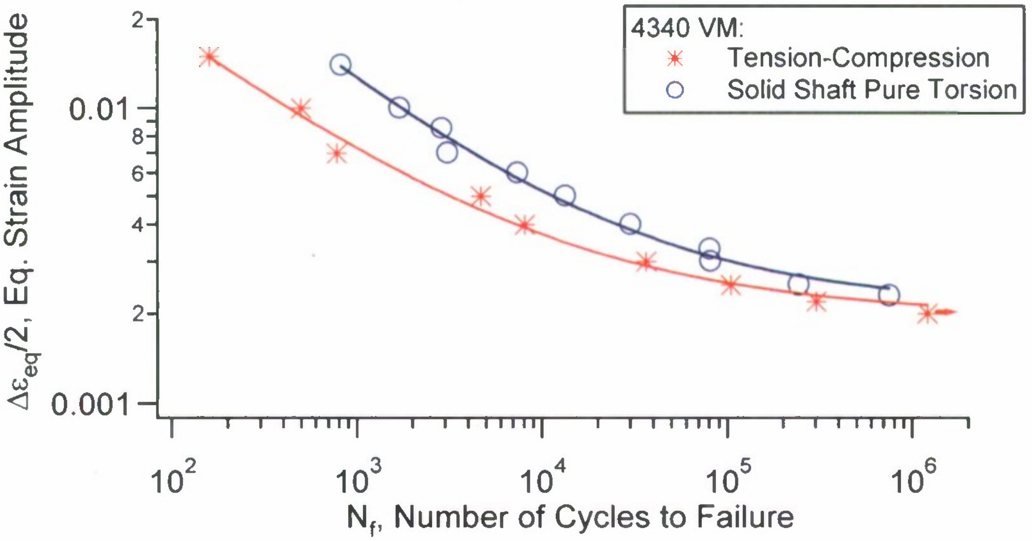

Fig.57 S-N curves of 4340 VM aerospace steel

The results of the fatigue experiments are combined and displayed as the strain-life curves and are shown in Fig.57. The vertical axis in Fig.57 represents amplitude of applied equivalent strain and the horizontal axis represents the fatigue life of the specimen. An arrow next to the data point indicates that the specimen did not fail at the end of experiment. Since the results are represented using equivalent strain a comparison between the fatigue curves corresponding to different loading can be made. It can be seen that the fatigue life of specimens tested in pure torsion is higher than the life of tension-compression specimens. The curves tend to merge together in the high cycle fatigue region.

The photographs of the fatigue cracks in selected axial tension-compression specimens are shown in Fig. 58 together with the pictures of the fracture surfaces in the cases when the specimen failed by complete separation due to fatigue loading. The average angle of cracking plane orientation with respect to the vertical axis of the specimen was measured to be 24^0. All of the specimens tested in fully reversed pure torsion failed by the cracks oriented at zero degrees with respect to the vertical axis thus demonstrating the shear cracking behavior (cracks are oriented along the planes of maximum shear).

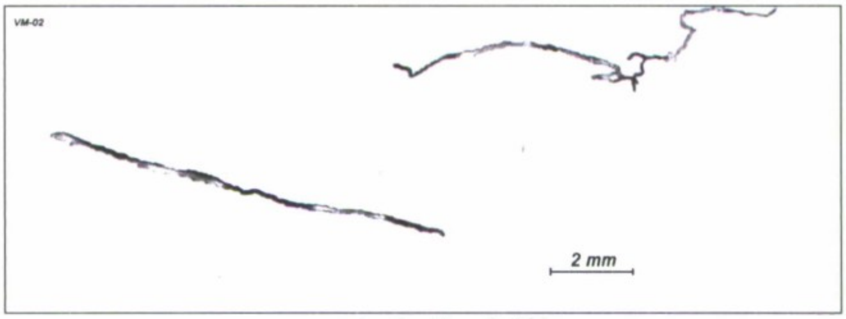

a) $\Delta\varepsilon/2 = 0.3\%$

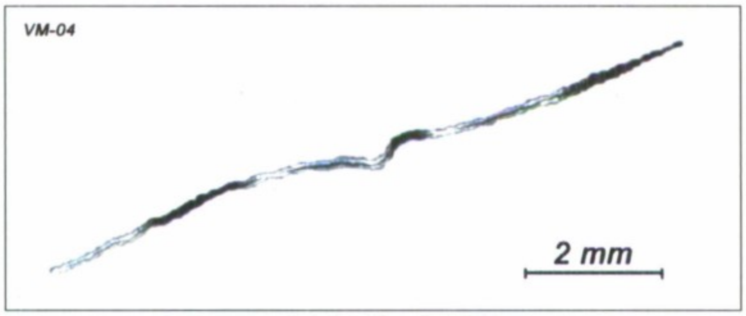

b) $\Delta\varepsilon/2 = 0.25\%$

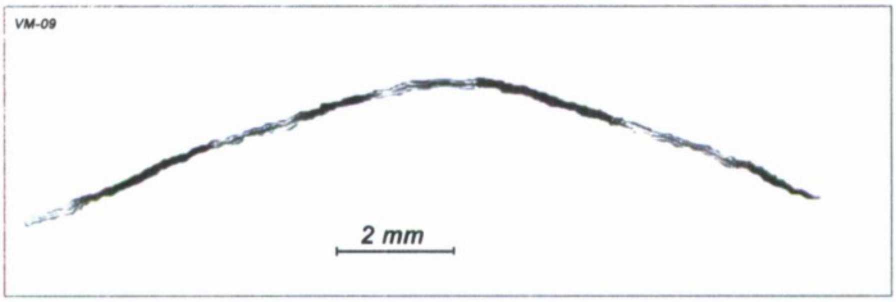

c) $\Delta\varepsilon/2 = 0.22\%$

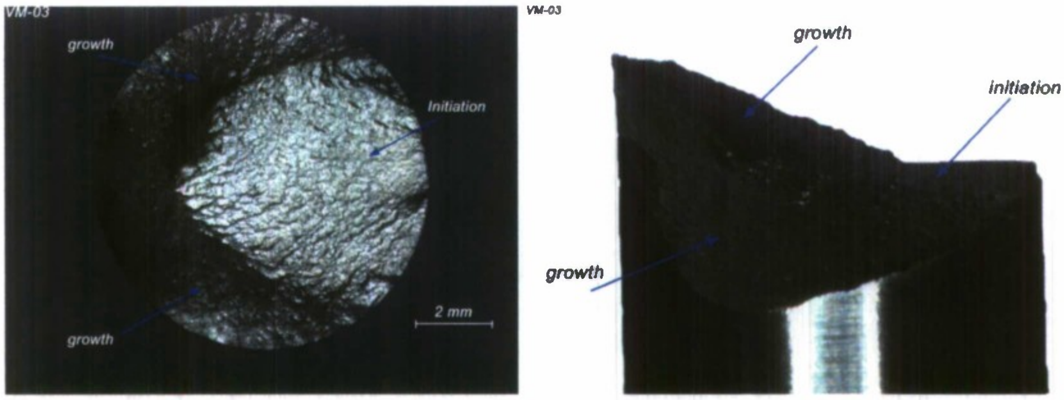

d) Δε/2 = 0.7%

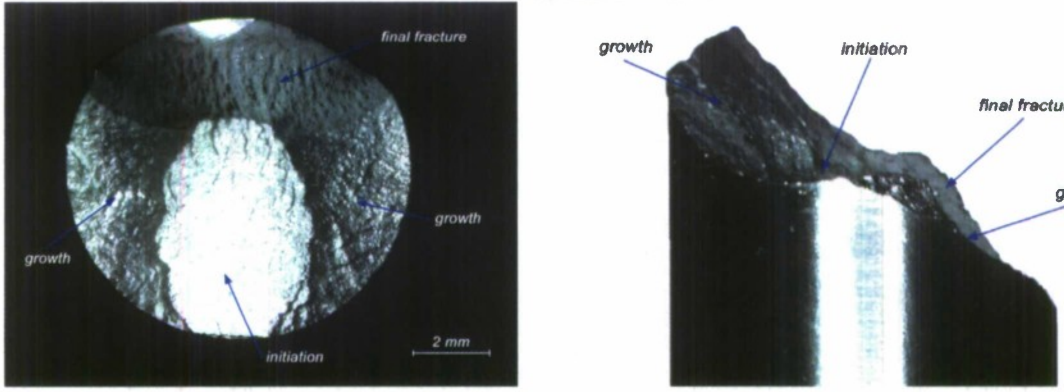

e) Δε/2 = 1.0%

Fig.58 Photographs of fatigue cracks in tension-compression specimens: 4340VM steel

4.2 CRACK GROWTH EXPERIMENTS

Fatigue crack growth experiments on 4340 VM were performed using round compact tension (CT) specimens with a single notch under sinusoidal load-controlled loading in laboratory environment. All of the experiments were conducted at room temperature. Mode I crack growth was investigated. All the specimens have a thickness of 3.8mm. The U-shape notches were made using the Electric Discharge Machine (EDM) in order to avoid residual stresses resulting from a traditional saw cutting. No heat treatment was done on the specimens prior to testing. The specimens is shown in Fig. 59. Crack extension from notch root was measured using an optical reading microscope with a magnification of 40. To facilitate convenient crack extension measurement, one side of each specimen was polished before installation on the test machine. The loading conditions include constant amplitude loading with different R-ratios, constant amplitude loading with a single tensile overload and high-low sequence loading. The results of the crack growth tests are represented in a standard way as a crack growth rate (da/dN) versus the stress intensity factor range (ΔK) for a given loading condition.

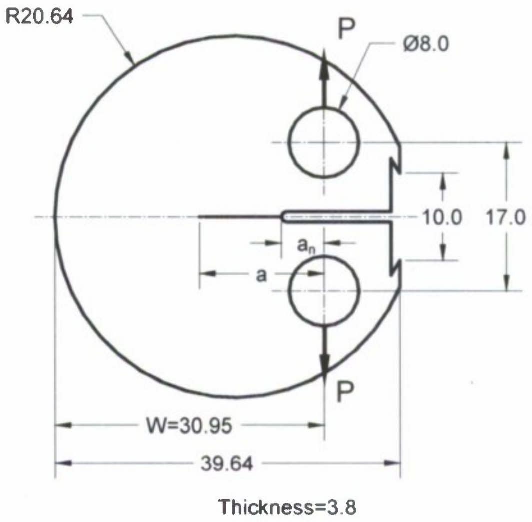

Fig.59 Round compact tension specimen used for crack growth experiment of 4340VM

4.2.1 Constant amplitude experiments

The constant amplitude crack propagation experiments were conducted with four different positive R-ratios. The primary goal was to investigate the mean stress effect on crack growth behavior in stable growth regime. The details of the experiments are summarized in Table 23.

Table 23 Constant amplitude crack growth experiments for 4340VM steel

Spec. ID	t, mm	ρ, mm	R-ratio	P_{max}, kN	f, Hz	a_n mm	a_f mm	N_f ,cycle
VM-C15	3.79	0.120	0.1	3.0	10-2	4.605	11.630	1,509,186
VM-C21	3.80	0.146	0.1	4.0	10	2.314	7.3005	802,159
VM-C08	3.81	0.119	0.1	4.0	10-2	4.516	12.057	285,167
VM-C09	3.80	0.127	0.2	5.0	10-2	4.320	11.453	121,633
VM-C10	3.81	0.141	0.2	4.5	10-2	4.538	10.112	149,220
VM-C06	3.78	0.127	0.5	5.2	10-2	4.713	12.869	305,376
VM-C12	3.76	0.141	0.5	7.2	10-2	4.539	11.068	107,500
VM-C07	3.79	0.142	0.75	7.6	15-5	4.706	13.219	759,067

R-ratio = minimum load over the maximum load in a loading cycle

$P_{\max}$ = maximum load in a loading cycle f = loading frequency

a_n = distance between the notch root and the line of action of the externally applied load

N_f = total cycles a_f =final crack length

In addition to the constant amplitude experiments, one specimen was tested under decreasing loading conditions to determine the threshold values corresponding to different R-ratios. Four steps of loading, each corresponding to one value of R-ratio, were performed on the specimen which enabled to generate the threshold stress intensity factor data for four R-ratios. The results of ΔK_{th} are shown in Fig. 60 as a function of the R-ratio.

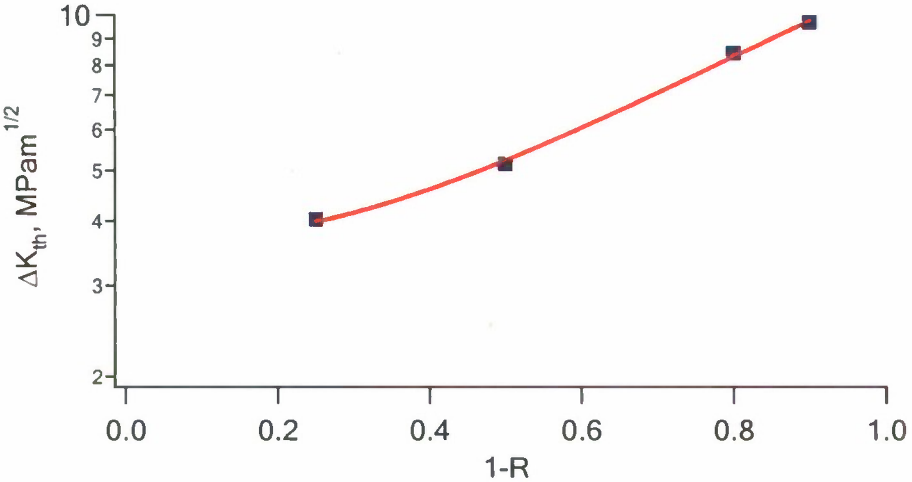

Fig.60 Threshold stress intensity factor as a function of R-ratio; 4340VM Aerospace Steel

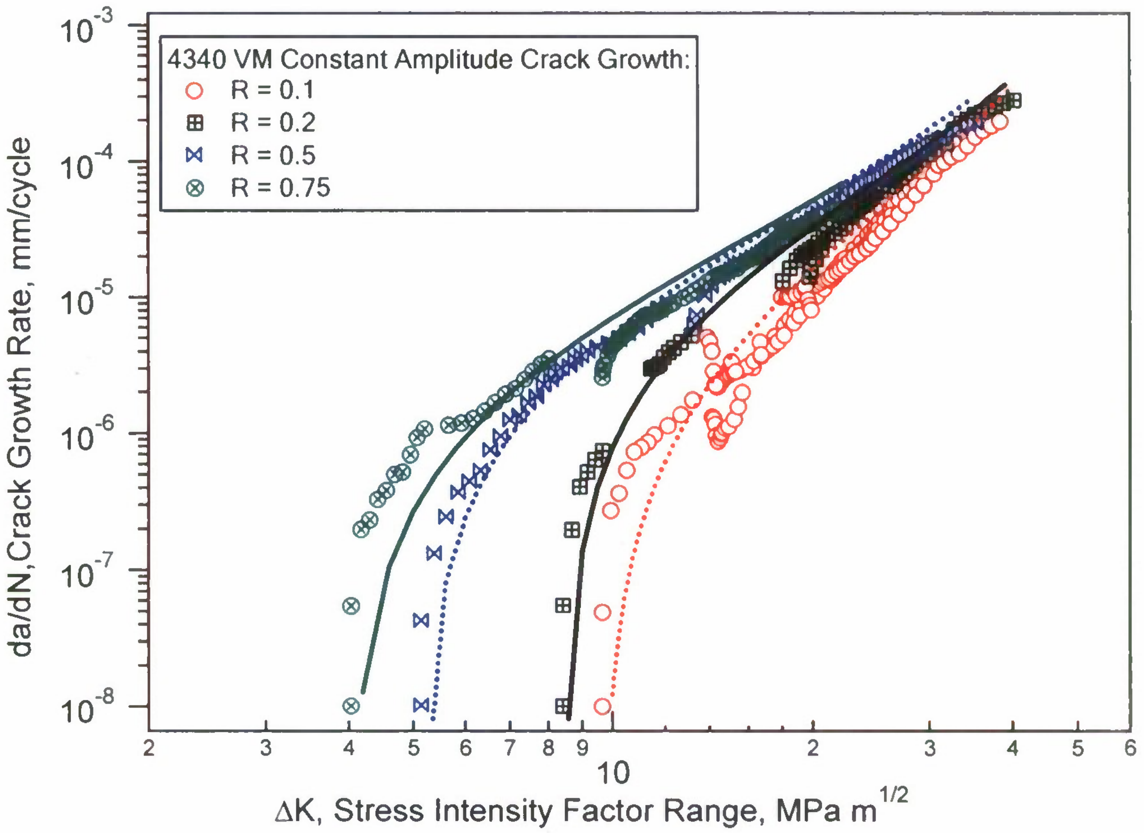

Fig.61 R-ratio effect in 4340 aerospace steel

The results of the crack growth experiments under constant amplitude loading are shown in Fig. 61. The vertical axis represents the crack growth rate (in millimeter per cycle) and the horizontal axis represents the stress intensity factor range. It can be seen that the material displays a R-ratio effect. This effect is more pronounced in the low ΔK region. With increasing stress intensity factor range, the curves corresponding to different R-ratio come close to each other. The near threshold crack growth data collected from the experiments with gradually decreasing loading is also placed in Fig. 61. In order to include the near threshold growth, a modified Paris law similar to that in [41] was used with the following form,

$$\frac{da}{dN} = C\left[\frac{\Delta K - \Delta K_{th}}{\Delta K_{\max} - \Delta K}\right]^{\alpha} \tag{6}$$

where $\Delta K_{\max}$ is the maximum value of stress intensity factor range, α is dimensionless fitting constant and C is a constant with a units of the crack growth rate. For 4340VM, $\alpha = 1.72$ and $C = 4.4 \times 10^{-4}$ mm/cycle. The corresponding fitting curves are shown as lines in Fig.61 and the experimental data is represented by markers.

4.2.2. Variable loading amplitude experiments

Two types of fatigue crack growth experiments were used for 4340VM steel: experiments with single tensile overload and high-low loading sequence experiments. Two specimens were tested under constant amplitude loading with a single spike of tensile overload in the middle of experiment, as schematically shown in Fig. 12. The constant amplitude loading part for both of the specimens were kept the same with R = 0.1, $\Delta P/2 = 1.8kN$ and the overloads were applied in both cases at approximately the same length of crack. The details of overload experiments are shown in Table 24.

Table 24 Single overload experiments

Spec. ID	ρ, mm	f, Hz	a_n mm	a_{OL} mm	a_f mm	P_{OL}, kN	N_f (cycle)
VM-C11	0.125	10-2	4.608	7.600	11.012	7.0	403,398
VM-C13	0.120	10-2	4.603	7.572	11.146	8.0	423,640

P_{OL} = magnitude of the overload or underload

a_{OL} = crack length at overload, as measured from the notch root

The results of overload experiments are shown in Fig. 62. The thick dotted line in each plot represents the stable crack growth rate in order to facilitate the observation of overload effect. From Fig.62, it can be seen that application of a tensile overload causes retardation of crack growth. The level of such retardation clearly depends on the magnitude of overload. It should be noticed that the short period of significant acceleration of crack growth can be observed immediately after application of overload. In fact, the magnitude of such acceleration can be greater than the magnitude of post-overload deceleration of crack growth. The maximum crack growth rate in the accelerated portion of post-overload growth curve can be five times greater than the rate of stable crack propagation. This is a noticeable phenomenon which distinguishes this material from other alloys discussed in present work. Short period of post-overload crack growth acceleration has been previously observed for other metallic materials [20, 51], however the magnitude of such acceleration was much lower. After initial acceleration, the crack growth slows down reaching a minimum point. With further application of loading cycles the crack growth rate reaches a stable growth curve.

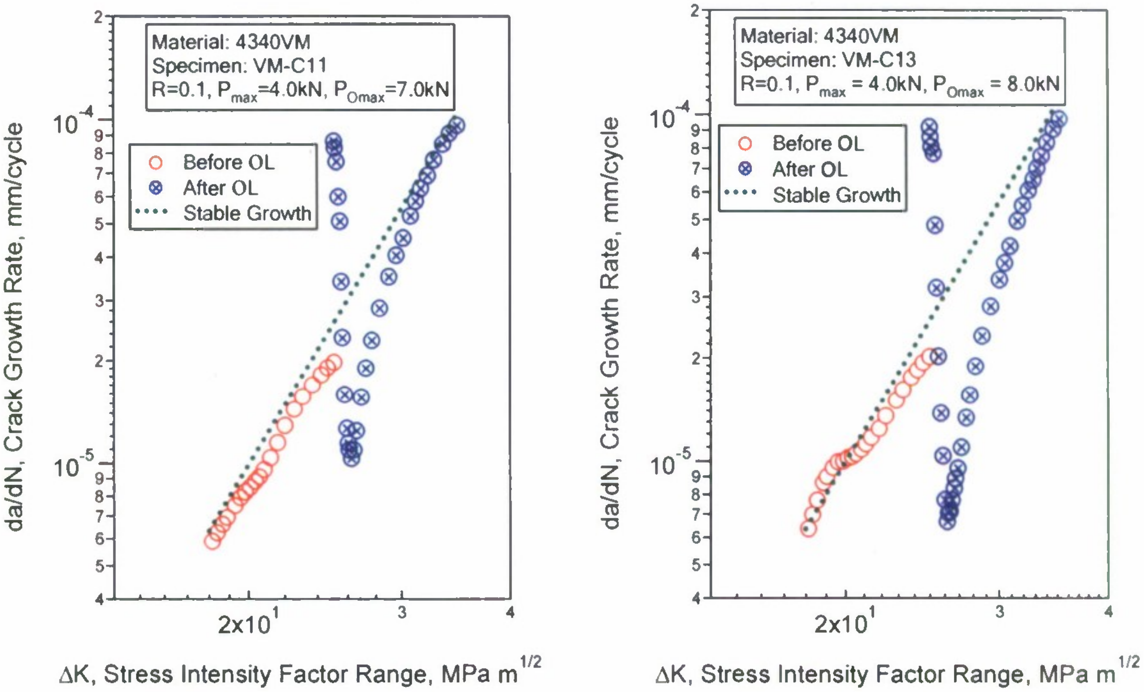

Fig.62 Single tensile overload experiments

Table 25 High-Low sequence loading experiments conducted for 4340 VM steel

Spec. ID	ρ mm	f Hz	$P_{H\max}$, kN	$P_{L\max}$, kN	R_H	R_L	a_n mm	a_H mm	a_f mm	N_H cycle	N_f cycle
VM-C47	0.100	5-2	6.0	4.20	0.10	0.14	6.332	8.713	12.948	11,015	62,001
VM-C48	0.115	10-2	5.0	5.00	0.10	0.40	6.259	9.289	13.228	31,666	56,396
VM-C49	0.115	5-2	5.0	3.33	0.10	0.10	6.535	9.553	13.819	26,551	134,383

R_H = R-ratio of the first step R_L = R-ratio of the lower loading amplitude step

$P_{H\max}$ = maximum load in first loading step $P_{L\max}$ = maximum load in second loading step

N_H = number of cycles in the higher amplitude step

a_H = crack length at the termination of the high amplitude test, as measured from the notch root

Three specimens were tested under the High-Low loading sequence conditions with constant amplitude loading within both "High" and "Low" parts of the experiment. Details of the two-step high-low sequence loading experiments are summarized in Table 25. The ratio of loading amplitude in the "High" step over the amplitude in the "Low" step was kept the same for all three experiments ($\Delta P_H / \Delta P_L = 1.5$). Similarly to experiments on other materials described in present work, the following loading conditions were chosen. The maximum load was the same for the two loading steps in one specimen (Fig.63(a)). In the second specimen, the minimum load was identical in the two loading steps (Fig.63(b)). The third specimen experienced two-step loading with identical *R*-ratio in the two loading steps (Fig.63(c)). The results shown in Fig.63 reveal that the influence of the high-low sequence loading depends on the details in the lower amplitude loading step. When the maximum load was kept the same in the two loading steps, the higher loading step had a little influence on the crack growth of the second loading step with a lower load amplitude (Fig.63(a)). However, a significant crack growth retardation was observed on the other two specimens, resembling the overload effect shown in Fig.62. Such a behavior appears to be similar to other steels investigated in present work. It should be mentioned that due to the fan-shaped behavior of crack growth curves (Fig.61) the stable growth lines corresponding to high and low steps in Fig.63(c) are not parallel.

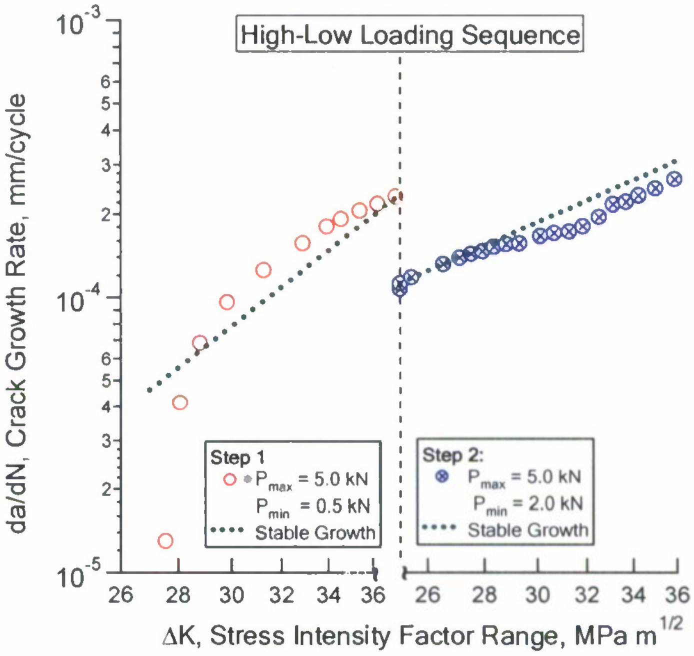

(a)

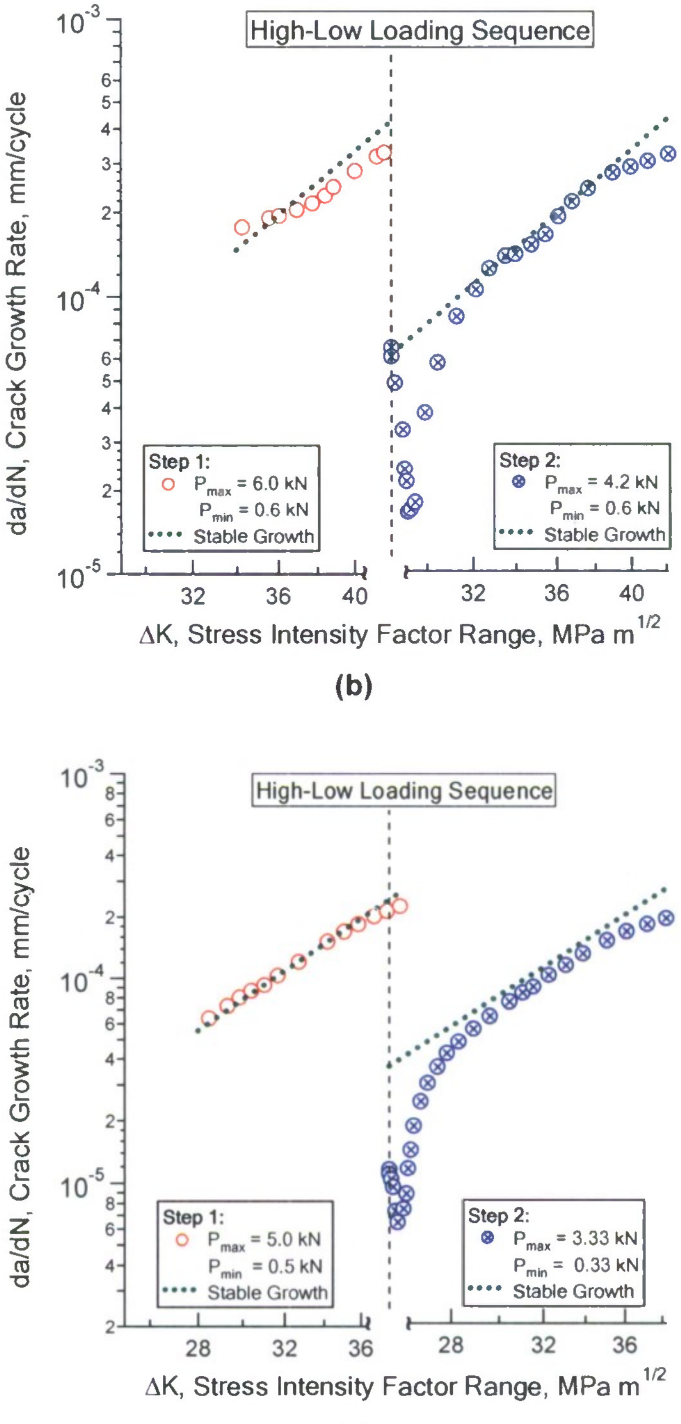

(b)

(c)

Fig.63 High-Low sequence loading (4340 VM)

II. MODELING

1 CRITICAL PLANE MULTIAXIAL CRITERIA

A number of multiaxial fatigue criteria have been developed in the past 40 years. A major development in fatigue life prediction is the confirmation of the critical plane approaches. A critical plane approach relates fatigue damage to the stress and strain on a material plane on which cracks nucleate and grow. The critical plane is defined as the material plane which experiences the maximum fatigue damage. Fatigue failure and cracking behavior can be predicted simultaneously in the critical plane approaches.

1.1 SWT CRITERION

Smith, Watson, and Topper [52] developed a fatigue criterion (SWT criterion) to consider the mean stress effect for uniaxial loading by using the cyclic strain amplitude and the maximum stress. The SWT fatigue parameter (FP) is expressed as,

$$FP = \sigma_{n\max} \frac{\Delta\varepsilon}{2} \tag{7}$$

where $\sigma_{n\max}$ is thc maximum normal stress and $\Delta\varepsilon$ is the normal strain range on the critical plane. The critical plane is defined as a material plane with maximum normal strain amplitude. The model was originally developed to describe fatigue of materials that exhibit tensile cracking behavior.

1.2 MODIFIED SWT CRITERION

Jiang and Sehitoglu [53] extended the SWT parameter to consider the general stress state and cracking behavior. With a slightly different form, the modified SWT criterion can bc expressed by,

$$FP = 2b\Delta\varepsilon\langle\sigma_{\max}\rangle + \frac{1-b}{2}\Delta\tau\Delta\gamma \tag{8}$$

where σ and τ are the normal stress and shear stress, respectively, on a material plane. ε and γ are the normal strain and shear strain corresponding to the normal stress, σ, and shear stress, τ, respectively. The symbol Δ denotes range in a loading cycle and the subscript "max" represents maximum in a loading cycle. The symbol $\langle\ \rangle$ in Eq. (8) represents the MacCauley bracket (*i.e.*, $\langle x\rangle = 0.5(x+|x|)$). The use of the MacCauley bracket is to ensure that no negative fatigue damage can be produced. The symbol b in Eq. (8) is a material constant and it ranges from 0 to 1.0. Chu et al. [54] and Chu [55] developed a fatigue criterion mathematically identical to that of Eq.(8). A similar paramcter was discussed by Glinka et al. [56].

1.3 FATEMI AND SOCIE CRITERION

A shear based parameter, developed by Fatemi and Socie [57] and Fatemi and Kurath [58] (FSK parameter) has the following mathematical form

$$FP = \frac{\Delta\gamma}{2}\left(1 + k\frac{\sigma_{n\max}}{\sigma_y}\right) \tag{9}$$

where $\Delta\gamma/2$ is the shear strain amplitude and $\sigma_{n\max}$ is the maximum normal stress. Both quantities are on the critical plane. σ_y is the yield stress of the material and k is the material constant. The critical plane is the plane of maximum shear strain. The fatigue constant k is determined from the experimental data based on tension-compression and pure torsion experiments. By selecting different values of k the uniaxial and torsional fatigue data come together and can be fitted with three-parameter equation. Using the baseline fit of fatigue parameter, the fatigue life can be determined for any multiaxial state with help of coordinate transformation.

1.4 JIANG'S MODEL

A multiaxial fatigue criterion recently developed by Jiang [59] is an energy based approach that can be expressed in the following incremental form

$$\begin{cases} dD = \left\langle \dfrac{\sigma_{mr}}{\sigma_0} - 1 \right\rangle^m \left(1 + \dfrac{\sigma}{\sigma_f}\right) dY, \\ dY = b\sigma d\varepsilon^p + \dfrac{1-b}{2}\tau d\gamma^p. \end{cases} \tag{10}$$

In the above equations D represents the fatigue damage and Y stands for plastic strain energy on a material plane. Quantities σ and τ are normal and shear stresses on a material plane; ε^p and γ^p are plastic strains corresponding to stresses σ and τ. The symbols b and m are material constants. Constants σ_0 and σ_f are correspondingly endurance limit and true fracture stress of the material and σ_{mr} is a memory stress. The use of MacCauley bracket ensures that when $\sigma_{mr} \le \sigma_0$ the fatigue damage is zero. This induced by the fact that when the stress is lower than endurance limit there is no formation of persistent slip bands and therefore the fatigue damage is minimal. The critical plane is defined as the material plane where the fatigue damage accumulation first reaches a critical value D_0.

In general, the cracking behavior of a material can be categorized in the following manner. If the cracking planes are consistent with the material planes of maximum shear, the behavior is termed as the shear cracking (Fig.64(a)). If a material displays tensile cracking the cracks are oriented along the plane of maximum normal stress (Fig.64(b)). Additionally, some materials display a mixed cracking mode, where the cracks initiate on the maximum normal stress planes under tension-compression but on the maximum shear planes in pure torsion (Fig.64(c)).

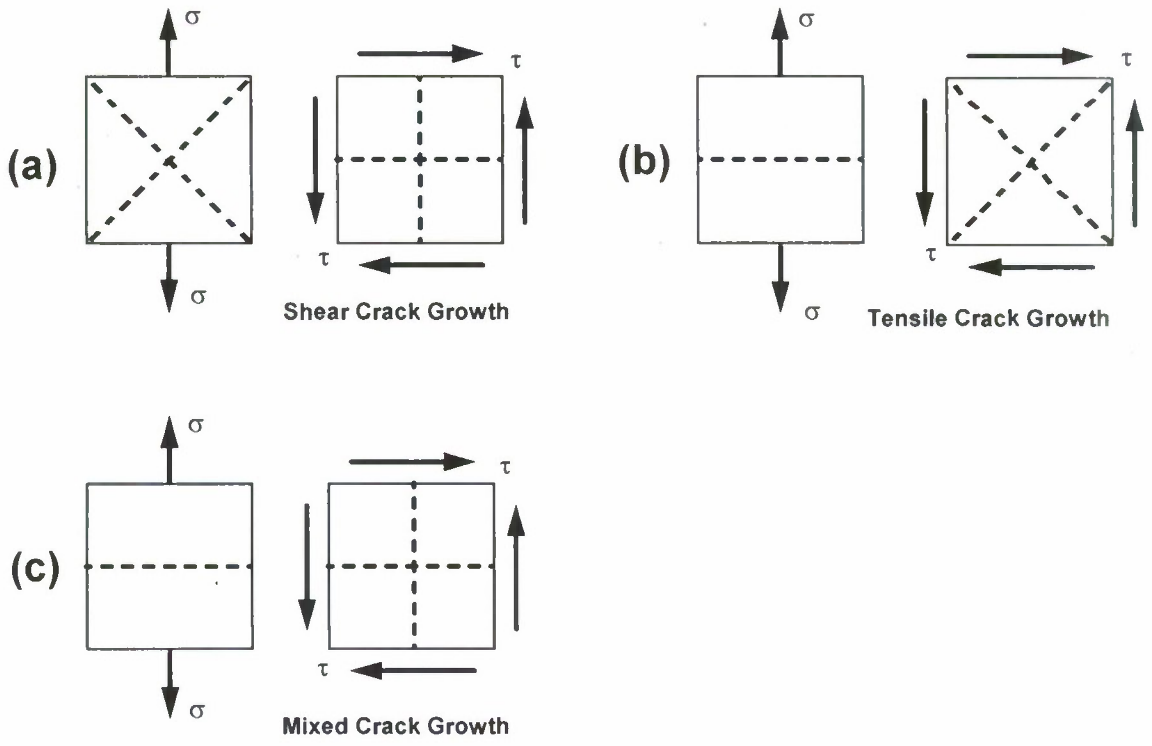

Shear Crack Growth

Tensile Crack Growth

Mixed Crack Growth

Fig.64 Fatigue cracking behavior. a) shear cracking; b) tensile cracking; c) mixed cracking

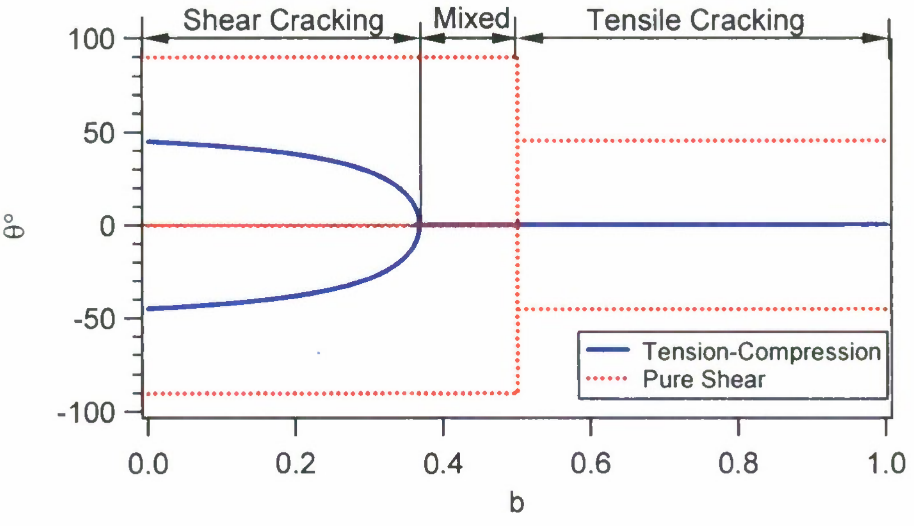

Fig.65 Dependence of critical plane orientation on parameter b

The Jiang's fatigue criterion is capable of predicting different cracking modes under different stress states. This is achieved with the help of constant b in Eq. (10). Figure 65 shows the orientation of the critical plane under the two typical loading conditions and the dependence of the critical plane on the material constant b [59]. When $0.37 \geq b \geq 0$, the criterion predicts shear cracking behavior. When $b \geq 0.5$, tensile cracking behavior is predicted. Mixed cracking behavior can be accounted for with a b value between 0.37 and 0.5.

2 APPICATION OF CRITICAL PLANE MULTIAXIAL FATIGUE CRITERIA

2.1 *7075-T651 ALUMINUM ALLOY*

Figure 66 shows the SWT parameter versus the fatigue life for the uniaxial specimens experimentally tested in the current investigation. The solid line in Fig.66 was obtained by fitting the fully reversed uniaxial fatigue data using the three-parameter equation mathematically identical to Eq. (1). The dotted lines are the factor-of-five boundaries. It is clear that the parameter correlates the experiments well for most of the uniaxial loading cases. Exceptions are the those under the loading conditions with large compressive mean stresses. Several specimens were tested with a positive maximum stress being close to zero. As a result, the SWT fatigue parameter was very small according to Eq. (7). These are the data points shown in Fig.66 that deviate significantly from the general tendency line. As has been well recognized, the SWT parameter assumes zero fatigue damage when the maximum stress is negative. The parameter fails to predict the fatigue failure under compression-compression that was experimentally observed. Since the logarithmic scale used, the specimens under compression-compression loading are not shown in Fig.66.

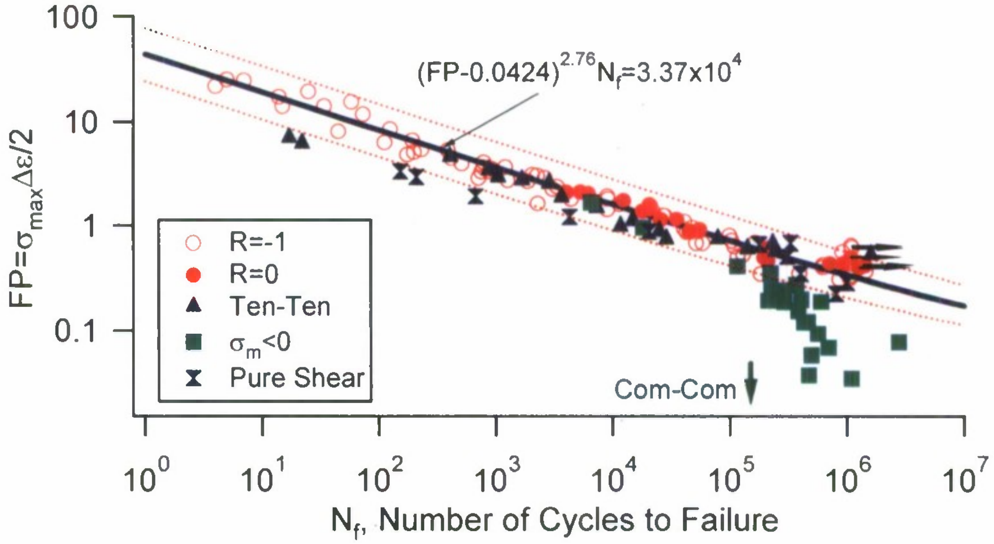

Fig.66 SWT parameter versus fatigue life under uniaxial loading

Once the relationship between the *FP* and the fatigue life is established based on the fully reversed uniaxial loading, fatigue life can be predicted for any given loading condition when the stress and strain histories are known. Fig.67 shows the comparison of the predicted fatigue life and the observed life for all the tubular specimens tested in the current investigation. The stress and strain responses were obtained experimentally. Through a rotation of the coordinates system, the *FP* for any given material plane can be determined using the SWT parameter, Eq. (7). The maximum *FP* can be determined and the fatigue life can be obtained using the relationship between *FP* and the fatigue life (Fig.66). At the same time, the orientation of the critical plane was determined.

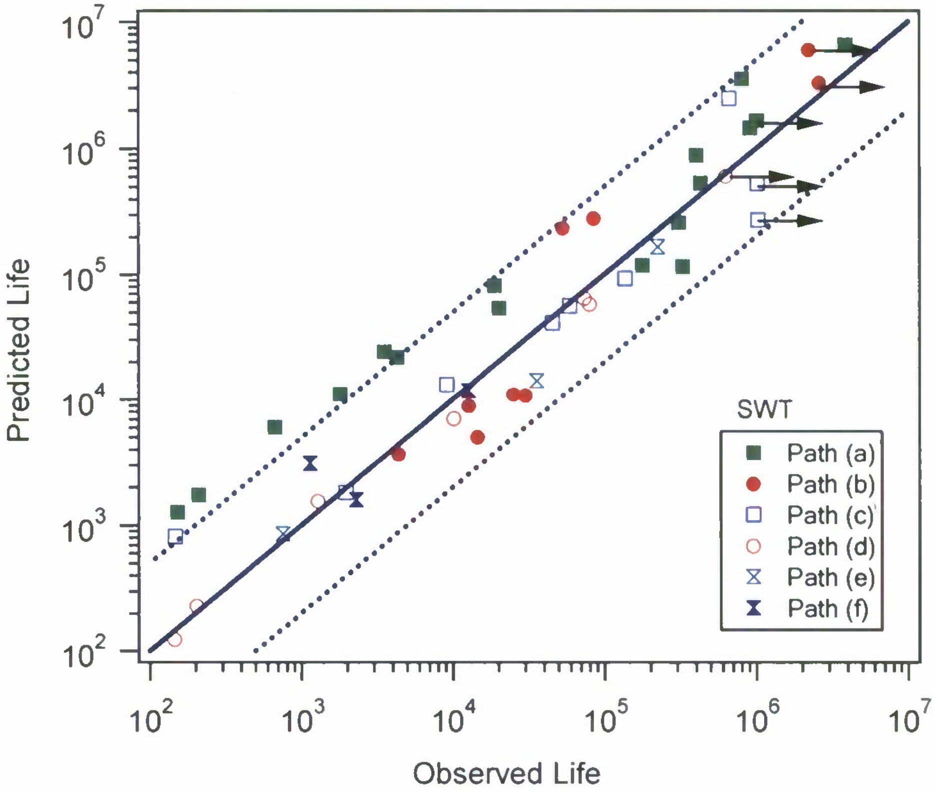

Fig.67 SWT parameter correlation with experiments under combined axial-torsion loading

The solid diagonal line in Fig.67 denotes a perfect prediction. The two dotted lines arc the factor-of-five boundaries. A glance at Fig.67 reveals that the SWT parameter can correlate well the fatigue experiments under combined axial-torsion loading in terms of fatigue life. Among a total of 38 tubular specimens, the predicted fatigue lives of 30 specimens (79%) are within the factor-of-five lines, indicating a reasonable fatigue life prediction.

A critical plane approach is based upon the notion that a fatigue crack is initiated on a ccrtain material plane where the fatigue damage is the maximum. Therefore, a critical plane approach can predict both the fatigue life and the critical planes where cracks are predicted to initiate. For an axial-torsion tubular specimen or a uniaxial tension-compression specimen, the material plane can be represented by its normal direction using one angle, θ, measured counter-clockwise from the axial direction (refer to the upper-right insert in Fig.68). For a given loading condition, it is often found that several material planes or a range of material planes may experience identical or vcry similar fatigue damage according to a given fatigue criterion. Due to the inherent data scatter in fatigue experiments, it would be preferable to identify the material planes with similar fatigue damage by using a given fatigue criterion. In the current investigation, a range of 10% from the maximum fatigue damage is used for the discussion of possible cracking material planes predicted by a fatigue criterion. As shown in Fig.68, the distribution of the fatigue damage per loading cycle over the material plane orientation can be determined according to a criterion for a given loading condition. The fatigue damage per loading cycle is the reciprocal of the predicted fatigue life under constant amplitude loading. The fatigue damage shown in Fig.68 is normalized so that the maximum fatigue damage with respect to all the possible material planes is unit. Theoretically, the maximum peak points are predicted to be the critical planes and cracks are predicted to form on these particular material planes. By considering a range of 10% from the maximum fatigue damage, a range of the cracking directions can be obtained. It should be noted that a 10% range was arbitrarily selected without a physical consideration.

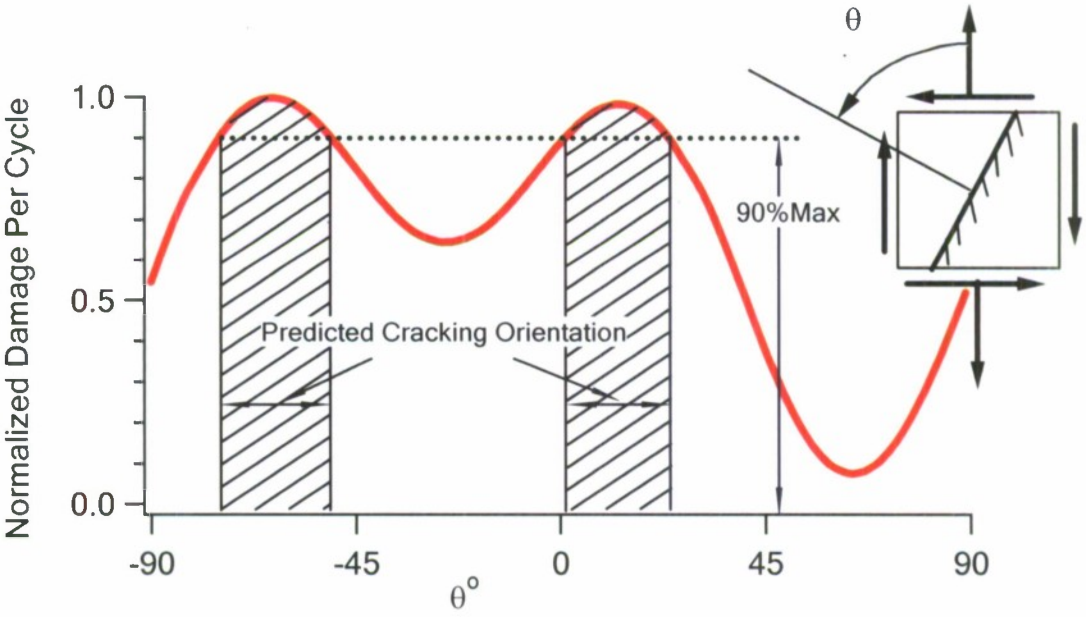

Fig.68 Dependence of fatigue damage on material plane orientation

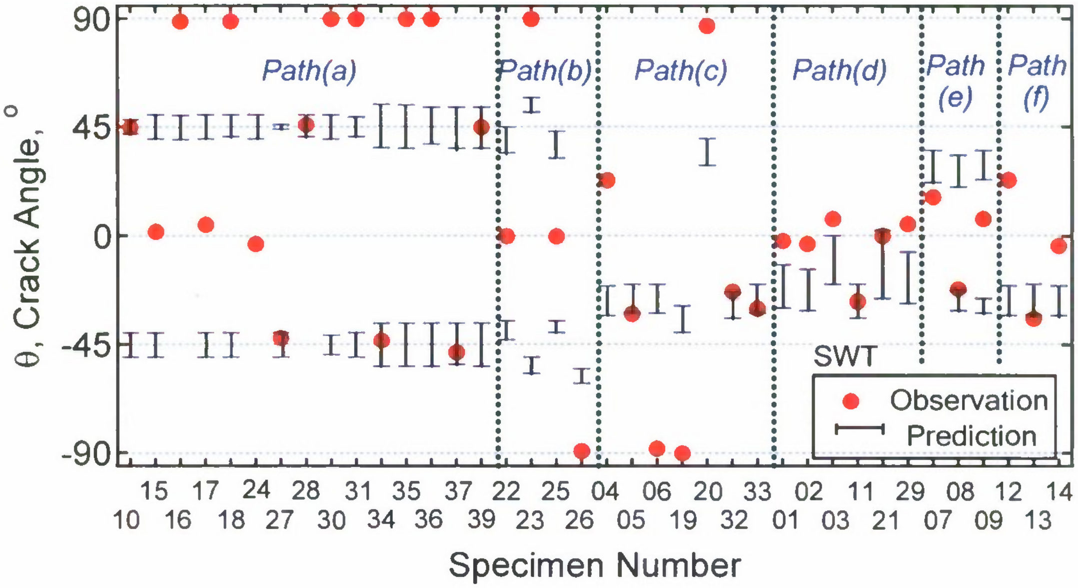

Fig.69 Comparison of the experimentally observed cracking directions with the predictions by the SWT criterion

Figure 69 summarizes the comparison of the observed cracking directions and the predictions obtained from using the SWT fatigue criterion. The solid dots represent the observed crack orientations. The size of the dots signifies the general scatter existed in the experimental measurement of the cracking angle. The range bars in the figure are the predicted ranges of the cracking directions. Observations on the experimental cracking behavior were made in the millimeter scale of the crack length. As will be discussed in a later section, such a treatment is consistent with the macroscopic continuum assumption adopted in the current investigation for the stress and strain.

The results in Fig.69 show that among the 38 tubular specimens tested under axial-torsion loading, the SWT model can only predict correctly the cracking behavior for 13 specimens (34%). Such a poor predictability of the SWT criterion for cracking behavior is not surprising because the criterion predicts tensile cracking behavior while the material under investigation displays "diverse" cracking behavior. For the material subjected to uniaxial loading, the SWT criterion predicts a cracking plane that is perpendicular to the loading axis in the uniaxial specimen. For a specimen under cyclic torsion, the parameter predicts a crack plane with its normal making ±45° angle from the loading specimen axis. 7075-T651 alloy displays different cracking behavior dependent on the loading magnitude or fatigue life. The SWT criterion can predict cracking direction correctly for both uniaxial and pure shear when the fatigue lives are longer than approximately 3×10^5 cycles.

The material constant b in the fatigue criterion, Eq. (8), is determined by comparing the fatigue results under fully uniaxial loading and those under fully reversed pure torsion fatigue of tubular specimens. Theoretically speaking, the $FP_{\max}$ - N_f (the number of loading cycles to failure) curves should coincide for a right choice of the material constant b. In addition, the selection of b should reflect the observed cracking behavior from the uniaxial loading and torsion loading.

Clearly, 7075-T651 displays cracking behavior that is dependent on the loading magnitude. Since the material constant b in the criterion describes the cracking behavior, a convenient and practical way is to relate the material constant b to the equivalent stress magnitude using a linear relationship,

$$b=\left\langle a_1-a_2\sigma_{eq}\right\rangle \tag{11}$$

where a_1 and a_2 are two constants that can be determined by the observed cracking behavior. The use of the MacCauley bracket is to ensure a non-negative b value. In addition, b should not be larger than unity.

σ_{eq} in Eq.(11) is the equivalent stress magnitude following the definition by Jiang and Kurath [60]. The mathematic expression for the equivalent stress magnitude is,

$$\sigma_{eq}=Min\left\{Max\sqrt{\frac{3}{2}\left(S_{ij}-S_{ij}^{0}\right)\left(S_{ij}-S_{ij}^{0}\right)}\right\} \tag{12}$$

where S_{ij} denotes the components of the deviatoric stress tensor and S_{ij}^0 represents a point in the deviatoric stress space. The maximum inside the braces is taken with respect to the time within a loading cycle. The minimum is taken in terms of any possible point S_{ij}^0 in the deviatoric stress space. Under tension-compression, the equivalent stress magnitude is equal to the stress amplitude. For pure shear loading, the equivalent stress magnitude is equal to the shear stress amplitude multiplied by $\sqrt{3}$.

Two points can be approximately identified from the cracking behavior observed on the material under fully reversed tension-compression and pure torsion. When the fatigue life is 2,000 cycles under fully reversed tension-compression loading, the material transits from shear cracking to mixed cracking (Fig.5). The corresponding equivalent stress is 393 MPa. At this point, b should be equal to 0.37 [53]. From the pure torsion experiments, it can be identified that the material switches from mixed cracking to shear cracking when the fatigue life is in the region of 3×10^5 cycles (Fig.9). Since the corresponding equivalent stress magnitude is 290 MPa, it can be identified that b=0.5 when σ_{eq}=290 MPa. With these two particular points for Eq.(11), a_1=0.862 and a_2=0.00125 were obtained for 7075-T651 aluminum alloy. Eq.(11) with the consideration of the dependence of the cracking behavior on the loading magnitude warrants that the modified SWT criterion will predict cracking behavior correctly for most of the fully reversed uniaxial and shear specimens.

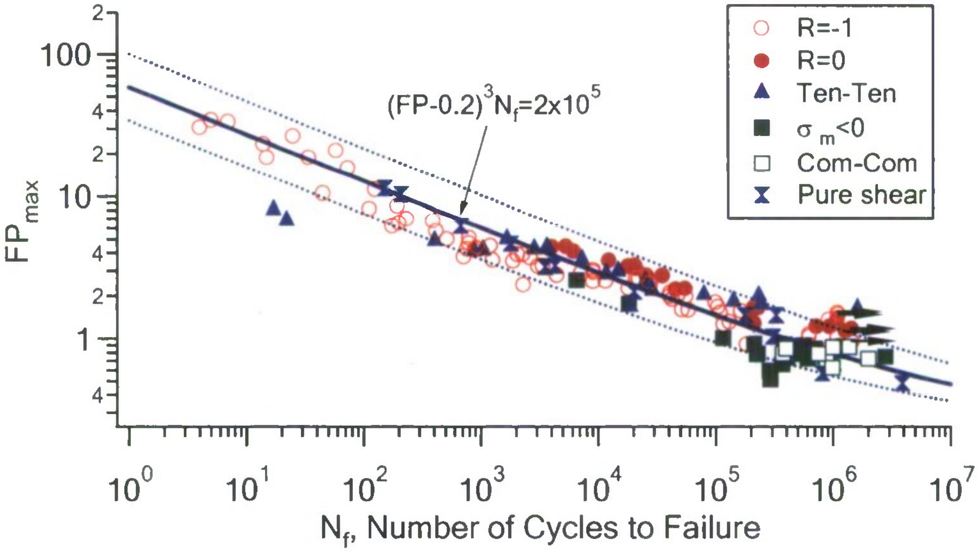

Fig.70 $FP_{\max}$ versus N_f for uniaxial and torsion loading

Figure 70 shows the $FP_{\max}$ - N_f relationship for uniaxial loading and pure torsion. $FP_{\max}$ is the maximum FP value of Eq.(8) with respect to any possible orientations of the material plane. Again, a three-parameter relationship between $FP_{\max}$ and N_f mathematically identical to Eq.(1) is used to best fit the results experimentally obtained under fully reversed tension-compression. As shown in Fig.70, this relationship serves as the baseline for comparison. The dotted lines are factor-of-five boundaries away from the baseline. Clearly, most of the experimental data points are within the factor-of-five boundaries. It should be noted that all the uniaxial experiments including those with high compressive mean stresses and compression-compression loading conditions have been included in Fig.70.

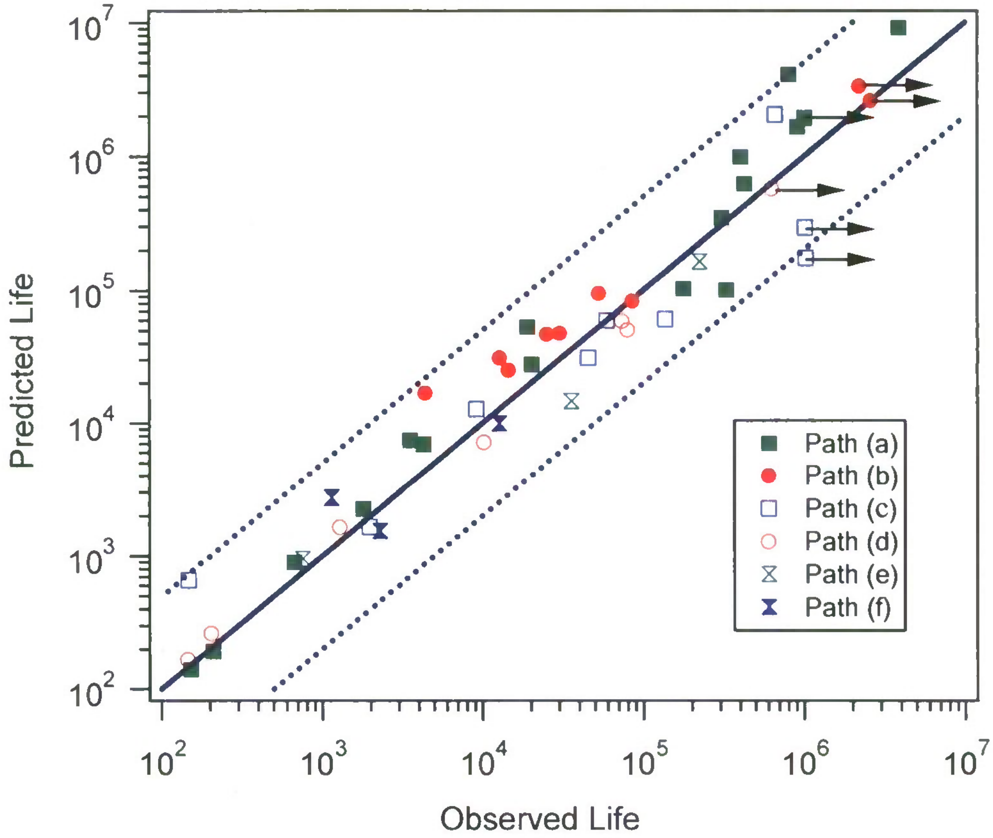

Fig.71 Experimental observations versus predicted life obtained by using the criterion Eq.(8)

Once the material constant b is selected, the critical plane and $FP_{\max}$ for each specimen conducted can be determined. Figure 71 shows the comparison of the predicted fatigue lives and the experimentally observed fatigue lives of the tubular specimens subjected to axial-torsion loading. The stress and strain were obtained experimentally for each specimen. The solid line in Fig.71 signifies a perfect prediction and the two dotted lines are the factor-of-five boundaries. Among the 42 tubular specimens tested with different axial-torsion loading paths, only one specimen is out of the factor-of-five lines.

Figure 72 summarizes the comparison of the observed cracking behavior and the predicted cracking orientations by the modified SWT fatigue criterion. The solid dark dots represent the observed crack orientations in the figure. The range bars in the figure are the predicted ranges of the cracking directions. Again, observations on the experimental cracking behavior were made in the millimeter scale of the crack length. The results shown in Fig.72 reveal that the modified SWT criterion provides cracking direction predictions more satisfactorily than does the SWT criterion. Most of the cracking directions are predicted correctly. Among 42 tubular specimens presented in Fig.72, the cracking directions of 35 specimens (83.3%) were predicted correctly.

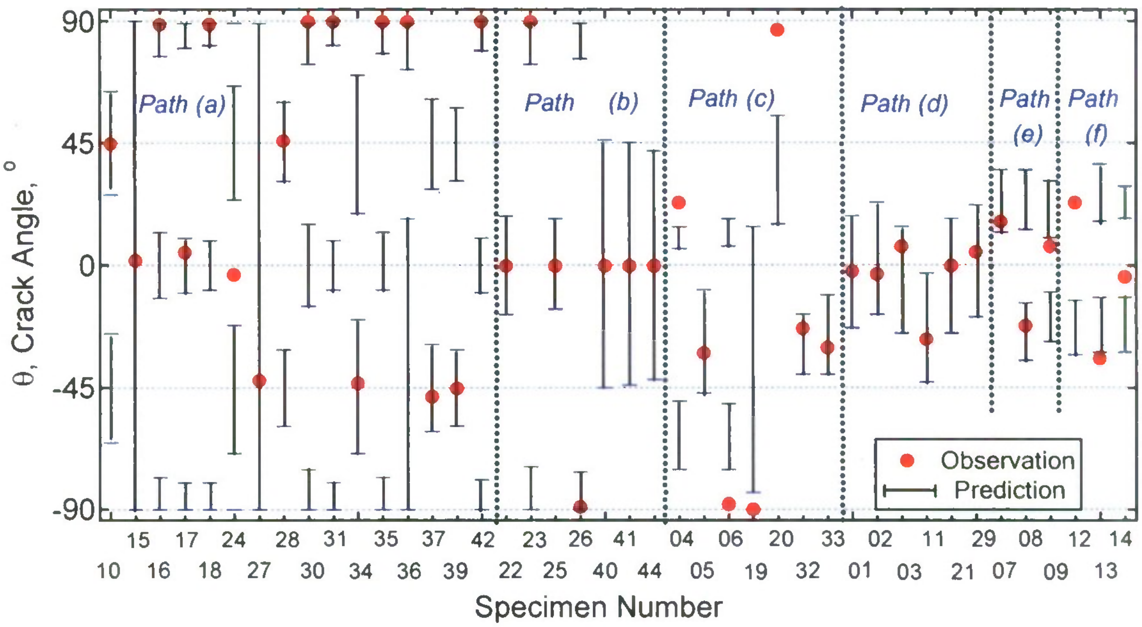

Fig.72 Comparison of the experimentally observed cracking directions with the predictions made by using the modified SWT criterion

It is noted that multiple critical planes can be predicted when using a critical plane approach. Figure 73 shows the predicted *FP* versus the material plane orientation for specimen Tu08. The specimen was subjected to nonproportional loading with a loading path shown in Fig.4(e). The experiment was conducted under the stress-controlled loading condition. The axial stress amplitude was 147.5 MPa and the shear stress amplitude was 86.9 MPa. The observed fatigue life of this specimen was 225,000 cycles. Two peak *FP* values can be identified at "A" and "B," respectively, in Fig.73. As a result, two critical planes are predicted. As shown on the right side picture in Fig.73, the observed cracking orientation is consistent with the critical plane indicated by point "A."

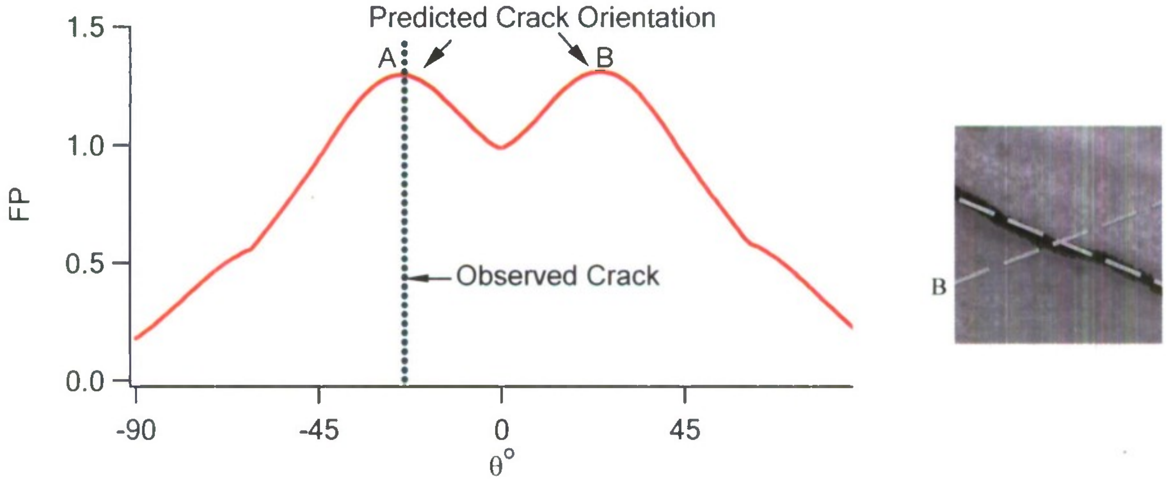

Fig.73 Predicted *FP* as a function of the material plane orientation (Specimen Tu08)

It is possible that a great range of material planes can experience similar fatigue damage. Specimens Tu24 and Tu36 are two special cases where any material planes with their normal perpendicular to the radial direction of the tubular specimen are predicted to experience very similar fatigue damage. As a result, the predicted crack can be on any of these material planes. This is because for these two pure torsion specimens the stress amplitudes are at the level which results in the material constant b being approximately 0.5. It is noted that the fatigue damage is independent of the angle θ when b=0.5.

2.2 *AL6-XN STAINLESSS STEEL*

Figure 74 shows the correlation between fatigue parameters (SWT and FSK parameters) and experimental data from the tension-compression and pure torsion experiments on AL6-XN alloy. It should be mentioned that fitting the fatigue parameter in Fig.74 was done as an average between the tension-compression data and pure torsion data. As was indicated before, the strain-life curve in pure torsion for this material is divided into two parts (Fig.40); one being close to tension-compression curve and one in which fatigue life can be about two times different from the fatigue life in tension-compression with identical strain amplitude. Therefore, such an average fitting was done in order to give a relatively close fatigue life prediction for both parts of the shear *S-N* curve.

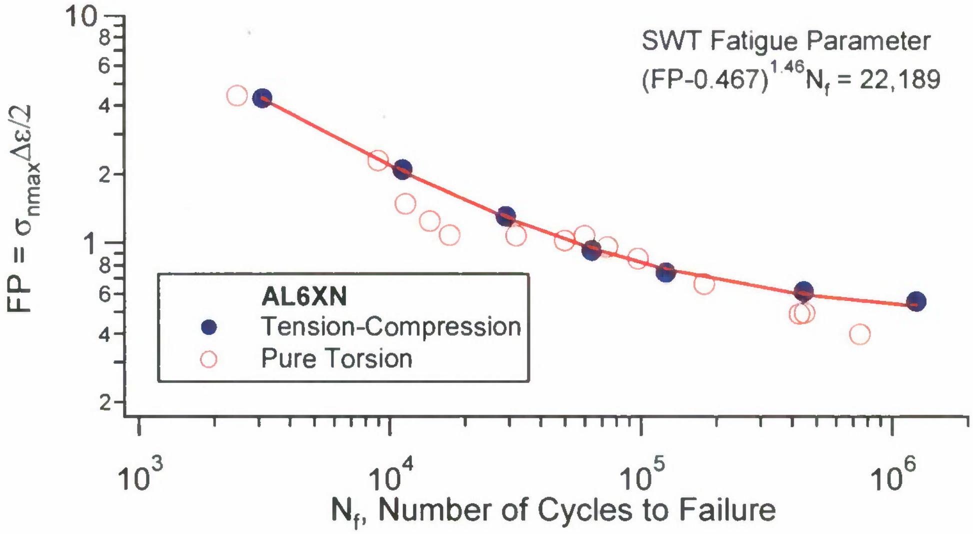

(a)

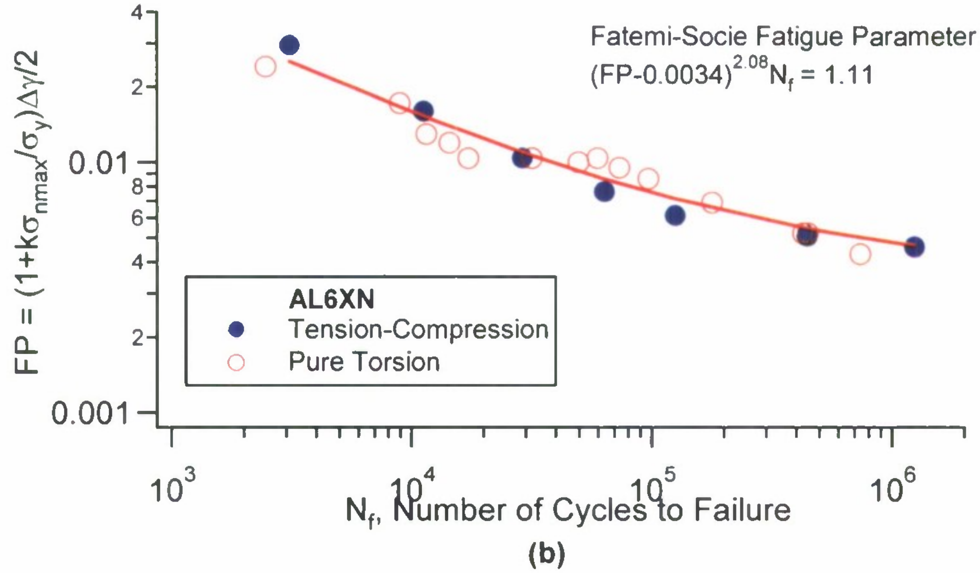

Fig.74 Baseline experimental data correlated using: (a) SWT model and (b) FSK model

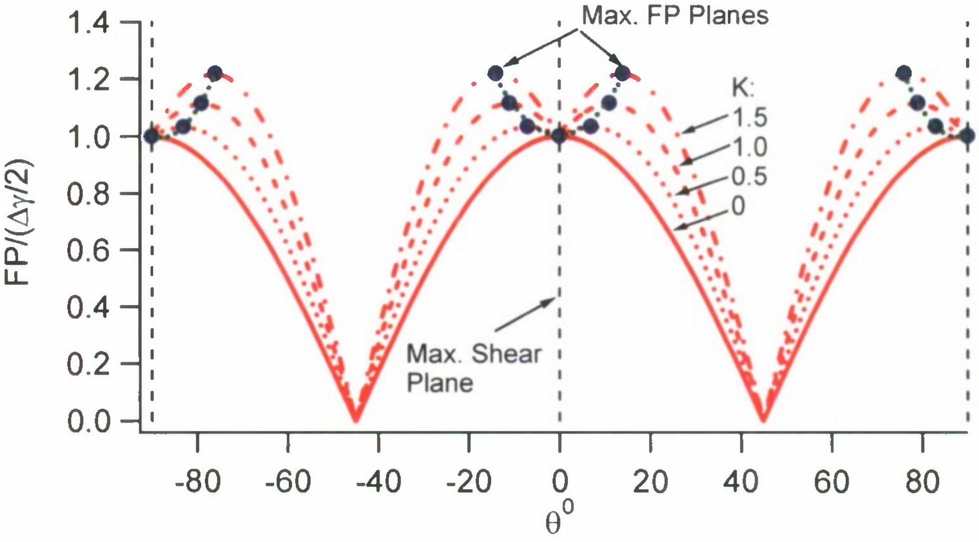

Fig.75 Dependence of FSK fatigue parameter on the orientation of material plane for pure torsion loading

In the original statement of the Fatemi-Socie-Kurath criterion (Eq(9)) the critical plane is the plane of maximum shear strain. In the present investigation, the critical plane is defined as a plane of maximum fatigue parameter (*FP*). The difference in the fatigue life predictions based on the two definitions of the critical planes is minimal for the experiments conducted in the current investigation. However, by defining a critical plane as a plane of maximum damage it is possible to evaluate the range of cracking orientations based on maximum *FP*, as will be discussed later in the report. Figure 75 demonstrates the variation of FSK fatigue parameter normalized with the shear strain amplitude as a function of an angle of material plane orientation for pure torsion loading. The fatigue parameter is plotted for different values of the material constant, K. A yield stress of 380 MPa was used. $K = 0$ corresponds to the original definition of the critical plane orientation. As the value of K is increased, the predicted orientations of critical plane deviate from the maximum shear planes.

The fatigue constant, K, is determined using the experimental data obtained from the tension-compression and torsion experiments. By selecting a value of K, the tension-compression and torsion fatigue data come together and can be fitted with the three-parameter equation, as shown in Fig.74(b). For AL6-XN, it was determined that $K = 1.7$ with the yield stress σ_y=380 MPa. The best fit with three-parameter equation was done as an average between the tension-compression and pure torsion data following the previously described reasons. Using the baseline fit of the fatigue parameter, the fatigue life can be determined for any multiaxial stress state with the help of the stress and strain transformations.

The material constants used in Jiang's model for fatigue life predictions of AL6-XN stainless steel are represented in Table 26. Constants D_0 and m are determined by comparing the results of tension compression tests with the results of fully reversed pure torsion tests. The endurance limit σ_0 is found from the strain-life curve for fully reversed tension-compression tests. The true fracture stress σ_f is found from the monotonic torsion experiment. The detailed description of the procedure of the material constants determination can be found in the corresponding paper [59].

Table 26 Fatigue material constants for AL6-XN steel

m	σ_f (MPa)	σ_0 (MPa)	D_0 (MJ/m^3)
0.6	1,133	300	10,000

According to the classification of cracking behavior given in Fig.64, the material under investigation exhibits mixed cracking under high stress amplitudes and shows tensile cracking in the high cycle fatigue regime. Therefore, the constant b in Jiang's model must be a function of stress amplitude. The stress amplitude corresponding to the transition between the two cracking modes is estimated from the experimental data to be 360 MPa and the value of b corresponding to this point must be equal to 0.5. The following function of the cracking orientation parameter was constructed based on experimental observations

$$b(\sigma_{mr}) = 0.35 + 5.355e^{-0.0102\sigma_{mr}} \tag{13}$$

where σ_{mr} equals to the maximum stress in the loading cycle.

For many materials, the fatigue damage reaches the stable value after a few loading cycles and the choice of a stable stress-strain response is rather straightforward. Due to the cyclic softening (Fig.37) of the AL6-XN material, the selection of the stable hysteresis loop is somewhat ambiguous. For all the specimens tested the fatigue life prediction is made based on the hysteresis loops taken at 80% of fatigue life of the specimen. This rule was impelled by the fact, that the stress amplitudes corresponding to 80% of fatigue life when placed on the cyclic stress-strain curve follow the curve produced by the incremental step tests (Fig.38).

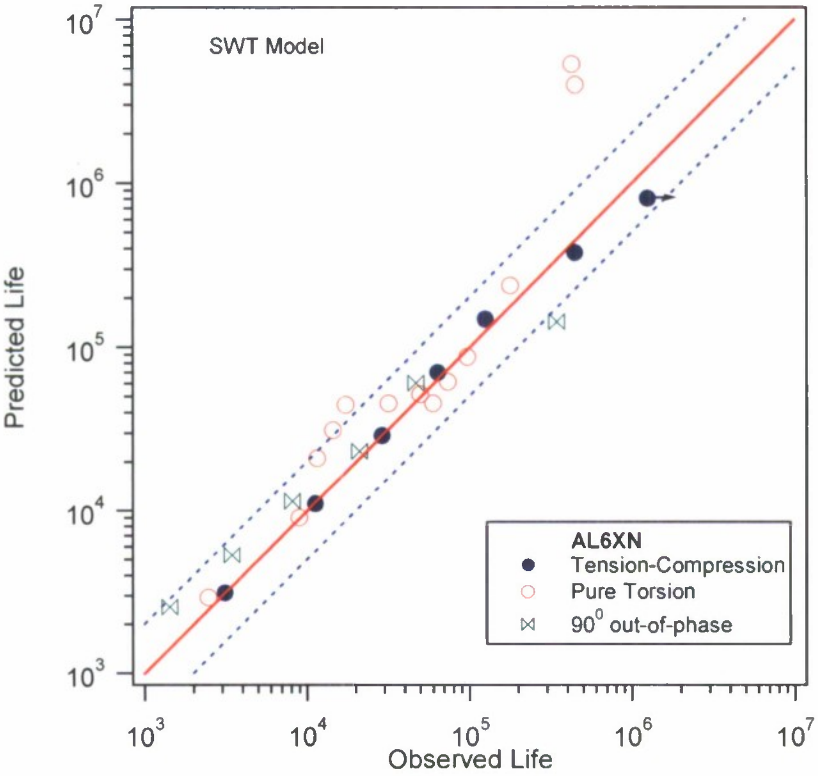
SWT Model
Predicted Life
Observed Life
10^3
10^4
10^5
10^6
10^7
AL6XN
● Tension-Compression
○ Pure Torsion
⋈ 90^0 out-of-phase

(a)

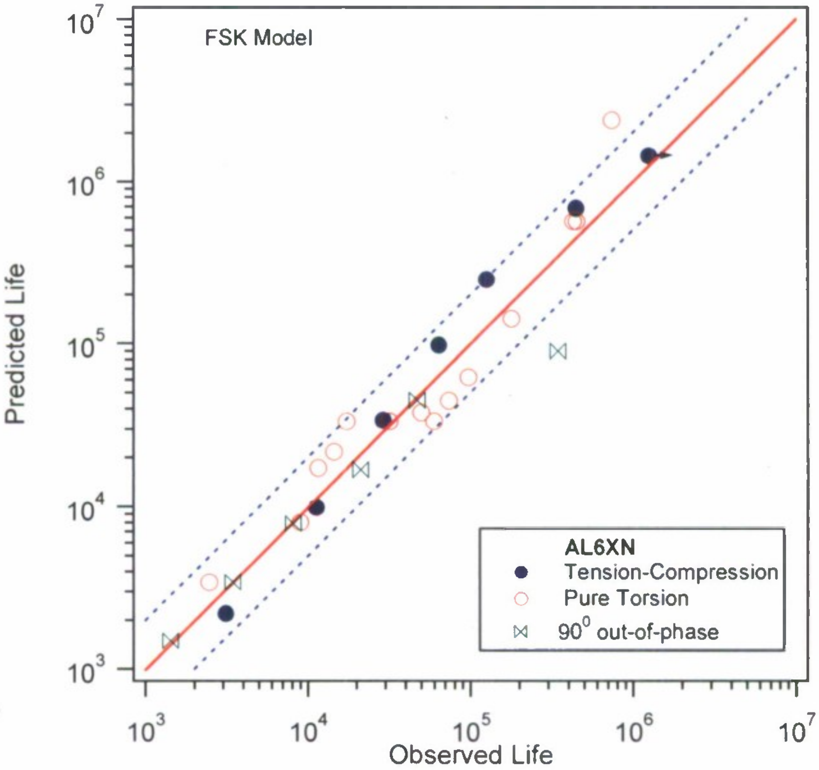
FSK Model
Predicted Life
Observed Life
10^3
10^4
10^5
10^6
10^7
AL6XN
● Tension-Compression
○ Pure Torsion
⋈ 90^0 out-of-phase

(b)

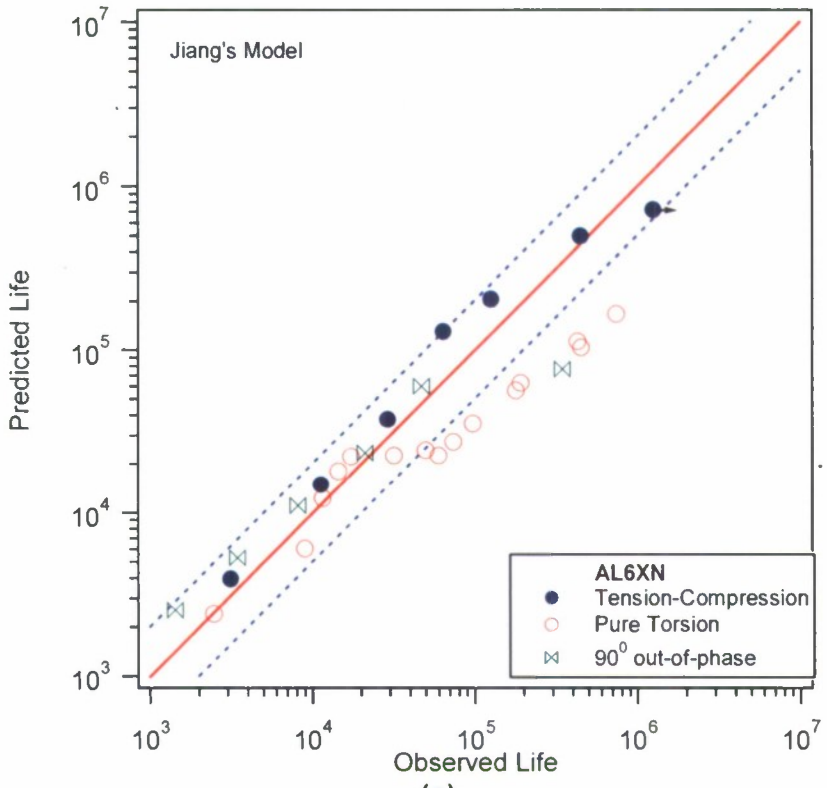

(c)

Fig.76 Fatigue life prediction of AL6-XN steel based on: (a) SWT model; (b) FSK model; (c) Jiang's model

The predictions based on three abovementioned fatigue models are shown in Fig.76. The solid lines on the plots in Fig.76 represent perfect correlation between experimentally observed and predicted fatigue lives. The dashed lines show the boundaries of factor of two difference between observed and predicted lives. An arrow next to the data point indicates that the specimen did not fail at the end of the test. It can be seen from Fig.76 that all of the three models predict the fatigue life of the AL6-XN steel reasonably well with probably the best prediction being made when using Fatemie-Socie-Kurath (FSK) fatigue parameter (Fig.76(b)).

AL6-XN alloy is a material in which cracking behavior is a function of applied loading amplitude. The orientation of a fatigue crack is defined as an angle formed between the normal to the cracking plane and the vertical axis (the centerline of the specimen). In fully reversed tension-compression tests, the material develops 0^0 oriented cracks within the whole range of applied strain amplitudes. The same is true for non-proportional 90^0 out-of-phase loading. The difference in cracking orientation as a function of stress level is revealed when material is tested in pure torsion (Section 3.2.4, Fig.41). The strain-life curve under pure torsion can be divided in two regions, associating with different cracking modes – mixed cracking in the region where equivalent strain amplitude is higher than 0.6% and tensile cracking in the region where $\Delta\varepsilon_{eq}/2 \leq 0.6\%$. In other words, when the specimen is tested under pure torsion, the critical planes in the first region can be associated with the planes of maximum shear, while the cracking occurs along the planes with maximum normal stresses in the second region. Therefore, the way the critical plane is defined as a part of fatigue model is especially important for this material.

Two fatigue models considered here (SWT and FSK models) are designed to target a single particular cracking mode. The SWT model postulates that the critical plane is a plane with the maximum normal strain amplitude. Within the FSK fatigue model, the critical plane is predicted as a plane with maximum shear strain. Therefore the FSK model predicts shear crack growth. When these models are used to predict cracking behavior of AL6-XN material tested in pure torsion, they can accurately describe cracking orientation only for particular part of the strain-life curve. Thus SWT parameter can describe correctly only the part of the curve where tensile cracks are developed, while FSK model correctly predicts cracking in the region where higher strain amplitudes are applied (the critical planes are oriented either at 0 degree or 90 degree).

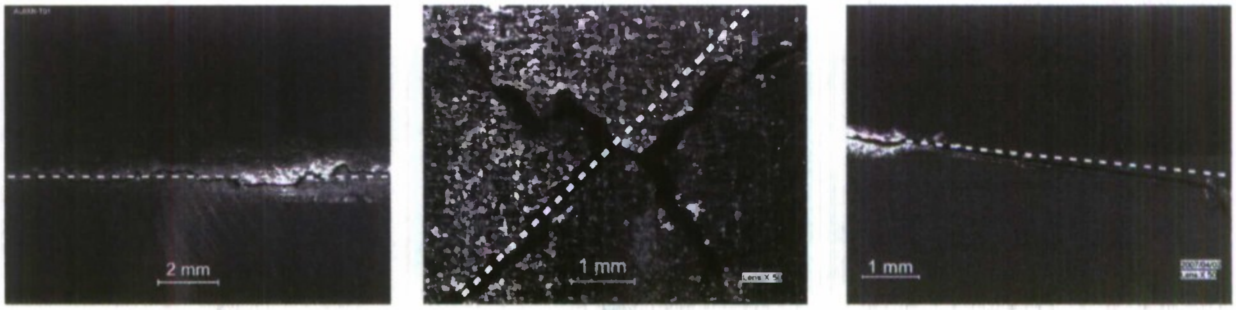

(a) **(b)** **(c)**

Fig.77 Prediction of cracking orientation using Jiang's model: (a) pure torsion $\Delta\varepsilon_{eq}/2 = 0.69\%$ **; (b) pure torsion** $\Delta\varepsilon_{eq}/2 = 0.50\%$ **; (c) 90^0 out-of-phase** $\Delta\varepsilon_{eq}/2 = 0.32\%$

In Jiang's model, the critical plane is defined as a material plane with the maximum fatigue damage. The accumulation of fatigue damage is a result of plastic deformation, i.e. is a function of plastic strain energy which consists of parts representing shear and normal components on a material plane (Eq.(10)). The interplay between those shear and normal terms is described by the parameter b and the choice of this parameter serves to predict the cracking orientation. Since the cracking behavior of this material depends on the loading conditions, the parameter b is represented as a function of a stress amplitude (Eq.(13)). With such a formulation, the model predicts the orientation of fatigue cracks with good accuracy which can be seen in Fig. 77.

The dashed lines on the photographs in Fig.77 represent the cracking planes predicted by Jiang's model. Three cases are depicted, with two of them representing pure torsion and one representing non-proportional axial-torsion loading. The pure torsion fatigue cracks represent two regions of the strain-life curve: one showing the mixed cracking mode (Fig.77 (a)) and one showing tensile cracking mode (Fig.77 (b)). It should be noted, that under non-proportional load the fatal cracks are not oriented exactly at 0 degrees but rather tilted slightly. The prediction based on Jiang's model with the choice of parameter b represented by the Eq.(10) can depict this situation (the predicted angle is 6^0).

Figure 78 is the comparison between the experimentally observed cracking orientations and the angles predicted by the three models. The markers in Fig.78 represent the experimentally measured orientation of the fatigue cracks. The vertical lines represent the range of 10% from the maximum damage plane prediction by the fatigue model. The dots within the range bars represent the points corresponding to the maximum value of fatigue damage. The choice of 10% range was not based on any physical considerations and was introduced to consider the range of material planes that may experience similar fatigue damage following a given multiaxial fatigue criterion. It should be noted that in some cases the fatigue criterion gives two ranges with maximum values of the fatigue parameter and therefore, two possible orientations of the critical plane are predicted. The plots are divided by thick dotted lines into two parts corresponding to the 90^0 out-of-phase axial-torsion experiments and pure torsion experiments, respectively.

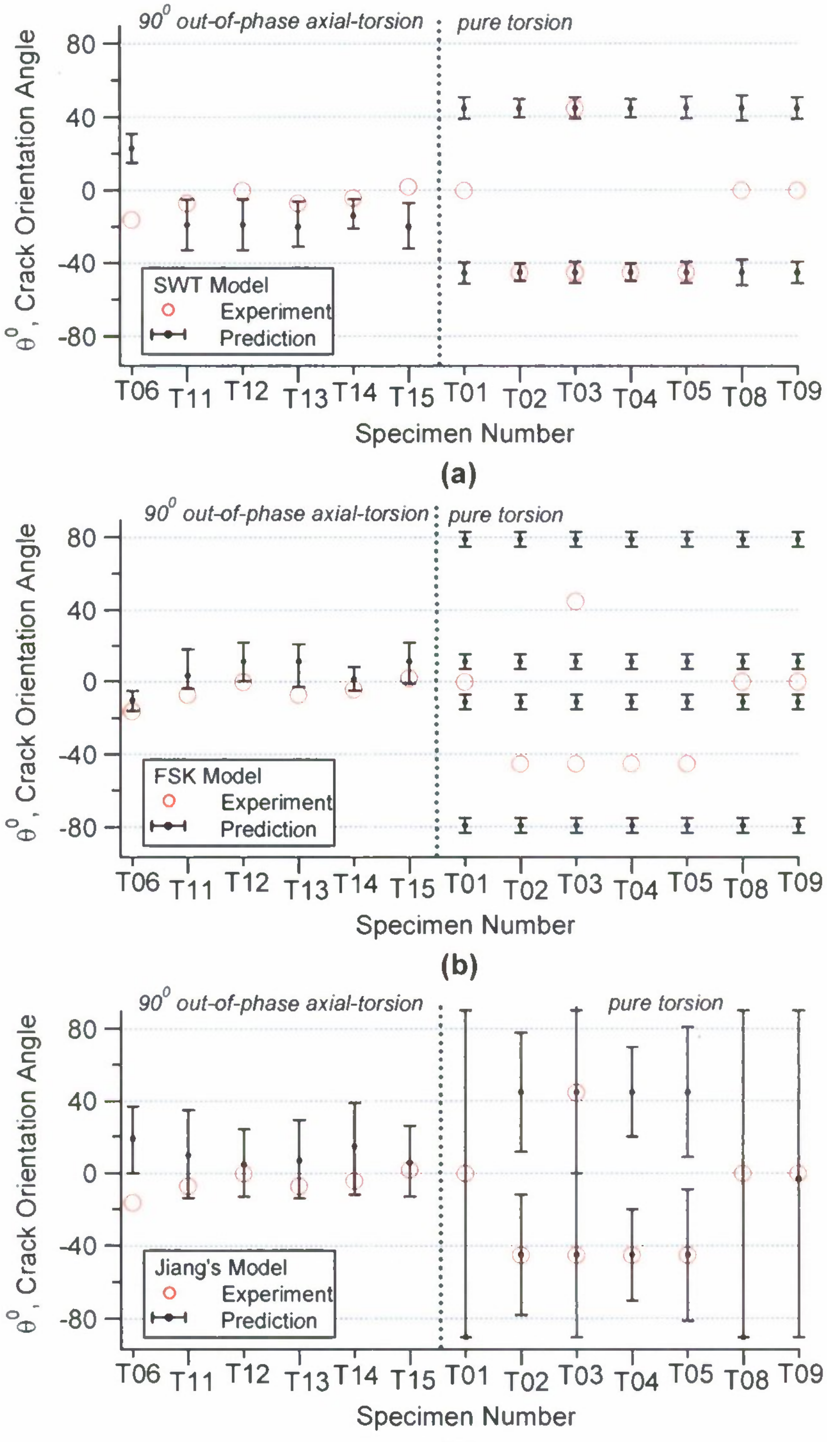

(a)

(b)

(c)

Fig.78 Comparison between observed and predicted orientations of fatigue cracks based on: a) SWT model; b) FSK model and c) Jiang model

It can be seen that when 90^0 out-of-phase axial-torsion cracking behavior is considered, all of the models under consideration predict cracking angles close to zero degrees, which is in agreement with experimental observations. In the case of pure torsion experiments, however, the predicted orientation based on the SWT criterion is always 45°, i.e., it corresponds to the tensile cracking. At the same time, it can be seen from Fig. 78 that the FSK model predicts cracking orientation close to zero or 90 degree for the torsion cases, which corresponds to shear cracking mode. In other words, the SWT and FSK models can make a close prediction of cracking orientation only for a part of strain-life curve (Fig.39). Due to the fact that the cracking orientation in the Jiang criterion is modeled through the parameter b, which in turn is a function of equivalent stress (Eq.(13)), the cracking behavior of the material in pure torsion can be predicted with considerably good accuracy (Fig.78).

3 CRACK GROWTH MODELING

3.1 *CONSTANT AMPLITUDE LOADING*

A number of equations have been developed to describe the sigmoidal da/dN - ΔK relationship in the past 50 years. Since the fatigue crack growth rate is mainly controlled by the stress intensity factor range, ΔK, and the maximum stress intensity factor, $K_{\max}$, Vasudevan, Sadananda and co-workers [61-66] developed a two-parameter unified approach for the fatigue crack growth description. Kujawski [67,68] proposed a two-parameter model combining ΔK and $K_{\max}$ to form the crack driving force. The driving force does not invoke disputable and non-repeatable crack closure data. Instead, it is determined using the positive part of the range of the applied stress intensity factor, ΔK^+, and the corresponding maximum value, $K_{\max}$. It unifies the overall crack rate prediction methodology regarding the load ratio effects for both the long- and short-crack growth behavior. The two-parameter driving force parameter yields a fairly good correlation with the experiments with regard to the R-ratio effect and the threshold conditions for a number of engineering materials. Considering that the compressive external load has minimal contribution to the fatigue crack growth, the fatigue driving force, κ, proposed by Kujawski [67,68] can be expressed as,

$$\kappa = (K_{\max})^{\alpha} (\Delta K^{+})^{1-\alpha} \tag{14}$$

where $K_{\max}$ is the maximum stress intensity factor in a loading cycle, ΔK^+ is the positive part of the range of the stress intensity factor, and α is a material constant. For a positive R-ratio, the fatigue driving force proposed by Kujawski [67,68] is mathematically identical to the effective stress intensity factor proposed by Walker [69]. For a number of engineering materials, Eq. (14) can model the R-ratio effect well for both short- and large-crack growth [67]. For aluminum alloys tested in ambient environment, α was found to be $\alpha \cong 0.5$ [68].

For the three materials in the current study, it is found that the relationship between da/dN and κ follows Paris type power law for a wide range of κ in Region II,

$$da/dN = C\kappa^{n} \tag{15}$$

where C and n are material constants.

3.2 *MODELING OF OVERLAODING EFFECT*

Traditionally, the Wheeler's model [70] is used to consider the overloading effect due to its simplicity. The Wheeler's model can be expressed as,

$$da/dN = \phi_R C^{'}(\Delta K)^n \tag{16}$$

where ΔK is the stress intensity factor range, ϕ_R is a correction factor to consider the overloading effect, and $C^{'}$ is a constant dependent on stress ratio. It is clear that ϕ_R=1 is for constant amplitude loading. Considering that the two-parameter fatigue driving force (Eq. (14)) correlates the crack growth rate at different stress ratios very well, it is reasonable to adopt the following formula to consider the overloading effect,

$$da/dN = \phi_R C \kappa^n \tag{17}$$

where κ is the two-parameter fatigue driving force defined by Eq. (14) and C is a material constant *independent of stress ratio*. Compared to Eq. (16), the advantage of using Eq. (17) is apparent. The parameters C and n in Eq.(17) are independent of the stress ratio. Therefore, Eq.(17) is convenient to use. It is also promising to use Eq. (17) to deal with the crack growth rate in a complex loading history, as long as the correction factor (ϕ_R) can be appropriately determined.

In the traditional Wheeler's model [70], ϕ_R is defined as,

$$\phi_R = \begin{cases} \left[\dfrac{r_{pi}}{a_{OL} + r_{p,OL} - a_i} \right]^m, & a_i + r_{pi} \le a_{OL} + r_{p,OL} \\ 1, & a_i + r_{pi} \ge a_{OL} + r_{p,OL} \end{cases} \tag{18}$$

where a_i represents the current crack length at the ith loading cycle, r_{pi} denotes the current plastic zone size due to the ith loading cycle, a_{OL} is the crack length at which the overload was applied, $r_{p,OL}$ is the plastic zone created by the overload, and m is the Wheeler's empirically adjustable shaping exponent which can be simply taken as the value that best fits the data. Typical value for Wheeler's shaping exponent, m, ranges from 1 to 3. According to Wheeler [70], the crack growth retardation will occur as long as the current plastic zone lies within the plastic zone created by the overload. As soon as the boundary of the current plastic zone reaches the boundary of the plastic zone created by the overload, the crack growth retardation will cease (i.e., ϕ_R=1). A graphical explanation of the parameters used in Wheeler model is shown in Fig.79.

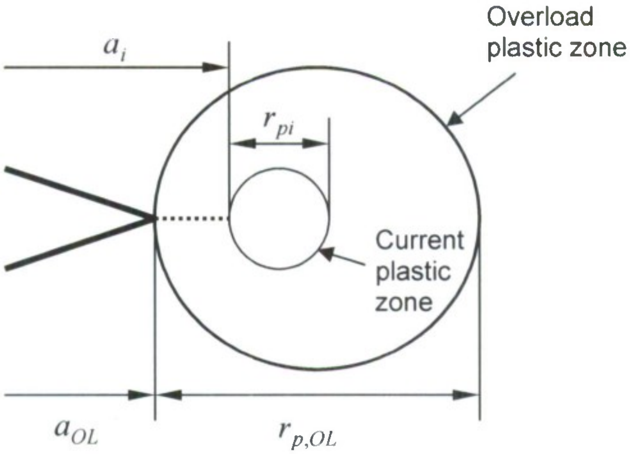

Fig.79 Schematic representation of the parameters used in the Wheeler model

The plastic zone sizes in Eq. (18) are often calculated by using Irwin's method [71]. The plastic zone diameter under cyclic loading is estimated as [72],

$$r_{pi} = \frac{1}{\beta\pi}\left(\frac{\Delta K_i}{2\sigma_y}\right)^2 \tag{19}$$

while the monotonic overload plastic zone size is calculated as [73],

$$r_{p,OL} = \frac{1}{\beta\pi}\left(\frac{K_{OL}}{\sigma_y}\right)^2 \tag{20}$$

In Eqs. (19) and (20), β=1 and 3 for plane stress and plane strain conditions, respectively. ΔK_i is the stress intensity factor range at the ith loading cycle and K_{OL} is the stress intensity factor corresponding to the overload. σ_y is the yield stress of the material. In the current investigation, the thickness of specimens is less than 5 mm and plane stress conditions are expected to prevail. Therefore β=1 is used in Eqs. (19) and (20). For 7075-T651 aluminum alloy under consideration, the yield stress (σ_y) is estimated to be 420.3 MPa. For SS304 and AL6-XN stainless steels, σ_y are estimated to be 340 MPa and 420 MPa, respectively.

A prediction of the crack growth rate after overloading using Eq. (18) is shown in Fig. 80 for different materials. The following values of constants in Wheeler's model were used (Table 27)

Table 27 Constants in Wheeler's model

Material	7075-T651	AL6-XN	AISI 304L
m	1.056	1.200	0.720
σ_y, MPa	420.3	420	340

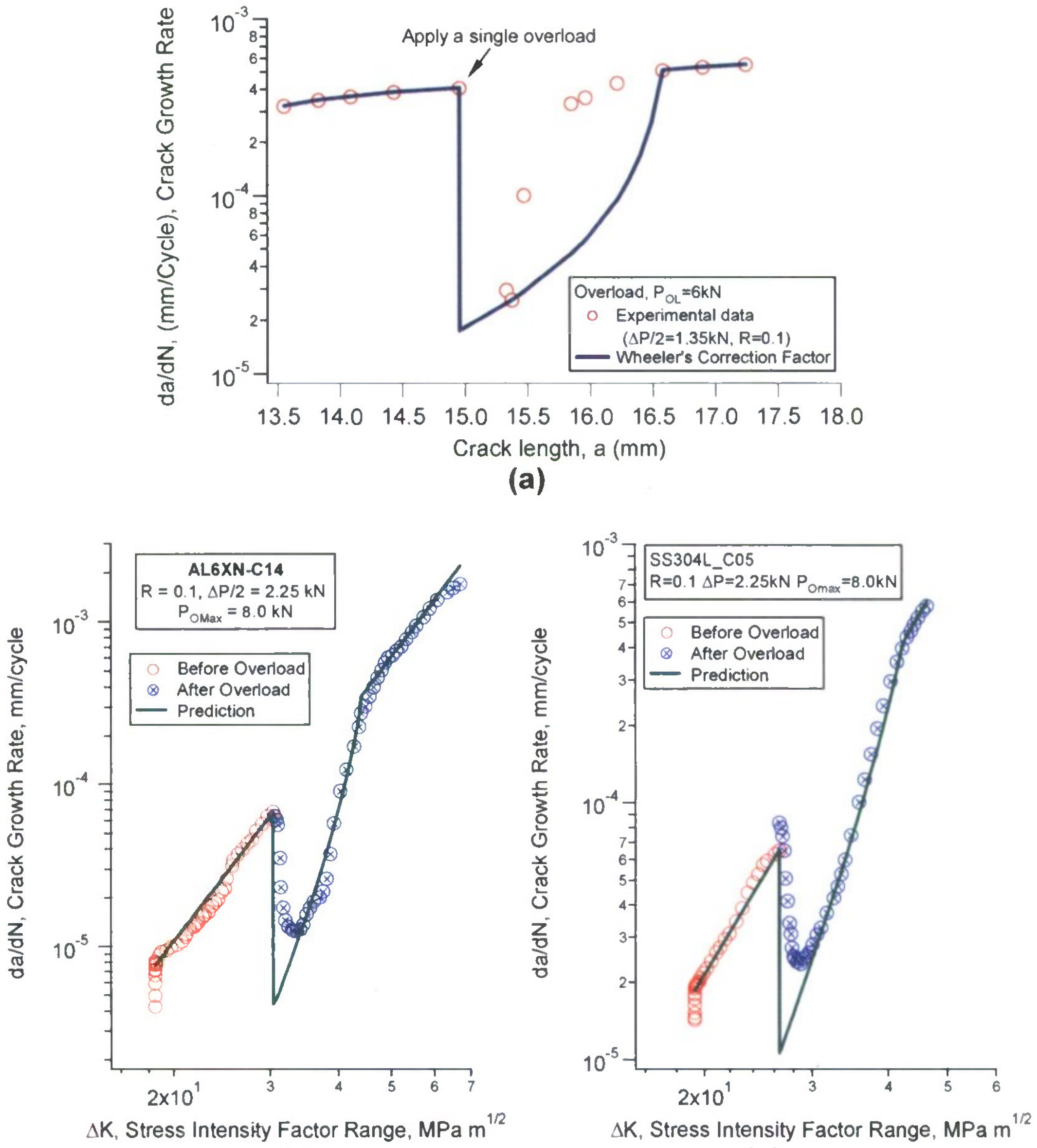

(a)

(b)

(c)

Fig.80 Predictions of crack growth rate after overloading using Eq. (17): (a) 7075-T651; (b) AL6-XN; (c) AISI 304L

It can be seen from Fig.80, that an accurate prediction of post-overload behavior based on Wheeler's correction factor cannot be achieved for either of the materials. The worst prediction occurs in case of 7075-T651 aluminum alloy (Fig.80(a)), where the predicted growth rate curve differs significantly from the experimentally observed one. When adopting Wheeler's correction factor for 7075-T651 alloy, the post-overload predicted curve increases slowly at first and then increases rapidly until it resumes the normal crack growth rate. However, the experimental results indicate that once the minimum growth rate after overloading is reached, the growth rate increase sharply and then asymptotically approaches the normal rate. In case of two stainless steels under consideration, the overall behavior is predicted rather well (Fig.80(b) and (c)). However, the model predicts a much lower stationary point of the crack growth rate after the application of overload. The material constants can be adjusted to fit the point well with the lowest crack growth rate in Fig.80. However, such a change will alter the prediction of the crack growth rate within the overload influencing zone through a shift-up of the prediction. In this way, the predicted crack growth in the rest of the overload influencing zone will be higher than the experimental data. In addition, the Wheeler's correction factor cannot predict the phenomenon of crack growth acceleration which can be observed immediately after overload in AISI 304L stainless steel (Fig.80(c)).

It is clear that the Wheeler's factor cannot predict correctly the details of the crack growth after overloading. It is necessary to make a modification to Wheeler's correction factor in order to give a better prediction of the crack growth in the retardation zone. In order to capture the post-overload behavior better, the modifications to the original Wheeler's model were proposed for each material. These modifications are discussed in detail in the subsequent sections corresponding to each of the materials under investigation.

4 APPICATION OF CRACK GROWTH RATE MODELING

4.1 *7075-T651 ALUMINUM ALLOY*

The consideration of the R-ratio effect using Eq.(14) with α =0.35 is shown in Fig. 81 for the aluminum alloy tested under constant amplitude loading. Except for R =0.75, a good correlation is achieved for the constant amplitude loading with different R-ratios. The model especially works well in Region II. Fitting the experimental data in Region II in Fig. 81 by Eq. (15) using the least-squares method gives $C = 6.0\times10^{-8}$ and $n = 3.32$.

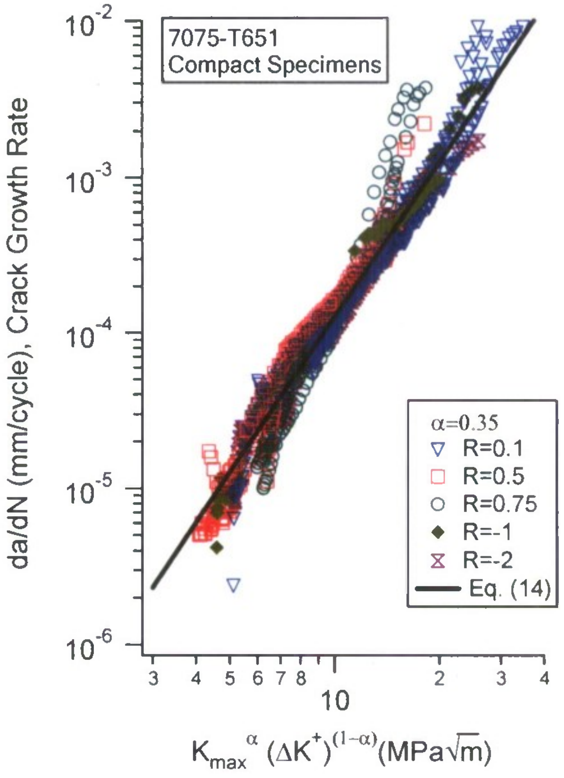

Fig.81 Constant amplitude crack propagation with the effect of the R -ratio using Eq.(14)

Modeling of crack growth behavior under variable amplitude loading was done based on the correction parameter introduced in Paris law. The form of correction factor proposed by Wheeler did not yield satisfactory predictions, as was shown above (Fig.80). In the current investigation, the correction factor, ϕ_R, is modified and defined with the following form,

$$\phi_R = \left(\frac{r_{pi}}{r_{pmr}} \right)^m \tag{21}$$

where r_{pi} denotes the current plastic zone size and r_{pmr} represents the effective residual plastic zone size with the combined consideration of overloading and the crack propagation. Immediately after the overloading, r_{pmr} reaches its maximum value to reflect the instantaneous effect of overloading. During the subsequent crack propagation, r_{pmr} reduces rapidly until it recovers to the value of the current plastic zone size. r_{pmr} should satisfy the following conditions: when $a_i = a_{OL}$, $r_{pmr} = r_{pOL}$; when $a_i = a_R$, $r_{pmr} = r_{pi}$, where a_R presents the crack length at which the crack growth rate resumes to its stable level of the constant amplitude loading. Considering the trend of the crack growth rate in the transient zone, many expressions can be chosen, such as,

$$\left(\frac{a_i - a_{OL}}{a_R - a_{OL}} \right)^p + \left(\frac{r_{pmr} - r_{pi}}{r_{pOL} - r_{pi}} \right)^p = 1 \tag{22}$$

and,

$$r_{pmr} = r_{pi} + (r_{pOL} - r_{pi}) \left[\exp\left(-\frac{a_i - a_{OL}}{a_R - a_i} \right) \right]^p \tag{23}$$

The two expressions give very close results. In the current investigation, Eq. (23) is employed.

The value of a_R in Eq. (23) can be estimated by,

$$a_R = a_{OL} + r_{p,OL} - r_{pR} \tag{24}$$

where r_{pR} represents the plastic zone size at the crack length of a_R and can be determined by using Eq. (19), *i.e.*,

$$r_{pR} = \frac{1}{\beta\pi} \left(\frac{\Delta K_R}{2\sigma_y} \right)^2 \tag{25}$$

ΔK_R is the stress intensity factor range at the crack length of a_R and can be calculated by using Eqs. (3~5). It is clear that r_{pR} in Eq. (24) in turn is a function of a_R. By using the iteration method, the value of a_R can be easily determined. The estimated transient zone size ($a_R - a_{OL}$) agrees with experimentally measured values very well.

It should be mentioned that different materials exhibit different fatigue cracking behavior in the transient zone after the application of an overload. The specific expression of ϕ_R in Eq. (18) depends on the material. In the current investigation, Eq. (23) is used for 7075-T651 aluminum alloy. In the traditional Wheeler's model (Eqs. (17) and (18)), the parameter m in Eq. (18) is dependent on the stress ratio and the overload ratio [73]. In the proposed model, the stress ratio effect is incorporated into the two-parameter fatigue driving force (Eq. (14) and Eq. (17)). It is highly possible that parameter m in Eqs. (18) and (21) and parameter p in Eqs. (22) and (23) are independent of stress ratio when using Eq. (17) to predict the crack growth rate after overloading. In the primary examination on the application of the proposed model, the parameter m in Eqs. (18) and (21) and the parameter p in Eq (23) are simply assumed to be constants that best fit the experimental data.

According to the proposed correction factor in Eq. (21), the minimum value of the crack growth rate occurs immediately after overloading or switching the loading amplitude from a higher value to a lower value. The crack growth rate increases sharply with the crack propagation. When the crack approaches the boundary of the transient zone, the crack growth rate slows down and gradually resumes to the normal level under constant amplitude loading. Compared to the Wheeler's correction factor, the modified correction factor can predict qualitatively the details of the crack growth within the retardation zone.

The fatigue crack growth results predicted by using Eqs (14~15), (17), (19~21) and (23~25) are shown in solid lines in Figs.16 and 18 for the specimens subjected to the overloading and high-low sequential loading conditions. For the retardation zone of the crack growth rate after overloading or after switching the loading amplitude to a lower value, Eqs. (17), (19~21) and (23~25) are employed to predict the crack growth rate. The value of m in Eq. (21) and the value of p in Eq. (23) are adjusted to best fit the experimental data of specimen 90_C16. The fitting result gives that $m = 2.6$ and $p = 5.3$. The same values of m and p are applied to the predictions of the other three overloading and high-low sequential loading specimens. The normal crack growth rates before and after the retardation zone are calculated using Eq. (15). The proposed model can predict the crack growth well for the influence of overloading and high-low sequence loading.

4.2 *AISI 304L STAINLESS STEEL*

The crack growth rate versus fatigue driving force defined in Eq. (14) under constant amplitude loading is shown in Fig. 82. A good correlation between crack growth rate and stress ratio can be achieved with constant $\alpha = 0.36$ for the tests under constant amplitude loading with different R-ratios. In region of stable growth the relationship between the crack growth rate and fatigue driving force can be expressed by Eq. (15) with constants $C = 1.25 \times 10^{-10}$ and $n = 3.97$.

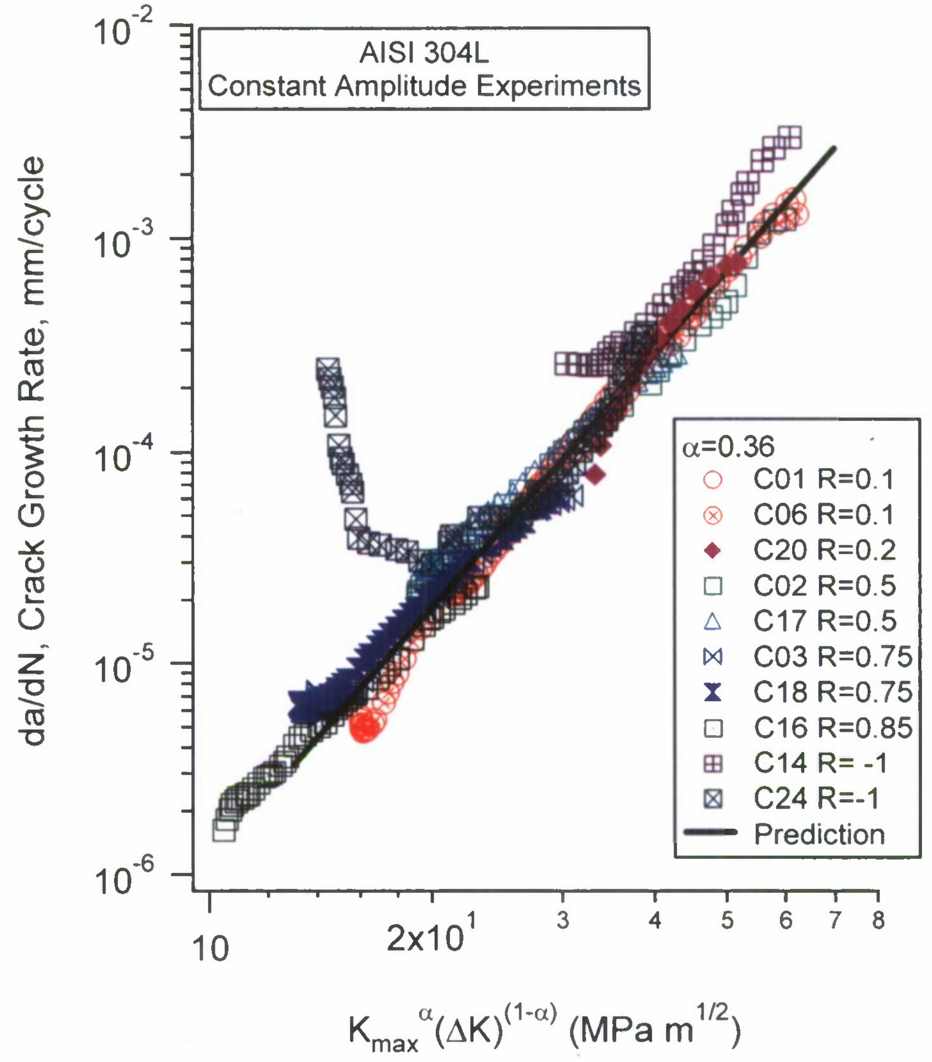

Fig.82 Constant amplitude crack propagation

Modeling of crack propagation behavior under variable amplitude loading was done based on the modification of Wheeler's approach. Since in the original formulation the model targets the crack growth rate retardation after the application of an overload, it cannot predict a period of acceleration in crack growth upon overloading, a phenomenon observed in the material under investigation (Fig.80(c)). Furthermore, the original Wheeler model postulates that the minimum point in crack growth will be reached immediately after overloading, which is true for some materials [74] but it is not the case for other metallic alloys [75]. In order to overcome this drawback of the original Wheeler's model, Yuen and Taheri [51] added two correction factors to Wheeler's model in the following form,

$$da/dN = \phi_R \phi_D C(\Delta K_{acc})^n \tag{26}$$

where ϕ_R and ϕ_D are two parameters introduced to model the retardation and delayed-retardation growth, respectively. C and n are the constants in the Paris law for stable crack growth. ΔK_{acc}

is so-called accelerated stress intensity factor range that will be defined. For stable crack growth, $\phi_R = 1$, $\phi_D = 1$, and $\Delta K_{acc} \equiv \Delta K$.

The retardation factor ϕ_R is identical to the one in Wheeler's model (Eq.(18)). The delay retardation parameter ϕ_D introduced in Eq.(26) is defined as,

$$\phi_D = \left[\frac{a_{OL} + r_{D,OL} - a_i}{r_{p,i}} \right]^{m^*} \quad \text{if } a_i + r_{p,i} < a_{OL} + r_{D,OL} \tag{27}$$

where m^* is an additional shaping exponent and $r_{D,OL}$ denotes the size of the overload effective delay zone which is related to $r_{p,OL}$ by $r_{D,OL} = \xi \cdot r_{p,OL}$, where ξ is an experimentally based fitting constant.

The sizes of plastic zones in the plane stress condition can be determined following Irwin's method (Eqs(19 and 20)). The accelerated stress intensity factor range, ΔK_{acc}, is defined as,

$$\Delta K_{acc} = \Delta K_i + (\Delta K_{OL} - \Delta K_i) \cdot \left(1 - \frac{r_{p,i}}{a_{OL} + r_{D,OL} - a_i} \right)^{m^*} \quad \text{if } a_i + r_{p,i} < a_{OL} + r_{D,OL} \tag{28}$$

The fitting constants employed in the modified Wheeler's model for AISI 304L stainless steel are: m=0.72, m^*=1.0, ξ=0.2, and σ_y=340 MPa. These constants were obtained by best fitting the experimental data obtained from specimen C05.

The modified Wheeler's model described above was applied to the cases when a single overload was introduced into the constant-amplitude loading history. The results are shown in Fig. 83 together with the experimental results. It can be seen that the model is capable of predicting the general features of the post-overloading behavior of 304L steel. However, the model over predicts the magnitude of crack growth retardation after the application of an overload for the low overload ratio case (Fig. 83(a)). At the same time, the model over-predicts the crack growth acceleration after overloading for the cases with higher overload ratios (Fig. 83(c) and Fig. 83(d)).

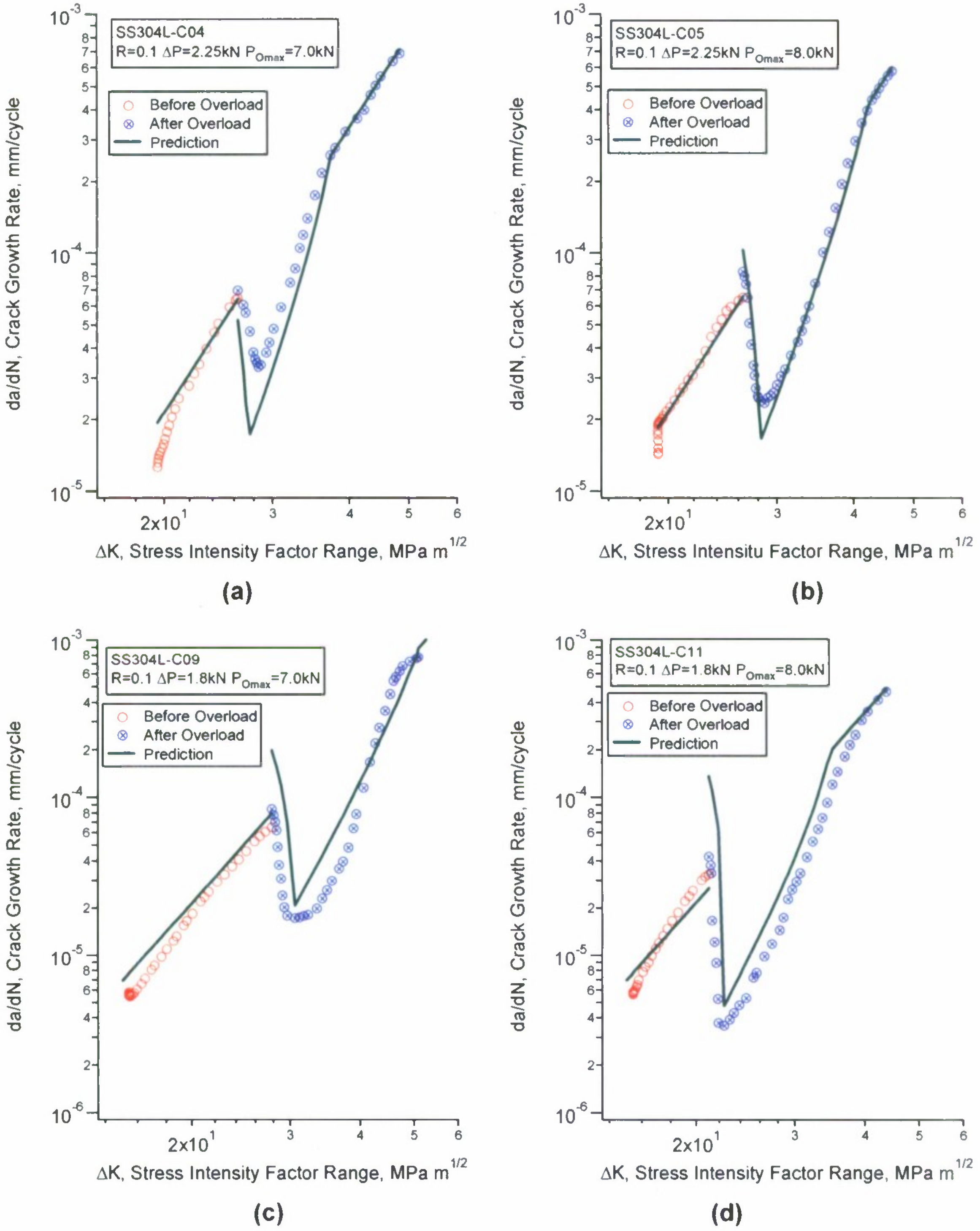

Fig.83 Prediction of crack growth behavior in single overload experiments based on modified Wheeler's model

A comparison between predictions based on the modified Wheeler's model and the experimental data for the two-step loading histories is shown in Fig. 84. The model predicts the crack growth behavior under high-low loading sequence reasonably well. It is noticed that the model is capable of distinguishing the differences of the three loading situations depicted in Fig.84.

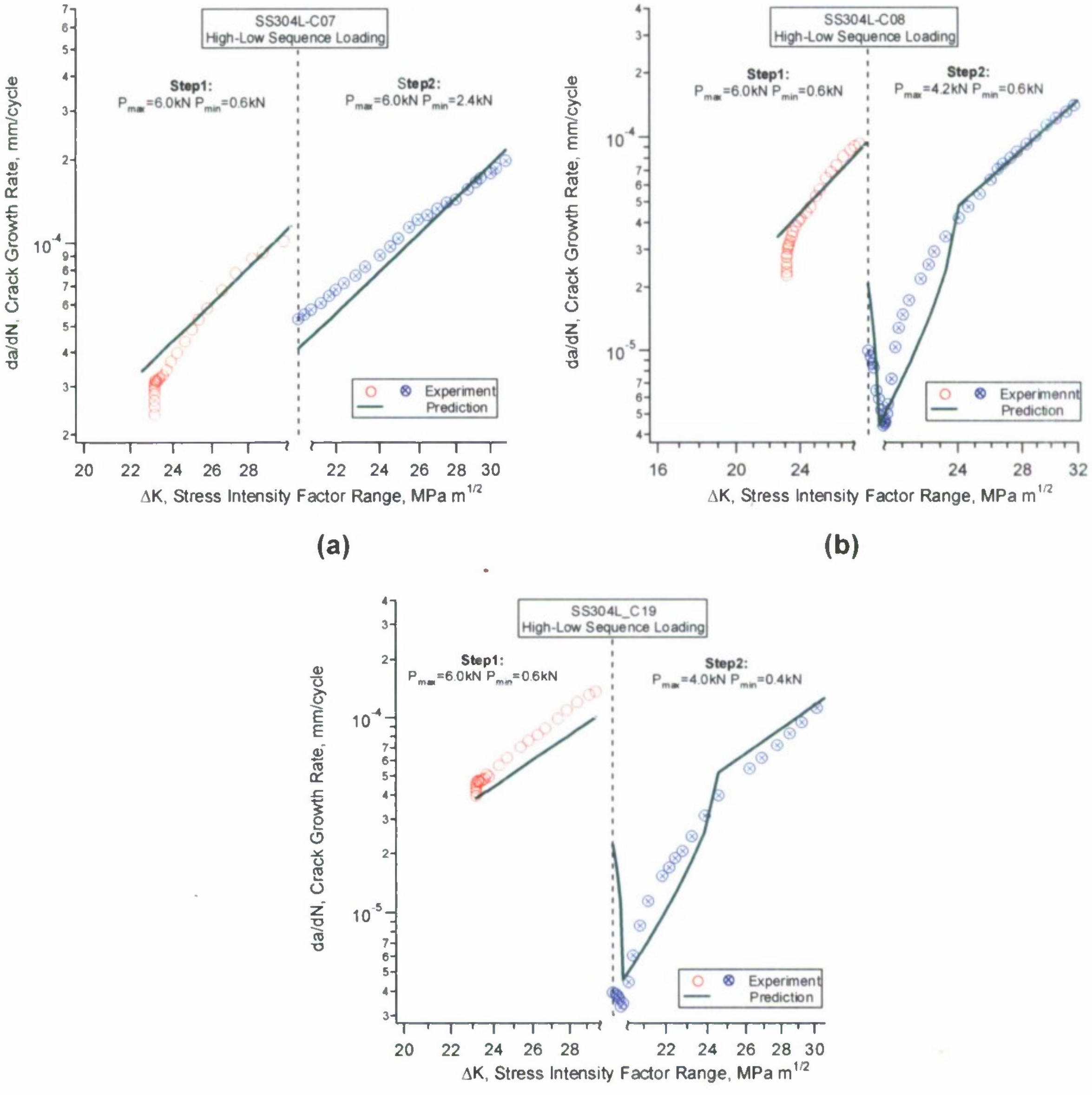

(a)

(b)

(c)

Fig.84 Prediction of crack growth rate in two-step high-low step loading

4.3 *AL6-XN SUPERAUSTENITIC STAINLESS STEEL*

Figure 85 summarizes the relationship between the constant amplitude crack growth rate of AL6-XN stainless steel and two-parameter fatigue driving force with $\alpha = 0.25$. The curves of crack growth rate with different stress ratios practically coincide extremely well, especially when the two-parameter fatigue driving force is larger than 20 $\mathrm{MPa}\sqrt{\mathrm{m}}$. The relationship between crack growth rate and fatigue driving force can be described by Eq. (15) with $C = 1.8 \times 10^{-11}$ and $n = 4.4$.

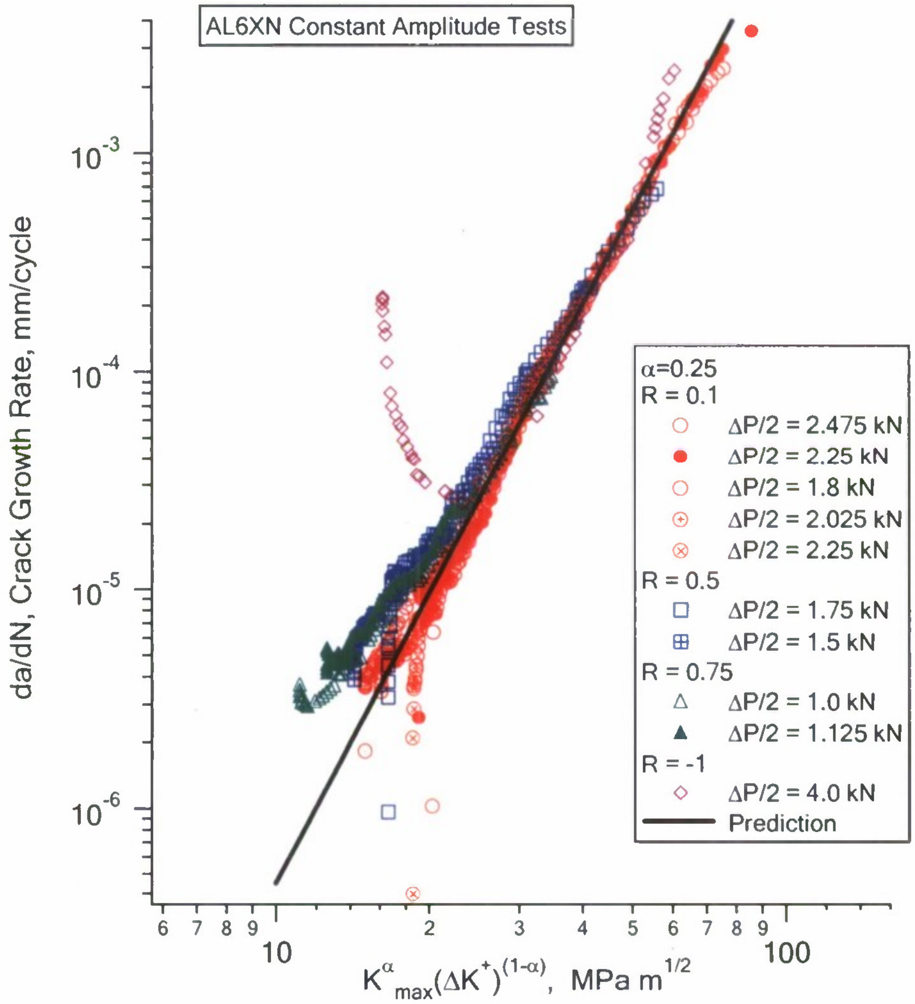

Fig.85 Constant amplitude crack propagation

A modification to the original Wheeler model is proposed for AL6-XN stainless steel in order to better capture the effect of the application of variable amplitude loading on the crack growth. Departing from the Paris law description of the stable crack growth (Eq.(15)), and adopting Irwin's model for the plastic zone size (Eq.(19)), the crack growth rate can be expressed in terms of r_p for constant amplitude loading,

$$da/dN = \chi(r_{pi})^{n/2}, \tag{29}$$

where $\chi = C\left(2\sqrt{\pi}\sigma_y\right)^n$ and C and n are the constants in the Paris law. The current approach makes use of the assumption that crack growth is related to the plastic zone size and Eq.(10) is valid for variable amplitude loading. Equations (10) and (9) are identical in the stable crack growth regime with constant-amplitude loading. For variable amplitude loading, the key is to determine the plastic zone size at a given moment.

Referring to Fig.86, the evolution of the post-overload plastic zone size follows,

$$r_{pi} = r_{pR} + \left(r_{pL} - r_{pR}\right)\left[1 - \left(\frac{a_i - a_{OL}}{a_R - a_{OL}}\right)^p\right]^{\frac{1}{p}} \tag{30}$$

where r_{pL} is the cyclic plastic zone size of a propagating crack immediately after the application of the overload, which is considered to be corresponding to the lowest crack growth rate in the overload influence zone. r_{pR} is the cyclic plastic zone size of the crack size a_R corresponding to the point where the "post-overload" curve merges with the stable growth curve. a_{OL} is the crack length at which overload is applied and a_i is the crack length at the *i-th* loading cycle after the application of the overload. The parameter p serves as a fitting constant. It can be seen that when $a_i = a_{OL}$ the plastic zone size is equal to r_{p1} and when the crack length reaches the value of a_R the plastic zone is $r_{pi} = r_{pR}$.

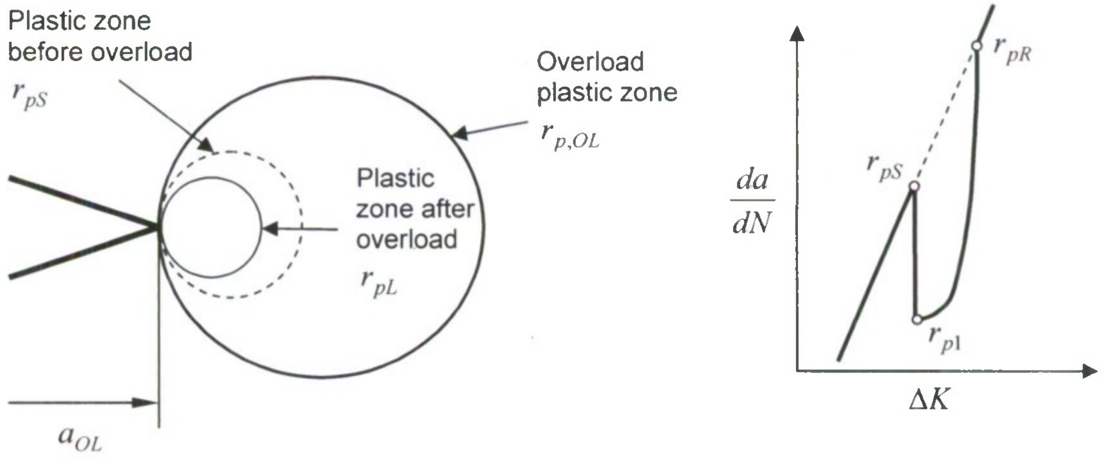

Fig.86 Schematic illustration of the plastic zone size and the crack growth rate before and after overloading

The key is to determine the plastic zone size, r_{pL}, right after the application of the overload. r_{pL} is related to the maximum stress intensity factor before overload $K_{\max S}$ to the stress intensity factor of the overloading,

$$\left(\frac{r_{pL}}{r_{pS}}\right)^{\frac{n}{2}} = \left(\frac{K_{\max S}}{K_{OL}}\right)^{\beta} \tag{31}$$

The parameter β in Eq. (31) is considered to be a material constant used to describe the degree of the crack growth retardation for a given overload. The value of a_R in the Eq.(30) is determined following Wheeler's approach (Fig.79)

$$a_R = a_{OL} + r_{p,OL} - r_{pR} \tag{32}$$

Since r_{pR} is a function of a_R, Eq.(32) can be solved through iterations.

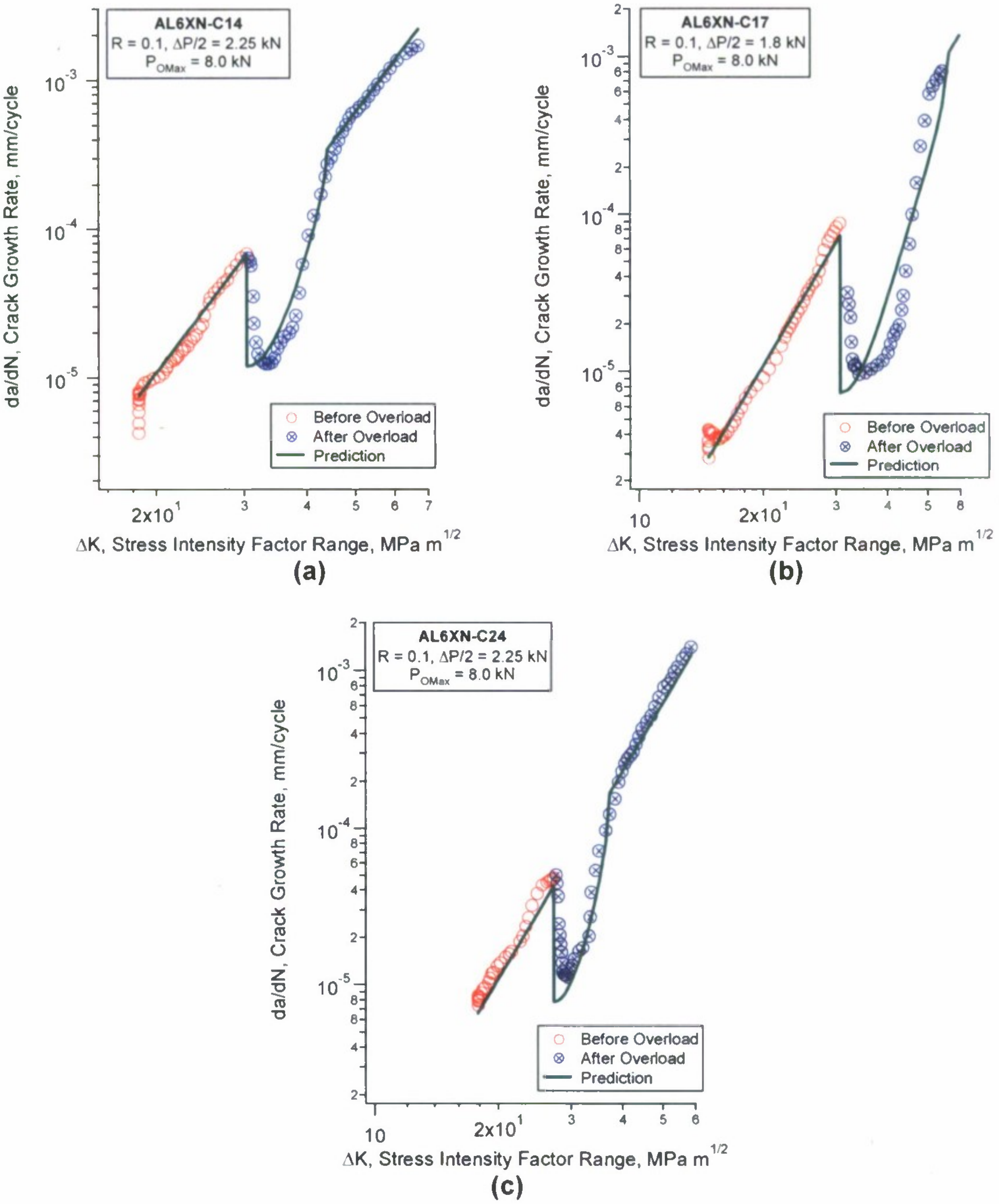

Fig.87 Prediction of overload effect on crack growth rate based on modified Wheeler's model

The predicted crack growth results based on the modified Wheeler model are reported in Figs. 87 and 88 together with the experimental data for the overload cases and high-low loading sequence cases, respectively. The constants in the model are $\beta = 3.6$ and $p = 2$ and these constants were used in predictions of all the cases of crack growth rate under the variable amplitude loading conditions investigated on AL6-XN. It can be seen that the modification can capture the fatigue crack growth behavior under the application of the overload and the high-low sequence loading with a good accuracy. The model can properly distinguish the three cases of the high-low sequence loading with the dependence of the crack growth rate on the maximum value of stress intensity factor within loading cycle (Fig.88). This is achieved with the use of Eq.(31). Since the crack growth retardation depends on the overload ratio (or in the case of high-low loading sequence, on the $K_{\max,Low} / K_{\max,High}$ ratio), no retardation is predicted when the specimen is tested with the same maximum load in both steps (Fig.88(a)).

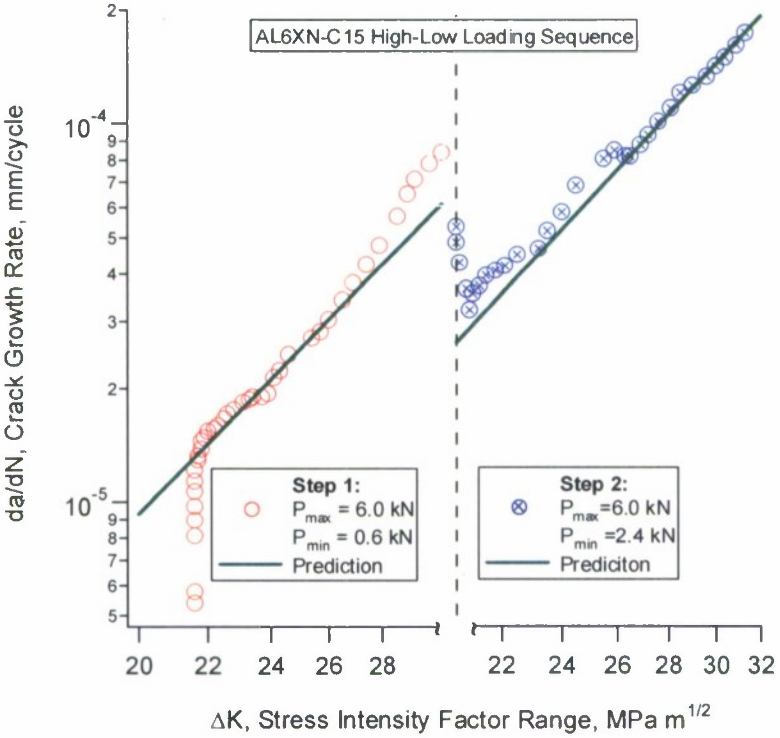

(a)

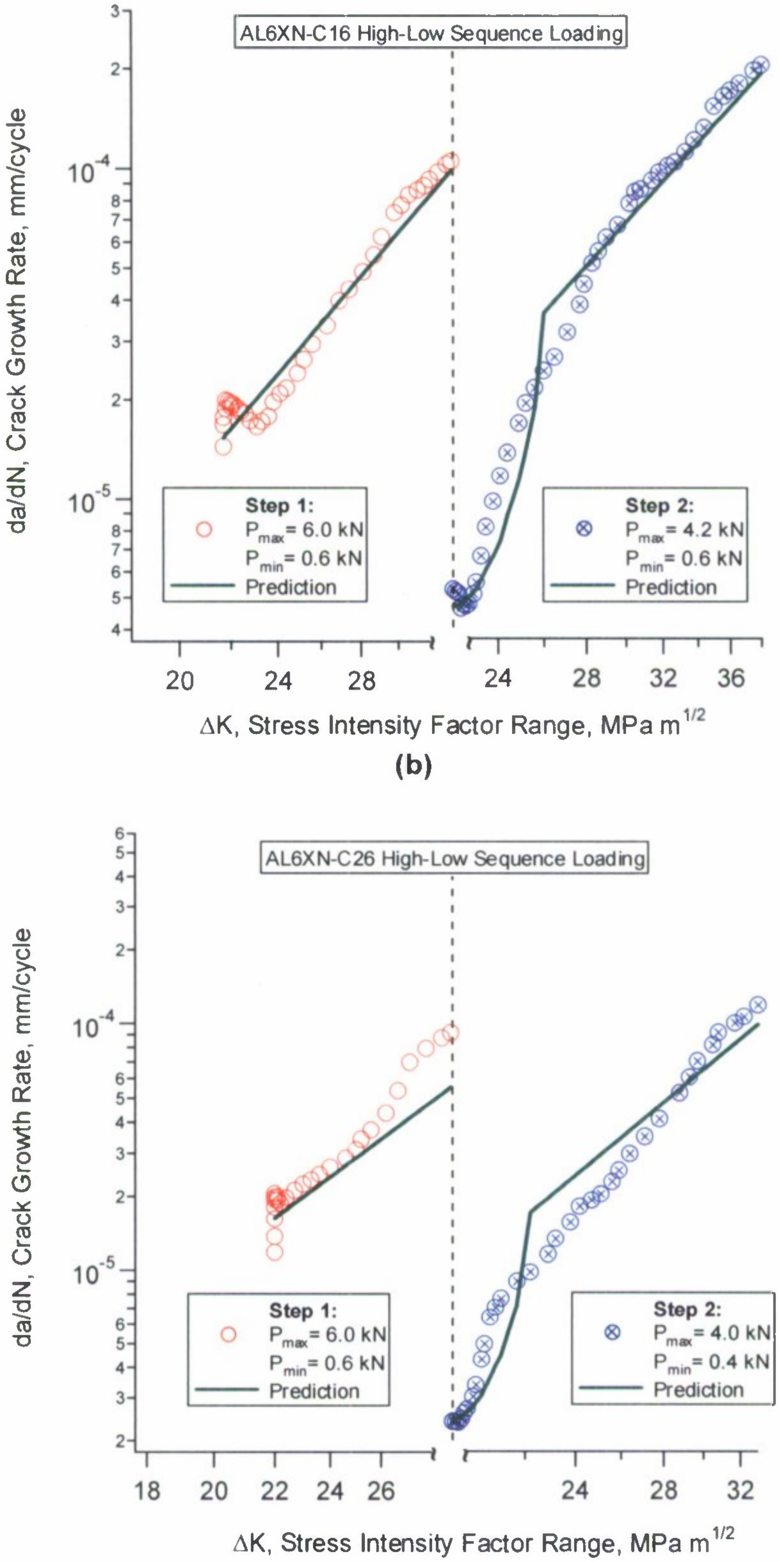

(b)

(c)

Fig.88 Prediction of High-Low loading sequence effect

5. NEW APPROACH

An approach developed by Jiang and Feng [74] based on two-dimensional elastic-plastic stress analysis for fatigue loading was employed to simulate fatigue crack growth. The cyclic plasticity model of Armstrong-Frederick type developed by Jiang and Sehitoglu [76, 77] and a multiaxial fatigue criterion developed by Jiang [59] were used to predict fatigue crack propagation in AISI 304L stainless steel. The stress-strain response obtained from finite element simulation was used to compute the fatigue damage accumulation, from which in turn crack growth rate was calculated. The geometry of the models and the loading conditions were identical to those used in the crack growth experiments described previously in the report.

5.1. CYCLIC PLASTICITY MODEL AND FATIGUE CRITERION

The modeling of fatigue failure of the material generally consists of two major steps:

a) Determination of the stress-strain response of the material point subjected to cyclic loading using a cyclic plasticity model; and,

b) Determination of the fatigue damage on the critical plane based on the stress-strain response using a multiaxial fatigue criterion.

Table 28 Cyclic plasticity model used in the finite element simulations

Yield Function	$f=(\tilde{S}-\tilde{\alpha}):(\tilde{S}-\tilde{\alpha})-2k^2=0$	$\tilde{s}$ = deviatoric stress $\tilde{\alpha}$ = backstress k = yield stress in shear
Flow Law	$d\tilde{\varepsilon}^{p}=\frac{1}{h}\langle d\tilde{S}:\tilde{n}\rangle\tilde{n}$	$\tilde{n}$ = normal of yield surface h = plastic modulus function $\tilde{\varepsilon}^{p}$ = plastic strain
Hardening Rule	$\tilde{\alpha}=\sum_{i=1}^{M}\tilde{\alpha}^{(i)}$ $d\tilde{\alpha}^{(i)}=c^{(i)}r^{(i)}\left(\tilde{n}-\left(\frac{\|\tilde{\alpha}^{(i)}\|}{r^{(i)}}\right)^{\chi^{(i)}+1}\frac{\tilde{\alpha}^{(i)}}{\|\tilde{\alpha}^{(i)}\|}\right)dp$ *(i=1, 2, 3, ... M)*	$\tilde{\alpha}^{(i)}$ = ith backstress part M = number of backstress parts dp = equivalent plastic strain increment $c^{(i)}$, $r^{(i)}$, $\chi^{(i)}$ = material constants

Earlier studies indicate that an accurate stress analysis is the most critical part for the fatigue analysis of the material [60, 78, 79]. If the stresses and strains can be obtained with accuracy, fatigue life can be reasonably predicted by using a multiaxial fatigue criterion. The elastic-plastic stress analysis of a notched or cracked component requires the implementation of a cyclic plasticity model into FE software package. Cyclic plasticity deals with the nonlinear stress-strain response of a material under repeated external loading. The selection of an appropriate cyclic plasticity model is crucial for an accurate stress analysis of a component subjected to cyclic loading. The cyclic plasticity model implemented in the present study was developed by Jiang and Sehitoglu [76] and has been successfully applied to the cyclic plasticity modeling of a variety of materials [76, 77]. The basic mathematical equations constituting the model are listed in Table 28. The choice of the model was based on its capability to describe the general cyclic material behavior including cyclic strain ratchetting and stress relaxation that occur in the material near the notch or crack tip. The detailed description of the model can be found in the corresponding papers and the present section is limited to the brief introduction of the major concepts within the approach.

The details of the determination of the material constants in the model can be found in the corresponding paper [77]. It should be mentioned however, that the material constants in Table 28 are determined directly from the cyclic-stress strain curve for a given material.

The plasticity model was implemented into the general purpose FE package ABAQUS through the user defined subroutine UMAT [80]. A backward Euler algorithm is used in an explicit stress update algorithm. The algorithm reduces the plasticity model into a nonlinear equation that can be solved by Newton's method. The corresponding consistent tangent operator is derived for the global equilibrium iteration, which ensures the quadratic convergence of the global Newton-Raphson equilibrium iteration procedure [81].

A critical plane multiaxial fatigue criterion developed by Jiang [59] is used for the assessment of fatigue damage based on the stress-strain output from the FE simulations. The description of Jiang's fatigue criterion is given in Section II.

5.2. FINITE ELEMENT MODEL

Due to the small thickness, plane-stress condition was assumed for the round compact specimen. Four-node plane-stress elements were used in FE mesh model. The FE mesh model shown in Fig.89 was created by using the FE package Hypermesh [82]. Due to the symmetry in geometry and loading, only half of the specimen was modeled. To properly consider the high stress and strain gradients in the vicinity of the notch or crack tip, very fine mesh size was used in these regions. The size of the smallest elements in the mesh model was 0.05mm. There were approximately 3058 to 5067 elements used in the mesh model depending on the crack size. The knife edges for the attachment of the open displacement gage in the specimen (Fig. 27) were not modeled because the free end of the specimen does not affect the stress and strain of the material near the crack tip or notch.

Referring to the coordinates system employed in Fig.89, the tensile external load, P, is applied in the y direction uniformly over nine nodes on the upper surface of the loading hole. To mimic the actual loading condition, the compressive load is applied in the negative y direction uniformly over nine nodes on the lower surface of the loading hole. The displacements in the x direction of the middle nodes on the upper edge of the loading hole are set to be zero. The displacements in the y direction for all the nodes on the plane in front of the crack tip or the root of the notch are set to be zero.

In order to consider the possible contact between the upper and lower surfaces of a crack, the FE model incorporates the contact pairs defined in ABAQUS [80]. The crack surface of the lower symmetric half of the specimen is considered as a rigid surface which acts as the master surface. The corresponding crack surface of the upper half of the specimen serves as the slave surface.

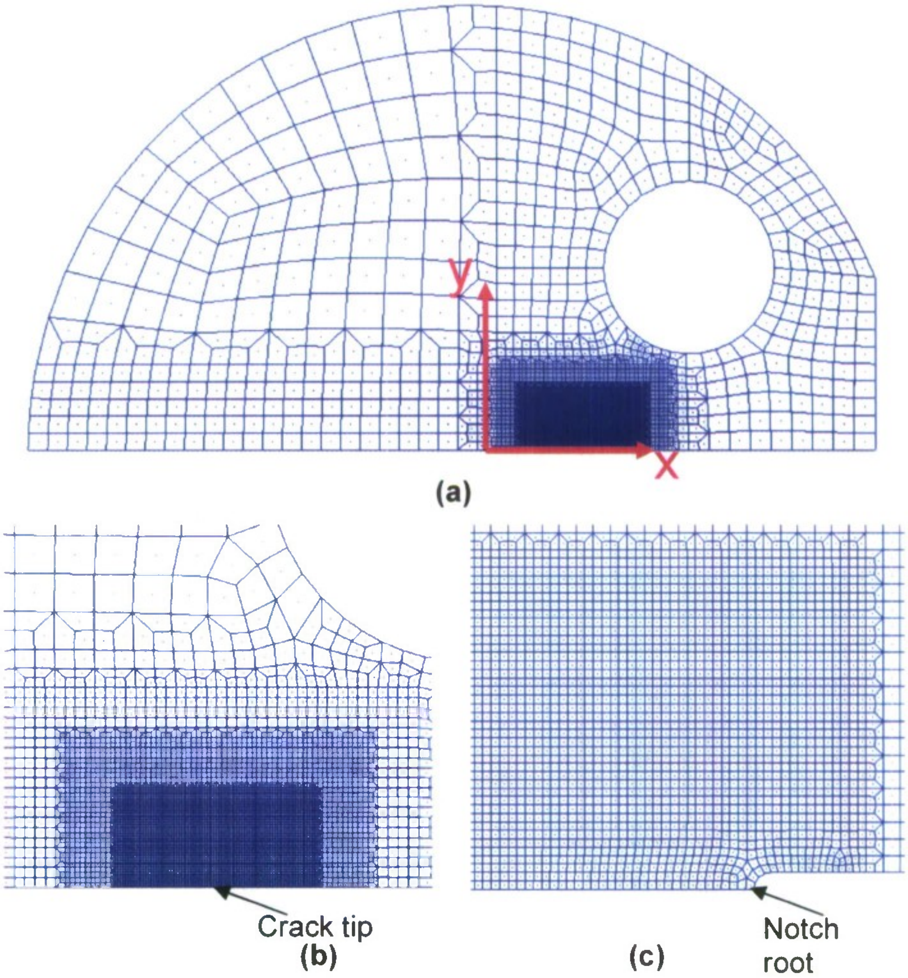

Fig.89 Finite element mesh model: (a) half of the specimen; (b) crack-tip area; (c) notch area

In order to consider the contact between upper and lower surfaces of a crack, the finitc element modeling incorporated the use contact pairs defined in the ABAQUS software [80]. The lower symmetric half of the specimen was considered as a rigid body which acted as the master surface, and the upper half served as the slave surface. In the current finite element simulation, $y = 0$ plane was attached to a two-dimensional analytical rigid surface which worked as the master surface. The slave surface started from the first node after the crack tip and extended to the node at the notch root.

5.3. CRACK GROWTH SIMULATION

Following the description of Jiang's fatigue model (Section II, Eq. (10)) fatigue damage per loading cycle was calculated by using the stabilized stress and strain response, in order to obtain the crack growth rate corresponding to the certain length. The results of cyclic plasticity modeling in the present work show that the stress-strain response stabilizes after ten loading cycles and the fatigue damage .can be computed based upon stresses and strains from the stabilized hysteresis loop.

The crack advance scheme was adopted in order to simulate crack growth behavior under variable loading conditions, such as overloading, underloading, two-step sequence loading. This was done in order to investigate in detail the effects of change in loading on crack propagation behavior, including the acceleration and retardation of crack growth rate, as well as the size of influencing zone.

In order to simulate crack propagation in the overload or underload influencing zone, the nodes between the original crack tip when overload or underload was applied (including the original crack-tip node) and the new crack tip of a designed crack length were set to a node set. The nodes of this node set were bonded at first, and during the subsequent constant amplitude loading, these nodes were de-bonded one by one. The node-release method—crack length versus time in ABAQUS [80]—was adopted to simulate the crack advancement. After all desirable nodes releasing, ten cycles of constant amplitude loading were applied to stabilize the stress strain response and get stabilized crack growth rate corresponding to the new crack length. After the crack penetrates the transient zone, the crack growth rate curve obtained using crack advance scheme coincides with the prediction by using the method for constant amplitude loading without de-bonding nodes. As a result, the overload or underload influencing zone was determined in finite element simulation.

When it comes to two-step sequence loading, the crack advance scheme mentioned above was used to simulate loading sequence effect. Similarly, the bonded node set included the nodes from the original crack length to the first node right after the designated crack tip. The first-step constant amplitude loading was applied at the crack length identical to the length at which loading condition was switched to the second-step loading in the experiment. Following enough cycles of first-step loading, the second-step constant amplitude loading was applied with releasing nodes. After all nodes in the node set were released, ten loading cycles of the second step was applied at the new crack length to get stabilized stress and strain response leading to crack growth rate. When the crack propagated to a certain length, there was little difference between the rate calculated by using node-releasing scheme and that expected in constant amplitude loading of the second step without effect of first-step loading history. Therefore, the transient zone started from the original crack length to this certain length.

5.4. DETERMINATION OF CRACK GROWTH RATE

For continuous crack growth under constant amplitude loading with small yielding, a simple formula was derived for the determination of the crack growth rate [74],

$$\frac{da}{dN} = \frac{A}{D_0}, \tag{33}$$

where

$$A = \int_0^{r_0} \Delta D(r)dr\,, \tag{34}$$

r is the distance from the crack tip and r_0 is the damaging zone size ahead of the crack tip where the fatigue damage is non-zero. $\Delta D(r)$ is the maximum fatigue damage per loading cycle with respect to all possible material planes at a given material point. $\Delta D(r)$ is determined by integrating Eq.(33) over one loading cycle,

$$\Delta D = \oint_{cycle} \left\langle \frac{\sigma_{mr}}{\sigma_0} - 1 \right\rangle^m \left(1 + \frac{\sigma}{\sigma_f}\right)\left(b\sigma d\varepsilon^p + \frac{1-b}{2}\tau d\gamma^p\right) \tag{35}$$

for a given material point once the stress-strain response at the point is known. In Eq.(34), A denotes the damaging area enclosed by the $\Delta D(r) - r$ curve.

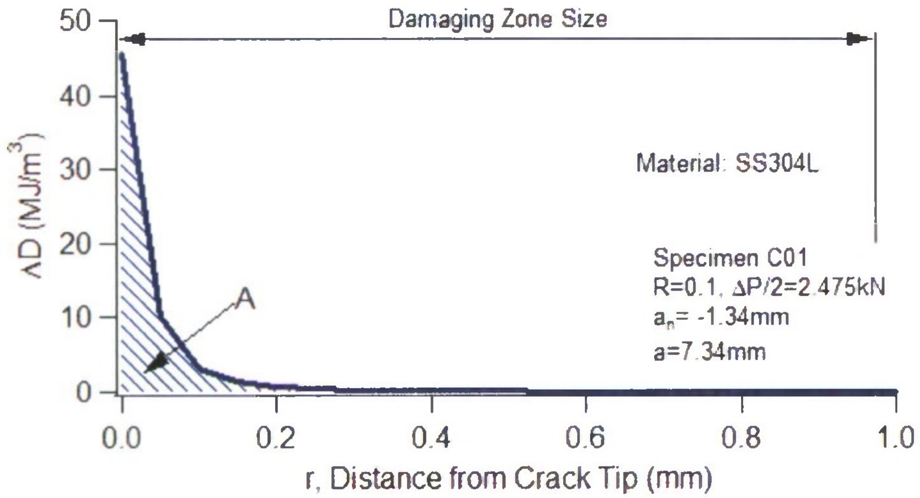

Fig.90 Distribution of fatigue damage per loading cycle as a function of the distance from the crack tip

Figure 90 shows the distribution of $\Delta D(r)$ along the x-direction for Specimen C01 which was subjected to constant amplitude loading with $R = 0.1$ and $\Delta P/2 = 2.475\text{kN}$. According to the fatigue criterion, Eq.(33), a material plane will accumulate fatigue damage when the memory stress is higher than the endurance limit and the material point experiences plastic deformation. For a cracked component, only the material near the crack tip accumulates fatigue damage. The values of $\Delta D(r)$ are determined along all radial directions in a polar coordinate system. The direction at which the crack growth rate is a maximum or the value of A is a maximum is the predicted cracking direction. The corresponding crack growth rate is the predicted crack growth rate.

The approach described in the previous sub-sections assumes that a material point fails to form a fresh crack on the critical plane when the accumulation of the fatigue damage on the critical material plane reaches a critical value, D_0. The rule applies to the initiation of a crack and the crack extension after a crack has been formed. Therefore, the approach unifies both the initiation and the subsequent crack propagation stage. The distribution of the stress-plastic strain field in the vicinity of a notch root, however, influences the early crack growth, which should be properly considered.

The definition of crack initiation used in the current study is different from that of the traditional way. The crack initiation of a fatigue crack is judged by using the fatigue criterion, Eq.(33). Once the fatigue damage on a material plane for the material point at the notch root reaches the critical fatigue damage, D_0, the notched member is called to have initiated a fatigue crack.

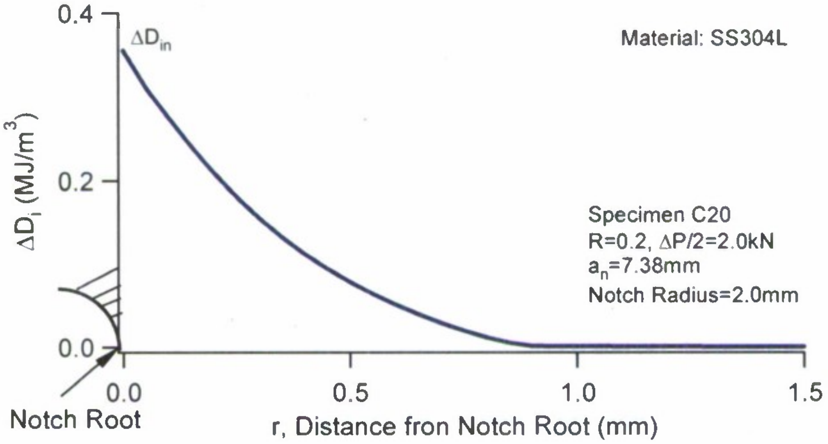

Fig.91 Fatigue damage per loading cycle during crack initiation

The FE stress analysis is conducted with the notched member for the designated loading condition. For a notched component, the maximum fatigue damage occurs at the notch root. The fatigue damage per loading cycle can be determined and it can be plotted as a distribution along the radial direction from the notch root. Fig. 91 shows an example for Specimen C20 ($R = 0.2$, $\Delta P/2 = 2.0\text{kN}$, notched depth $a_n = 7.38$ mm, notch radius = 2.0 mm). The distance, r, from the notch root is along the x-axis (refer to Fig.89). ΔD_i denotes the fatigue damage per loading cycle on the critical plane during crack initiation. ΔD_i is a function of the location of the material point.

The maximum fatigue damage occurs at the notch root during crack initiation. The crack initiation life is predicted to be,

$$N_i = \frac{D_0}{\Delta D_{in}}, \tag{36}$$

where N_i is the predicted crack initiation life, D_0 is a material constant, and ΔD_{in} is the fatigue damage per loading cycle on the critical plane at the root of the notch. ΔD_{in} is ΔD_i shown in Fig.91 when $r = 0$.

During crack initiation, the fatigue damage is also accumulated in the vicinity of the notch root and should be considered in the determination of the crack growth near the notch. The area where the fatigue damage accumulation is non-zero during crack initiation (Fig.91) is referred to as the notch influencing zone (NIZ). For a specimen under a given loading condition, the NIZ can be determined by applying the fatigue criterion, Eq.(33), with the stress and strain histories outputted from the FE analysis. For Specimen C20 shown in Fig.91, the NIZ size is approximately 0.85 mm ahead of the notch root.

For each material plane at any material point, the total fatigue damage at the end of the fatigue crack initiation is $N_i \Delta D_i$. It should be reiterated that the discussion is based on the assumption that the material is stable in stress-strain response and the applied loading has constant amplitude. The crack growth rate within the NIZ can be determined by using the following equation with the consideration of pre-existing fatigue damage accumulation [83]:

$$\frac{da}{dN} = \frac{A}{D_0 - N_i \Delta D_i(r)} \tag{37}$$

where A is the damage area enclosed by the $\Delta D(r) - r$ curve, as explained above. In Eq.(37), N_i and $\Delta D_i(r)$ are related to the fatigue damage accumulation during crack initiation in the NIZ. For a given crack size within the NIZ the FE analysis is conducted. The distribution of the fatigue damage per loading cycle, $\Delta D(r)$, can be determined as a function of the distance from the crack tip, as shown in Fig.90. The enclosed area made by the $\Delta D(r) - r$ curve is A in Eq.(37). For any direction radiated from the crack tip, the direction which has the highest crack growth rate is the predicted cracking direction and the corresponding crack growth rate is the predicted crack growth rate. It can be seen that the difference between the crack growth rate determination near the notch (Eq.(37)) and that away from the notch root (Eq.(33)) lies in the consideration of the fatigue damage caused during the crack initiation stage.

Generally, the stress-strain response becomes stabilized after a limited number of loading cycles. It was shown [74] that the predicted crack growth results obtained based on the stress-strain response from the 10th loading cycle were very close to those based on the stabilized stress and strain response. Therefore, the FE analysis for a given notch or crack length under a designated loading amplitude is conducted for 10 loading cycles. The stress and strain results at the 10th loading cycle are used for the fatigue analysis.

The stress and strain results obtained from analyzing the notched component during crack initiation will determine the fatigue damage per loading cycle for each material plane at each material point. Eq. (36) is used to determine the crack initiation life. FE stress analyses are conducted with different crack lengths for a given loading condition. When the crack tip is within the notch influencing zone, Eq.(37) is used for the crack rate determination. $\Delta D_i(r)$ in Eq.(37) is the fatigue damage per loading cycle for a given material point during crack initiation. Once the crack grows out of the NIZ, Eq.(33) is used for the crack growth rate determination. In fact, $\Delta D_i(r)$ is determined during crack initiation. As a result, Eq.(37) can be used for both situations since $\Delta D_i(r)$ is zero for the material points out of the notch influencing zone.

It should be noticed that the FE simulation is conducted cycle by cycle mimicking the real crack growth procedure. The crack initiation life is determined first. The crack growth rates at several crack lengths are predicted by using the approach. Therefore, the prediction is the relationship between the crack growth rate, da/dN, and the crack length for a given notched component. With the crack initiation life obtained from using Eq.(36), the relationship between the crack length and the number of loading cycles can be established through a numerical integration.

Simulations are also conducted for the high-low step loading conditions. In a high-low step loading experiment, an external load with higher loading amplitude is applied until a crack length reaches a certain value. The amplitude of the external load is switched to a lower value in the second loading step. In the simulations for the high-low loading sequence, one special consideration is made. The memory stress, σ_{mr}, in Eq.(35) is kept the same before and immediately after the change of the external load from a higher amplitude to a lower amplitude. After an extension of the crack in the second loading step, the memory stress returns to that under the lower constant amplitude loading.

5.5. RESULTS OF FINITE ELEMENT SIMULATIONS

Table 29 and Table 30 give the constants used in the cyclic plasticity model and the fatigue constants for 304L stainless steel. The material constants listed in both Table 29 and Table 30 were obtained from cyclic and monotonic tests on smooth specimens.

Table 29 Constants used in the cyclic plasticity model. Material: AISI 304L

$E = 200\,\text{GPa}, \mu = 0.3, k = 115.5\,\text{MPa}$
$c^{(1)} = 1381.0, c^{(2)} = 507.0, c^{(3)} = 172.0, c^{(4)} = 65.0, c^{(5)} = 4.08$
$\gamma^{(1)} = 93.0\text{MPa}, \gamma^{(2)} = 130.0\text{MPa}, \gamma^{(3)} = 110.0\text{MPa}, \gamma^{(4)} = 75.0\text{MPa}, \gamma^{(5)} = 200.0\text{MPa}$
$\chi^{(1)} = \chi^{(2)} = \chi^{(3)} = \chi^{(4)} = \chi^{(5)} = 8.0$

Table 30 Fatigue model constants. Material: AISI 304L

$\sigma_0 = 270\,\text{MPa}; m = 1.5; b = 0.5; \sigma_f = 800\,\text{MPa}; D_0 = 15000\,\text{MJ/m}^3$

The primary results obtained from using the fatigue approach presented in the current investigation is the crack growth rate as a function of the crack length from the notch root for a given loading condition. However, the traditional way to present the crack growth results in $da/dN - \Delta K$, where ΔK is the stress intensity factor range, is adopted, considering the general familiarity of the traditional presentation of the crack growth results.

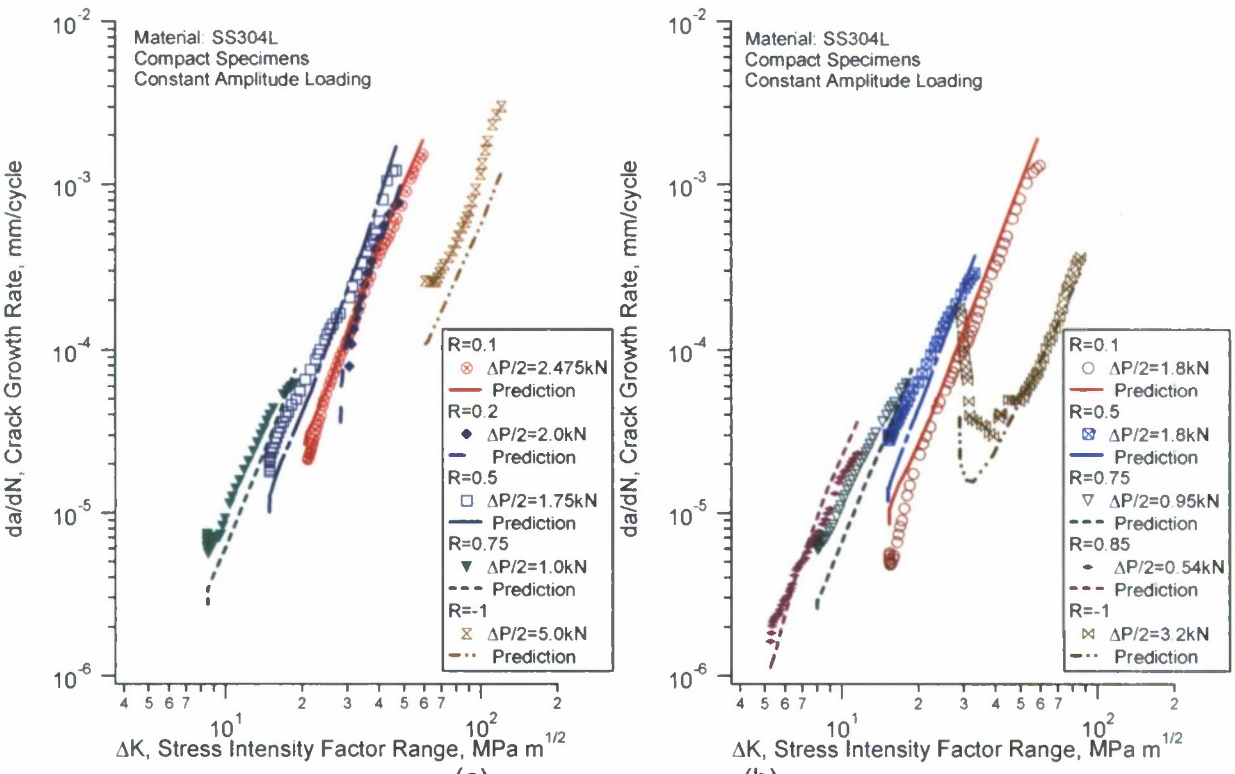

(a) (b)

Fig.92 R**-ratio effect on crack propagation under constant amplitude loading**

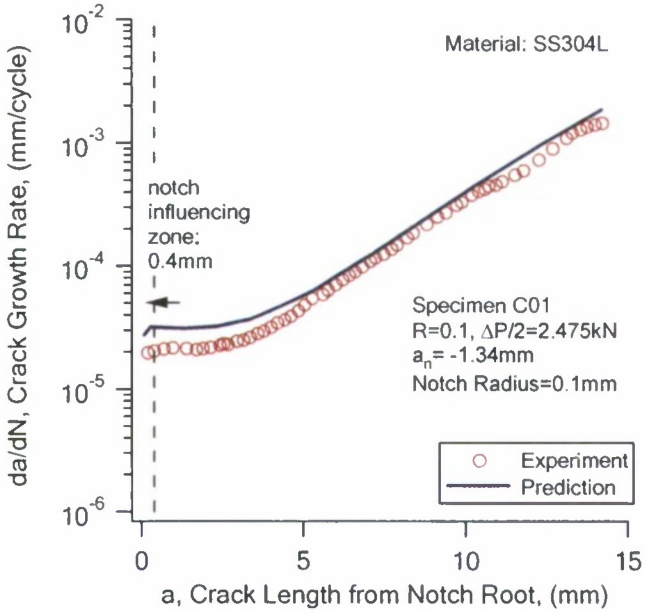

Fig.93 Notch effect for specimen C01

Comparisons of the experimental crack growth results with the predictions are shown in Fig. 92 for the constant amplitude cases. The markers in the figure denote the experimentally obtained crack growth results and the lines are the predictions. A general good agreement can be found between the predictions and the experimental observations. It should be reiterated that all of the specimens were subjected to constant amplitude loading without a pre-crack except for specimens C16 and C14, to which pre-cracking was applied (Table 11). Therefore, the results shown in Fig. 92 include the effect of the notch on the early crack growth.

The notch effect is dependent on the notch size. A larger effect is expected if the notch size is larger. Since all of the specimens except Specimen C20 ($R = 0.2$, $\Delta P/2 = 2.0\text{kN}$, notch radius=2.0mm) and Specimen C24 ($R = -1$, $\Delta P/2 = 3.2\text{kN}$, notch radius=1.0mm) had small notch sizes with the notch radius being 0.1mm, the notch effect is not significant. Figure 93 shows the results for Specimen C01 ($R = 0.1$, $\Delta P/2 = 2.475$ kN, and the notch depth $a_n = -1.34\text{mm}$) in terms of the crack growth rate versus the crack length measured from the notch root. The size of the notch influencing zone is predicted to be 0.4 mm.

Figure 94 shows the comparison of predicted crack growth rate with experimental observation for the four specimens tested under constant amplitude loading with a single tensile overload. The markers show the results of the experiments and the thick dotted lines represent the prediction based on the finite element modeling. It can be seen from Fig.94 that the simulation predicts all major features of overload effect with good accuracy. It should be particularly mentioned that the model is capable of predicting the crack growth acceleration after application of overload. The point of minimum crack growth in the retardation zone is also predicted with good accuracy. After the crack propagates out of the overloading influencing zone, the curve of crack growth rate merges the stable growth curve of constant amplitude loading.

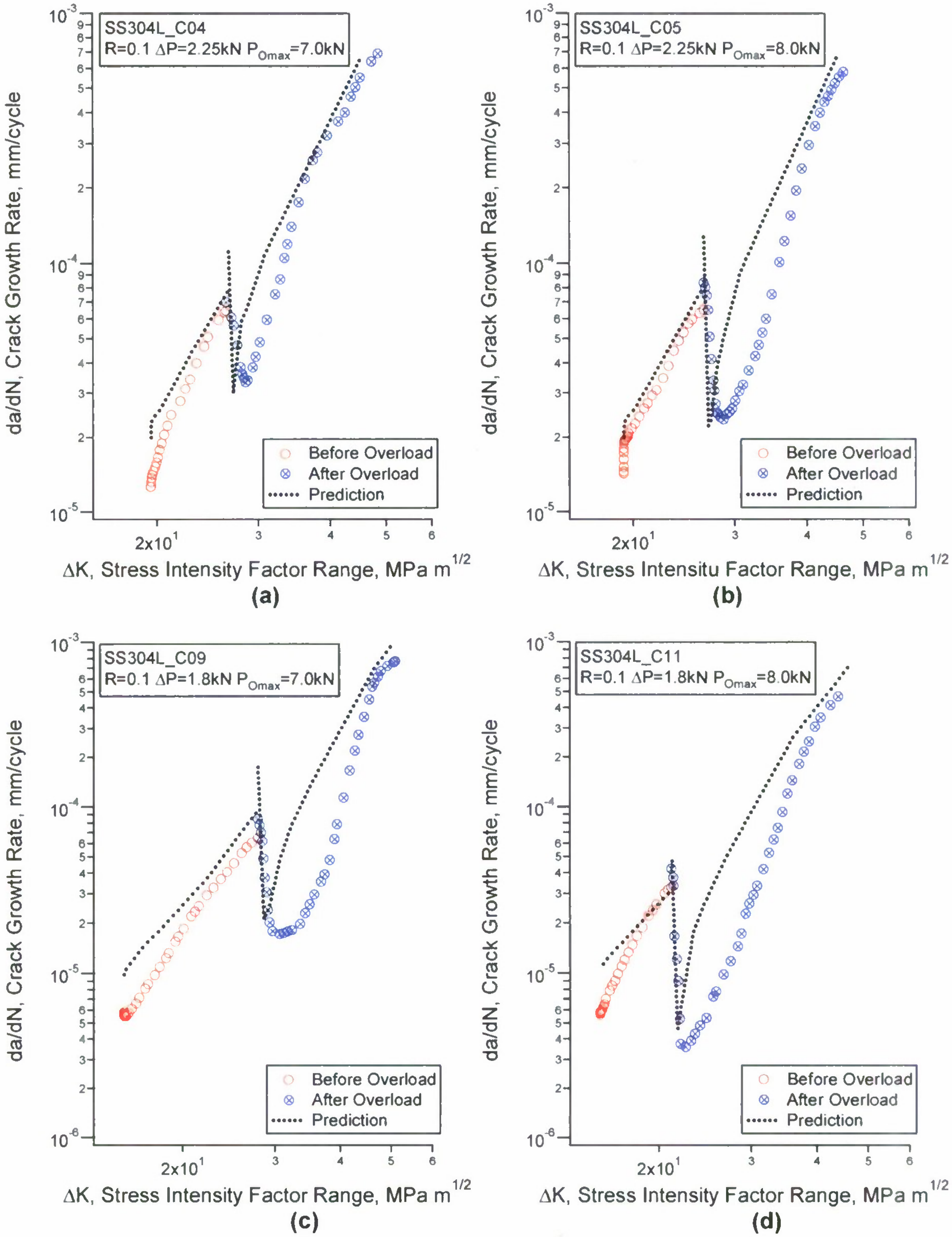

(a) (b)

(c) (d)

Fig.94 Overload effect on crack growth

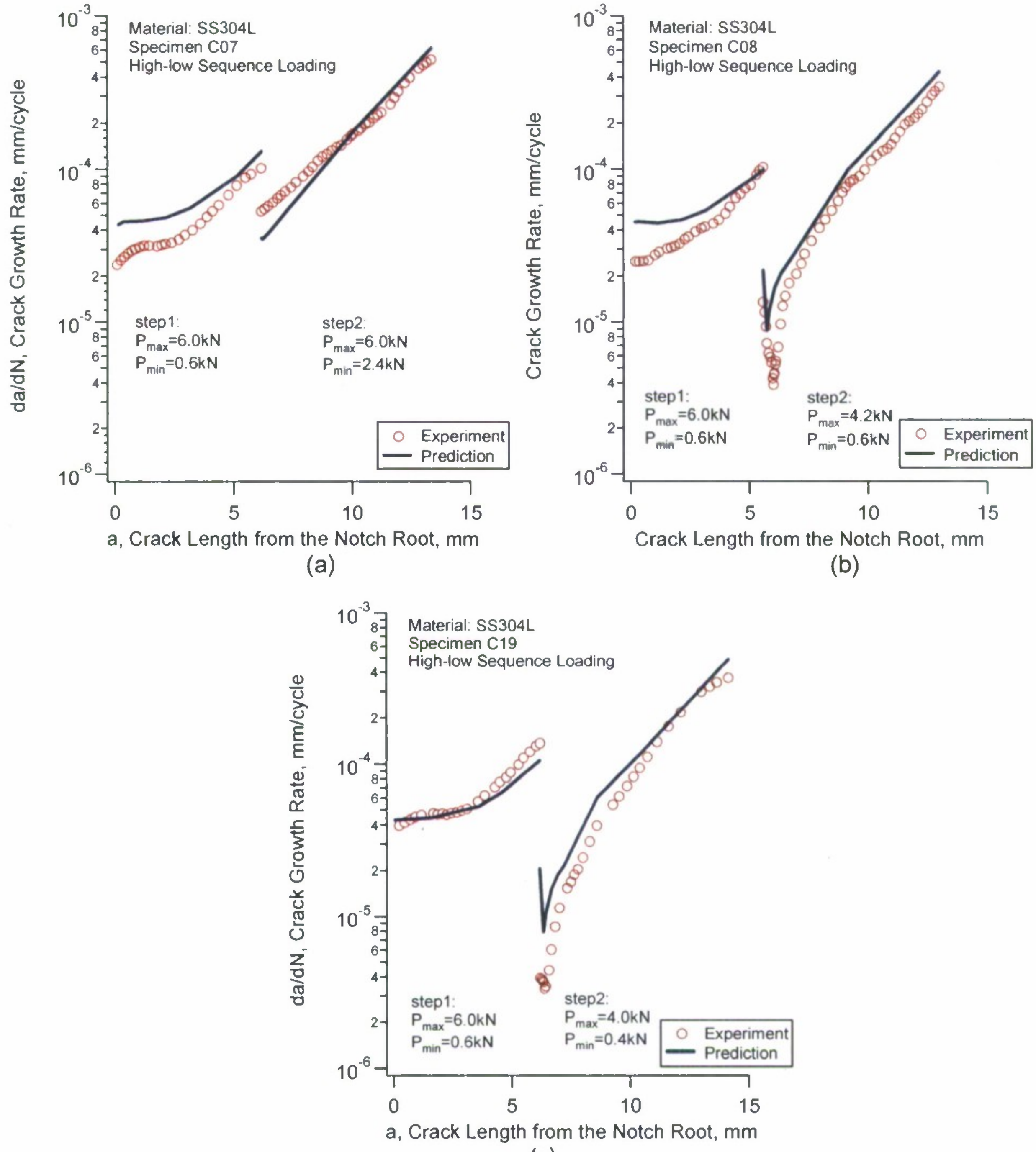

(a)

(b)

(c)

Fig.95 Modeling of the two-step high-low loading sequence effect on crack propagation (AISI 304L stainless steel)

The results of experiments involving two step high-low loading sequence are shown in Fig. 95 and are displayed as a function of the crack length measured from the notch root. The markers in the figure represent the experimental data and solid lines represent the predicted crack growth rate based on the current approach. The details of the experimental conditions are summarized in Table 13, Section I. The results shown in Fig. 95 demonstrate that the crack growth behavior under high-low loading depends on the loading conditions in the lower amplitude loading step. When the experiment is performed with the same maximum load in both steps, the first (high amplitude) step has little influence on the subsequent crack growth in the second (low amplitude) step. However, in other two cases (Fig.95(b) and (c)), a significant crack growth retardation can be observed at the beginning of the low amplitude block of the experiment. It can be seen from Fig. 95 that the predictions of the crack growth for the two-step loading agree well with the experimental observations and capture crack growth behavior in all three cases described above.

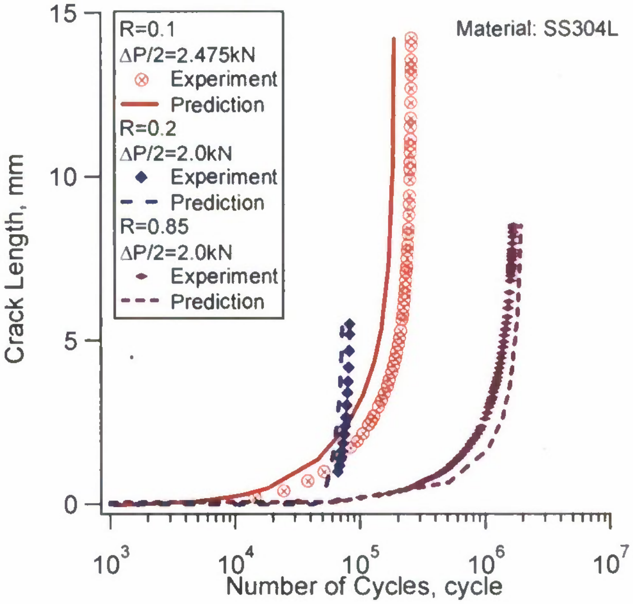

Fig.96 Crack length versus number of loading cycles

An appropriate approach should be able to predict the relationship between the crack length, a, and the number of loading cycles, N. Fig. 96 shows the comparison of the experimentally obtained $a-N$ results and the predictions obtained from using the fatigue approach. The predicted fatigue life for a given crack length is obtained using the following equation,

$$N = N_i + \int_0^{a_1} \frac{da}{f(a)}, \tag{38}$$

where N is the number of loading cycle corresponding a crack length of a, and N_i is the crack initiation life predicted for the specimen by using Eq.(36). $f(a)$ is the crack growth rate as a function of the crack length predicted by using the approach. Eq.(38) is integrated numerically and is applicable after crack initiation. An overall good correlation between the experiments and the predictions can be observed from the results shown in Fig.96.

Another way to evaluate the approach for the capability to predict fatigue life is to compare the crack initiation life and the fatigue failure life of the specimen with those observed experimentally. As was mentioned in an early section, the crack initiation used in the current study is different from the traditionally used concept. The current definition of the initiation life is a mathematic concept since it is very difficult to experimentally identify the exact moment of crack initiation. However, a practical pseudo crack initiation life can be used to check the capability of the models. The pseudo crack initiation can be defined as the fatigue life corresponding to a small crack length. In the current study, a crack length of 0.5 mm from the notch root is chosen as the "pseudo crack initiation". A crack length of 10 mm measured from the line of action of the externally applied load is used for fatigue failure. In other words, two fatigue lives with an order of difference in the crack length are used to check the capability of the models in predicting the fatigue life.

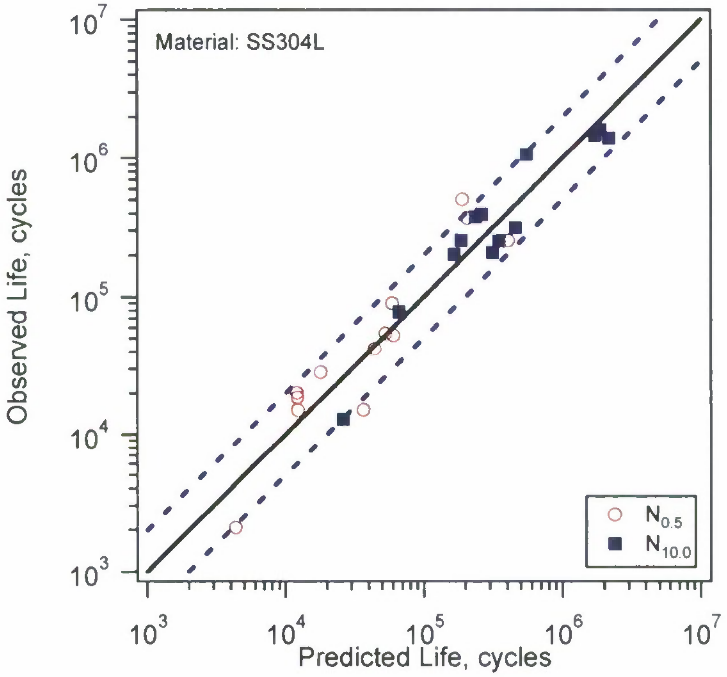

Fig.97 Comparison of experimental fatigue life with prediction

Figure 97 shows the comparison of the predicted fatigue lives and the experimentally measured fatigue lives when the crack lengths are 0.5 mm ($N_{0.5}$) and 10 mm ($N_{10.0}$). The vertical axis is for the observed fatigue life and the horizontal axis is for the predicted fatigue life. The logarithmic scales are used for both axes. The open circles are for the "pseudo crack initiation" (when the crack length from the notch root is 0.5mm) and the solid markers are the "fatigue failure" lives corresponding to a crack length of 10 mm from the line of action of the externally applied force. The thick solid diagonal line signifies a perfect prediction and the two dashed lines are the factor-of-two boundaries. Almost all the results are within the factor-of-two boundaries, signifying a very reasonable prediction.

While the overall predictions of the crack "initiation" and crack growth are in general and reasonable agreement with the experimental observations, the predicted results are not as satisfactory as those using 1070 steel [74, 83]. The major reason is the less accurate description of the cyclic plastic deformation of the SS304L than that for 1070 steel. 1070 steel displays very stable stress-strain response with practically no cyclic hardening/softening or non-proportional hardening. The material under consideration exhibits significant non-proportional hardening and cyclic hardening/softening. The simple version of the cyclic plasticity model listed in Table 28 does not consider cyclic hardening/softening or the non-proportional hardening.

It is found that while the material displays significant non-proportional hardening and the stress state is multiaxial in the material near the crack tip, the loading is practically proportional for Mode I crack growth. Figure 98 shows the response of the two normal stresses at the Gauss point closest to the crack tip for a loading cycle. The loading condition is $R = 0.1$ and $\Delta P/2 = 2.7$ kN. For the plane-stress condition, the material point under consideration has a minimal shear stress. It can be seen in Fig.98 that the two normal stress components are practically proportional. It is further confirmed that for Mode I loading the results obtained from considering the nonproportional hardening are practically the same as those without considering the nonproportional hardening in the finite element analysis.

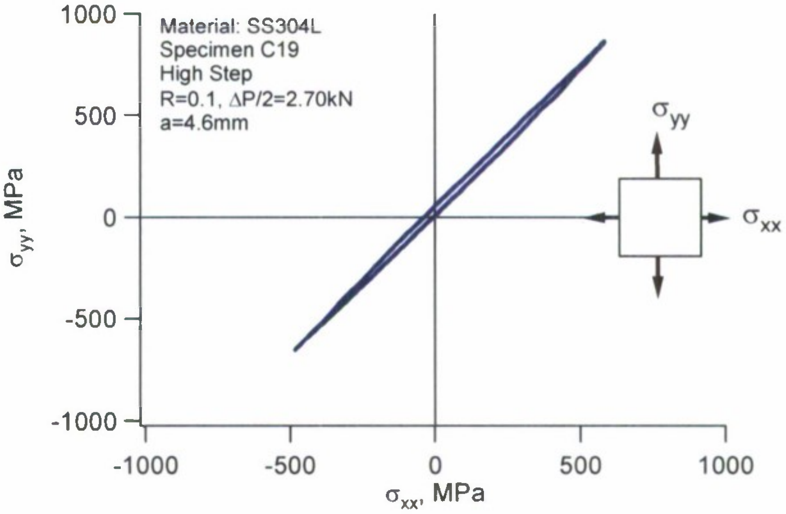

Fig.98 Stress state in the material near the crack tip

The exclusion of the cyclic hardening/softening in the constitutive modeling of the cyclic plastic deformation of stainless steel 304L contributes to the discrepancy between the experimentally observed fatigue behavior and the predictions for the notched member under consideration. From Fig. 23 (Section I) it can be seen, that the material experiences a period of cyclic softening followed by cyclic hardening. In other words, the stress response of the stainless steel 304L never becomes stabilized. Cyclic hardening/softening is very difficult to model accurately. In the deformation analysis particularly with the FE analysis, the transient cyclic hardening/softening is always ignored.

Another difference between the real cyclic plastic deformation and the model simulation is the ignorance of the non-Masing or strain-range effect on the cyclic plasticity in the constitutive model. Most engineering materials display non-Masing behavior, while the constitutive model listed in Table 28 is based on Masing behavior. The stress-plastic strain hysteresis loops shown in Fig.99 were obtained from the strain-controlled constant amplitude loading experiments using dog-bone shaped smooth cylindrical specimens. The stress-plastic strain loops shown in Fig. 99 were taken at the number of cycles corresponding to half of the fatigue life of the specimen. The loops were tied together at the lower tips. If the material displays Masing behavior, all the upper braches of the hysteresis loops shown in Fig.99 should coincide. It is evident from Fig. 99 that stainless steel 304L displays non-Masing behavior or strain range effect particularly when the loading amplitude is large.

It is possible to include the non-Masing behavior, nonproportional hardening, and cyclic hardening/softening in the constitutive relations for cyclic plasticity. The inclusion of all these considerations results in a very complicated constitutive model. It is also required to implement the model into an FE software package such as the UMAT in ABAQUS. Furthermorc, the consideration of all the cyclic plasticity behavior will slow down the already slow elastic-plastic FE stress analysis of a real component. Further work is needed to properly consider the material deformation in the numerical stress analysis.

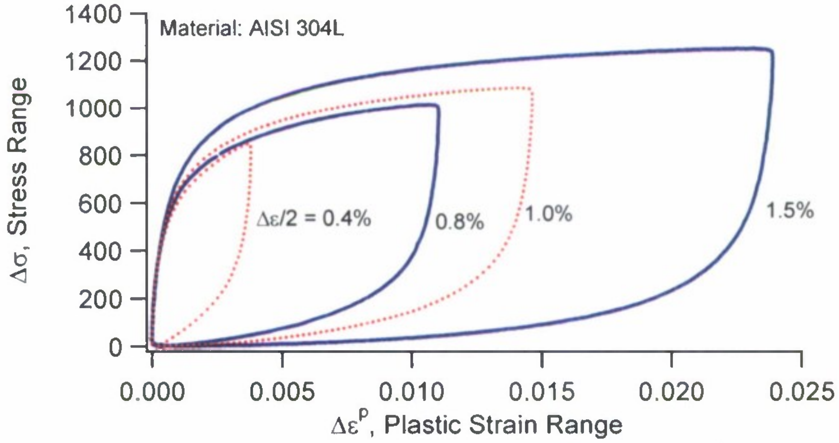

Fig.99 Stabilized stress-plastic strain hysteresis loops with the lower tips tied together

The approach by using the multiaxial fatigue criterion, Eq.(10), does not need to dcfine a loading cycle. However, for all the experiments that were used, a loading cycle can be easily defined. The only purpose to use the loading cycle as a unit in fatigue damage accumulation was to facilitate the presentation of the results.

When a cracked component is subjected to external loading, the material near the crack tip always experiences elastic-plastic deformation and both the stresses and the strains at the crack tip are theoretically infinite if the material displays strain hardening. Since a cracked component can withstand a certain external load, the theoretical singular problem is caused by the basic assumption of a continuum for a material. The real stresses and strains in a cracked component should be finite when the external load is below a certain level. The FE methods average out the stress and strain in the highly gradient area and it may provide reasonable and realistic results to serve a given purpose. It is found that the considerations of the nonlinear material deformation and the nonlinear geometry near the crack tip do not considerably influence the stress-strain results near the crack tip for the crack growth rate below the unstable crack growth region. However, the stress and strain results near the crack tip obtained from the elastic-plastic FE stress analysis of a cracked component is sensitive to the FE size near the crack tip. When the mesh size is extremely small for the material near the crack tip, the stresses and strains at the crack tip obtained from the FE analysis will be unrealistically high, which will result in a very high predicted crack growth rate. The FE size near the crack tip is a "model" constant. A preliminary study [74] reveals that an appropriate element size is in the order of one to three times the average grain size of the polycrystalline material. Within such an element size range, the fatigue results obtained from using the approach are not very sensitive to the element size used near the crack tip. For the stainless steel 304L under investigation, the average grain size is approximately 20 μ. In the current FE simulations, the smallest element size near the crack tip was 50 μ. Further investigations are needed to explore the influence of the element size and the element type on the simulation results for the stresses and strains near the crack tip.

The approach combining cyclic plasticity modeling with multiaxial fatigue criterion was also applied to simulate crack growth results under constant amplitude loading for AL6-XN stainless steel. Tables 31 and 32 list the material constants used in cyclic plasticity model and fatigue material constants for fatigue criterion. Figure 100 gives the comparison of the predictions obtained by using the new approach and the experimental results of selected specimens under constant amplitude loading with different R-ratios. The approach can predict R-ratio effect and the obvious short crack behavior for the case of $R = -1$.

Table 31 Constants used in the cyclic plasticity model. Material: AL6-XN

$E = 195\,\text{GPa},\ \mu = 0.3,\ k = 144.3475\,\text{MPa}$

$c^{(1)} = 252.0, c^{(2)} = 55.0, c^{(3)} = 15.5, c^{(4)} = 7.7, c^{(5)} = 4.08$

$\gamma^{(1)} = 100.0\text{MPa}, \gamma^{(2)} = 80.0\text{MPa}, \gamma^{(3)} = 57.0\text{MPa}, \gamma^{(4)} = 36.0\text{MPa}, \gamma^{(5)} = 200.0\text{MPa}$

$\chi^{(1)} = \chi^{(2)} = \chi^{(3)} = \chi^{(4)} = \chi^{(5)} = 8.0$

Table 32 Fatigue model constants. Material: AL6-XN

$\sigma_0 = 260\text{ MPa}; m = 0.5; b = 0.5; \sigma_f = 1133\text{ MPa}; D_0 = 20000\text{ MJ/m}^3$

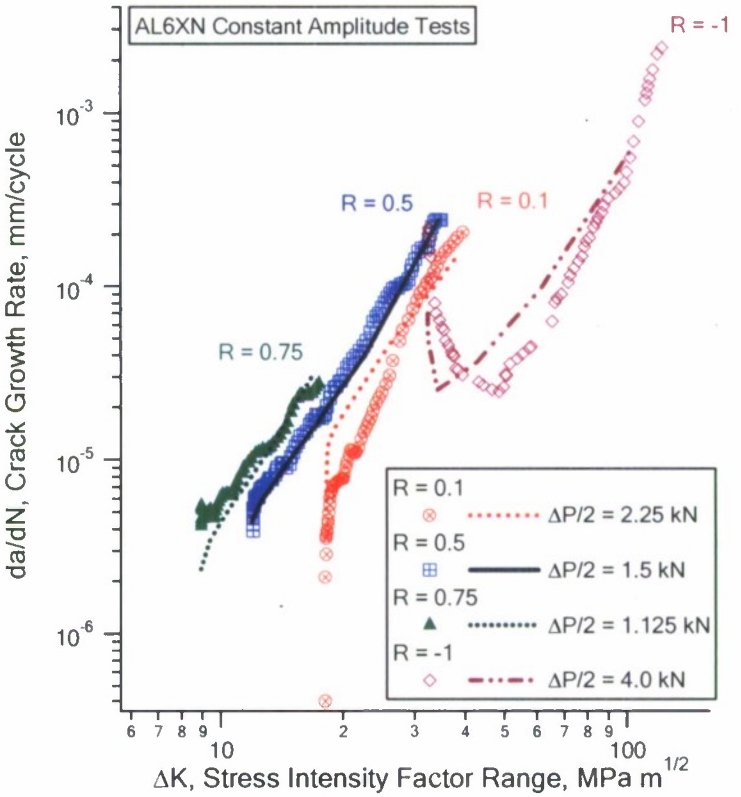

Fig.100 Prediction of R-ratio effect in AL6-XN alloy based on the new approach

DISCUSSION

The present report summarizes the results of an extensive experimental investigation of fatigue properties of four different materials together with modeling work. The materials under investigation are: 7075-T651 aluminum alloy, two types of stainless steel (AL6-XN and 304L), and 4340 VM aerospace steel. The results reported here allow to draw a comparison among the fatigue behavior features of these metallic alloys. Among four of alloys investigated, only one material, 4340VM, displays consistent shear cracking behavior regardless of the loading amplitude. For the other three alloys, a transition in cracking modes was observed. 7075-T651 aluminum alloy displays shear cracking, mixed cracking, and tensile cracking, depending on the loading magnitude. Earlier investigations indicate that many materials are dominated by mixed cracking behavior [53, 59] and few exhibit primarily tensile cracking [10]. One characteristic of the fatigue behavior of 7075-T651 is the distinct kink observed in the shear strain versus fatigue life curve that is accompanied by the change of cracking behavior. Such a behavior in pure torsion fatigue loading has never been documented for an aluminum alloy, to the best of the author's knowledge. A similar kink was observed in strain-life curve of an induction hardened steel where the gradient material properties resulted in subsurface cracking [84].

Two alloys similar in primary austenitic phase structure were investigated for fatigue and crack propagation properties. One is the traditionally used austenitic steel AISI 304L. The other is a relatively new stainless steel AL6-XN developed by Allegheny Ludlum Corporation. The primary goal of development of the latter alloy was increase in corrosion resistance as compared to the traditional 300-series steels, which was achieved by addition of higher Nickel content, lowering the Carbon content and introducing Nitrogen to the alloy. The major application of the AL6-XN material was considered in off-shore platforms, however since its introduction to the industry it has been used in variety of applications requiring high corrosion resistance, from pharmaceutical equipment to cooling systems of nuclear reactors. Significant amount of research has been done on corrosion and stress corrosion properties of AL6-XN stainless steel and it is well accepted now that the material has superior resistance to corrosion, chloride pitting and stress corrosion. At the same time, the research on fatigue properties of this alloy has not been completely developed. Overall, the cyclic response of the two materials under axial tension-compression loading is different. The resulting stresses in AISI 304L material are higher than the cyclic stresses in AL6-XN. This is illustrated in Fig.101(a) where two representative hysteresis loops from low cycle fatigue regime are shown. The differences in cyclic behavior in tension-compression are also evident from comparison of the corresponding cyclic stress-plastic strain curves (CSSC) (Fig.101(b)). It can be seen that the CSSC for AL6-XN material shows a clear plateau regime in which the stress amplitude remains almost constant within a wide range of plastic strain amplitudes. In case of AISI 304L, similar to other stainless steels [85], such a plateau is rather hard to define. It can be also noticed that the two curves intersect each other at approximately $\Delta\varepsilon^{p}/2 = 3\times 10^{-4}$ and when the plastic strain amplitude is below this value, the corresponding stresses of AL6-XN alloy are higher the the stress amplitudes in 304L material. This observation can serve as an additional explanation of the strain-life behavior of two materials shown in Fig. 101.

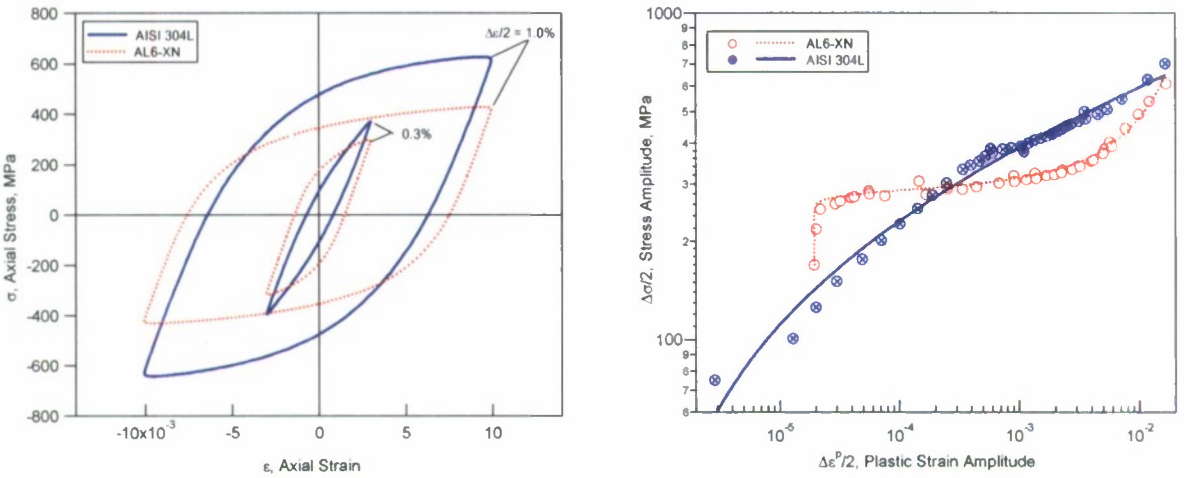

(a) (b)

Fig.101 Comparison of cyclic behavior of the two stainless steels. a) stress-strain hysteresis loops; b) cyclic stress-plastic strain curves under tension-compression

Both the AL6-XN and AISI 304L stainless steels display a dependence of the cracking behavior on the loading amplitude. In case of AL6-XN alloy, the material displays tensile cracking when the equivalent plastic strain amplitude is less than 3.7×10^{-3} or the equivalent stress amplitude is less than 360 MPa. The material exhibits mixed cracking when the equivalent plastic strain amplitude is higher than 3.7×10^{-3}. In AISI 304L such a demarcation line between mixed and tensile cracking modes corresponds to equivalent plastic strain amplitude of 2.5×10^{-3} and equivalent stress amplitude equal to 370 MPa.

The AL6-XN alloy under pure torsion displays an "abnormal" phenomenon. The shear strain-life curve shown in Fig.41 consists of two distinct regimes associated with different cracking behavior. More importantly, these two regimes are separated by a transitional plateau in the *S-N* curve characterized with a shear strain amplitude of approximately $\Delta\gamma/2 = 1.04\%$. Within the plateau in the shear strain-life curve, the fatigue life can differ by a factor of three. To the best of the authors' knowledge, there has been no previous report of the phenomenon similar to the plateau in the *S-N* curve on a polycrystalline metallic material. An observation on the shear stress-strain hysteresis loops reveals no difference between the two specimens at the two ends of the plateau. In other words, for the same plastic strain energy and macroscopic stress-strain response, the fatigue life can be significantly different. Such a feature obviously requires a further investigation. The phenomenon could be related to the details in the distribution of the deformation bands and the inclusions at the microscopic level.

Many multiaxial fatigue criteria have been proposed by researchers over the years. The most widely accepted are the Smith-Watson-Topper (SWT) and the Fatemi-Socie-Kurath (FSK) multiaxial fatigue parameters. The general concept of a critical plane approach is the consistency of the fatigue damage with the observed dependence of the cracking behavior on the stress and the loading path. Accordingly, a critical plane approach not only predicts fatigue life but also the material plane where the fatigue crack is formed. Generally, the critical plane approaches were developed for materials displaying either shear or tensile cracking. The FSK criterion is designed for shear cracking and the SWT parameter is for a material displaying tensile cracking. If critical plane orientation within the FSK model is defined as a plane of maximum fatigue parameter, a theoretical possibility of predicting tensile cracking exists. By increasing the value of constant K in Eq.(9) the orientation of critical plane deviates from maximum shear orientation (Fig.74) and generally speaking, for sufficiently large K a tensile orientation of crack can be predicted. Such situation however would lead to absolutely unreasonable prediction of fatigue life, since the value of constant K is determined from the baseline fatigue data. In other words, the FSK criterion was developed targeting the materials which display shear cracking and the constant K is used to correlate the fatigue life data of those materials.

It has been widely accepted that the SWT criterion particularly works well for the aluminum alloys. The current investigation on 7075-T651 aluminum alloy suggests that the SWT criterion can predict fatigue life reasonably well for most of the fatigue experiments conducted in the current study. It confirms an early conclusion that the criterion cannot correctly predict the results of tension-compression experiments with the maximum stress being very low. It is obvious that the criterion does not predict fatigue failure under compression-compression loading. Finally, the SWT criterion fails to predict correct cracking orientations of most specimens tested in present investigation.

A significant improvement is achieved with the modified SWT criterion in terms of life prediction and prediction of cracking direction. The results shown in Fig. 69 indicate that the modified SWT criterion can consider the mean stress effect fairly well for all of the experiments conducted in the current investigation. Since the selection of material constants in Eq.(8) has incorporated the dependence of the observed cracking behavior on the loading magnitude, the modified SWT criterion correlates very well the fully reversed tension-compression and pure shear experiments in terms of orientation of fatigue cracks. For the tubular specimens subjected to the combined axial-torsion loading, the predictions of fatigue life and cracking direction have also been improved by using the modified SWT fatigue criterion. The modified SWT criterion, Eq.(8), integrates both the normal components and the shear components of the stress and strain on a material plane. The two terms are combined using a material constant b which ranges from 0.0 to 1.0. When b equals 1, the criterion is identical to the SWT criterion. When $b = 0$, the criterion is for a material that the normal stress and strain components do not contribute to fatigue damage on a material plane. Since the criterion is an extension of the SWT fatigue parameter, the good consideration of the mean stress effect is inherited. One of the advantages of using the SWT criterion is that the baseline can be fully determined from the fully reversed tension-compression fatigue experiments. This is because the SWT criterion contains no material constants. Clearly, the introduction of the material constant, b, in Eq.(4), will require more fatigue experiments in order to determine it. However, this material constant is necessary to consider the varying cracking behavior of the material with the loading magnitude.

Although the modified SWT criterion can predict fatigue failure under the compression-compression loading, it should be noted that the criterion is not able to properly predict the cracking direction under compression-compression. The cracking surface in the compression-compression specimen was found to be perpendicular to the loading axis while the predicted cracking surface has its normal being $\pm 45°$ to the loading axis.

Jiang [59] developed a critical plane multiaxial fatigue criterion that incorporates both the shear and normal stress and strain components on a material plane. The criterion is based upon the plastic deformation and is in an incremental form. Comparing the modified SWT criterion, Eq. (8), with the multiaxial fatigue criterion developed by Jiang [59], it can be found that both models consider the mean stress effect and can be used for materials displaying different cracking behavior. An obvious advantage of the incremental fatigue criterion by Jiang [59] is the elimination of a cycle-counting method for any general loading histories. On the other hand, cyclic plasticity is necessary for fatigue to occur in the incremental fatigue criterion. Therefore, the incremental fatigue criterion is difficult to use for a material that displays very small or minimal cyclic plasticity in the high cycle fatigue regime. An advantage of the fatigue parameter of Eq. (8) is that it can be applied for a material that does not have significant cyclic plasticity. However, the SWT criterion and its modification use stress/strain quantities such as strain amplitude and maximum stress that are based on the definition of a loading cycle or reversal. As a result, a cycle-counting method is needed to assess fatigue damage under variable amplitude loading conditions. Currently, the only accepted cycle-counting method that is designed to find the closed stress-strain hysteresis loops in a loading history. For uniaxial loading, the use of the rain-flow method to identify a cycle or reversal is straightforward. However, when the rain-flow counting method is used for nonproportional multiaxial loading, difficulties arise because the stress and strain quantities on a material plane may not form consistent stress-strain hysteresis loops for normal and shear components. On a given material plane or direction, both the magnitude and direction of the shear components may vary with time.

As far as modeling of the fatigue behavior of AL6-XN stainless steel is concerned, its fatigue properties under torsion and the dependence of the cracking behavior on the loading amplitude result in a difficulty for the multiaxial fatigue criteria to model. When dealing with baseline correlation based on the SWT and FSK models, the choice of which part of the shear *S-N* curve to use for baseline fit can yield different predictions. The part corresponding to mixed cracking (above the plateau in Fig.40) lies close to the S-N curve under tension-compression and when this part is used as a baseline fit, the close fatigue life predictions are made only for the lower cycle fatigue regime. At the same time, taking the part corresponding to tensile cracking as a baseline would give close predictions for higher cycle fatigue data. As an attempt to give a prediction for the whole spectrum of fatigue data, an average fit was adopted (Fig.73).

In terms of the fatigue life predictions, the FSK criterion appears to provide a slightly better prediction for the AL6-XN steel within the loading cases investigated. The Jiang model provides a least satisfactory fatigue life prediction for the loading cases investigated. In terms of cracking direction prediction, the Jiang criterion does the best among the three criteria evaluated. This is because the Jiang criterion is designed for considering different cracking behavior using a material constant while the other two criteria are either for tensile cracking or shear cracking. Since the cracking behavior of material under investigation depends on the loading magnitude, the parameter b is represented as a function of a memory stress (Eq.(13)) that reflects the loading amplitude. With such a formulation, the model predicts the orientation of fatigue cracks with good accuracy which can be seen from the examples of fatigue cracks in Figs. 76, 77.

When discussing the fatigue initiation cracking direction, there exist different opinions with regard to the definition of the experimentally observed cracking direction due to the inherent roughness of the crack surface. The current investigation adopts a macroscopic crack definition with the crack length being in the millimeter scale. This is because the stress and strain used in most fatigue criteria are based upon the traditional continuum mechanics concepts. A polycrystalline material consists of grains that are oriented in different directions. An implicit assumption in macroscopic continuum mechanics is that a material point is small enough so that it can be treated as a mathematical point but it is large enough to contain at least several grains so that the material can be treated as homogeneous. In other words, the stress and strain are defined in a macroscopic level. Considering the general range of the grain size of a metallic polycrystalline material, the size of the basic material "element" should be in the millimeter scale rather than the micrometer scale. As a result, discussions on cracking behavior in the current report are limited to the visible and macroscopic cracks.

While uniaxial and pure shear fatigue experiments are often used to provide the baseline fatigue data for a material, the two basic loading modes also provide the basic cracking behavior. The cracking behavior of a material can be classified according to the observations of the specimens under fully reversed tension-compression and pure shear loading. The transition of cracking behavior from one type to another due to the change of loading magnitude has been well recognized. However, the cracking behavior under the two basic loading modes has not been well considered in the development of the critical plane multiaxial fatigue models. In fact, the cracking behavior observed on the two basic loading modes can serve as the critical observations to evaluate a critical plane approach. If a critical plane approach is not able to mimic the cracking behavior observed under fully reversed tension-compression and pure shear, its capability to predict cracking behavior under more general stress states is naturally in doubt. The rich cracking behavior observed on the 7075-T651 aluminum alloy and AL6-XN stainless steel can serve as benchmark experiments that can be used to critically evaluate a critical plane approach.

The crack growth experiments conducted under constant-amplitude loading confirm the sensitivity of the crack growth of all of the alloys under investigation to the R-ratio in ambient air. The curves of the crack growth rate under different R-ratios appear parallel in the traditional log-log da/dN - ΔK coordinates system and tend to merge at very high R-ratios. The R-ratio effect in 4340 VM steel is more pronounced in the near-threshold crack growth than in the stable crack growth stage, which produces a fan-shaped crack propagation rate curves for this material (Fig.60). It was pointed out [67] that the crack growth was the result of the action of both ΔK and $K_{\max}$ parameters. Under low values of R-ratios, the crack was driven mainly by $K_{\max}$ while ΔK plays more important role as a driving force under high values of R-ratios. The two driving forces, ΔK and $K_{\max}$, responsible for fatigue crack propagation are incorporated into Kujawski's parameter. This parameter is capable of correlating well the crack growth curves for different R-ratios (Figs.80, 81, and 84) with especially good correlation produced for AL6-XN steel.

Most of metallic materials display crack growth retardation due to application of tensile overload. The severity of the retardation depends on the material and on the magnitude of overloading. At the same time, effect of underloading (application of compressive overload) is either negligible (7075-T651, AL6-XN) or produces a short period of crack growth acceleration (AISI 304L). While the major manifestation of overload effect lies in deceleration of crack propagation, the details of crack growth behavior in post-overloading zone are different for the materials investigated in the present study. Recovery of crack growth rate after overloading occurs rather quickly in 7075-T651 aluminum alloy. At the same time, the overload effect is more prolonged in case of AL6-XN and 304L stainless steels. Additionally, the immediate response to tensile overload in 304L stainless steel and in 4340VM alloy displays a short period of acceleration of the crack growth. Such acceleration is especially pronounced in 4340VM aerospace steel (Fig.62).

Behavior under high-low loading sequence was found to be similar for the materials under investigation. When tested under conditions with the same R-ratio in both high and low loading steps, crack growth retardation similar to the overload effect can be observed in the low amplitude loading part of the experiment. The same behavior is observed when the same minimum load is applied throughout the experiment (Figs 19, 32(b,c), 50(b,c), and 62(b,c)). However, reduction in loading amplitude has no effect on crack growth when the value of the maximum load in a loading cycle is kept constant in both parts of the experiment (Figs 32(a), 50(a) and 62(a)).

The Wheeler's model [70] is often used to describe the overload effect on crack growth. The current study shows that the Wheeler model can describe the overall crack growth retardation reasonably well after the application of an overload. However, the model misses the detailed crack growth upon an overload (Fig.79). The model cannot capture the gradual decrease in the crack growth rate right after the application of the overload for 304L and AL6-XN materials. There is a tradeoff between a proper modeling of the lowest crack growth rate and the crack growth in the overload plastic influencing zone. More importantly, the model assumes that the plastic zone size right before overloading is identical to that right after the application of the overload. This is inconsistent with the results from the finite element analysis of the plastic zones near the crack tip due to overloading [74]. In fact, the plastic zone size ahead of a crack tip is significantly reduced by the overload.

Modifications of Wheeler's model were introduced targeting the fatigue crack growth behavior in post-overloading zone of different materials under investigation. By modifying the size of the plastic zone after application of overload (Eqs(23, 30)) closer predictions can be made for AL6-XN and 7075-T651 alloys (Figs. 17, 19, 86 and 87). In order to consider the short period of crack growth acceleration in AISI 304L stainless steel, the modified Wheeler's model introduced by Yuen and Taheri [51] was used. By introducing a delay retardation parameter in Wheeler's model (Eq. (27)), the gradual deceleration of the crack growth to the minimum value in the post-overload zone can be described. In addition, the ΔK_{acc} (Eq.(28)) parameter represents the change of stress intensity factor range from its value during the overload to the value corresponding to the minimum on the crack growth curve. The parameter enables the model to predict the acceleration of crack growth after overloading. It should be mentioned that the model used in the present paper was adopted from [51] with some modifications. In the description of the model [51], the size of the plastic zone is determined as,

$$r_{pi} = \lambda_p \left(\frac{K_i}{\sigma_y} \right)^2 \tag{37}$$

where K_i is the stress intensity factor corresponding to crack length a_i. The constant λ_p is determined based on Wheeler's approach from the following equation,

$$a_f = a_{OL} + r_{pOL} - r_{pf} = a_{OL} + \frac{\lambda_p}{\sigma_y^2} \left[K_{OL}^2 - K_f^2 \right] \tag{38}$$

where a_f is the crack length at which the crack growth rate returns to the stable growth regime, and K_f is the stress intensity factor corresponding to a_f. Similar to Eq. (37), the delay retardation zone is determined by,

$$r_{Di} = \lambda_D \left(\frac{K_i}{\sigma_y} \right)^2 \tag{39}$$

and the constant λ_D is found from the relation similar to Eq.(38) but based on the delay retardation zone parameters with the following form,

$$a_{Df} = a_{OL} + r_{DOL} - r_{Df} = a_{OL} + \frac{\lambda_D}{\sigma_y^2}\left[K_{OL}^2 - K_{Df}^2\right] \tag{40}$$

where a_{Df} is the final crack length at the end of delay retardation zone and K_{Df} is the stress intensity factor corresponding to a_{Df}. In such a formulation, the parameters a_f and a_{Df} are needed to be known from the crack growth curve in order to establish the plastic zone size following Eqs. (37) and (38), which practically reduces the concept of modeling to curve fitting of experimental data. In other words, the experimentally obtained crack growth curve is needed in order to model the same crack growth curve.

The current work adopts Irwin's formulation for the size of the plastic zone (Eq.19) and sets the relation $r_{D,OL} = \xi \cdot r_{p,OL}$ with ξ being a fitting constant. Furthermore, for the *i*-th loading cycle, $r_{Di} = r_{pi}$. With such a modification in the formulation, a total of three constants are needed in the model to predict the post-overload crack growth behavior. These constants can be obtained by fitting the experimental data of one overloading experiment. The same values of constants were used in crack growth predictions for all the other specimens subjected to overloading and high-low loading histories. The predictions shown in Figs.63 and 64 suggest that the model works rather well and it captures the major trends of the post-overload crack growth behavior. It should be noted that, similar to Wheeler's model, the approach described above targets the crack growth deceleration after tensile overload. Neither Wheeler's model nor the modification discussed in the current investigation can capture the crack growth rate increase observed after the application of a compressive underload.

Modifications to Wheeler's model proposed in the current investigation can predict the tendency of crack growth rate in the post-overload zone rather well. However the form of the model itself suggests its empirical nature based on the stress intensity factor concept. The exponents in the model bear little or no physical significance and are determined based on the "best fit" approach. It is difficult for such a concept to consider the physical mechanisms governing the local plastic deformation and fracture at the crack tip which is crucial for accurate description of the process of fatigue crack growth.

As a part of the current work, an effort is made to develop a unified physically based approach, which incorporates cyclic plasticity and accumulation of fatigue damage. The approach consists of two steps: (1) elastic-plastic finite element (FE) analysis of the component; (2) the application of a multiaxial fatigue criterion for the crack initiation and growth predictions based on the outputted stress-strain response from the FE analysis. The FE analysis is characterized by the implementation of an advanced cyclic plasticity theory that captures the important cyclic plasticity behavior of the material under the general loading conditions. The fatigue approach is based upon the notion that a material point fails when the accumulated fatigue damage reaches a certain value and the rule is applicable for both crack initiation and growth. As a result, one set of material constants is used for both crack initiation and growth predictions. All the material constants are generated by testing smooth specimens. The approach was used to simulate the crack growth behavior of 304L and AL-6XN stainless steels. The results shown in Figs 92-100 reveal a rather good prediction.

It should be stressed, that the approach under discussion used in the current investigation for the crack growth prediction is fundamentally different from the commonly used methods where a stress intensity factor or J-integral is used. There are three major features that distinguish the current approach from the traditional methods. The stress intensity factor was developed to avoid the stress and strain singularity of the material at the crack tip. The stress intensity factor is based on the elastic deformation concept and it is a bulk measure of the stressing severity of the material near the crack tip upon the application of the external loading. It has been well known that while the stress intensity factor can be used to deal with the cases with constant amplitude loading, modifications and additional coefficients have to be added in order to consider such factors as the notch effect, the R-ratio effect, and effects of variable amplitude loading. As a result, many constants are introduced and they are determined by best fitting the experimentally obtained crack growth data. The methods tend to become a curve fitting technique instead of predictions. The current approach attempts to use the local stress and strain directly for the fatigue damage assessment. Therefore, no crack growth experimental data is used for the determination of the material constants in the models.

Traditionally, crack initiation is modeled using the continuum mechanics method where stress and strain are used to access fatigue damage. A separate model, often based on the stress intensity factor concept, is needed to deal with the crack growth. In order to use the fracture mechanics approach for the crack growth prediction, an initial crack length or an initiation crack length must be defined. Since the predicted crack propagation life is very sensitive to the initial crack length, the definition of the crack initiation size is more to fit the experimental data than to have a physical base, or rather, the initial crack size characterizing crack initiation in the traditional methods is a fitting constant. Within the fatigue approach discussed in the current investigation the integrated consideration of the crack initiation and crack growth is employed. One single fatigue criterion is used for both crack initiation and crack propagation. The unified consideration allows for a seamless transition from crack initiation to crack growth without necessity to define a crack initiation crack size.

For the prediction of crack growth, a separate criterion is generally needed for the determination of the crack growth direction. For example, a minimum strain energy density factor theory [86-88] specifies that the fatigue crack growth rate is related to the range of the strain energy density but the crack growth direction is determined by the minimum strain energy density factor with respect to the orientation of the material plane in a loading cycle. Within the maximum tangential stress approach, the crack growth rate is assumed to be related to an effective stress intensity factor range while the crack growth direction is determined by using a maximum tangential stress criterion [89]. By using the critical plane multiaxial fatigue criterion, Eq.(10), the current approach predicts the crack growth rate and the crack growth direction in an integrated manner. The fatigue criterion determines the critical plane where the cracking surface is to be formed and the stress and strain quantities on the critical plane determine the crack growth rate. The approach was used to predict with success the cracking direction under a loading condition involving change in loading directions [90].

CONCLUSIONS

A systematic experimental investigation was conducted on the fatigue behavior of 7075-T651 aluminum alloy. The following conclusions were obtained from the study,

1) The mean stress has a significant effect on fatigue life.
2) Fatigue damage was found to occur under compression-compression loading.
3) The material displays shear cracking, mixed cracking, and tensile crack behavior dependent on the loading magnitude.
4) The Smith, Watson, and Topper (SWT) fatigue criterion can predict the fatigue life well for most of the experiments except those with very low or negative maximum stresses. However, the SWT parameter does not predict correctly the cracking behavior for most of the specimens.
5) A modified SWT criterion combines the normal and shear components of the stresses and strains on material planes. The modified criterion significantly improves the predictions of the fatigue life and cracking behavior.
6) Comprehensive crack growth experiments were conducted on 7075T651 aluminum alloy. The influences of the R-ratio, overloading, underloading, and high-low sequence loading were experimentally studied.
7) An effective fatigue crack driving force, $(K_{\max})^{\alpha}(\Delta K^{+})^{1-\alpha}$ defined by Kujawski can correlate well the fatigue growth rate for the effect of different R-ratio when the R-ratio was in the range of -2 to 0.5.
8) The retardation of fatigue crack growth rate after a single overloading or after reducing the loading amplitude in a high-low sequence loading was very significant. However, the acceleration of crack growth rate after a single underloading was not significant.
9) A modified Wheeler's model based on the evolution of remaining influencing plastic zone can very well predict the influence of overloading and high-low sequential loading on the fatigue crack growth.

Work on AISI 304L stainless steel results in the following conclusions,

1) The crack growth of the material is sensitive to the R-ratio based upon the traditional $da/dN - \Delta K$ representation;
2) The application of a single tensile overload in an otherwise constant-amplitude loading history results in a short period of acceleration in crack growth followed by a significant crack growth retardation;
3) The application of a compressive overload (underload) results in a short-lived period of acceleration in crack growth right after underloading; The magnitude of such an acceleration depends on the loading amplitude applied during the constant-amplitude loading;

4) A higher loading amplitude followed by a lower loading amplitude in a two-step loading sequence has no effect on the crack growth if the maximum load in the two loading steps is the same;
5) In a two-step high-low loading experiment, the first loading step has a significant influence on the subsequence crack growth in the second loading step if the minimum load or the R-ratio is the same in the two loading step.;
6) The parameter combing ΔK^+ and $K_{\max}$ demonstrates a good correlation with the experimental results for the R-ratio effect. The effects of overloading and high-low sequence loading can be reasonably modeled using a modified Wheeler's model in which a delay retardation parameter is introduced.
7) An approach was applied for the prediction of the fatigue behavior of notched members under constant-amplitude loading and step loading. Elastic-plastic stress analysis was conducted to determine the detailed stress and strain in the notched and cracked component. The application of a multiaxial fatigue criterion using the stress and strain outputted from the numerical stress analysis resulted in the prediction of the fatigue initiation and crack growth rate. With the material constants determined solely from testing the smooth specimens, the crack initiation and the crack growth of a notched member can be properly modeled.

The results obtained from studying AL6-XN stainless steel lead to the following conclusions,

1) The material displays significant nonproportional hardening and overall cyclic softening.
2) With identical equivalent strain amplitude, the fatigue life under pure torsion is higher than that under tension-compression, and the 90^0 out-of phase strain-controlled axial-torsion fatigue experiment yields the lowest fatigue life.
3) Two distinct regimes in the strain-life curve under pure torsion loading can be identified: one corresponding to tensile cracking and the other corresponding to mixed cracking mode. The two regimes are separated by a transition zone characterized by a plateau in the strain-life curve.
4) The observed intragranular crack growth contributes to the higher fatigue resistance of the AL6-XN alloy as compared to the traditional 300-series stainless steels.
5) Three different critical plane multiaxial fatigue criteria were evaluated based upon the experimental results obtained from the AL6-XN alloy. While the SWT and FSK models provide fatigue life predictions in reasonable agreement with the experimental observations, they cannot properly predict the dependence of the cracking behavior on the loading magnitude.
6) The Jiang criterion can predict the fatigue cracking behavior of the AL6-XN steel in the most accurate way but the fatigue life prediction is less desirable.
7) The models have a difficulty to describe the fatigue behavior of the material under pure shear loading.
8) The crack growth of AL6-XN is sensitive to the R-ratio.

9) Crack propagation is observed to be intragranular.

10) The application of a single tensile overload in an otherwise constant amplitude loading results in a significant crack growth retardation.

11) The application of a compressive overload (underload) can result in a short-lived period of acceleration in crack growth right after underloading.

12) A higher loading amplitude followed by a lower loading amplitude in a two-step loading sequence has no effect on the crack growth if the maximum load in the two loading steps are identical.

13) In a two-step high-low loading experiment, the first loading step has a significant influence on the subsequence crack growth in the second loading step if the minimum load or the R-ratio is the same in the two loading step.

14) The parameter combing ΔK^{+} and $K_{\max}$ demonstrates a good correlation with the experimental results for the R-ratio effect. The effects of overloading and high-low sequence loading can be reasonably modeled using a modified Wheeler's model considering the plastic zone size.

The following conclusions can be made based upon the results obtained from studying AISI 4340 VM steel,

1) The material displays overall cyclic softening under cyclic loading.

2) With identical equivalent strain amplitude, the fatigue life under pure torsion is higher than that under tension-compression in the low-cycle fatigue. The torsion and tension-compression S-N curves merge together in high cycle fatigue part.

3) The cyclic stress-strain curve shows a distinct plateau. Non-Masing behavior was observed for this material.

4) Cracks in smooth un-notched specimens formed consistently on planes of maximum shear in pure torsion and were oriented and approximately 24^{0} with respect to the vertical axis of a specimen when tested in fully reversed tension-compression.

5) The crack growth of 4340 VM is sensitive to the R-ratio. The R-ratio effect is especially pronounced in the near threshold crack growth and diminishes with increasing ΔK, which results in "fan-shaped" curves of crack growth rate.

6) The application of a single tensile overload in an otherwise constant amplitude loading results in crack growth retardation. The short period of significant acceleration of crack growth can be observed immediately after application of overload.

7) A higher loading amplitude followed by a lower loading amplitude in a two-step loading sequence has no effect on the crack growth if the maximum load in the two loading steps are identical.

8) In a two-step high-low loading experiment, the first loading step has a significant influence on the subsequence crack growth in the second loading step if the minimum load or the R-ratio is the same in the two loading step.

PUBLICATIONS GENERATED FROM THE CURRENT SUPPORT

(1) Fan, F., Kalnaus, S., and Y. Jiang, Y., 2008, "Modeling of Fatigue Crack Growth of Stainless Steel 304L," *Mechanics of Materials*, Vol.40, pp.961-973

(2) Kalnaus, S. and Jiang, Y., 2008, "Fatigue of AL6XN Stainless Steel," ASME *Journal of Engineering Materials and Technology*, Vol.130, 031013

(3) Zhao, T., Zhang, J., and Jiang, Y., 2008, "A Study of Fatigue Crack Growth of 7075-T651 Aluminum Alloy," *International Journal of Fatigue*, Vol.30, pp.1169-1181

(4) Zhao, T. and Jiang, Y., 2008, "Fatigue of 7075-T651 Aluminum Alloy," *International Journal of Fatigue*, Vol.30, pp.834-849.

(5) Zhang, J. and Jiang, Y., 2008, "Constitutive Modeling of Cyclic Plasticity Deformation of a Pure Polycrystalline Copper," *International Journal of Plasticity*, Vol.24, pp.1890-1915.

(6) Jiang, Y. and Zhang, J., 2008, "Benchmark Experiments and Characteristic Cyclic Plasticity Behavior," *International Journal of Plasticity*, Vol.24, pp.1481-1515

(7) Ding, F., Feng, M., and Jiang, Y., 2007, "Modeling of Fatigue Crack Growth from a Notch," *International Journal of Plasticity*, Vol.23, No.7, pp.1167-1188

(8) Ding, F., Zhao, T., and Jiang, Y., 2007, "A Study of Fatigue Crack Growth with Changing Loading Direction," Eng Fract Mech **74**, pp.2014-2029

(9) Kalnaus, S. and Jiang, Y., 2006, "Fatigue Life Prediction of Copper Single Crystals Using a Critical Plane Approach," *Engineering Fracture Mechanics*, Vol.73, pp.684-696.

(10) Kalnaus, S. and Jiang, Y., 2009, "An Experimental Study of Fatigue Behavior of 4340 Steel," To be submitted to *Engineering Fracture Mechanics*

(11) Jiang, Y., 2008, "Multiaxial Fatigue," *International Conference on Fracture Mechanics*, Nov.1-5, 2008, Hangzhou, China

(12) Jiang, Y., 2008, "An Experimental Evaluation of Critical Plane Multiaxial Fatigue Criteria," *International Conference on Fatigue Damage of Structural Materials VII*, Hyannis, MA, Sept.14-19, 2008

(13) Jiang, Y., 2008, "The Applicability of Macroscopic Continuum Mechanics to Fatigue Life Prediction," *2nd International Conference on Heterogeneous Material Mechanics* (ICHMM-2008), Huangshang, China, June 3-8, 2008

(14) Jiang, Y., Feng, M., and Gao, Z.L., 2008, "Finite Element Modeling of Crack Tip Plasticity with the Consideration of Element Size and Element Type," *Plasticity'08: International Symposium on Plasticity 2008 and Its Current Applications*, Kona, Hawaii, Jan.3-8, 2008

(15) Jiang, Y., 2006, "A Fatigue Prediction Approach Based upon Cyclic Plasticity of Materials," *Plasticity'2006*, Halifax, Canada, July 19-23, 2006

(16) Kalnaus, S., Fan, F., and Jiang, Y., 2007, "Fatigue and Cyclic Plasticity Properties of a super-austenitic Stainless Steel," P*roceedings of PVP2007, 2007 ASME Pressure Vessels and Piping Division Conference*, July 22-26, 2007, San Antonio, Texas, PVP200726478

(17) Jiang, Y. and Zhao, T., 2006, "Multiaxial Fatigue of 7075-T651 Aluminum," *International Conference on Fatigue Damage of Structural Materials VI*, Hyannis, MA, Sept.16-22, 2006

(18) Jiang, Y., Ding, F., Zhao, T., and Zhang, J., 2006, "An Elastic-Plastic Finite Element Analysis of Residual Stresses near Notch and Crack Tip," *International Conference on Fatigue Damage of Structural Materials VI*, Hyannis, MA, Sept.16-22, 2006

REFERENCES

[1] Endo, T., Morrow, J., 1969, "Cyclic Stress-Strain and Fatigue Behavior of Representative Aircraft Metals," J of Mater JMLSA, **4**(1), pp.159-175.

[2] Nowack, H., Trautmann, K.H. In: Materials Data for Cyclic Loading, Part D: Aluminum and Titanium Alloys. Boller CHR, Seeger T, editors. Elsevier, NY, 1987, pp. 69-77

[3] Kurath, P. In: Materials Data for Cyclic Loading, Part D: Aluminum and Titanium Alloys. Boller CHR, Seeger T, editors. Elsevier, NY, 1987, pp. 81-89

[4] Bergmann, J.W. Zur Betriebsfestigkeitsbemessung gekerbter Bauteile auf der Grundlage der ortlichen Beanspruchungen. Veroffentilichungen des Instituts fur stahlbau und Werkstoffmechanik d. TU Darmstadt, 1983; Heft 37

[5] Sanders Jr, T.H., Mauney, D.A., and Staley, J.T. In: Strain control fatigue as a tool to interpret fatigue initiation of aluminum alloys. Fundamental aspects of structural alloy design. Jaffee RI, Wilcox BA, editors. NY, USA: Plenum Publishing, 1977

[6] Fatemi, A., Plaseied, A., Khosrovaneb, A.K., and Tanner, D., 2005, "Application of bi-Linear log–log S–N Model to Strain-Controlled Fatigue Data of Aluminum Alloys and its Effect on Life Predictions," Int J of Fatigue, **27**, pp. 1040-1050.

[7] DeBartolo, E.A., Hillberry, B.M., 2001, "A Model of Initial Flaw Sizes in Aluminum Alloys," Int J of Fatigue, **23**, pp. S79-S86

[8] Xue, Y., Jordon, B., Horstemeyer, S., and Horstemeyer, M.F., 2005, "Fatigue Experiments, Damage Evaluation and Multiscale Modeling for AA 7075-T651." Proceedings of the 2005 SEM Annual Conference and Exposition on Experimental and Applied Mechanics 2005, pp. 1443-1450

[9] Nadai, A., 1950, "Theory of Flow and Fracture of Solids." Vol. 1, 2nd Ed., McGraw-Hill Book Company, Inc., New York, Toronto, and London.

[10] Socie, D. F., 1987, "Multiaxial Fatigue Damage Models," ASME J. Engng. Mater. Tech. **109**, pp. 293-298.

[11] Socie, D. F., Kurath, P., and Koch, J., 1989, "A Multiaxial Fatigue Damage Parameter," Biaxial and Multiaxial Fatigue, EGF3, Miller, K. J., Brown, M., W., Eds. Mechanical Engineering Publications, London 1989, pp. 535-550.

[12] Hua, C. T., and Socie, D. F., 1985, "Fatigue Damage in 1045 Steel under Variable Amplitude Biaxial Loading," Fat. Eng. Mater. Struct. **8**(2), pp. 101-104.

[13] Segan, E., 1989, "Corrosion Fatigue of 7005-T53 Aluminium Alloy," PhD. Thesis.

[14] Sakai, T., Sakai. T., Okada, K., Furuichi, M., Nishikawa, I., and Sugeta, A., 2006, "Statistical Fatigue Properties of SCM435 Steel in Ultra-long-life Regime Based on JSMS Database on Fatigue Strength of Metallic Materials," Int. J. Fatigue **28**, pp. 1486-1492.

[15] Marines, I., Bin, X., and Bathias, C., 2003, "An Understanding of Very High Cycle Fatigue of Metals," Int. J. Fatigue **25**, pp. 1101-1107.

[16] ASTM E647-05, Standard Test Method for Measurement of Fatigue Crack Growth Rates. ASTM International.

[17] von Euw, E. F. J., Hertzberg, R. W., and Robert, R., 1972, "Delay Effects in Fatigue-Crack Propagation," ASTM STP 513, American Society for Testing and Materials, Philadelphia, 230-259.

[18] Atanasiu, N.E., 1983, "Fatigue Crack Propagation and Threshold of Type 304L Austenitic Stainless Steel." Mechanical Behavior of Materials IV: Proceedings of the 4th International Conference, Stockholm, Sweden, 15-19 August 1983

[19] Andriamiharisoa, H., Habashi, M., Talbot-Besnard, S., Galland, J., and Azou, P., 1980, "Effects of Internal and Environmental Hydrogen on Fatigue Crack Growth Rate in Metastable Austenitic Structure." Hydrogen Effects in Metals: Conference Proceedings. Moran, Wyo, 26-31 Aug. 1980, TMS/AIME, pp. 619-628.

[20] Wheatley, G., Hu, X.Z., and Estrin, Y., 1999, "Effect of a Single Tensile Overload on Fatigue Crack Growth in a 316L Steel," Fatigue Fract Engng Mater Struct **22,** pp. 1041-1051.

[21] Source Book on Stainless Steels. American Society for Metals. Metals Park, OH, USA, 1976: 408 pp.

[22] Mei, Z., Morris J.W. Jr., 1990, "Influence of Deformation-Induced Martensite on Fatigue Crack Propagation in 304-Type Steels," Metal Tran A **21A**(12), pp. 3137-3152.

[23] Katz, Y., Bussiba, A., and Mathias, H., 1981, "The Influence of Austenite Stability on Fatigue Crack Growth Retardation." Materials, Experimentation and Design in Fatigue: Conference Proceedings, Warwick University, England, 24-27 Mar. 1981, pp. 147-158.

[24] Katz, Y., Bussiba, A., and Mathias, H., 1982, "The Role of Induced Phase Transformations on Fatigue Processes in AISI 304L." Fracture and the Role of Microstructure: Conference Proceedings, Vol. 2: Fatigue; Leoben, Austria, 22-24 Sept 1982, pp. 503-511.

[25] Bayerlein, M., Christ, H-J, and Mughrabi, H., 1989, "Plasticity-Induced Martensitic Transformation of AISI 304L Stainless Steel," Mat Sci Eng **A114**, pp. L11-L16.

[26] Krupp, U., Christ, H-J, Lezuo, P., Maier, H.J., and Teteruk, R.G., 2001, "Influence of Carbon Concentration on Martensitic Transformation in Metastable Austenitic Steels Under Cyclic Loading Conditions," Mat Sci Eng **A319-321**, pp. 527-530.

[27] Rho, B.S., Hong, H.U., and Nam, S.W., 1998, "The Fatigue Crack Initiation at the Interface Between Matrix and δ-Ferrite in 304L Stainless Steel," Scrip Mat **39**(10), pp. 1407-1412.

[28] Hong, H.U., Rho, B.S., and Nam, S.W., 2002, "A Study on the Crack Initiation and Growth From δ-ferrite/γ Phase Interface Under Continuous Fatigue and Creep-Fatigue Conditions in Type 304L Stainless Steels," Int J Fatigue **24**, pp. 1063-1070.

[29] Nemat-Nasser, S., Guo, W., and Kihl, D. P., 2001, "Thermomechanical Response of AL6XN Stainless Steel over A Wide Range of Strain Rates and Temperatures," J. Mech. Phys. of Solids **49**, pp. 1823-1846.

[30] Huang, Y.L., Oguocha, I.N.A., and Yannacopoulos, S., 2005, "The Corrosion Wear Behavior of Selected Stainless Steels in Potash Brine," Wear, **258,** pp. 1357-1363.

[31] Anderko, A., Sridhar, N., Yang, L., Grise, S.L., Saldanha, B.J., and Dorsey, M.H., 2005, "Validation of Localized Corrosion Model Using Real Time Corrosion Monitoring in a Chemical Plant," Corrosion Engng, Sci. and Techn., **40**(1), pp. 33-42.

[32] Zhang, L., Han, E., Zhang, Z., Guan, H., and Ke, W., 2003, "The Corrosion of Stainless Steel and Nickel Base Alloys in Subcritical Water Condition," Acta Metall. Sinica, **39**(6), pp. 649-654.

[33] Lewis, A. C., Bingert, J. F., Rowenhorst, D. J., Gupta, A., Geltmacher, A. B., and Spanos, G., 2006, "Two – and Three-Dimensional Microstructural Characterization of a Super-Austenitic Stainless Steel," Mater. Sci. and Engng. **A418**, pp.11-18.

[34] Stauffer, A. C., Koss, D., A., and McKirgan, J. B., 2004, "Microstructural Banding and Failure of A Stainless Steel," **35** (4), pp. 1317-1324.

[35] Kusko, C.S., Dupont, J.N., and Marder, A.R., 2004, "The Influence of Microstructure on Fatigue Crack Propagation Behaviour of Stainless Steel Welds," Welding Journal, **83**(1), pp. 6s-14s.

[36] Metrovich, B., Fisher, J.W., Yen, B.T., Kaufmann, E.J., Cheng, X., and Ma, Z., 2003, "Fatigue Strength of Welded AL-6XN Superaustenitic Stainless Steel," Int. J. Fatigue, **25**(9-11), pp. 1309-1315.

[37] Guo, W., 2006, "Plastic Flow Stresses and Constitutive Models of Four Newer Naval Vessel Steels," Acta Metall. Sinica, **42**(5), pp. 463-468.

[38] Dawson, P.R., Boyce, D.E., Hale, R., and Durkot, J.P., 2005, "An Isoparametric Piecewise Representation of the Anisotropic Strength of Polycrystalline Solids," Int. J. Plast., **21**(2), pp. 251-283.

[39] Abed, F.H. and Voyiadjis, G.Z., 2005, "Plastic Deformation Modeling of AL-6XN Stainless Steel at low and High Strain Rates and Temperatures Using a Combination of bcc and fcc Mechanisms of Metals," Int. J. Plast., **21**(8), pp. 1618-1639.

[40] Liaw, P.K., Leax, T.R., and Donald, J.K., 1987, "Fatigue Crack Growth Behavior of 4340 Steels," Acta Metall. **35**(7), pp. 1415-1432.

[41] Dowling, N.E. Mechanical Behaviour of Materials. Englewood Cliffs (NJ): Prentice-Hall; 1999.

[42] Taylor, D.A. Compendium of Fatigue Threshold and Growth Rates. Warley, UK: EMAS Ltd.; 1985.

[43] Swain, M.H., Everett, R.A., Newman, J.C., and Phillips, E.P. The Growth of Short Cracks in 4340 Steel and Aluminum–Lithium 2090. In: Edwards, P.R., Newman, J.C., editors. AGARD R-767; 1990. p. 7.1–7.30.

[44] Wei, R.P., 1979, "On Understanding Environment-Enhanced Fatigue Crack Growth – a Fundamental Approach," Fatigue Mechanisms, ASTM STP 675, J.T. Fong, Ed., ASTM International, West Conshohocken, PA, pp. 816-840.

[45] Pao, P.S., Wei, W., and Wei, R.P., 1979, "Effect of Frequency on Fatigue Crack Growth Response of AISI 4340 Steel in Water Vapor." In: Environment Sensitive Fracture of Engineering Materials, Z.A. Faroulis, Ed., The Metallurgical Society of AIME, pp. 565-580.

[46] Lee, E.U., Vasudevan, A.K., 2005, "Environmentally Influenced Fatigue in High Strength Steels," Fatigue and Fracture Mechanics, 34(STP1461), pp. 151-163.

[47] Hwang, J-R., Peng, K-P., and Wang, C-C., 1996, "Effect of second phase on the fatigue crack growth in AISI 4340 steel," Journal of Materials Science Letters (UK), 15(3), pp. 192-196.

[48] Kim, S.H., Tai, W.P., 1992, "Retardation and arrest of fatigue crack growth in AISI 4340 steel by introducing rest periods and overloads," Fatigue Fract Engng Mater Struct (UK), 15(6), pp. 519-530.

[49] Ellyin, F., Wu, J., 1992, "Elastic-plastic analysis of a stationary crack under cyclic loading and effect of overload," Int J Fract (The Netherlands), 56(1), pp. 189-208.

[50] Nayeb-Hashemi, H., 1989, "Effect of Mode I and Mode II overloads on subsequent Mode I crack growth in AISI 4340 steels," Mechanical Engineering Publications, Biaxial and Multiaxial Fatigue, pp. 265-283.

[51] Yuen, B.K.C, Taheri, F., 2006, "Proposed Modifications to the Wheeler Retardation Model for Multiple Overloading Fatigue Life Prediction," Int J Fatigue **28**, pp. 1803-1819.

[52] Smith, K. N., Watson, P., and Topper, T. H., 1970, "A Stress Strain Function for the Fatigue of Metals," J. Mater. **5** (4), pp. 767-778.

[53] Jiang, Y., Sehitoglu, H., 1992, "Fatigue and Stress Analysis of Rolling Contact," Report No. 161, UILU-ENG 92-3602, College of Engineering, University of Illinois at Urbana-Champaign.

[54] Chu, C. C., Conle, F. A., and Bonnen, J. J., "Multiaxial Stress-Strain Modeling and Fatigue Life Prediction of SAE Axle Shafts," In: Advances in Multiaxial Fatigue, ASTM STP 1191.

[55] Chu, C. C., 1993, "Fatigue Damage Calculation Using the Critical Plane Approach," ASME J. Eng. Mat. Tech. **117**, pp. 41-49.

[56] Glinka, G., Shen, G., and Plumtree, A., 1995, "A Multi-Axial Fatigue Strain Energy Density Parameter Related to The Critical Fracture Plane," Fatigue Fract. Eng. Mat. Struct. **18**, pp. 37-46.

[57] Fatemi A, and Socie DF, 1988, "A Critical Plane Approach to Multiaxial Fatigue Damage including Out of Phase Loading," Fatigue Fract. Engng Mater. Struct. **11**, pp. 149-165.

[58] Fatemi, A., and Kurath, P., 1988, "Multiaxial Fatigue Life Predictions under The Influence of Mean Stress," ASME J. Engng. Mater. Tecnh. **110**, pp. 380-388.

[59] Jiang, Y., 2000, "A Fatigue Criterion for General Multiaxial Loading," Fat. Fract. Eng. Mat. Struct. **23**, pp. 19-32.

[60] Jiang, Y., and Kurath, P., 1997, "NonProportional Cyclic Deformation: Critical Experiments and Analytical Modeling," Int. J. Plasticity **13**, pp. 743-763.

[61] Sadananda, K., and Vasudevan, A. K., 1996, In: Lutjering G, Nowack H, editors. A unifed framework for fatigue crack growth. Fatigue 96, vol. 1. Berlin: Pergamon, pp. 375-80

[62] Vasudevan, A. K., Sadananda, K., and Louat, N. A., 1994, "A Review of Crack Closure, Fatigue Crack Threshold and Related Phenomena," Mater. Sci. Eng. **A188**, pp. 1-22.

[63] Vasudevan, A. K., and Sadananda, K., 1999, "Application of Unified Fatigue Damage Approach to Compression-Tension Region," Int. J. Fatigue **21**, pp. S263-S273.

[64] Sadananda, K., Vasudevan, A. K., and Holtz, R. L., 2001, "Extension of The Unified Approach to Fatigue Crack Growth to Environmental Interactions," Int. J. Fatigue **23**, pp. S277-S286.

[65] Vasudevan, A. K., Sadananda, K., and Glinka, G., 2001, "Critical Parameters for Fatigue Damage," Int J. Fatigue **23S**, pp. S39-S53.

[66] Sadananda, K., and Vasudevan, A. K., 2004, "Crack Tip Driving Forces and Crack Growth Representation under Fatigue," Int. J. Fatigue **26**, pp. 39-47.

[67] Kujawski, D., 2001, "A Fatigue Crack Driving Force Parameter with Load Ratio Effects," Int. J. Fatigue **23**, pp. S239–S246.

[68] Kujawski, D., 2001, "A New Driving Force Parameter for Crack Growth in Aluminum Alloys," Int. J. Fatigue **23**, pp. 733–740.

[69] Walker, K., 1970, "The Effect of Stress Ratio during Crack Propagation and Fatigue for 2024-T3 and 7075-T6 Aluminum," In: Effects of Environment and Complex Loading History on Fatigue Life, ASTM STP 462, Philadelphia (PA), American Society for Testing and Materials, pp. 1–14.

[70] Wheeler, O. E., 1972, "Spectrum Loading and Crack Growth," J. Basic Eng, Trans. ASME, **D94** (1), pp. 181–186.

[71] Irwin, G. R., 1957, "Analysis of Stresses and Strains near The End of A Crack Traversing A Plate," Trans. ASME J. Appl. Mech. **E24**, pp. 361.

[72] Antunes, F. V., Borrego, L. F. P., Costa, J. D., and Ferreira, J. M., 2004, "A Numerical Study of Fatigue Crack Closure Induced by Plasticity," Fatigue Fract. Engng. Struct. **27**, pp. 825-835.

[73] Rushton, P. A., and Taheri, F., 2003, "Prediction of Crack Growth in 350WT Steel Subjected to Constant Amplitude with Over- and Under-loads Using A Modified Wheeler Approach," Marine Structures **16**, pp. 517–539.

[74] Jiang, Y., Feng, M., 2004, "Modeling of Fatigue Crack Propagation," ASME J Eng Mater Techn **126**, pp. 77-86.

[75] Wang, X., Gao, Z., Zhao, T., and Jiang, Y., 2009, "An Experimental Study of the Crack Growth Behavior of 16MnR Pressure Vessel Steel," ASME J. Pressure Vessel Technol **131**, 021402

[76] Jiang, Y., and Sehitoglu, H., 1996, "Modeling of Cyclic Ratchetting Plasticity: Part I - Development of Constitutive Equations," J. Appl. Mech. **63**, pp. 720-725.

[77] Jiang, Y., and Sehitoglu, H., 1996, "Modeling of Cyclic Ratchetting Plasticity: Part II – Implementation of The New Model and Comparison of Theory with Experiments," J. Appl. Mech. **63**, pp. 726-733.

[78] Jiang, Y., Kurath, P., 1997, "An Investigation of Cyclic Transient Behavior and Implications on Fatigue Life Estimates" ASME J Engng Mater Techn **119**, pp. 161-170.

[79] Jiang, Y., Hertel, O., and Vormwald, M., 2007, "An Experimental Evaluation of Three Critical Plane Multiaxial Fatigue Criteria," Int. J. Fatigue **29**, pp.1490-1502.

[80] ABAQUS, 1999, *User's Manual and Theory Manual*, Hibbit, Karlsson and Sorensen, Inc.

[81] Jiang, Y., Xu, B., and Sehitoglu, H., 2002, "Three-Dimensional Elastic-Plastic Stress Analysis of Rolling Contact," ASME Journal of Tribology **124**, pp. 699-708.

[82] Altair HyperMesh, Version 5.0. 2001, Altair Engineering, Inc.

[83] Ding, F., Feng, M., and Jiang, Y., 2007, "Modeling of Fatigue Crack Growth from a Notch," Int J Plasticity, **23**(7), pp.1167-1188.

[84] Kurath, P., Jiang, Y., 1997, "Analysis of Residual Stresses and Cyclic Deformation for Induction Hardened Components." In: Recent Developments in Fatigue Technology, Chernenkoff, R.A., Bonnen, J.J., Editors. SAE, Warrendale, PA, pp. 337-351.

[85] Obrtlik, K., Kruml, T., Polak, J., 1993, "Dislocation Structures in 316L Stainless Steel Cycled With Plastic Strain Amplitudes Over a Wide Interval," Mat Sci Engng **A187**, pp. 1-9.

[86] Sih, G. C., Barthelemy, B. M., 1980, "Mixed Mode Fatigue Crack Growth Predictions," Eng Fract Mech **13**, pp. 439-451.

[87] Sih, G. C., Bowie, O.L., 1992, "Mechanics of Fracture Initiation and Propagation," Applied Mechanics Reviews **45**(1), B6.

[88] Badaliance, R., 1980, "Application of Strain Energy Density Factor to Fatigue Crack Growth Analysis," Eng Fract Mech **13**, pp. 657-666.

[89] Tian, D.C., Lu, D.Q., Zhu, J.J., 1982, "Crack Propagation Under Combined Stresses in Three-Dimensional Medium," Eng Fract Mech **16**, pp. 5-17.

[90] Ding, F., Zhao, T., and Jiang, Y., 2007, "A Study of Fatigue Crack Growth with Changing Loading Direction," Eng Fract Mech **74**, pp.2014-2029